# MEASUREMENT OF THE $b\bar{b}$ CROSS SECTION AND CORRELATIONS USING DIMUON EVENTS IN $p\bar{p}$ COLLISIONS AT $\sqrt{s} = 1.8$ TeV

by

David Kevin Fein

---

A Dissertation Submitted to the Faculty of the

DEPARTMENT OF PHYSICS

In Partial Fulfillment of the Requirements
For the Degree of

DOCTOR OF PHILOSOPHY

In the Graduate College

THE UNIVERSITY OF ARIZONA

1 9 9 6

# STATEMENT BY AUTHOR

This dissertation has been submitted in partial fulfillment of requirements for an advanced degree at The University of Arizona and is deposited in the University Library to be made available to borrowers under rules of the Library.

Brief quotations from this dissertation are allowable without special permission, provided that accurate acknowledgement of source is made. Requests for permission for extended quotation from or reproduction of this manuscript in whole or in part may be granted by the head of the major department or the Dean of the Graduate College when in his or her judgement the proposed use of the material is in the interests of scholarship. In all other instances, however, permission must be obtained from the author.

SIGNED: _____

# ACKNOWLEDGEMENTS

A number of people have played an important role in helping make this dissertation possible. Clearly my advisor, Ken Johns, has played the largest role. His guidance, unwavering support, and friendship have made this endeavor both interesting and enjoyable. All graduate students would benefit from having an advisor as great as Ken. Alex Smith and Eric James also deserve special thanks. Without their assistance with this analysis I might still be analyzing events. Even more importantly, their friendship has made life, well, interesting at times. Our time in Batavia will not be forgotten anytime soon. Special thanks also goes to the high energy group at the University of Arizona, in particular Leif Shaver and Mike Eklund. Iris Wright also deserves a special thank you for her help with university red tape and for always having a laugh and a smile.

I have also enjoyed working with the members of the $b$ physics group at DØ. Dave Hedin and Andrzej Zieminski deserve special mention for their help and insight which they provided over the course of this analysis. A thank you also goes to everyone who has worked on the DØ detector and the Fermilab Tevatron collider. The hard work of these people has helped make high energy physics in the United States a rich and diverse field.

I owe thanks to my friends who have been an important part of my life. In particular, I would like to thank Andy Milder, Ron Norton, Jesus Pando, Michael "Kimone" Tooke, and life long friend Todd Betke. A special thank you goes to Sera Markoff who has always been there through the highs and lows. Finally, I would like to thank my entire family for their love and support through this long ritual. Not once did they question my desire, and sometimes blind commitment, to reach this goal. I hope this brings as much joy to them as it has for me.

To my parents,

Lillian, and Carl.

# TABLE OF CONTENTS

# LIST OF FIGURES

# LIST OF TABLES

# ABSTRACT

We have measured the $b$-quark production cross section for $|y| < 1$ using a sample of dimuon events collected with the DØ detector in $p\overline{p}$ collisions at $\sqrt{s} = 1.8$ TeV at the Fermilab Tevatron. The measured $b$-quark cross section is consistent with $\mathcal{O}(\alpha_s^3)$ QCD predictions, but lies at the upper limit of the theoretical uncertainties which is a factor of 1.5 above the mean value. A study of the difference in azimuthal angle of the two muons is in good qualitative agreement with the $\mathcal{O}(\alpha_s^3)$ QCD predictions.

# Chapter 1

# Introduction

Particle physics is the study of the fundamental components of nature and their interactions. We presently believe the elementary building blocks of nature to consist of 12 fermions (spin-$\frac{1}{2}$), their associated anti-particles, and the gauge bosons which mediate interactions between them. The fermions are grouped into three generations of leptons and quarks :

$$\begin{pmatrix} \nu_e \\ e \end{pmatrix} \quad \begin{pmatrix} \nu_\mu \\ \mu \end{pmatrix} \quad \begin{pmatrix} \nu_\tau \\ \tau \end{pmatrix} \quad \text{Leptons}$$

$$\begin{pmatrix} u \\ d \end{pmatrix} \quad \begin{pmatrix} c \\ s \end{pmatrix} \quad \begin{pmatrix} t \\ b \end{pmatrix} \quad \text{Quarks.}$$

Until recently, only the $t$ quark's existence had yet to be confirmed[1, 2]. It is the investigation of one of these particles, the *beauty* or *bottom* quark, which is the topic of this thesis.

The charged leptons, which include the $e$, $\mu$, and $\tau$, were the first family of fermions to be discovered. This is due in part to the fact that they interact

| Lepton | Electric Charge [$e$] | Mass [MeV/c$^2$] | Lifetime [s] |
|---|---|---|---|
| $\nu_e$ | 0 | $<$5.1 eV/c$^2$ | stable |
| $e$ | -1 | 0.51100 | stable |
| $\nu_\mu$ | 0 | $<$0.27 | stable |
| $\mu$ | -1 | 105.66 | $2.20\times10^{-6}$ |
| $\nu_\tau$ | 0 | $<$31 | stable |
| $\tau$ | -1 | 1777.1 | $2.96\times10^{-13}$ |

Table 1-1: The Lepton Spectrum

through the electromagnetic and weak forces and are not obscured through the strong interaction. The muon($\mu$) was discovered in cloud-chamber experiments in 1937[3], and the tau-lepton($\tau$) was first observed in 1975[4]. Both of these leptons are identical to the electron except for their mass and lepton family number.

The associated neutrinos($\nu_e, \nu_\mu, \nu_\tau$) are all assumed to be massless, although experimentally only upper limits on their masses have been established[5]. They are much more difficult to observe because they only interact through the weak force. The existence of the electron neutrino was used to describe the continuous electron energy spectrum in neutron $\beta$-decay($n \rightarrow pe^-\overline{\nu_e}$) in 1934 by Enrico Fermi[6]. The existence of the muon neutrino was firmly established by 1963[7], and there is evidence[8] for the existence of the tau neutrino. Table 1-1 lists the properties of the lepton spectrum[5].

The other half of the fermions consists of quarks. Quarks are very unlike leptons in that they can not be observed as free particles. This is a consequence of the strong interaction which binds the quarks into hadronic matter. The three lightest quarks, up($u$), down($d$), and strange($s$), were proposed by Gell-Mann and Zweig[9] in 1964 to explain the $SU(3)$ grouping of hadrons then observed. Later

| Quark | Electric Charge [$e$] | Effective Mass [GeV/c$^2$] |
|---|---|---|
| $u$ | +2/3 | $\sim$ 0.004 |
| $d$ | -1/3 | $\sim$ 0.005 |
| $c$ | +2/3 | $\sim$ 1.5 |
| $s$ | -1/3 | $\sim$ 0.2 |
| $t$ | +2/3 | $\sim$ 199 |
| $b$ | -1/3 | $\sim$ 4.5 |

Table 1-2: The Quark Spectrum

discoveries of bound $c\bar{c}$ states[10] and $b\bar{b}$ states[11] provided strong support for the quark structure of matter. Most recently, the existence of the top($t$) quark was confirmed[1, 2] with $M_{top}$ = 199 GeV/c$^2$[1]. A summary of quark parameters is given in Table 1-2.

The leptons and quarks interact via four forces: gravity, the weak force, electromagnetism, and the strong force. Each force is mediated by a different particle, or propagator, called a gauge boson(particles with integral spin). In addition, these forces act upon matter with different strengths which are referred to as couplings. Table 1-3 summarizes the properties of the four known forces.

The way in which these forces govern the behavior of particles is described by field theories. Each field theory is locally gauge invariant, which requires the introduction of gauge bosons. In the Lagrangian formalism, conserved quantities, such as charge in electrodynamics and color in quantum chromodynamics, appear as symmetries under which the Lagrangian is invariant. In each field theory, rewriting the Lagrangian after it is made locally gauge invariant, specifies the interaction.

In quantum electrodynamics (QED), the Lagrangian is constructed with the

| Force | Gauge Boson | | Coupling Strengths | Fermions Affected |
|---|---|---|---|---|
| | Name | Mass [GeV/c$^2$] | | |
| gravity | graviton | 0 | $\sim 10^{-38}$ | all fermions with mass |
| weak | intermediate bosons ($W^{\pm}, Z^{\circ}$) | $M_W$=80 $M_Z$=91 | $\sim 10^{-5}$ | all fermions |
| electro-magnetic | photon ($\gamma$) | 0 | $\frac{1}{137}$ | charged leptons and quarks |
| strong | gluon (g) | 0 | $\sim 1$ | quarks |

Table 1-3: Summary of Forces

proper symmetries which correspond to the interactions described by Dirac's equations. QED is a local gauge theory because the Lagrangian that describes it is invariant under transformations of the electron field

$$\psi(x) \rightarrow e^{ie\Lambda(x)}\psi(x), \tag{1.1}$$

and the photon field

$$A_\mu(x) \rightarrow A_\mu(x) + \partial_\mu\Lambda(x), \tag{1.2}$$

where $\Lambda(x)$ is arbitrary and $e$ is the electron-photon coupling. The phase factor $e^{i\Lambda(x)}$ belongs to the symmetry group $U(1)$ of unitary transformations in one dimension. In general, the gauge groups are more complicated than the $U(1)$ symmetry group of electromagnetism. To move to other forces, one must look for other possible symmetry groups and use them as the basis of more general gauge

transformations[12].

Leptons and quarks are arranged in doublets. The first family of doublets include $\begin{pmatrix} \nu_e \\ e \end{pmatrix}$ and $\begin{pmatrix} u \\ d \end{pmatrix}$ since they are the lightest leptons and quarks. These doublets can be described by a two-component field, $\psi = (\psi_{\nu_e}, \psi_e)$, for example. We can then introduce gauge transformations, $\Lambda$, where $\Lambda$ is a $2\times2$ hermitian matrix. Now, unlike the case in electromagnetism, these gauge transformations are more than simple phase factors since the off diagonal elements of $\Lambda$ can change one member of a doublet into the other. This assignment suggest an $SU(2)_L$ symmetry. Since local gauge invariance is still required, the introduction of three massless gauge bosons is needed. If this group is then combined with the electromagnetic group $U(1)$, which introduces another gauge boson, we get the $SU(2)_L \otimes U(1)$ Glashow-Salam-Weinberg theory[13] of electroweak interactions.

The strong interaction symmetry is an $SU(3)_C$ symmetry since each quark can occur in one of three possible colors. Therefore we describe any particular quark flavor by a three-component field, $\psi = (\psi(red), \psi(blue), \psi(green))$, and consider a local gauge transformation where $\Lambda(x)$ is now a $3\times3$ hermitian matrix. In this case, eight massless gauge bosons are required to ensure local gauge invariance. These gauge bosons are the gluons associated with the strong force mentioned earlier. This gauge theory is referred to as quantum chromodynamics (QCD).

Finally, if we combine the previous three symmetry groups together, $SU(3)_C \otimes SU(2)_L \otimes U(1)$, this gives a gauge invariant theory of the strong and electroweak forces known as the Standard Model.

## 1.1 The Standard Model

The Standard Model (SM) is the currently accepted theory which describes the electroweak and strong interactions and has proven to be very successful. There has yet to be any measurement to date which significantly contradicts it. At the same time, the SM has made very accurate predictions on many observables such as cross sections, decay rates, and most notably, the masses of the intermediate vector bosons ($W^{\pm}, Z^{\circ}$).

The SM can be thought of as a union of two different theories: the electroweak (EW) theory, which is represented by the $SU(2)_L \otimes U(1)_Y$ gauge group and describes the electromagnetic and weak interactions, and quantum chromodynamics (QCD), which describes the strong interaction and is represented by the gauge group $SU(3)_C$. Attempts have been made to try and unify these two theories into a single higher dimensional gauge group, or Grand Unified Theory (GUT). This would reduce the theoretically unsatisfying large number of arbitrary parameters associated with the SM(the three coupling constants, the Higgs mass, and all the fermion masses). Unfortunately, no GUT has been successfully developed, and it is still useful for us to view the electroweak and strong interactions as separate.

### 1.1.1 Electroweak Theory

The SM of weak interactions unifies both the electromagnetic (EM) interaction and the weak interaction. The EW theory was constructed to be invariant under two types of gauge transformations, both of which are described by the interaction of a weak current coupled to a vector boson:

- Weak Isospin, $T$, the generator of the $SU(2)_L$ gauge transformation, and

- Weak Hypercharge, $Y$, the generator of the $U(1)$ gauge transformation, where $Y$ is related to the electric charge and the weak isospin projection, $T_3$, by $Q = T_3 + \frac{1}{2}Y$. This relationship is in analogy with the Gell-Mann-Nishijima formula for strong interaction quantum numbers.

The gauge group of electroweak theory is taken to be the product of transformations under $T$ and $Y$, $SU(2)_L \otimes U(1)$. For this group of transformations, right-handed fermions are assigned to transform under $U(1)$ only with no right-handed neutrinos (right-handed neutrinos have yet to be discovered). The left-handed fermions transform under both $SU(2)_L$ and $U(1)$.

The requirement of local gauge invariance under $SU(2)_L \otimes U(1)$ transformations necessitates the introduction of four massless gauge bosons - three are generated from the $SU(2)_L$ group ($W_\mu$) and one for $U(1)$ ($B_\mu$). The gauge formalism used up to now describes only massless bosons (and fermions). The massless nature of the intermediate gauge bosons, $W^\pm$ and $Z^\circ$, clearly contradicts the observation that they must be massive in order to account for the short range of the weak force. Therefore, in order to generate the particle masses in a gauge invariant way, the Higgs mechanism[14] is used which spontaneously breaks the gauge symmetry while allowing the theory to remain renormalizable.

The Higgs mechanism is formulated such that the $W^\pm$ and $Z^\circ$ become massive while the photon remains massless. This is accomplished by introducing a coupling to an additional scalar isospin doublet with weak hypercharge $Y = 1$:

$$\phi = \begin{pmatrix} \phi^+ \\ \phi^\circ \end{pmatrix} \text{ with } \begin{array}{l} \phi^+ \equiv (\phi_1 + i\phi_2)/\sqrt{2}, \\ \phi^\circ \equiv (\phi_3 + i\phi_4)/\sqrt{2}. \end{array} \tag{1.3}$$

To generate the gauge boson masses from the coupling in (1.3), the Higgs potential,

$$V(\phi) = \mu^2\phi^\dagger\phi + \lambda(\phi^\dagger\phi)^2, \tag{1.4}$$

is chosen with $\mu^2 < 0$ and $\lambda > 0$. This has a non-zero vacuum expectation value of

$$\langle\phi\rangle_\circ = \frac{1}{\sqrt{2}}\begin{pmatrix} 0 \\ v \end{pmatrix}, \tag{1.5}$$

where $v^2 \equiv \frac{-\mu^2}{\lambda}$. It is the realization of this non-zero vacuum expectation value which spontaneously breaks the $SU(2)_L \otimes U(1)_Y$ symmetry and leads to the generation of the gauge boson masses.

In addition to supplying masses to the desired particles, the Higgs mechanism also creates a massive scalar called the Higgs boson. This particle has yet to be observed and its mass is left as a free parameter in the theory. The mass of the Higgs boson is one of the few experimentally untested predictions of the Standard Model.

### 1.1.2 QCD

Quantum Chromodynamics (QCD) is the currently accepted gauge field theory of the strong interaction. Only a brief introduction into QCD will be presented here since a test of QCD is the topic of this thesis. Aspects of QCD which are relevant to heavy quark production will be discussed in detail in Chapter 2.

The theory of QCD is based on the $SU(3)_C$ gauge group, where the associated quantum number is called color. $SU(3)_C$ requires 8 massless gauge bosons, called

gluons, which carry the color charge. Since QCD is a non-Abelian field theory, the gluons can interact with each other in much the same way the vector bosons do in the theory of weak interactions.

Color charge plays a crucial role in describing the final state particles observed. As shown in Table 1-3, only gluons and quarks, also known as partons, participate in the strong interaction. Each quark carries one of three colors, commonly referred to as red, green, and blue, while each gluon is bicolored. As a quark and antiquark separate, their color interaction becomes stronger. The color field lines of force between the two quarks are squeezed into a tube-like region because the gluons interact with one another. This is very different from the QED picture where nothing exists which prevents the lines of force from spreading out. If the color tube has a constant energy density per unit length, the potential energy between the quark and antiquark increases as they separate, thereby preventing the quarks and gluons from escaping. This feature of QCD is known as infrared slavery.

At some point, the potential energy between the $q\overline{q}$ pair is great enough to create another $q\overline{q}$ pair. The new $q\overline{q}$ pair now act as the end points for the color lines of force. Meanwhile, the original $q\overline{q}$ pair continue to separate and produce additional $q\overline{q}$ pairs until eventually the kinetic energy of the quarks is small enough so the color lines are not stretching any further. These final clusters of quarks and gluons have zero net color and low internal momentum and are therefore strongly color coupled. These clusters are known as hadrons and explains how quarks and gluons are confined to colorless final states. This feature of QCD will be discussed in further detail in Chapter 2.

There are two types of hadrons, mesons and baryons. Mesons are represented as a quark-antiquark bound state ($q\overline{q}$), while baryons are represented as a combination of a 3 (anti)quark bound state ($\overline{q}\overline{q}\overline{q}$ or $qqq$).

## 1.2 Importance of $b$-Physics

The general goal of this thesis is to make a benchmark test of perturbative QCD by making a quantitative comparison of experimental data with theoretical predictions of heavy quark production. This is possible because the $b$-quark can be identified experimentally. Also, the $b$-quark has a non-zero mass which makes theoretical predictions for its production more reliable than for lighter quarks because of the larger $p_T$ scale. Theoretical calculations correct to order $\mathcal{O}(\alpha_s^3)$ (NLO) exist for the $b$-quark inclusive cross section as well as the fully exclusive $b\bar{b}$ cross section. Thus, two distinct tests of perturbative QCD can be made. The first involves a comparison of the $b$-quark production cross section between data and theory. The second test is somewhat more subtle in that the production topologies of the heavy quark pair, such as their correlation in azimuthal angle, are compared. Both measurements provide a good test of the current procedures and pieces of perturbative QCD.

Several years ago when this analysis was first initiated, measurements by the CDF collaboration showed that the measured $b$-quark cross section was a factor of three higher than the $\mathcal{O}(\alpha_s^3)$ prediction which catalyzed theoretical efforts to explain this difference through various corrections. It also helped motivate additional measurements such as done in this thesis. Knowledge that perturbative QCD to a given order does or does not describe data is important towards understanding the reliability of other QCD predictions such as for top quark production. In addition, with measurements at even higher energies such as at the LHC anticipated, agreement between data and theory at lower energies gives one confidence in trusting and using predictions at higher energies.

# Chapter 2

# Theory of Heavy Quark Production

In hadron-hadron interactions, heavy quarks ($Q = c, b$) are produced in the hard collisions of a parton from each hadron. The general form of the heavy quark production cross section in collisions between hadrons $A$ and $B$ is[18]

$$d\sigma(s) = \sum_{i,j} \int dx_A dx_B d\hat{\sigma}_{ij}(x_A x_B s, m^2, \mu_1^2) F_i^A(x_A, \mu_2) F_j^B(x_B, \mu_2) \tag{2.1}$$

where $\sqrt{s}$ is the total center-of-mass energy of the $A + B$ hadron system, $F_i^A$ are the structure functions which measure the probability of parton $i$ in hadron $A$ to carry fractional momentum $x_A$, $m$ is the heavy quark mass, $\mu_1$ and $\mu_2$ are the renormalization and factorization scales, and $d\hat{\sigma}_{ij}$ is the short-distance partonic cross section for the process $ij \to Q\overline{Q}X$ which occurs at the effective center-of-mass energy

$$\hat{s} = x_A x_B s. \tag{2.2}$$

The terms involved in calculating $d\sigma(s)$ can not be calculated exactly. Instead, they are expanded into a perturbative power series in the strong coupling constant

$\alpha_s$

$$d\hat{\sigma}_{ij}(\hat{s}, m^2, \mu_1^2) = \alpha_s^2(\mu_1) f_{ij}^{(0)}(\hat{s}, m^2) + \alpha_s^3(\mu_1) f_{ij}^{(1)}(\hat{s}, m^2) + \cdots \quad (2.3)$$

$$F_i^A(x_A, \mu_2) = g_i^{A,(0)}(x_A, \mu_2) + \alpha_s(\mu_2) g_i^{A,(1)}(x_A, \mu_2) + \cdots \quad (2.4)$$

where the functions $f, g$ and the constants $\mu_1, \mu_2$ depend upon the scheme used for renormalization and factorization. The indices (0) and (1) refer to the leading order(LO) and next-to-leading order(NLO) terms respectively. To simplify calculations, it is usually customary to set the renormalization and factorization scales equal to each other, $\mu = \mu_1 = \mu_2$.

To calculate the total heavy quark production cross section is then an exercise in determining the partonic cross sections derived to some order in $\alpha_s$, and then convoluting them with the structure functions. This technique was followed using complete $\mathcal{O}(\alpha_s^3)$ calculations by Nason, Dawson, and Ellis (NDE)[18, 15, 20]. The following sections outline the formalisms of the NDE calculation and its predictions for heavy quark production at $p\overline{p}$ colliders.

## 2.1 The Strong Coupling Constant

The first step in calculating the heavy quark production cross section is deciding on what value to use for the strong coupling constant, $\alpha_s$. The strong coupling constant is not really a constant but depends upon the 4-momentum transfer of the process involved. It is useful to describe the strong coupling constant at some fixed scale $\mu = Q_0$, called the renormalization scale. Although $\mu$ is a free parameter, it should reflect the mass scale of the process being described and is usually chosen to be evaluated at the mass of the heavy quark. The scale dependence of the coupling

constant is determined by the renormalization group equation

$$\begin{aligned}\frac{\partial\alpha_s(\mu)}{\partial \ln \mu^2} &= \mu^2 \frac{\partial\alpha_s(\mu)}{\partial\mu^2} \\ &= \beta(\alpha_s(\mu)) \\ &= -b_0\alpha_s^2(\mu) - b_1\alpha_s^3(\mu) + \mathcal{O}(\alpha_s^4(\mu)) \end{aligned} \tag{2.5}$$

where

$$b_0 = \frac{33 - 2N_f}{12\pi} = \frac{11N_c - 2N_f}{12\pi} \tag{2.6}$$

and

$$b_1 = \frac{153 - 19N_f}{24\pi^2} = \frac{51N_c - 19N_f}{24\pi^2}. \tag{2.7}$$

Here, $N_f$ is the number of light flavors, defined as the number of flavors with $m_f < \mu$, and $N_c$ is the number of colors in $SU(3)$. The positive contributions from (2.6) and (2.7) correspond to non-Abelian 3-gluon vertex diagrams, while the negative contributions(terms involving $N_f$) come from quark loop diagrams. Neglecting all terms in (2.5) of order higher than $\mathcal{O}(\alpha_s^2)$, the solution yields the lowest order approximation to the 'running' coupling constant

$$\alpha_s(\mu) = \frac{\alpha_s(\mu_0)}{1 + b_0\alpha_s(\mu_0)\ln(\mu^2/\mu_0^2)}. \tag{2.8}$$

It appears as though (2.8) depends on both $\alpha_s(\mu_0)$ and $\mu_0^2$, but we know it has to be independent of the initial starting point $\mu_0$. It is convenient to write $\alpha_s(\mu)$ in terms of a single variable, $\Lambda$, the QCD mass scale, where

$$\ln\frac{\mu^2}{\Lambda^2} = -\int_{\alpha_s(\mu)}^{\infty}\frac{dx}{\beta(x)} \tag{2.9}$$

so that

$$\alpha_s(\mu) = \frac{1}{b_0\ln(\mu^2/\Lambda^2)}. \tag{2.10}$$

$\Lambda$ is a measure of the scale at which the QCD coupling approaches unity, and is typically less than 1 GeV.

If we examine the structure of $b_0$, we see that for standard QCD, $b_0$ is always positive since $11N_c > 2N_f$ ($N_c = 3$ and $3 \leq N_f \leq 6$). This implies that $\alpha_s$ increases with decreasing $\mu$. Therefore, $\alpha_s$ is unbounded as $\mu \to 0$(large distance interactions) and can become greater than the value of one above which the perturbative approach becomes meaningless. This indicates that an infinite amount of energy is needed to separate bound quarks and gluons from each other. Therefore, quarks and gluons can not exist as free particles, but must be bound into color singlet states, or hadrons. This feature of QCD is known as confinement. Conversely, $\alpha_s \to 0$ as $\mu \to \infty$(small distance interactions), and the forces between the quarks and gluons at small distances essentially vanishes. This is known as asymptotic freedom.

Allowing terms of $\mathcal{O}(\alpha_s^3)$ into (2.5) yields

$$b_0 \ln(\mu^2/\mu_0^2) = \frac{1}{\alpha_s(\mu)} - \frac{1}{\alpha_s(\mu_0)} + \frac{b_1}{b_0}\ln(\frac{\alpha_s(\mu)}{1+\frac{b_1}{b_0}\alpha_s(\mu)}) - \frac{b_1}{b_0}\ln(\frac{\alpha_s(\mu_0)}{1+\frac{b_1}{b_0}\alpha_s(\mu_0)}). \quad (2.11)$$

This gives the next-to-leading order solution to $\alpha_s$

$$\alpha_s(\mu) = \frac{1}{b_0 \ln(\mu^2/\Lambda^2)}\left[1 - \frac{b_1}{b_0^2}\frac{\ln(\ln(\mu^2/\Lambda^2))}{\ln(\mu^2/\Lambda^2)}\right]. \quad (2.12)$$

From (2.9) we see that the choice of $\Lambda$ depends on the somewhat arbitrary choice of $\mu$. This means that the leading order and next-to-leading order solutions to $\alpha_s(\mu)$ are not unique, but depend on the renormalization scheme used. Unless otherwise indicated, this thesis uses the "modified minimal subtraction", or $\overline{MS}$ scheme[21], to next-to-leading order to define $\Lambda$.

## 2.2 Parton-Parton Cross Sections

### 2.2.1 The Leading Order Calculation

To lowest order, $\mathcal{O}(\alpha_s^2)$, in QCD, heavy quarks, $Q$, are produced via gluon-gluon fusion and quark-antiquark annihilation:

$$\begin{aligned} g(p_1) + g(p_2) &\rightarrow Q(k_3) + \overline{Q}(k_4) \\ q(p_1) + \overline{q}(p_2) &\rightarrow Q(k_3) + \overline{Q}(k_4). \end{aligned} \tag{2.13}$$

These processes are represented by the Feynman diagrams in Fig. 2-1. The matrix elements for these processes have been available for some time[15] and are given in Table 2-1. Here, the squared matrix elements are averaged(summed) over initial(final) colors and spins, and the following ratios of scalar products are defined as

$$\tau_1 = \frac{2p_1 \cdot k_3}{\hat{s}} = \frac{m_Q^2 - \hat{t}}{\hat{s}}, \quad \tau_2 = \frac{2p_1 \cdot k_4}{\hat{s}} = \frac{m_Q^2 - \hat{u}}{\hat{s}}, \quad \rho = \frac{4m_Q^2}{\hat{s}}, \tag{2.14}$$

where $\hat{s}$, $\hat{t}$, and $\hat{u}$ are the Mandelstam variables describing the parton scattering process. In the center of mass system($\vec{k}_3 = -\vec{k}_4$, $y_3 = -y_4 = y$, where $y$ is the rapidity of the heavy quark), the partonic cross section for the production of a single heavy quark is

$$\frac{d\hat{\sigma}_{ij}}{dy d^2k_T} = \frac{1}{\hat{s}^2}\delta(1 - \tau_1 - \tau_2) \sum |\overline{\mathcal{M}_{ij}}|^2 \tag{2.15}$$

where $k_T$ is the heavy quark transverse momentum.

The leading order calculations for the heavy quark cross sections should be fairly reliable for $b$ and $t$ production, since their masses are well into the region where perturbation theory is expected to work(small $\alpha_s$). For $c$ quark production,

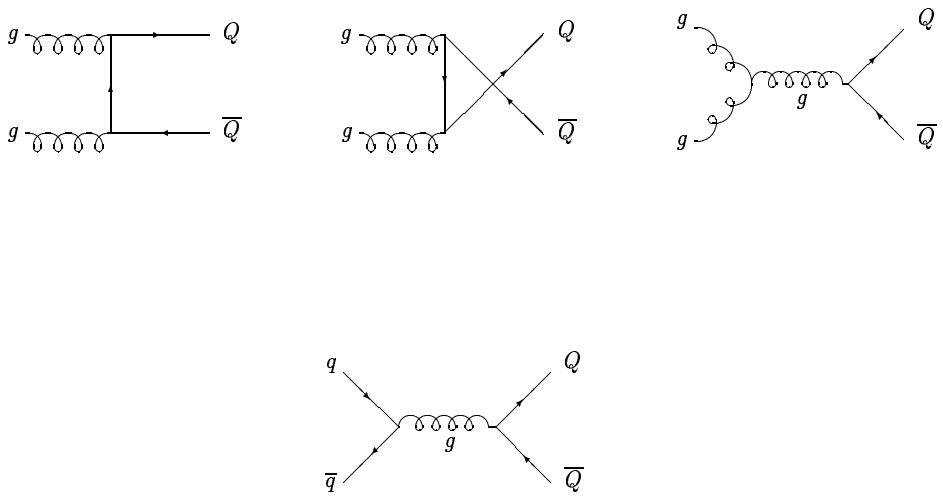


Figure 2-1: Feynman diagrams for lowest order heavy quark production.

| Process | $\sum \lvert\overline{\mathcal{M}_{ij}}\rvert^2$ |
|---|---|
| $gg \to Q\overline{Q}$ | $\frac{2T_f}{D_A}\alpha_s^2(\frac{C_f}{\tau_1\tau_2} - C_A)(\tau_1^2 + \tau_2^2 + \rho - \frac{\rho^2}{4\tau_1\tau_2})$ |
| $q\overline{q} \to Q\overline{Q}$ | $\frac{C_f^2}{D_A}\alpha_s^2(2\tau_1^2 + 2\tau_2^2 + \rho)$ |

Table 2-1: Squared matrix elements for the lowest order contribution to heavy quark production. The constants $C_A, C_f, D_A$, and $T_f$ depend on the representation used. For color $SU(3)_c$ their values are $C_A = 3,\ C_f = 4/3,\ D_A = 8$, and $T_f = 1/2$.

the results will be approximate at best since $m_c = 1.6$ GeV/c$^2$ approaches the region where $\alpha_s$ becomes large(see (2.10) with $\mu = m_q$). In addition, the leading order calculations predict that the heavy quarks be produced mainly in the region $\Delta y \leq 1$ and that the transverse momentum be on the order of the heavy quark mass: $\langle p_T \rangle \sim m_Q$.

### 2.2.2 Higher Order Corrections

Naïve expectations, which hold true for inclusive jet production, are that the contribution from higher order processes should be at the 10-20% level since these contributions are suppressed by at least one power in $\alpha_s$. Heavy flavor production turns out to be an exception to this general rule of QCD. This feature is most easily seen by noting that the process $gg \rightarrow gg$, which does not contribute to the lowest order cross section, is heavily favored over $gg \rightarrow Q\overline{Q}$[18]

$$\frac{\sigma(gg \rightarrow gg)}{\sigma(gg \rightarrow Q\overline{Q})} \sim 100, \tag{2.16}$$

and that the subsequent splitting of a final state gluon into a $Q\overline{Q}$ pair is suppressed by a power of $\alpha_s$. Thus, the higher order process

$$\begin{aligned} gg &\rightarrow g^* g \\ &\hookrightarrow Q\overline{Q} \end{aligned} \tag{2.17}$$

shown in Fig. 2-2(b), should have a sizeable contribution compared to lowest order production. Similarly, the process where an initial state gluon splits into a $Q\overline{Q}$ pair(also suppressed by one power of $\alpha_s$) and one of the heavy quarks then participates in the hard scatter(Fig. 2-2(c)) can also have a significant contribution. Note that (2.16) is only an estimate since it is only valid for on-mass-shell gluons. Since the virtual gluon, $g^*$, in (2.17), is off-mass-shell by an amount on the order

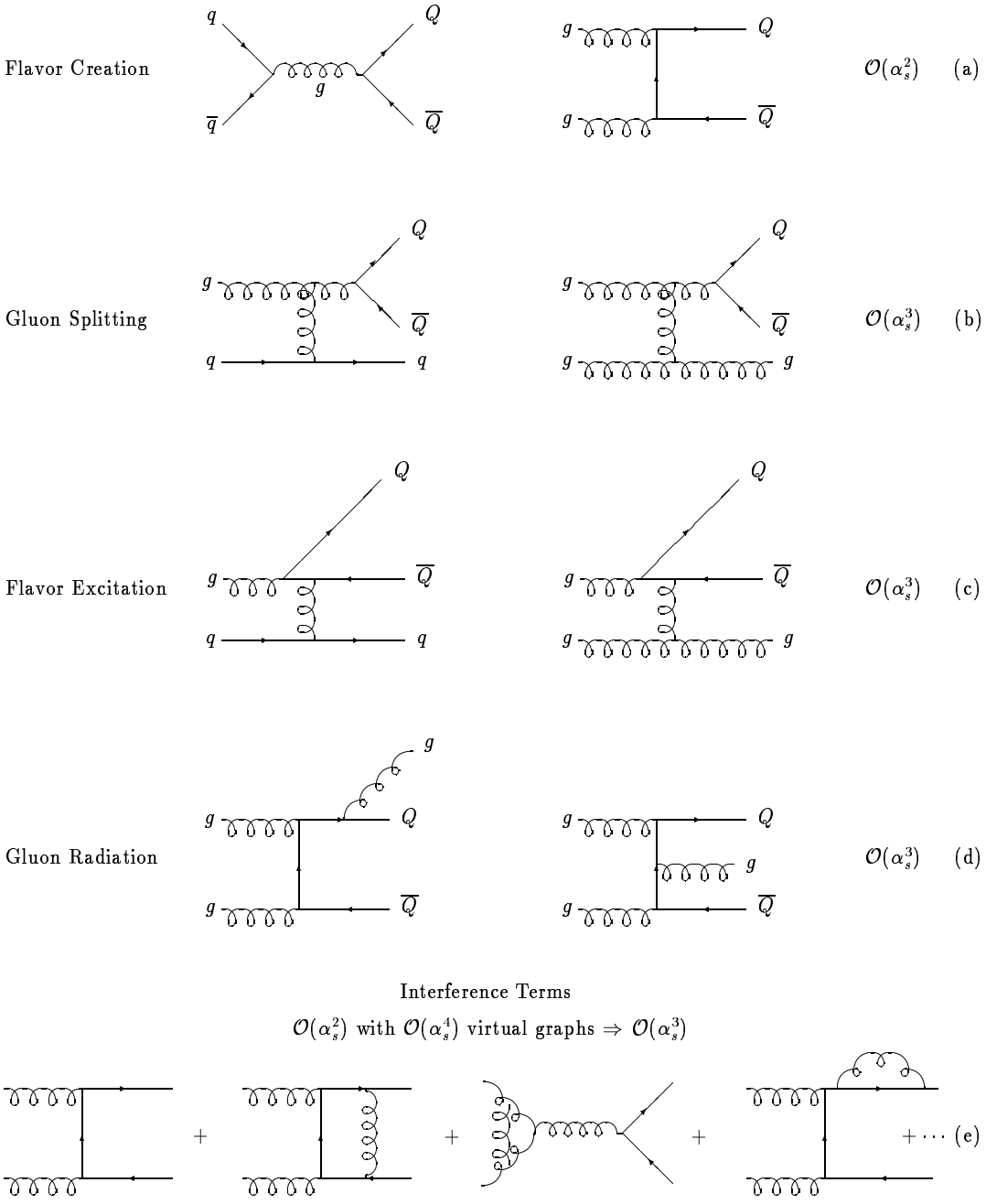


Figure 2-2: Feynman diagrams for $\mathcal{O}(\alpha_s^3)$ heavy quark production for lowest order 'flavor creation' process (a), next-to-leading order processes (b)-(d), and additional processes which include virtual diagrams that interfere with the leading order process (e).

of the heavy quark mass, this leads to a reduction in the ratio in (2.16).

Full $\mathcal{O}(\alpha_s^3)$ calculations for inclusive heavy quark production cross sections have been made by Nason, Dawson, and Ellis[18, 15, 16]. These calculations have also been extended into fully differential calculations by Mangano, Nason, and Ridolfi[20]. In these calculations, all of the following processes are considered:

$$\begin{aligned} q\overline{q} &\rightarrow Q\overline{Q}, \quad \alpha_s^2, \alpha_s^3 \\ gg &\rightarrow Q\overline{Q}, \quad \alpha_s^2, \alpha_s^3 \\ q\overline{q} &\rightarrow Q\overline{Q}g, \quad \alpha_s^3 \\ gg &\rightarrow Q\overline{Q}g, \quad \alpha_s^3 \\ gq &\rightarrow Q\overline{Q}g, \quad \alpha_s^3 \\ g\overline{q} &\rightarrow Q\overline{Q}g, \quad \alpha_s^3. \end{aligned} \tag{2.18}$$

Representative Feynman diagrams for the last four processes in (2.18) are shown in Fig. 2-2(b)-(d). These processes can give $Q\overline{Q}$ pair topologies that are very different from those in LO processes. While the leading order processes produce back-to-back, in phi, the azimuthal angle, heavy quarks with the same transverse momentum, the NLO processes can produce nearly collinear heavy quarks which recoil against the light parton left over from the hard scatter. This results in heavy quarks which are no longer back-to-back in phi.

The first two processes in (2.18)(Figs. 2-1 and 2-2(a)) are supplemented by virtual diagrams, some of which are shown in Fig. 2-2(e). Interference terms between these diagrams and their LO partners contribute in $\mathcal{O}(\alpha_s^3)$ and are necessary to cancel infra-red and collinear singularities in the real emission diagrams[15].

## 2.3 The Structure Functions

All terms that are needed to evaluate heavy quark production from the partonic cross section(2.1) are known except for the $F_i$'s, or structure functions. The structure functions describe the probability of finding a particular parton with a specific momentum within a hadron. These functions are evaluated at an arbitrary mass scale, usually representative of the momentum transfer of the hard scatter, called the factorization scale. The factorization scale is conventionally set equal to the renormalization scale at which $\alpha_s$ is evaluated. This implies that the structure functions are scale dependent.

In physical applications, the structure functions are obtained by parameterizing them at some scale $\mu_0$, and then evolving them to some other scale $\mu$ using a QCD scale $\Lambda$. The scale $\mu$ is where results on the $x$- and $Q$- dependence are available from data. Fits are then made to the data at different $\mu$'s giving best values for the structure function parameters.

Many different parameterizations have been developed to describe the structure functions. The ones used in this thesis are from Eichten, Hinchliffe, Lane, and Quigg(EHLQ)[22], the CTEQ Collaboration(CTEQ)[23], and Martin, Roberts, and Sterling(MRS)[24]. A complete compilation of available sets of structure functions can be found in [25]. The CTEQ set, which is used almost exclusively in this thesis' Monte Carlo simulations, uses LO QCD evolution for the structure functions. (The EHLQ set is used in a small fraction of the Monte Carlo, and it also uses LO QCD evolution.) The MRS set is evaluated to NLO and is used in the theoretical predictions of heavy quark production. Table 2-2 lists some parameters for these structure functions. Figure 2-3 shows the gluon structure functions for these sets evaluated at $Q = 20$ GeV, a typical momentum transfer for heavy quark

| Structure Function Set | Factorization Scheme | $\Lambda_4^{QCD}$ [MeV] |
|---|---|---|
| EHLQ Set 1 | LO | 200 |
| CTEQ2L | LO | 200 |
| MRSD0 | $\overline{MS}$ | 215 |

Table 2-2: Properties of the structure functions used in this thesis.

production at the Tevatron.

## 2.4 Predictions for Heavy Flavor Production at $p\overline{p}$ Colliders

Having now determined all the components of the parton level cross section, we can use (2.1) to obtain predictions for heavy flavor production at the Tevatron. The following sections show results of the theoretical predictions of Nason, Dawson, and Ellis(NDE)[15] for single inclusive heavy quark production and those of Mangano, Nason, and Ridolfi(MNR)[20] for heavy quark correlated production.

### 2.4.1 Single Inclusive Heavy Quark Production

The NDE predictions for single inclusive heavy quark production use an extension of the usual $\overline{MS}$ scheme for both renormalization and factorization[15]. For inclusive beauty production, the following parameters are used in the calculation:

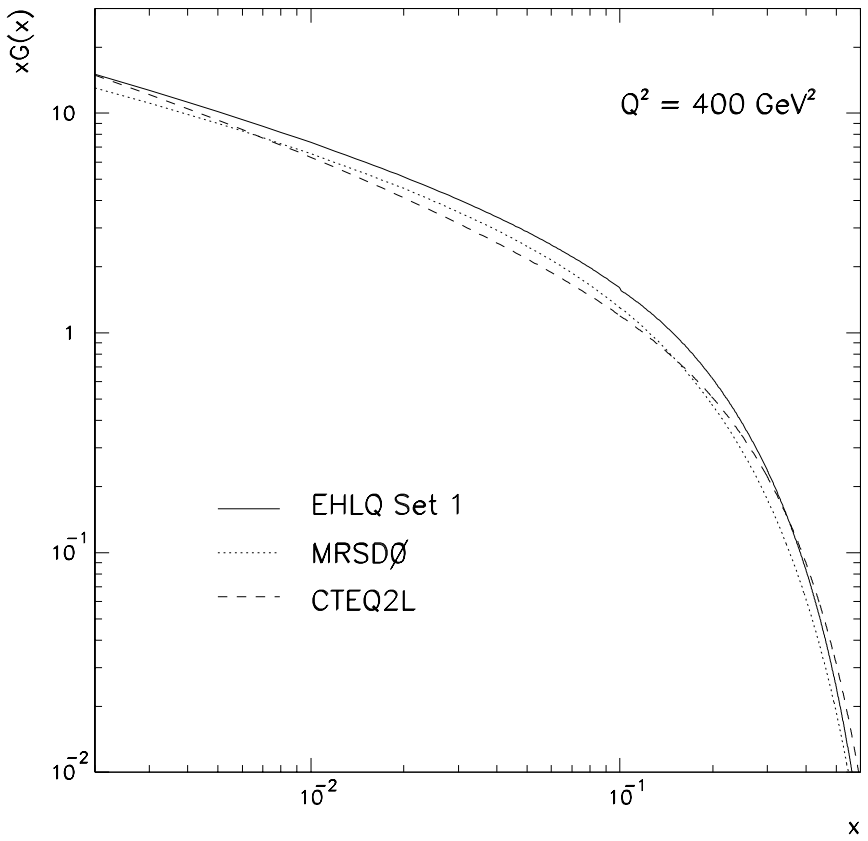


Figure 2-3: The gluon structure functions used in this thesis.

- $b$-quark mass, $m_b = 4.75$ GeV/c$^2$
- renormalization/factorization scale, $\mu_1 = \mu_2 = \sqrt{m_b^2 + p_T^2}$
- MRSD0 structure function with $\Lambda_4^{QCD} = 215$ MeV.

To facilitate the comparison between the predictions of the theory with experimental results, the differential cross section of (2.1) must be put in a form which is directly related to a measurable quantity. Experimental data are usually only sensitive to $b$-quarks with a $p_T$ above a certain threshold and in a certain rapidity region defined by the detector acceptance. For these reasons, a more useful quantity derived from the theory is:

$$\sigma(p\overline{p} \to bX; p_T^b > p_T^{min}, |y_b| < y_{max}) = \int_{-y_{max}}^{y_{max}} dy_b \int_{p_T^{min}}^{\infty} dp_T^b \frac{d^2\sigma(p\overline{p} \to bX)}{dy_b dp_T^b}. \quad (2.19)$$

The NDE predictions for this cross section are shown in Fig. 2-4 for $\sqrt{s} = 1.8$ TeV and $y_{max} = 1$.

### 2.4.2 Correlated $Q\overline{Q}$ Pair Production

One advantage that the single inclusive heavy quark cross section has over a correlated heavy quark cross section is that only one of the two heavy quarks needs to be detected. Unfortunately, any information regarding the underlying QCD production mechanism is lost. Therefore, comparisons between calculated $Q\overline{Q}$ correlations and data can yield important tests of the underlying QCD dynamics which are lost in a single inclusive cross section measurement.

Recently, Mangano *et al.*(MNR)[20] have calculated the fully differential heavy quark cross section to $\mathcal{O}(\alpha_s^3)$. Up until this time, an exact calculation was not

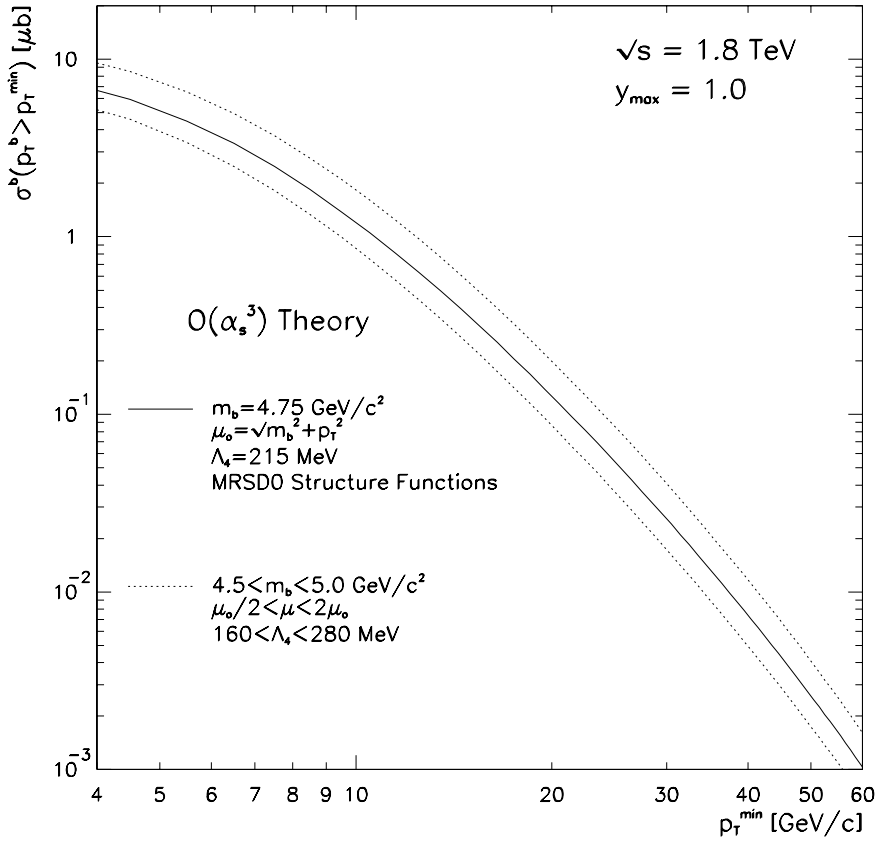


Figure 2-4: Cross section for $b$-production in $p\overline{p}$ collisions calculated to $\mathcal{O}(\alpha_s^3)$ for $\sqrt{s} = 1.8$ TeV and $y_{max} = 1$. Also shown are the error bands.

available due to problems with infrared and collinear divergences in the phase-space integrals of the formula used to calculate the cross sections. Mangano *et al.* have overcome these problems through the implementation of a subtle cancellation scheme.

The quantity we will find useful in studying $Q\overline{Q}$ correlations is the difference in azimuth angle, $\Delta\phi^{Q\overline{Q}}$, of the heavy quark pair. For the leading order processes, this angle should be exactly $\pi$. Any deviations from this value should indicate the presence of higher order contributions.

This differential calculation uses the same parameters as the single inclusive cross section calculation of NDE except the renormalization and factorization scales have been modified to include information about the second heavy quark:

- renormalization/factorization scale, $\mu_1 = \mu_2 = \sqrt{m_b^2 + (p_T^{1^2} + p_T^{2^2})/2}$.

The MNR calculation for the differential $\Delta\phi^{b\bar{b}}$ distribution for $\sqrt{s}$ = 1.8 TeV and $y_{max} = 1$ is shown in Fig. 2-5. A cut on the transverse momentum of the $b$-quark is made at $p_T^b > 8$ GeV/c.

## 2.5 Uncertainties in the Theoretical Predictions

The uncertainties in the theoretical calculation are due to the $b$-quark mass, the renormalization/factorization scale $\mu$, the QCD scale $\Lambda^{QCD}$, and the structure functions. Each is described briefly below.

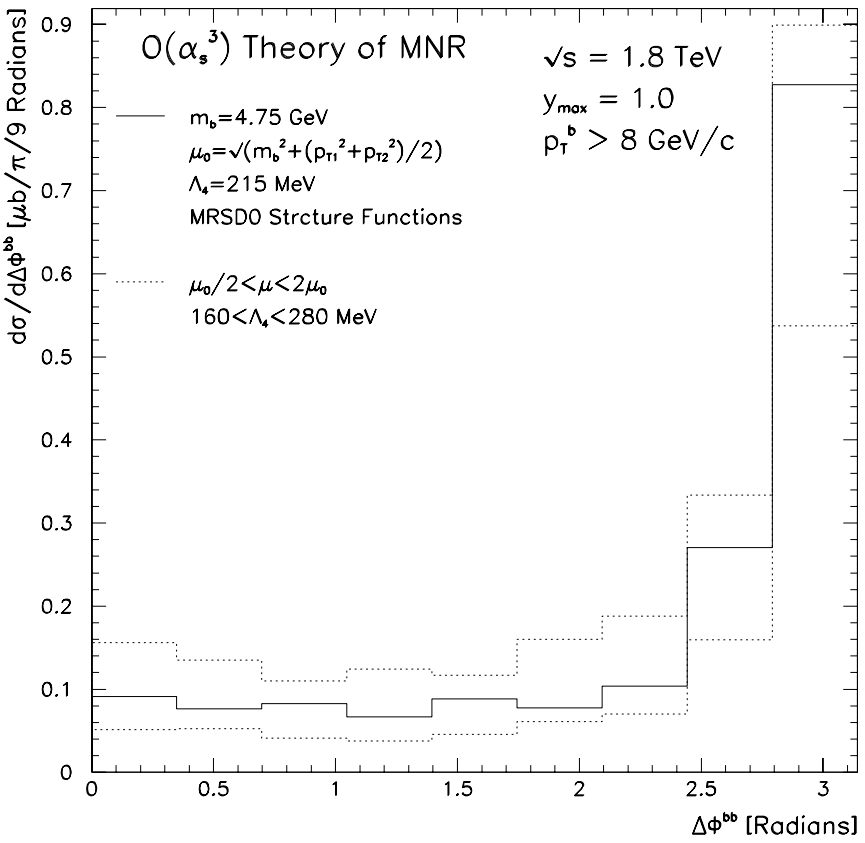


Figure 2-5: Differential $\Delta\phi^{b\overline{b}}$ cross section in $p\overline{p}$ collisions calculated to $\mathcal{O}(\alpha_s^3)$ for $\sqrt{s} = 1.8$ TeV and $y_{max} = 1$. Also shown are the error bands.

### $b$-quark Mass

The current estimates for the mass of the $b$-quark approximately lie in the range[5]

$$4.5 \leq m_b \leq 5.0 \text{ GeV/c}^2. \tag{2.20}$$

Therefore a value of $m_b = 4.75$ GeV/c$^2$ is chosen.

### Renormalization/Factorization Scale $\mu$

In general, the $\mu$-dependence of a perturbative calculation will give an estimate on the effect of including higher orders of $\alpha_s$ in the calculation. Additionally, any $\mu$-dependence should vanish if all orders of $\alpha_s$ are included. The NDE calculation chooses the central value for the renormalization/factorization scale to be $\mu_0 = \sqrt{m_b^2 + p_T^2}$. This choice of scale is motivated by the two different natural scales, $m_b$ and $p_T$, inherent in the process. The errors due to the scale dependence are estimated by allowing $\mu$ to vary between $\mu_0/2$ and $2\mu_0$.

### QCD Scale $\Lambda^{QCD}$

For the set of structure functions used in this calculation, $\Lambda_4^{QCD}$ is chosen to be in the range $160 \leq \Lambda_4^{QCD} \leq 280$ MeV.

### Structure Functions

The uncertainties due to the choice of structure functions are from:

- the lack of precise experimental data on the shape of the gluon distribution, especially at small $x$, where this uncertainty is correlated with errors in

$\Lambda_4^{QCD}$[26], and

- errors due to uncertainties in the choice of $\Lambda_4^{QCD}$ which is used for the structure function evolution.

Fig. 2-3 shows the different shapes of a few of the structure functions used. The MRSD0 set is chosen as the default structure function in the theoretical calculations.

# Chapter 3

# Models of Beauty Production and Decay

The previous chapter dealt with the theory of heavy quark production in the framework of QCD. These calculations led us to the predicted cross section for $b\overline{b}$ production, specifically:

$$\sigma(p\overline{p} \rightarrow bX; p_T^b > p_T^{min}, |y_b| < y_{max}).$$

The problem now lies in how to measure these theoretical predictions based on the quantities which are directly accessible in the experiment. Specifically, we need to find a relation between the produced $b$-quarks and the resulting muons which are measured in the detector.

In order to model hadron-hadron collisions, all of the following processes must be taken into account:

- the structure functions
- the hard scattering of partons

- a treatment of initial and final state gluon radiation
- hadronization of the scattered and radiated partons
- decays of the resulting hadrons which are short lived
- hadronization and decay of the partons not directly involved in the hard scatter(underlying event)
- effects of the detector on the event

This modeling is generally accomplished using Monte Carlo techniques where the events are generated at random according to a probability which is based on the physics process being modeled.

## 3.1 ISAJET

The ISAJET [27] Monte Carlo model is used for all the physics simulations presented in this thesis. ISAJET is used to generate events from $p\overline{p}$ collisions at a center of mass energy, $\sqrt{s}$ = 1.8 TeV. These events are modeled in all steps of the evolution described above to the final(observable) particles seen in the detector. The DØ detector simulation is carried out after the events are generated. The following sections describe how ISAJET models each phase of the event evolution. Comparisons to NLO theoretical predictions will be reserved until Chapter 6.

### 3.1.1 Parton-Parton Interactions

Figure 3-1 shows a schematic representation of a $p\overline{p}$ inelastic scattering generated with ISAJET. The first step in event generation is to produce a parton-parton hard

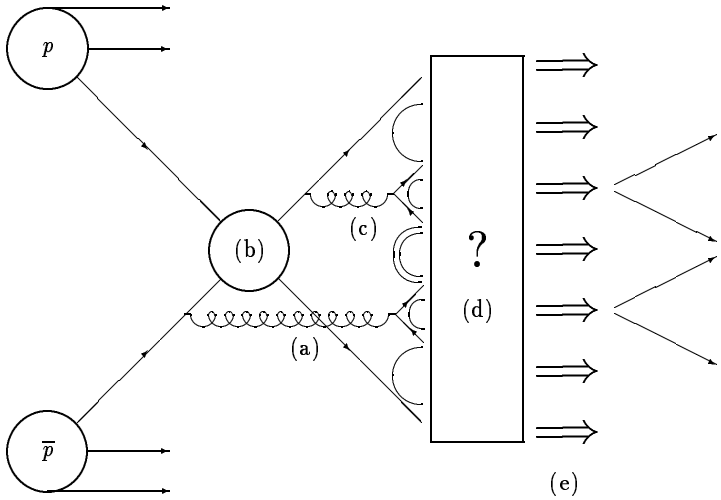


Figure 3-1: Schematic diagram of a $p\overline{p}$ inelastic scattering. Shown in the diagram are the initial state gluon radiation (a), the hard scattering (b), final state gluon radiation (c), quark fragmentation and hadronization (d), and the decay of unstable hadrons (e).

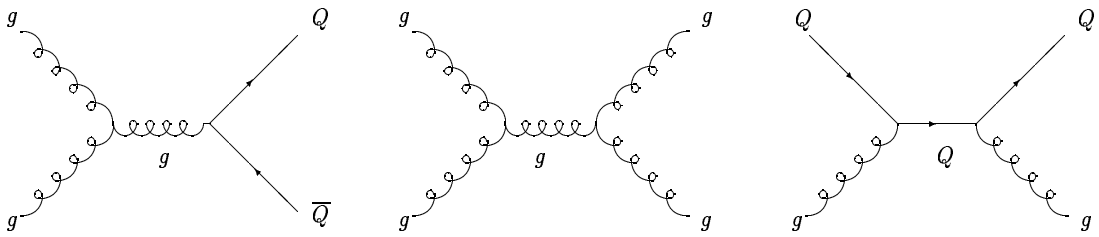


Figure 3-2: Lowest order Feynman diagrams used to produce the hard scatter in ISAJET.

scattering according to the lowest order matrix elements. Figure 3-2 shows the lowest order diagrams. The cross sections obtained from these hard scatters depends upon what structure functions are used for the hadrons. ISAJET v7.02 and earlier use the parameterization of Eichten, Hinchliffe, Lane, and Quigg (EHLQ1)[22]. The later versions of ISAJET, starting with v7.06, use the CTEQ2L structure functions as defined by the CTEQ Collaboration[23]. Most of the Monte Carlo used in this thesis is generated with the CTEQ2L structure functions.

The next step in event generation is to add QCD radiative corrections to the initial and final state partons. These corrections are included by allowing both the initial and final state partons to emit gluons, and gluons to split into $q\overline{q}$ pairs. These processes are governed by the Altarelli-Parisi splitting functions which determine the probability for one parton to split into two. ISAJET uses the branching approximation of Fox and Wolfram[28] to model the splitting.

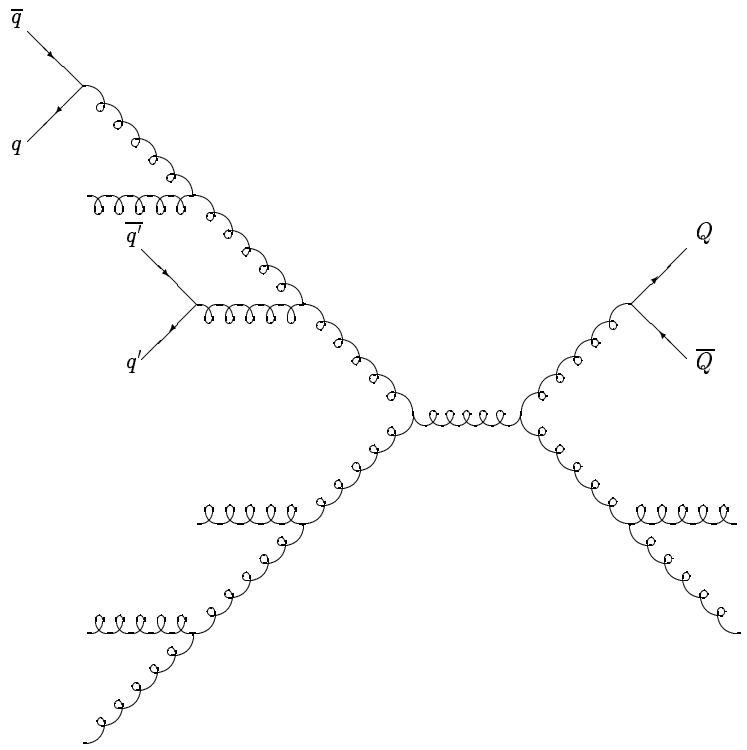


Figure 3-3: ISAJET hard scatter showing complete parton evolution.

In order to avoid problems with infrared and collinear singularities, each parton in the cascade must have an energy greater than some cutoff, $t_c$, to continue emitting gluons and quarks. This cutoff serves to divide the parton evolution into a perturbative region, where the radiated gluons with $p^2 > t_c$ are allowed to continue to cascade, and a non-perturbative region, where gluons with $p^2 < t_c$ are incorporated in the hadronization model. The default ISAJET cutoff is $t_c = (6\ \text{GeV})^2$, and is chosen because a lower cutoff value would result in the production of too many hadrons from overlapping partons. Figure 3-3 shows an ISAJET hard scatter where all of the initial and final state partons were allowed to evolve according to the previous prescription.

Fortunately, this cutoff does not directly effect beauty production, since the

minimum $Q$ value to produce $b\overline{b}$ pairs is approximately 10 GeV. However, it will effect the production of $c\overline{c}$ pairs from gluon splitting and also soft final state gluon radiation.

Using the above method, ISAJET has evolved the simple lowest order reactions into events that approximate the effects of higher order corrections. We can then separate the lowest and higher order contributions to heavy quark production into three topologically different processes called flavor creation(FC), gluon splitting(GS), and flavor excitation(FX). Figure 3-4 shows the Feynman diagrams for each of these processes.

$$q\overline{q}, gg \rightarrow Q\overline{Q} \qquad \text{(Flavor Creation)} \tag{3.1}$$

$$\begin{aligned} gg &\rightarrow gg \\ &\hookrightarrow Q\overline{Q} \end{aligned} \qquad \text{(Gluon Splitting)} \tag{3.2}$$

$$\begin{aligned} gQ &\rightarrow gQ \\ qQ &\rightarrow qQ \end{aligned} \qquad \text{(Flavor Excitation)} \tag{3.3}$$

FC is the leading order $2 \rightarrow 2$ process for heavy quark production. The two higher order processes include GS, where a final state gluon splits into a $Q\overline{Q}$ pair, and FX, which is similar to GS except that an initial state gluon splits into a heavy quark pair, and then one of the resulting heavy quarks scatters with another parton.

Figure 3-5 shows the relative cross sections for each of the heavy quark production processes described above(GS,FX, and FC). These are plotted as a function of the $b$-quark transverse momentum. These distributions are produced by generating ISAJET $p\overline{p} \rightarrow b\overline{b}$ events in several bins of $p_T$ of the hard scattering process

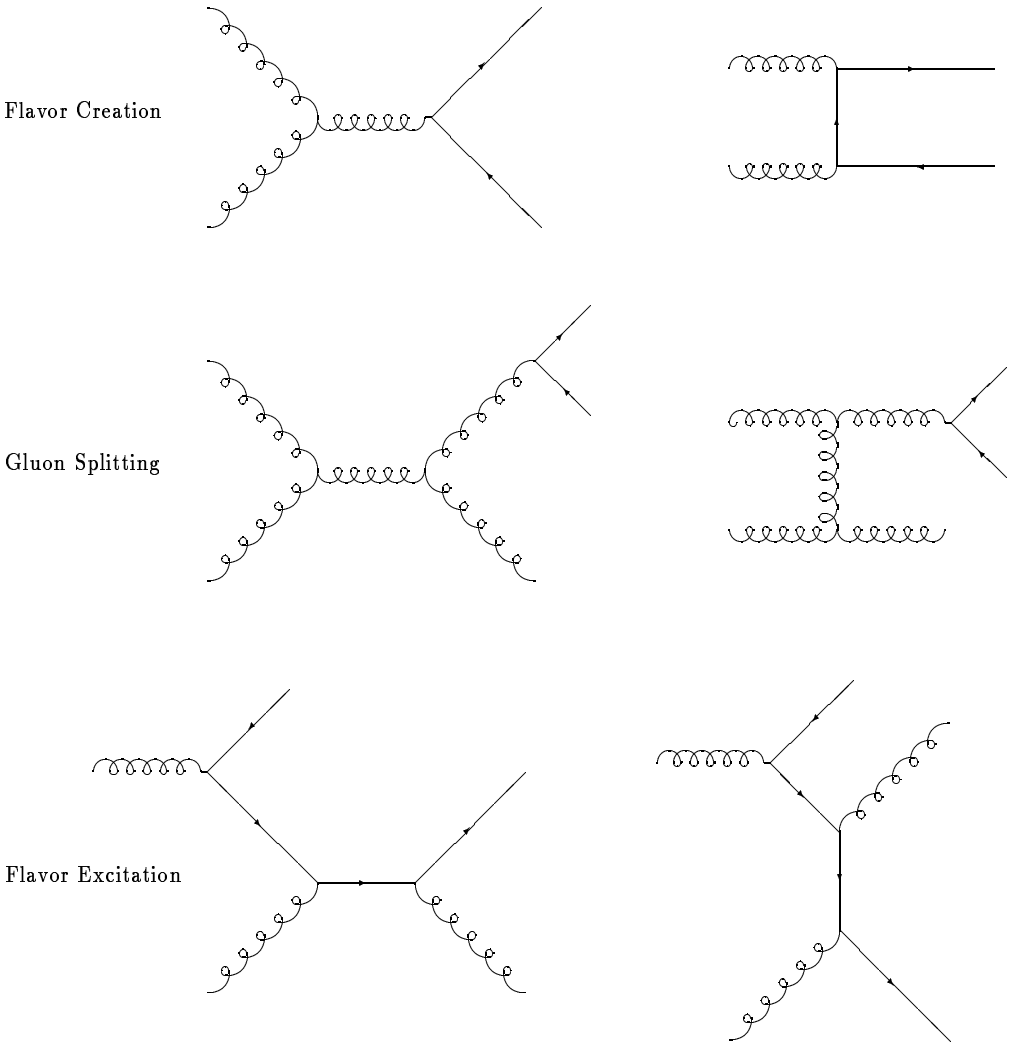


Figure 3-4: Feynman diagrams for flavor creation, gluon splitting, and flavor excitation.

between the values of 4 and 200 GeV/c. A lower cutoff of 4 GeV/c was used for two reasons. First, the lowest order cross section diverges as $p_T \to 0$, and second, the DØ detector is not sensitive to those events which contain small values of $p_T^b$.

### 3.1.2 Quark Fragmentation

The next step in the ISAJET process is to form hadrons from the final state partons. This process is called hadronization and several models have been developed which approximate this process. The model used by ISAJET is called the independent fragmentation ansatz originally proposed by Field and Feynman[29]. In this model, a new quark-antiquark pair($q'\overline{q}'$) is formed from the original quark's(q) color field. The new $q'\overline{q}'$ pairs are formed in the ratio $u : d : s = 0.43 : 0.43 : 0.14$. This ratio reflects the fact that the $s$-quark is heavier than the $u$ or $d$ and is thus less probable of being produced in the color field. A new meson($q\overline{q}'$) is then formed, which carries a fraction $z$ of the original quarks momentum with average $\langle p_T \rangle = 0.35$ GeV/c with respect to the original quark direction. $z$ is defined as

$$z = \frac{E^{had} + p_L^{had}}{E^q + p^q}, \tag{3.4}$$

where $p_L^{had}$ is the momentum of the hadron in the direction of $p^q$. Baryons are also produced by generating di-quark pairs with probability of 0.10 instead of a single quark.

A quark-antiquark pair is most likely to combine into a meson when they have the same velocity. If the fragmenting parton is a heavy quark, then it only needs a small amount of its energy to produce several light quark pairs. If the heavy quark then combines with one of the light quarks, the resulting hadron will carry

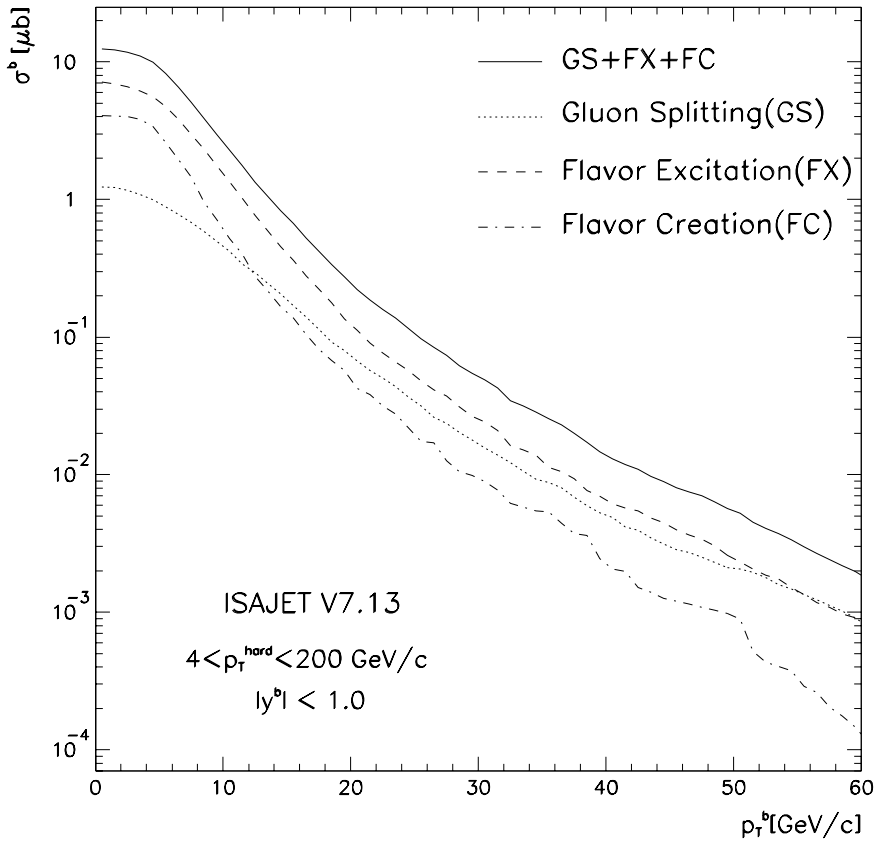


Figure 3-5: Integrated $p\overline{p} \to bX$ cross section for gluon splitting, flavor excitation, flavor creation, and all processes. These distributions are generated with ISAJET V7.13.

a large fraction of the original energy so that $z \sim 1$. So, quantitatively, we expect the fragmentation of the heavy quarks to be harder than those of the light quarks.

ISAJET uses the Peterson[30] model which produces the features described above. The fragmentation function, $f(z)$, is generated differently for light and heavy quarks. For light quarks$(u, d, s)$ and gluons, the function has the form

$$f(z) = 1 - a + a(b+1)(1-z)^b \tag{3.5}$$

with $a = 0.96$ and $b$=3. For heavy quarks, the Peterson form is used

$$f(z) = \frac{z(1-z)^2}{[(1-z)^2 + \epsilon z]^2}. \tag{3.6}$$

The parameter $\epsilon$ is expected to scale with the quark mass and is defined as

$$\epsilon_q = \frac{k_q}{m_q^2} \tag{3.7}$$

where $k_c = 0.80$ and $k_b = 0.50$ are the default values supplied by ISAJET. Figure 3-6 shows the relative shapes of the Peterson fragmentation function for charm and bottom.

### 3.1.3 Decays of $B$-Hadrons

The final component in ISAJET's modeling of hadronic collisions is the treatment of the decay of heavy hadrons. All heavy hadrons formed in the fragmentation process will decay into other particles. The decay channel we are interested in is the semileptonic decay of heavy mesons.

ISAJET treats the semileptonic decays of heavy mesons using the spectator $V$-$A$ model. In this model, the heavy quark is considered to be a free particle independent of the other light quark(the spectator) in the meson. The heavy quark

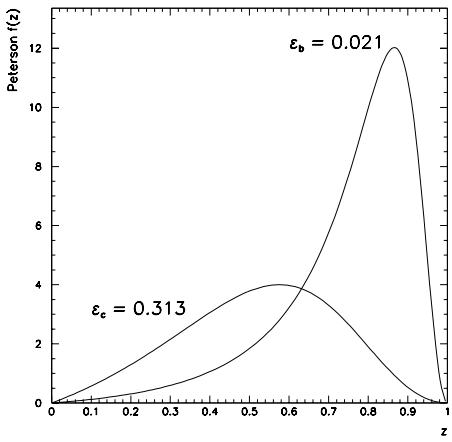


Figure 3-6: The relative shapes of the Peterson fragmentation function for charm and bottom quarks. Note that the curve for $\epsilon_c$ and has been multiplied by a factor of five.

is then allowed to decay via the normal $V$-$A$ weak current, as shown in Fig. 3-7. This is of course not an exact description of semileptonic meson decay, but for the relatively large mass of the $b$-quark , any modifications due to perturbative and nonperturbative QCD corrections become small. This follows from the assumption that the forces between the quarks and gluons vanish at small distances (asymptotic freedom).

In addition to the direct, or first generation, production of leptons from $B$-meson decays, second generation decays of $B$-mesons can produce leptons via the chain decay

$$\begin{aligned} B &\rightarrow DX \\ &\quad\downarrow \\ &\quad\hookrightarrow l\nu X. \end{aligned} \tag{3.8}$$

The branching fractions used by ISAJET for the semileptonic decays of $B$ and $D$-

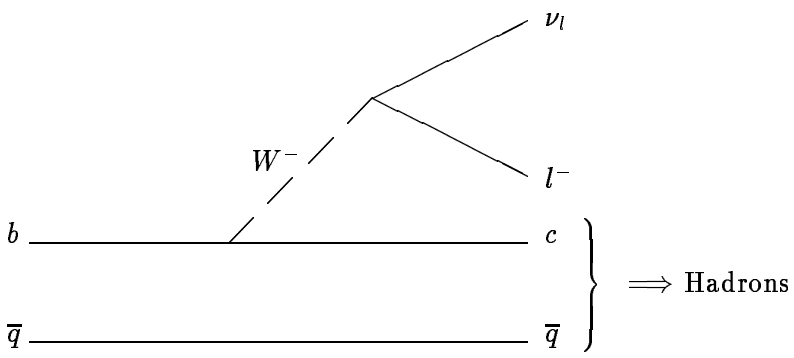


Figure 3-7: Semileptonic spectator decay of a $B$-meson

| Hadron($H_i$) | BR($H_i \to \mu X$) | |
|---|---|---|
| | ISAJET | Data |
| $D^\circ$ | 0.075 | 0.100±0.026 |
| $D^\pm$ | 0.15 | 0.172±0.019 |
| $D_s$ | 0.065 | 0.063±0.032 |
| $B$ | 0.12 | 0.110±0.005 |

Table 3-1: ISAJET and data branching fractions for $B$ and $D$-hadrons.

hadrons are summarized in Table 3-1. Also shown in Table 3-1 are the branching fractions given by Ref. [31].

Recent measurements from LEP experiments show the inclusive semileptonic branching fraction for $B$-hadrons to be

$$\mathrm{BR}(B \to \mu^\pm \nu_\mu X) = 11.0 \pm 0.3 \pm 0.4\% [31].$$

This is different from the value used in ISAJET. Thus, in order to use the ISAJET predictions of the muon level cross section, $\sigma(p\overline{p} \to b\overline{b} \to \mu\mu)$, the branching fraction must be modified. Naïvely, one would expect the correction to be the ratio $(\frac{11.0}{12.0})^2 = 0.840$ with a factor of $(\frac{11.0}{12.0})$ coming from each direct semileptonic $b \to \mu$ decay. The modification is complicated because the $b \to \mu$ sample contains both $B \to \mu$ and $B \to D \to \mu$ events.

The cross sectional weight of each dimuon Monte Carlo event is reduced by a factor of $(\frac{11.0}{12.0}) = 0.9167$ for each muon in the event which is found to be the result of a direct semileptonic decay of a $b$-quark. No additional correction is made to the Monte Carlo event weight due to the $c$-quark semileptonic decay since the default ISAJET branching fraction values agree with experimental measurements.

### 3.1.4 ISALEP

As we have seen, ISAJET produces events that contain higher order processes, such as gluon splitting and flavor excitation. For heavy quark production, these processes account for a substantial portion of the total reaction cross section[18]. Since the emission of heavy quark pairs may occur at any step in the ISAJET event evolution, there is no formal procedure to force these processes to occur. Therefore, the generation of these events is very slow.

The ISALEP package, contained within the ISAJET Monte Carlo, was developed to increase the efficiency for producing events which contain higher order processes. ISALEP allows up to $n_1$ QCD evolutions for each hard scatter, and rejects events without the desired partons(e.g. $b$-quarks). It then performs $n_2$ fragmentations for each successful evolution. Since the hadrons which result from heavy quark fragmentation have a probability of decaying into muons on the order of 10-20%, the chance of a single fragmentation producing a dimuon event is quite small. Each of these fragmentations may also be rejected if the specified final state particles are not found(e.g. muons). Therefore, the use of multiple fragmentations and subsequent decay for each successful evolution make it much more likely that a dimuon event be produced from the original hard scatter. Each hard scatter can then produce up to $n_1 * n_2$ events, and can greatly reduce the amount of time needed to produce higher order processes.

ISALEP is used to produce all Monte Carlo dimuon events originating from heavy quarks. The ISALEP parameters used are

$$\begin{aligned} \text{NEVOLVE} = \#\ \text{Evolutions} &= n_1 = 10 \\ \text{NHADRON} = \#\ \text{Fragmentations} &= n_2 = 10. \end{aligned}$$

These parameters are chosen in order to increase event acceptance from the initial hard scatter without significantly increasing the probability for producing multiple events from one hard scatter.

## 3.2 Other Models

Three other models of high energy hadronic collisions exist which are widely available. Each is briefly described below. A good description of the different fragmentation models used in Monte Carlo event generators can be found in Ref. [32].

- **PYTHIA** The PYTHIA Monte Carlo[33], developed by the Lund group[34], incorporates the string fragmentation model into their Monte Carlo. This model uses a space-time picture of a string being spanned between the $q$ and $\overline{q}$ of a simple two jet event. It is the string which fragments into hadrons of well defined masses. Additional gluons are introduced as an energy and momentum carrying kink in the string. This model is widely used to describe $e^+e^-$ collisions.

- **HERWIG** The HERWIG Monte Carlo[35], utilizes the cluster fragmentation model to describe the hadronic interactions. This model produces clusters of particles which are allowed to decay isotropically in the rest frame of the cluster. The internal structure of each cluster is deemed irrelevant, and what matters is the overall mass and the flavor quantum numbers. This approach describes overall event shapes of the interaction including jet properties.

- **NDE and MNR** The NLO calculations of Nason *et al.* and Mangano *et al.* have been used as parton level event generators. Unfortunately, a widely available program to fragment and decay these partons is still not available.

# Chapter 4

# The DØ Experiment

The DØ experiment was designed to study a wide range of physics phenomena for proton-antiproton collisions at $\sqrt{s} = 1.8$ TeV in the Fermilab Tevatron Collider. The physics under investigation focused primarily on high mass and high-$p_T$ phenomena which includes: top quark search, $W$ and $Z$ boson measurements, $b$-quark production, tests of perturbative QCD, as well as searches for new phenomena which lie outside the Standard Model.

## 4.1 The Fermilab Tevatron

The Fermilab Tevatron is a $p\overline{p}$ collider which accelerates protons and antiprotons to 900 GeV providing a center-of-mass energy of $\sqrt{s} = 1.8$ TeV. The Tevatron is presently the world's highest energy hadron collider.

Both the proton and antiproton beams originate in the preaccelerator. Here, hydrogen ions, $H^-$, are accelerated to 750 keV by an electrostatic Cockroft-Walton accelerator. From here, the ions are bunched and inserted into the Linac which

is a 150 m long linear accelerator. This accelerates the ions to 200 MeV. After the Linac, the ions are passed through a carbon foil which strips off the electrons. The resulting protons are sent to the Booster synchrotron, accelerating them to an energy of 8 GeV. From here, the protons are injected into the Main Ring, a 1000 m radius synchrotron composed of conventional magnets. The protons are either stored here and accelerated to 120 GeV or used to produce antiprotons.

In the Main Ring, the protons are focused into six "bunches" of high density and extracted onto a nickel target. Each collision produces a spray of nuclear debris which includes some antiprotons. Approximately one antiproton is produced for every $10^5$ protons. The antiprotons are removed, focused, and sent to a storage ring until enough have accumulated to fill the Tevatron($\sim 10^{11}$ antiprotons). The antiprotons are then injected in bunches into the main ring and accelerated in the direction opposite the proton bunches. Both the protons and antiprotons are then injected into the Tevatron and accelerated to the collider energy of 900 GeV. The Tevatron, which is located 60 cm below the Main Ring and in the same tunnel, uses a string of 774 dipole and 216 quadrapole magnets to maintain a circular orbit of radius 1000 m. All the dipole and quadrapole magnets in the Tevatron are superconducting and are maintained at a temperature of 4.6 K.

The Tevatron had two interaction regions during the 1992-1993 run. The CDF [36] detector was situated at the B0 interaction region and the DØ detector was at the D0 region. The instantaneous luminosities, or the proton-antiproton flux, reached as high as $10\times10^{30}\mathrm{cm}^{-2}\mathrm{s}^{-1}$. Additionally, the position of proton-antiproton collisions had a Gaussian longitudinal vertex distribution along the beam direction($z$-axis). The mean vertex position in the DØ detector was $z \approx$-10 cm with a sigma of 30 cm with respect to the center of the DØ detector. Figure 4-1 shows the main components of the Tevatron and the two interaction regions

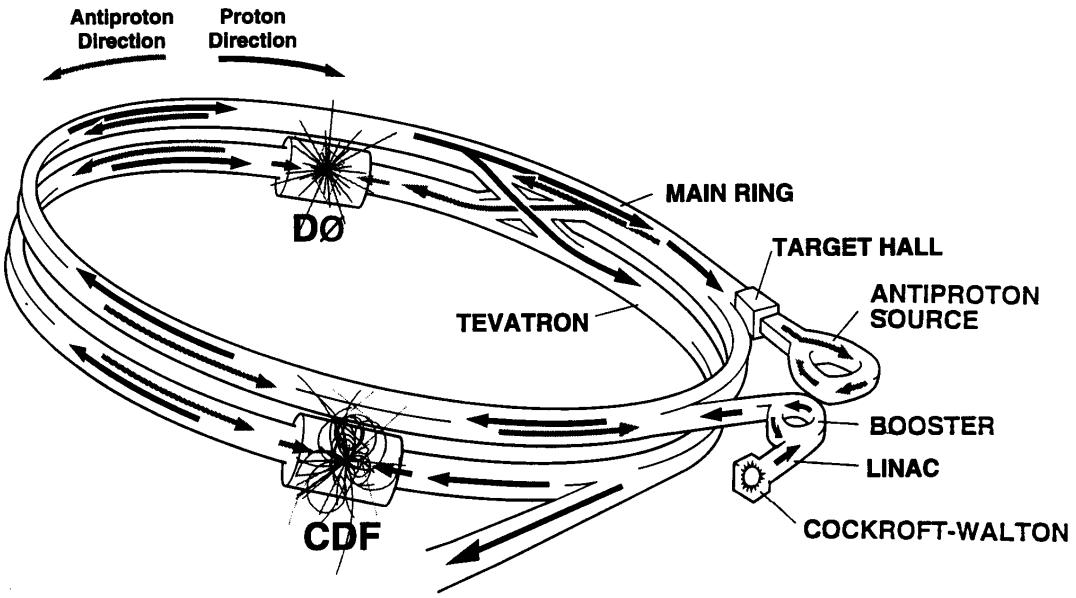


Figure 4-1: The Fermilab Tevatron $p\overline{p}$ collider with luminous regions at D0 and B0 .

located at D0 and B0.

## 4.2 The DØ Detector

The DØ detector, shown in Fig. 4-2, was optimized to identify and measure leptons, parton jets at large $p_T$, and missing transverse energy $\not\!\!E_T$ , the signal of neutrinos and other non-interacting particles. The detector consists of three major subsystems listed below:

- the Central Detector (CD), which includes:

  1. Vertex Drift Chamber (VTX)

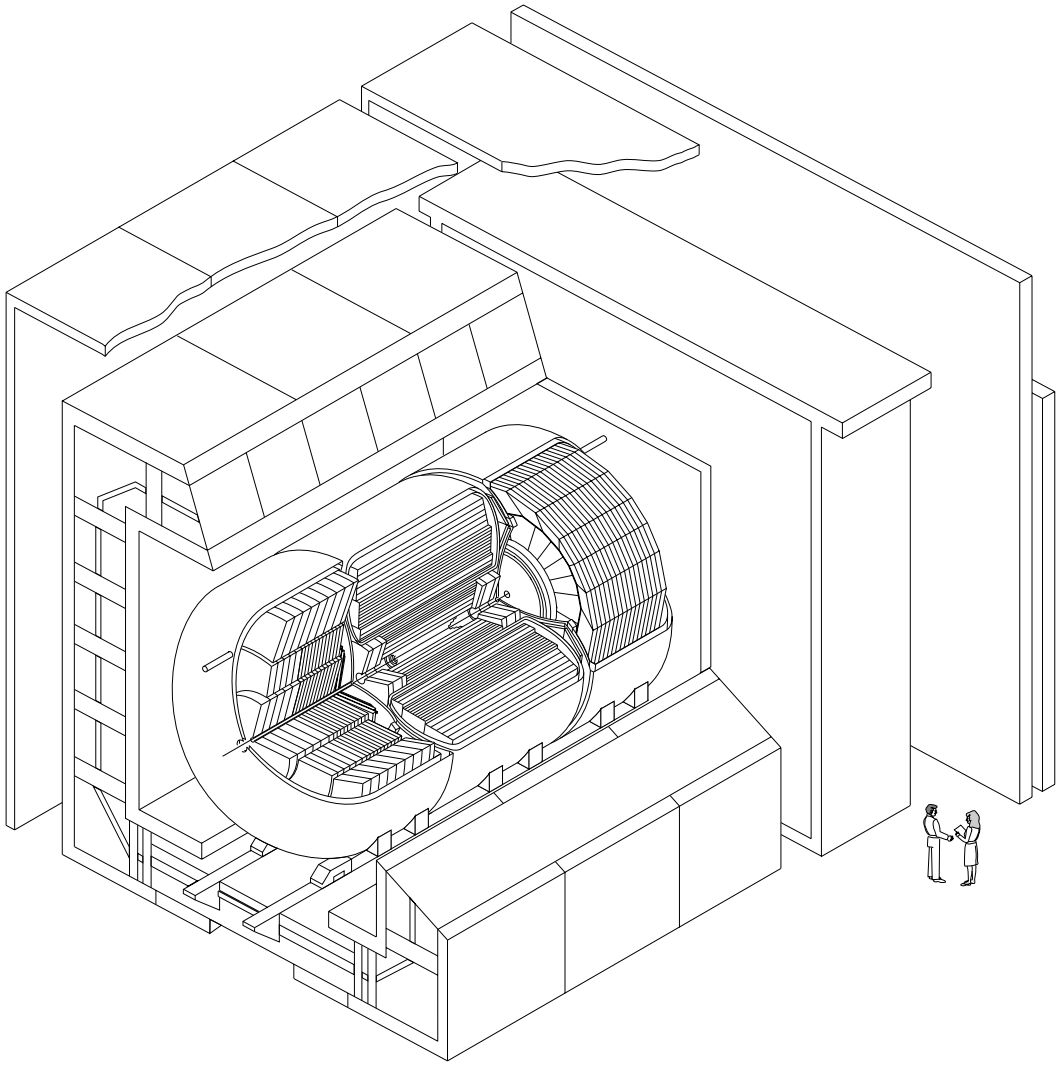


Figure 4-2: Cutaway view of the DØ detector, showing the central detector, the calorimeter, the central toroidal magnet, and muon chambers.

2. Transition Radiation Detector (TRD)
3. Central Drift Chamber (CDC)
4. Forward Drift Chambers (FDC)

- the Liquid Argon Calorimeter
  1. Central Calorimeter (CC)
  2. End Calorimeter (EC)
  3. Intercryostat Detectors (ICD)
- the Muon System and Toroids
  1. Wide Angle Muon System (WAMUS)
  2. Small Angle Muon System (SAMUS).

The following sections will highlight each of the detectors components in more detail. A full description of the DØ Detector is in reference [37]. Also, a description of the DØ coordinate system is given in Appendix A.

### 4.2.1 The Central Detector

The central detector consists of four major subsystems which are oriented in two different directions. The large angle region, which includes the VTX, TRD, and the CDC, is arranged in cylinders concentric with the beams, and the forward region, which contains the FDC's, is oriented perpendicular to the beams. The main goal of the central detector is to reconstruct the trajectory of charged particles that pass through them. This information is then used to determine the location of the

event vertex, origin of electromagnetic showers(either $e$ or $\gamma$), and help in muon momentum measurements. Figure 4-3 shows the design of the central detector.

When a charged particle passes through a gas, it interacts electromagnetically with nearby atomic electrons crating electron-ion pairs along the path of the particle. The number of electron-ion pairs created depends on the energy of the particle and the type of gas used, but typically, the number of pairs formed will be on the order of 100/cm. When an electric field is applied, the electrons will drift through the gas towards the positive electrode, undergoing repeated collisions with the gas molecules along the way. If the electric field is strong enough, the electrons gain enough energy between collisions to knock another electron free from a gas molecule. This additional electron can then continue in the same manner. In this way, an avalanche of electrons forms in which the number of electrons increases exponentially. This current can then be read out on the positive anode, which will be proportional to the original number of ions created.

Because the electrons only initiate an avalanche when they get close to the anode, they drift with approximately constant speed through the rest of the gas. Thus, a measurement of the time it takes an electron to drift to the anode can be turned into a measurement of the distance of the original source particle from the anode. This is the type of measurement made in a drift chamber, and the principle behind the operation of the VTX, CDC, and the FDC's. The TRD detects transition radiation, and its operation is discussed later.

### Vertex Drift Chamber (VTX)

The VTX chamber[38] lies directly outside the beam pipe and is the first detector system which particles pass through originating from the $p\overline{p}$ collision point.

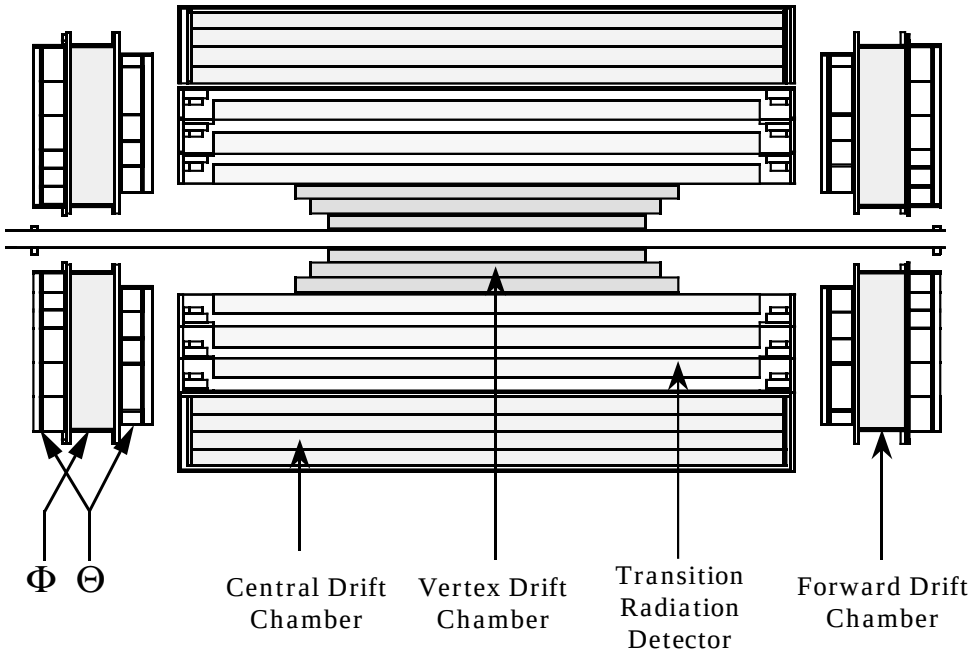


Figure 4-3: Design of the Central Detector.

Its primary use is to accurately determine the event vertex position. The VTX chamber has an active region extending from an inner radius of 3.7 cm out to a radius of 16.2 cm. This chamber consists of three independent concentric layers of cells. The active length of the inner layer is 97 cm, with each successive layer being about 10 cm longer. The innermost layer has 16 cells in azimuth, while the outer two layers have 32 cells. Each cell contains eight sense wires, which are 25 $\mu$m NiCoTin[39], and are used to measure the $r - \phi$ coordinate. Adjacent sense wires are offset by $\pm$ 100$\mu$m to resolve left-right ambiguities. A $CO_2$-ethane gas mixture (95%:5%) with a small amount of $H_2O$ added[40], is used to obtain good spatial resolution. The average drift velocity is about 7.3 $\mu$m ns$^{-1}$, which results in a maximum drift time of 2.2 $\mu$s, well within the Collider bunch-time interval of 3.5 $\mu$s. The vertex resolution along the $z$-axis is approximately 1.5 cm.

**Transition Radiation Detector (TRD)**

The TRD is the next outermost detector system. It provides an independent identification of electrons to that given by the calorimeters. The DØ TRD contains three independent sections, each of which contains a radiator and an X-ray detector.

In 1946, Ginzberg and Frank predicted that transition radiation X-rays are produced when highly-relativistic particles ($\gamma > 10^3$) pass between media with different dielectric constants[41]. The energy of the X-rays, for a given particle and momenta, is determined by the thickness of the radiator foils and the gaps between the foils. Each DØ TRD unit contains a radiator section with 393 foils of 18 $\mu$m thick polypropylene in a volume filled with nitrogen gas. The mean gap between the radiator foils is 150 $\mu$m, which results in an X-ray spectrum which peaks at 8 keV and is mostly contained below 30 keV[42].

The detection of transition-radiation X-rays is done using a two-stage time expansion radial-drift PWC located just after the radiator. Since the X-rays convert mainly in the first stage of the chamber, the resulting charge drifts radially outward to the sense cells, where the avalanche ionization occurs.

The radiator and detector volumes are separated by two 23 $\mu$m mylar windows. To help insure that the nitrogen from the radiator does not leak into the detector volume, dry $CO_2$ gas flows between the two mylar windows. The detector volume is filled with a mixture of Xe, $CH_4$, and $C_2H_6$ (91%:7%:2%) which has an efficient X-ray absorption since Xe has a high Z (Z=54)[43]. The outer mylar window is aluminized which serves as a high-voltage cathode in the detection stage. The 15 mm conversion stage and the 8 mm amplification stage are separated by a cathode grid of 70 $\mu$m gold-plated tungsten wire. The outer cathode of the amplification stage is constructed of helical copper strips, also used in measuring the $z$-coordinate of the $p\overline{p}$ collision. The anodes are 30 $\mu$m gold-plated tungsten wires separated by 100 $\mu$m gold-plated copper/beryllium potential wires. Each TRD chamber has 256 anode readout channels.

### Central Drift Chamber (CDC)

The Central Drift Chamber (CDC) is located just outside the TRD and just inside the Central Calorimeter, providing coverage for tracks at large angles. The CDC is a cylindrical shell of length 184 cm and with an active radius from 49.5 cm out to a radius of 74.5 cm. It contains four concentric rings of 32 azimuthal cells per ring, with each cell housing seven 30 $\mu$m gold-plated tungsten sense wires which are read out at one end. Adjacent wires within the cell are staggered in $\phi$ by $\pm$ 200 $\mu$m to remove the left-right ambiguity. There are also two delay lines, which are read out at both ends, located just before(after) the first(last) sense wire. The

delay lines allow a determination of the $z$-coordinate of the track by measuring the difference of arrival times at the two ends.

The CDC contains an AR, $CH_4$, and $CO_2$ gas mixture (92.5%:4%:3%) with 0.5% $H_2O$.

### Forward Drift Chambers (FDC)

The Forward Drift Chambers (FDC)[44, 45] provide coverage for charged particles down to $\theta \approx 5^\circ$ with respect to the beam axis. The FDC's are located at each end of the VTX, TRD, and CDC(see Figure 4-3) and extend out to the inner walls of the end calorimeters. The active region of the FDC extends out to a radius of 61 cm.

Each of the two FDC chambers is made up of three separate modules. The $\Phi$ module with sense wires radial to the beam axis measures the $\phi$ coordinate. This module is sandwiched between two $\Theta$ modules whose sense wires measure the $\theta$ coordinate. The $\Phi$ module is a single chamber which contains 36 sections covering the full azimuth. Each section has 16 anode wires along the $z$-coordinate. In each of the $\Theta$ modules, there are four independent quadrants, each containing six rectangular cells. Each of these cells has eight anode wires directed in $z$. To remove the left-right ambiguity, only the sense wires of the three inner cells are at one edge so that the electrons in these cells drift in just one direction. In addition, each $\Theta$ module has one delay line, like those in the CDC, to give a local measurement of the orthogonal coordinate. The upstream and downstream $\Theta$ modules are rotated by $45^\circ$ in $\phi$ with respect to each other. In both the $\Phi$ and $\Theta$ modules, all of the adjacent anode wires are staggered by $\pm$ 200 $\mu$m to help resolve ambiguities. All of the FDC chambers operate with the same gas mixture as the CDC.

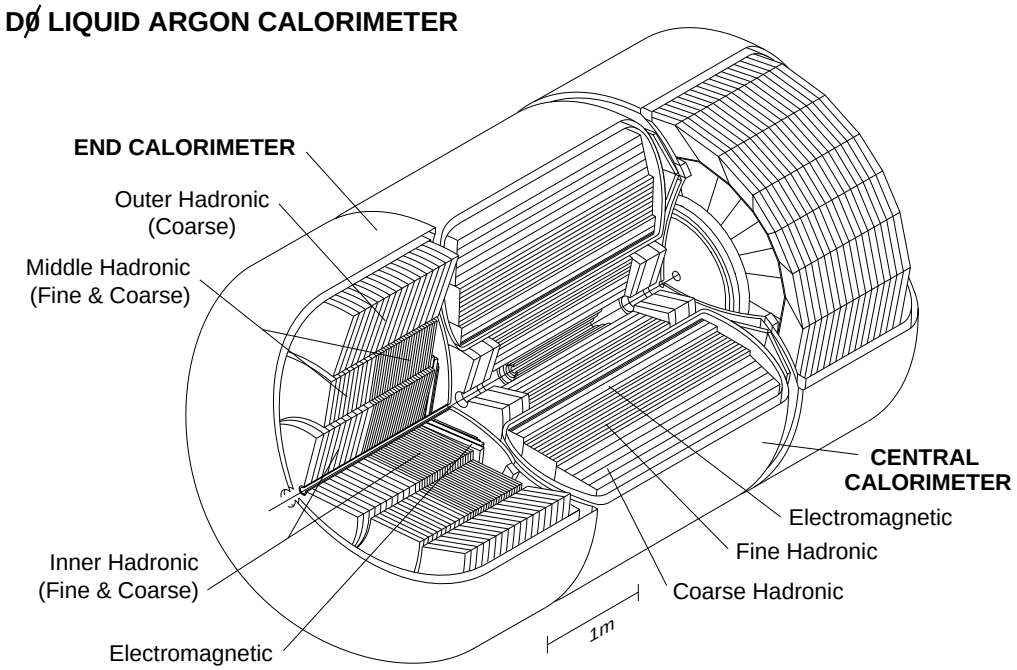


Figure 4-4: The DØ Calorimeter, showing both the Central Calorimeter (CC) and End Calorimeter (EC) components.

### 4.2.2 The Calorimeter

The DØ calorimeter serves an important role in this analysis, as it is used to help identify muons as minimum ionizing particles(MIPS) and jets associated with $b$-quarks. Figure 4-4 shows the DØ Calorimeter. The central calorimeter (CC) covers approximately $|\eta| \leq 1$ while the two end calorimeters, (ECN (north) and ECS (south)), extend the coverage out to $|\eta| \approx 4$. Both the CC and EC contain three distinct types of modules: an electromagnetic section (EM) with relatively thin uranium absorber plates, a fine-hadronic section with thick uranium plates, and a coarse-hadronic section with either thick copper or stainless steel plates.

Two types of particle showers develop in the calorimeter: electromagnetic and

hadronic. Electrons whose energy is greater than the critical energy($\sim$100 MeV for uranium) lose energy almost entirely through Bremsstrahlung. This is when a charged particle interacts with the Coulomb field around the nucleus and emits an energetic photon. This photon typically carries off a large fraction of the electron's initial energy. A high energy photon will then interact mainly through pair production in which the photon converts into an electron-positron pair. These electrons(positrons) can themselves Bremsstrahlung, continuing multiparticle production until all the particles' energies fall below the 100 MeV threshold. At this point, dissipative processes such as ionization and excitation dominate in the particles energy loss. Thus, a single electron or photon can develop into a shower of secondary electrons, positrons, and photons. This process is called an electromagnetic shower.

Hadronic particles can also initiate showers, but the physical processes that cause a hadronic shower are quite different from the processes of an electromagnetic shower. Hadrons lose energy primarily through inelastic collisions with atomic nuclei. These collisions produce secondary hadrons which can then undergo further inelastic collisions. Typically half the incident hadron energy observed as ionization is associated with secondary collisions, while the other half is lost to nuclear binding energies and neutron kinetic energy. This process is called a hadronic shower, and it continues until all the particles have either been stopped by ionization losses or absorbed by nuclear processes.

To detect these showers, the DØ Calorimeter interleaves layers of dense, inert absorber with layers of a material(liquid argon, LAr) which is sensitive to particles passing through it. This is what is generically referred to as a sampling calorimeter since only a portion of the incident particles energy can de detected. The other portion of the energy is absorbed in the inert material.

The calorimeter is divided into a large number of modules, each of which contain a stack of interleaved absorber plates and signal boards. The absorber plates are separated from the signal boards by a LAr-filled gap of 2.3 mm. The signal boards consist of a copper pad layered between two 0.5 mm thick sheets of G10. A resistive coating resides on the LAr side of the G10. When a fast charged particle passes through the LAr, it leaves a trail of ionization. This ionization is collected on the resistive coating which is held at 2.0-2.5 kV with respect to the grounded absorber plates. The signal is read out from the inner copper pads.

Both the CC and EC have a typical readout cell space of 0.1 x 0.1 in $\eta - \phi$. An exception to this is in the third layer of the EM modules, where the cells have an area of 0.05 x 0.05. This is because electromagnetic showers typically deposit the bulk of their energy in this region. Also, the cells in the forward region with $|\eta| > 3.2$, have a $\phi$ cell size of 0.2 and larger cell size in $\eta$ as well. Figure 4-5 shows the calorimeter cell segmentation, while Fig. 4-6 shows the layout of the EC EM module.

### The Central Calorimeter (CC)

The central calorimeter (CC) includes three concentric cylindrical shells, corresponding to the EM, fine-hadronic (FH), and coarse-hadronic (CH) modules, from inside to out, and provides coverage out to a pseudorapidity of about 1.2. There are 32 EM modules which are thick enough to contain most electromagnetic showers, 16 FH modules which measure showers originating from hadronic particles, and 16 CH modules which measure any leakage from the FH modules and which also serve to reduce punchthrough into the muon system. Each ring of modules are rotated with respect to the adjacent ring so that no projective ray crosses more than one intermodule gap. The total radiation lengths, $\chi_0$, of each of the CC modules are

20.5, 96.0, and 32.9, for the EM, FH, and CH modules respectively.

### The End Calorimeter (EC)

The two end calorimeters (ECN and ECS) are made up of four different module types as shown in Figure 4-4. There is one EM module and one inner-hadronic (IH) module. Outside the EM and IH are concentric rings of 16 middle and outer-hadronic (MH and OH) modules. As with the CC, the MH and OH are offset to prevent multiple cracks which particles could pass through. The EC provides coverage on each side of the CC from a pseudorapidity of about 1.3 out to about 4.0.

### The Intercryostat Detectors and Massless Gaps (ICD)

Figure 4-5 shows that the region $0.8 \leq |\eta| \leq 1.4$ contains a large amount of uninstrumented material. This consists of cryostat walls, stiffening rings, and module endplates. To correct for energy deposited in this dead material, two scintillation counter arrays, called intercryostat detectors (ICD), were mounted on the front surface of the ECs. Each ICD contains 384 scintillator tiles of size $\Delta\eta = \Delta\phi = 0.1$, which exactly matches the cell size of the liquid argon calorimeter. Also, single-cell structures called massless gaps (see Figure 4-5) were installed in both the CC and EC calorimeters. Together, the ICD and massless gaps provide a good approximation to the standard liquid argon sampling of EM showers.

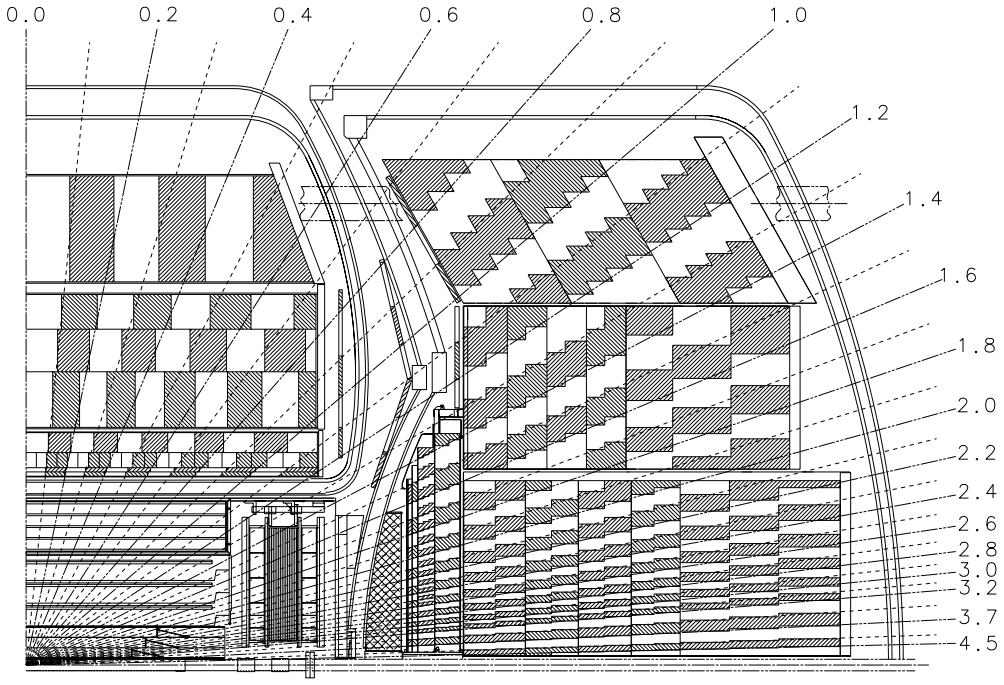


Figure 4-5: Cutaway view of the DØ Central and End Calorimeters showing the Intercryostat Detectors and Massless Gaps located between the CC and EC.

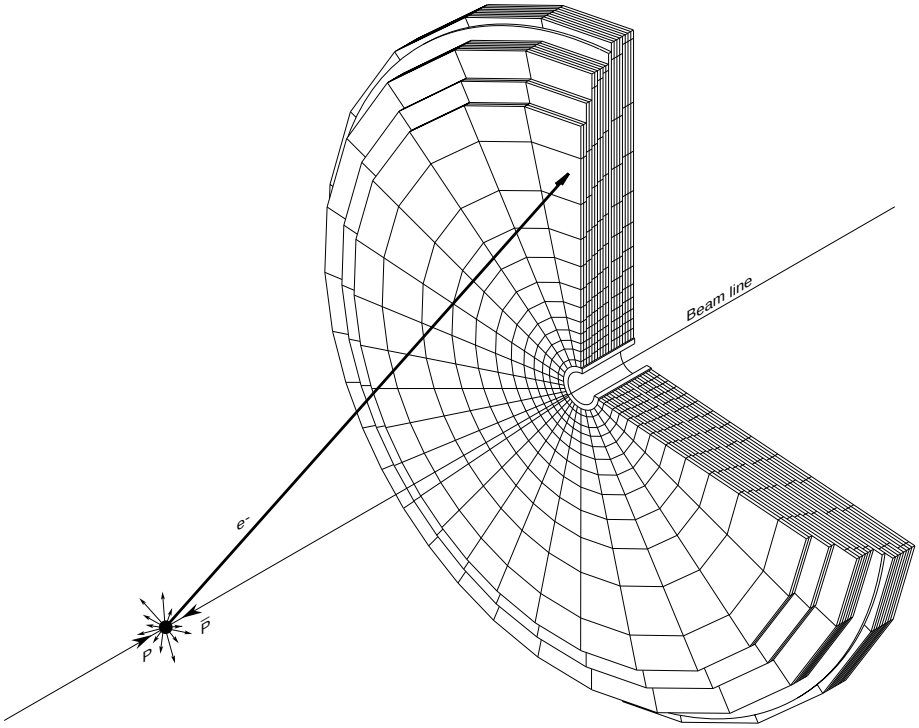


Figure 4-6: Segmentation of the end calorimeter electromagnetic module.

**The Calorimeter Performance**

The response of the calorimeter modules was studied using single electrons and pions in a test beam setup. The response for both the EM and hadronic modules is found to be linear within 0.5%. The resolution is parameterized as

$$\left(\frac{\sigma}{E}\right)^2 = C^2 + \frac{S^2}{E} + \frac{N^2}{E^2}, \tag{4.1}$$

where the constants $C, S,$ and $N$ represent calibration errors, sampling fluctuations, and noise contributions, respectively. For electrons, the measured resolutions are

$$C = 0.003 \pm 0.002, \quad S = 0.157 \pm 0.005(\mathrm{GeV})^{\frac{1}{2}}, \quad N \approx 0.140\mathrm{GeV}, \tag{4.2}$$

and for pions,

$$C = 0.032 \pm 0.004, \quad S = 0.41 \pm 0.04(\mathrm{GeV})^{\frac{1}{2}}, \quad N \approx 1.28\mathrm{GeV}. \tag{4.3}$$

### 4.2.3 The Muon System and Toroids

The DØ Muon System is located outside the calorimeter and is the outermost system of the DØ Detector. This system consists of five independent solid-iron toroidal magnets along with sets of proportional drift tube chambers (PDTs) which measure muon track coordinates down to $\theta \approx 3°$. The combined depth of material in the calorimeter and the toroids varies from 10 to 20 absorption lengths (see Figure 4-7). This feature reduces the hadronic punchthrough by a factor of $10^{-4}$ below prompt sources of muons and provides a clean environment to identify muons within hadron jets[46].

Muon directions are measured both before and after their bend in the toroids. A tight set of muon track coordinates is measured before the toroid and gives the

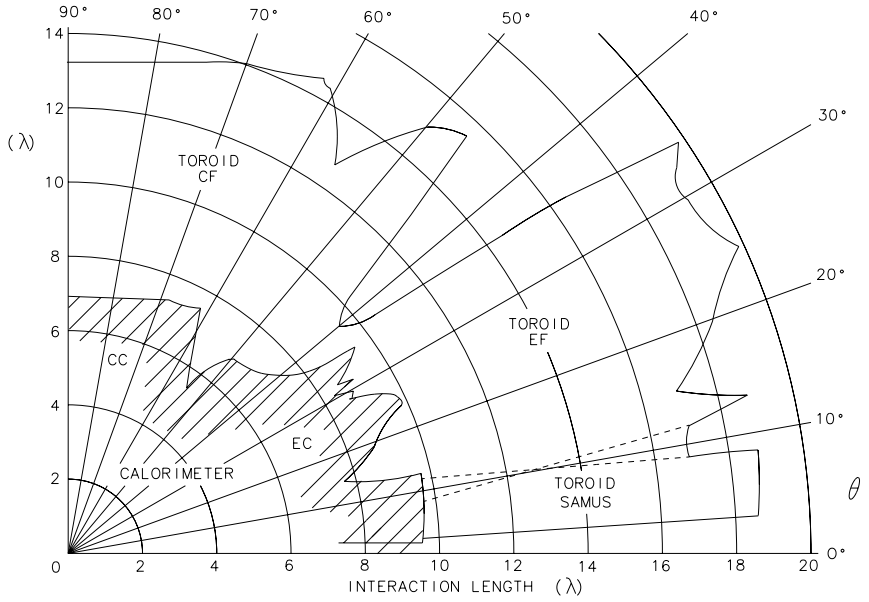


Figure 4-7: Thickness of the DØ Calorimeters and muon toroids as a function of polar angle.

entrance point. This point, along with position measurements from the primary interaction point and the central tracker, give the incident trajectory of the muon. Two sets of measurements after the toroid, which are separated by 1 to 1.5 meters, yield the exit direction. By comparing the incident and exit directions, the bend angle of the muon in the toroid is determined, and thus the momentum. The momentum resolution, $p$, is found to be

$$\left(\frac{\delta k}{k}\right)^2 = \left[\left(\frac{0.20(p-2)}{p}\right)^2 + (0.008p)^2\right]^{\frac{1}{2}}, \tag{4.4}$$

where $k = 1/p$. The first term on the right hand side of (4.4) is due to multiple Coulomb scattering, and the second term is due to chamber resolution. Also, above some value of transverse momentum($\approx$ 300 GeV/c), the finite position resolution of the chambers dominates.

The central toroid (CF) covers the region $|\eta| \leq 1$ and the end toroids (EF)

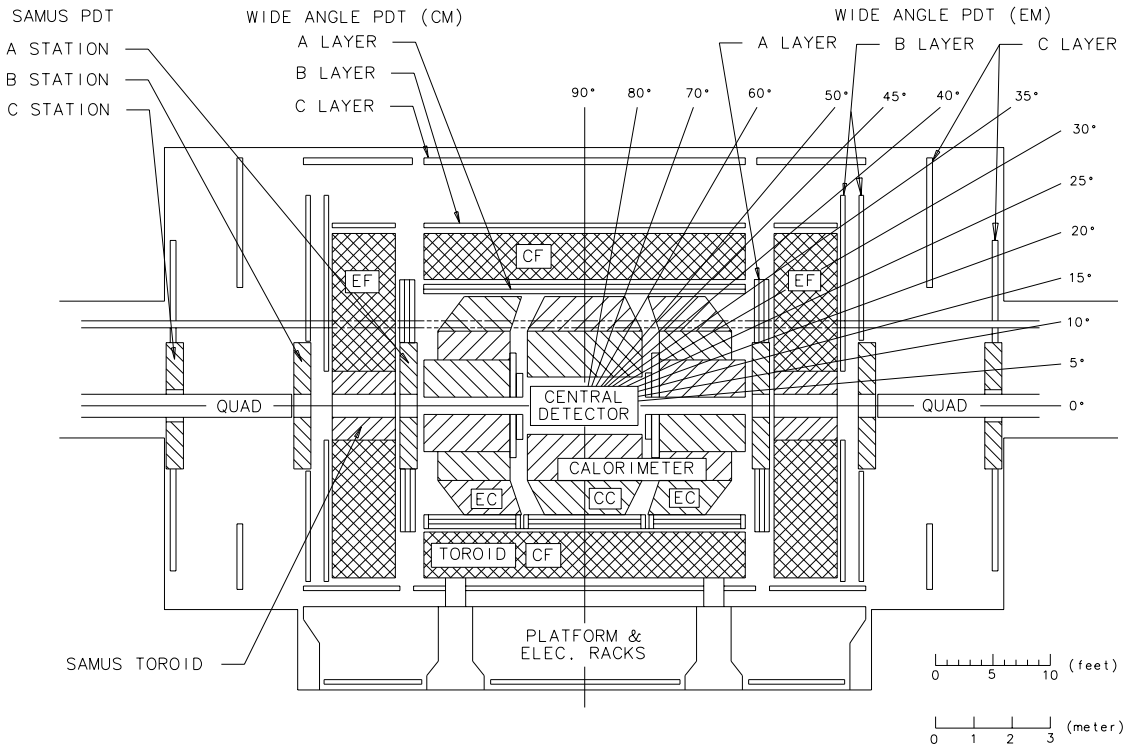


Figure 4-8: Elevation view of the DØ Detector showing the five muon toroids and the approximate arrangement of the A, B, and C layers of proportional drift tubes.

cover $1 < |\eta| \leq 2.4$. The small angle muon system (SAMUS) toroids fit in the center hole of the EF toroids and cover the region $2.4 < |\eta| \leq 3.4$. Figure 4-8 shows the elevated side view of the DØ Detector with the five toroids and their associated PDT layers.

### Muon Toroids

The CF toroid[47, 48] is a square annulus 109 cm thick centered on the Tevatron beam lines. The inner surface of the CF toroid is 317.5 cm from the beam. Three sections comprise the CF toroid. A middle bottom section which is fixed to the

detector platform and two C-shaped shells which can be moved perpendicular to the beams to allow access to the inner detectors. There are twenty coils of 10 turns each carrying currents of 2500 A which induce the 1.9 Tesla field. Fringe fields are moderately strong and can exceed 0.01T near the central beam. Leakage represents 3.7% of the total CF flux.

The two EF toroids have eight coils of eight turns each carrying 2500A (in series with the CF) and excite fields up to approximately 2.0T. These toroids are located at $447 \leq |z| \leq 600$ cm. Their outer surfaces are at 417 cm and each EF toroid has a 182 cm square inner hole centered around the Tevatron beams.

Each SAMUS toroid is located within the inner hole of the EF toroid. The SAMUS toroids have an outer surface at 170 cm from the Tevatron beams and a 102 cm square inner hole. Two coils of 25 turns each carrying a current of 1000 A provide a field which is aligned with the EF toroids.

### Wide Angle Muon Chambers

The wide angle muon system (WAMUS) provides muon measurement for the entire CF and most of the EF toroids. The WAMUS system is comprised of 164 individual proportional drift tube chambers (PDTs). The WAMUS chambers are arranged in three layers: the "A" layer before the iron toroids and the "B" and "C" layers after the magnets. Four PDT planes make up the "A" layer chambers while the "B" and "C" chambers have three PDT planes each.

The WAMUS PDTs are formed by interlocking aluminum extrusions as shown in Figure 4-9. The relative transverse offset between the layers of the chambers permits resolution of left-right drift-time ambiguities. The cells are comprised of two cathode pad strips inserted into the top and bottom of each cell with an anode

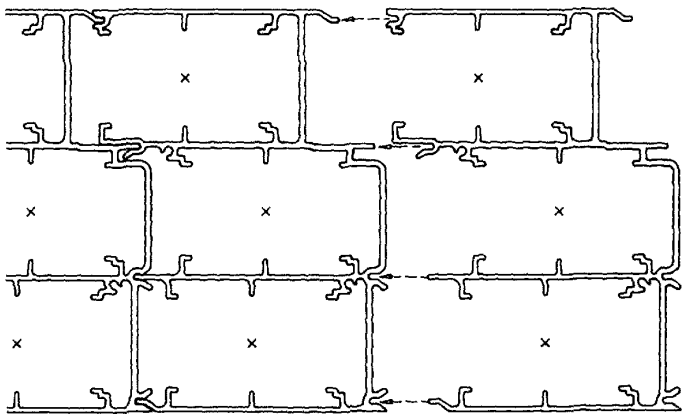

Figure 4-9: Extruded aluminum section of a "B" or "C" layer WAMUS PDT. The "A" layer chamber extrusions are similar, but have a 4 cell depth instead of 3. 'x' shows the location of the anode wire.

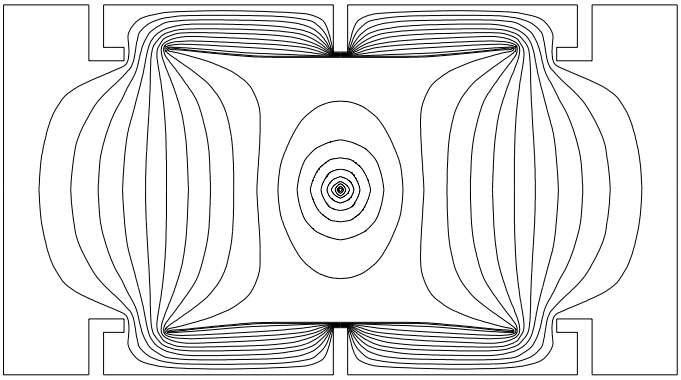

Fig. 4 ELECTROSTATIC EQUI-POTENTIAL LINES OF 4" PDT CELL
SIGNAL WIRE AT +5 KV, AND VERNIER PADS AT +2 KV

Figure 4-10: Single cell depiction of a WAMUS PDT showing the equipotential surfaces surrounding the cathode pads and anode wire.

wire held near the center of the cell, as shown in Figure 4-10. The 50 $\mu$m nickel-plated gold anode wires are held at +4.65 kV and the cathod pads are held at +2.3 kV. The individual cell structure for all WAMUS PDTs is the same. The chambers differ in size from differences in number of cells in depth (3 or 4 cells), width (between 14 and 24 cells), and length (between 191 and 579 cm). The cells have a maximum drift distance of 5 cm.

The coordinate ($\zeta$) along the wire direction (non-bend view) is measured using signals from the cathode strip. Each cathode strip contains two pads (inner and outer ganged pair) separated by a repetitive diamond shaped insulating pattern. Figure 4-11 shows the cathode and the pattern which repeats every 61 cm. The ratio of charge deposited on the inner and outer pads provides a measurement of the $\zeta$ coordinate, modulo the the repeat distance of the diamond pattern($\approx$ 30 cm). The ambiguity of the measurement is resolved by using the time difference of the signal arrival along the anode at the two ends of the chamber. The $\zeta$ resolution in a given chamber is approximately $\pm$ 3 mm. There are 11,386 cells in the WAMUS system.

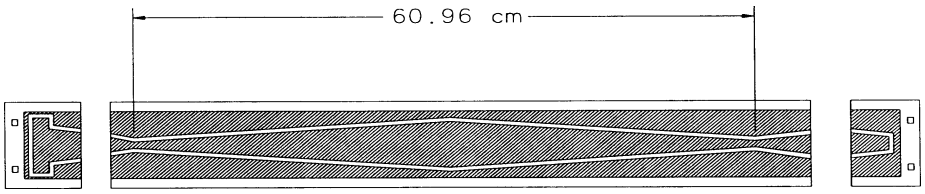


Figure 4-11: Layout of the two separate electrodes which make up the PDT cathodes. The signals from the outer and inner cathodes are measured independently.

The WAMUS chambers are operated with a gas mixture of Ar, $CF_4$, and $CO_2$ (90%:5%:5%), which has a drift velocity of about 6.5 cm$\mu$s$^{-1}$. The resolution of the WAMUS chambers is $\pm$0.53 mm in the bend view and $\pm$0.30 mm in the non-bend view. These resolutions are limited by diffusion and surveying inaccuracies.

### Small Angle Muon Chambers

The small angle muon system (SAMUS) is comprised of two mirror-image systems, one in the north and one in the south. The "A" station is located before the SAMUS toroid. The "B" and "C" stations are between the toroid and the beginning of the low-beta quadrapole for the DØ insertion. Each end of the SAMUS system contains three stations with three planes of paired 29 mm internal diameter cylindrical proportional drift tube chambers[49]. These pairs are oriented in $x, y$, and $u$ directions, where the $u$ direction is at 45° with respect to $x$ and $y$. There is a total of 5308 tubes in the SAMUS system.

The SAMUS PDTs are constructed from 3 cm external diameter stainless steel tubes with a 50 $\mu$m gold plated tungsten anode in the center held at +4.0 kV. The SAMUS system is operated with a $CF_4$-$CH_4$ (90%:10%) gas mixture with an average drift velocity of 9.7 cm $\mu s^{-1}$. This leads to a maximum drift time of 150 ns and a resolution of $\pm$0.35 mm in the bend view and $\pm$0.35 mm in the non-bend view.

## 4.3 The DØ Trigger System

The DØ trigger system is used to select interesting physics events from the $p\overline{p}$ collisions. The trigger has three basic levels, each of which reduces the event pass rate by making tighter cuts on event characteristics. With a typical running luminosity of approximately $\mathcal{L}$ = 5 x $10^{30}$cm$^{-2}$s$^{-1}$ during Run Ia, the Level 0 rate is about 150 kHz. This rate is passed into Level 1 which is a collection of hardware trigger elements from all detector components. These elements are arranged in a flexible software-driven design which allows for easy modification. All Level 1 trigger decisions are made within the 3.5 $\mu$s beam crossing and thus don't contribute any deadtime. Hardware triggers that require additional time to make their decision are referred to as Level 1.5. The overall Level 1 trigger rate is about 200 Hz. The Level 1.5 triggers serve to confirm the Level 1 trigger and provide an additional rejection factor of between 2 and 10. These events are then passed to the DØ microprocessor farm which serves as the event builders as well as the Level 2 trigger. The Level 2 trigger is a collection of sophisticated software algorithms which reduce the Level 1/1.5 rate to about 2 Hz. These events are then stored on 8mm magnetic tape for further analysis.

### 4.3.1 Level 0 Trigger

The Level 0 trigger is designed to detect events containing an inelastic collision. This condition is determined by the coincidence of hits in two hodoscopes of scintillation counters mounted on the front surfaces of the end calorimeters. An inelastic $p\overline{p}$ collision will typically include a large amount of activity in the forward region. The hodoscopes have partial coverage for $1.9 < |\eta| < 2.3$ and nearly full coverage for $2.3 > |\eta| < 3.9$. This coverage ensures that a coincidence of both Level 0 detectors be $\geq$99% efficient in detecting nondiffractive inelastic collisions.

The Level 0 trigger serves two other important functions as well. First, the Level 0 trigger provides information on the $z$-coordinate of the primary collision vertex by measuring the difference in arrival time for particles hitting the two Level 0 detectors. The time resolution is approximately 100-150 ps which provides a vertex position resolution of about 8 cm. Second, at the high luminosities delivered by the Tevatron in Run Ia, there is appreciable probability for multiple interactions. At $\mathcal{L} = 5$ x $10^{30}\text{cm}^{-2}\text{s}^{-1}$ there are on average 0.75 interactions per crossing with a higher probability for more multiple interactions as the luminosity increases. The Level 0 trigger identifies potential multiple interaction events and passes this information on to the higher level triggers.

### 4.3.2 Level 1 Trigger

The DØ Level 1 trigger is designed to make decisions within the 3.5 $\mu$s beam crossing time delivered by the Tevatron collider, thus introducing no dead time in the data acquisition process. The Level 1 framework collects digital information from each of the specific Level 1 trigger devices and makes trigger decisions based upon pre-programmed software and hardware conditions. This framework thus

allows for many possible configurations(see [37]). The analysis of this thesis is only based upon the use of the jet and muon components of the trigger, so only these trigger elements will be discussed here.

### Main Ring Veto Trigger

While the Tevatron is running in normal collider mode, the Main Ring accelerator is used to produce antiprotons with a cycle period of 2.4s. The Main Ring tunnel is located just above the Tevatron Ring, and passes through the Coarse Hadronic section of the calorimeter, just below the "A" layer muon chambers. (See Fig. 4-8 for the location of the Main Ring.) During injection and transition phases of the $\overline{p}$ production cycle, losses from the Main Ring show up in the detector. These losses tend to saturate the muon chambers near the Main Ring tunnel and cause the high voltage to temporarily sag. Approximately 400-500 ms are needed for the high voltage to recover after the initial injection. To avoid collecting data during this time, the MRBS_LOSS veto is used. MRBS_LOSS uses the clock signals from the accelerator to veto events during a 0.4 s window starting at injection, continuing through transition, and allowing time for high voltage recovery. This results in a loss of about 17% in luminosity.

Additional losses from the accelerator occur when a Main Ring bunch passes through the detector. If this happens to occur during a $p\overline{p}$ bunch crossing in the Tevatron, the MICRO_BLANK veto is invoked. The MICRO_BLANK veto is used if a Main Ring bunch is present in the detector within 800 ns of $p\overline{p}$ crossing. This adds an additional loss in luminosity of 9%. These veto terms are part of the input to the AND-OR network of the Level 1 Trigger Framework.

### Level 1 Calorimeter Trigger

The Level 1 calorimeter trigger is comprised of trigger towers with $\Delta\eta = \Delta\phi = 0.2$ and coverage out to $|\eta| = 3.2$. Separate trigger towers are defined for the EM and hadronic sections of the calorimeters.

The calorimeter trigger definition used for the collection of data in this thesis was to require at least one jet with $E_T$ greater than 3 Gev. A trigger jet is defined as the sum of energy in the hadronic and EM trigger towers with the same $\eta$ and $\phi$.

### Level 1 Muon Trigger

The Level 1 muon trigger is divided up into 5 separate eta regions: CF($|\eta|$ <1.0), EF-North(1.0< $\eta$ <2.4), EF-South(-1.0< $\eta$ <-2.4), SAMUS-North(2.4< $\eta$ <3.3), and SAMUS-South(-2.4< $\eta$ <-3.3). The basic information provided by the muon chambers to the muon trigger system is a single latch bit for each of the approximately 16,700 drift cells[37]. This information gives the bend coordinate of fired drift cells with a granularity of 10 cm in WAMUS($|\eta|$ <1.7) and 3 cm in SAMUS(2.4< $|\eta|$ <3.3). Along with the analog time and charge signals, these bits are sent to the counting house where they are received by the 200 Module Address Cards(MAC's). The MAC cards and subsequent Level 1 and Level 1.5 muon trigger electronics are kept physically distinct for the five separate eta regions.

The MAC cards receive the latch bits, perform zero-suppression for data acquisition, and generate bit patterns corresponding to centroids found in each muon chamber. A centroid is defined as the most-likely half-cell traversed by a track, which is then projected to the midplane of the chamber. Centroid finding logic is programmed into PALs using information from pairs of drift cells. The centroid

logic is optimized to find the correct centroid in the presence of geometrical inefficiencies and delta rays. Bit patterns consisting of a logical OR of the centroids is then sent to the Level 1 muon trigger called the Coarse Centroid Trigger, or CCT. A full list of centroids is sent to the Level 1.5 trigger, called the OTC or Octant Trigger Card, described in the next section.

The CCT cards receive the OR'd bit pattern from up to 13 MAC cards, corresponding to 3 chambers in the "A" layer, 5 in the "B" layer, and 5 in the "C" layer(see Fig. 4-12 ). The CCT's then further OR the centroid bit pattern by a factor of four which gives a hodoscopic pattern 6 cells wide(60 cm) for each layer. The final bit patterns from the "B" and "C" layer MAC's produce a 12 bit output pattern corresponding to 12 possible roads for "A" layer bits. These bits are then compared to the actual 12 bit "A" layer pattern to determine good Level 1 trigger muons.

The output of all CCT's for a given $\eta$ region is sent to a second CCT-like card which counts the muon candidates in that region. Two bits of muon multiplicity information for each $\eta$ region are sent to the Trigger Monitor Card(TRGMON) described below. CCT decisions are available within the 3.5 $\mu$s bunch crossing time. In addition, the results from individual CCT cards are latched and readout using the CCT LATCH card which is located in the Level 1.5 VME crates.

### Level 1.5 Muon Trigger

After a trigger framework decision on any Level 1 muon trigger, the MAC full centroid lists are strobed into the OTC cards for Level 1.5 decision making. The Level 1.5 trigger has a sharper $p_T$ threshold and is used to confirm Level 1 muon triggers. Each OTC accepts inputs from 3 layers of MAC's. The mapping of

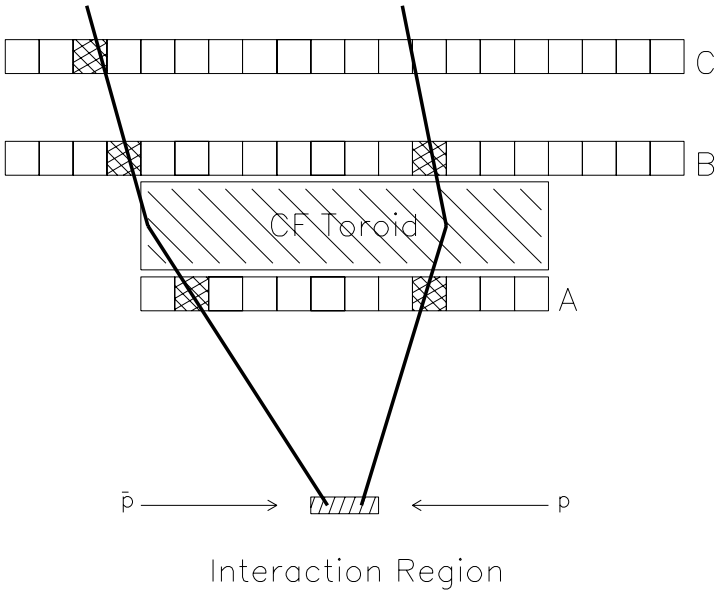


Figure 4-12: Coarse centroids used by the Level 1 trigger. Hits on two or three layers may form a Level 1 trigger.

MAC's to OTC's is identical as the CCT's except that centroids for a given layer are transmitted serially and not in parallel as is done with the bit patterns for the CCT's. The OTC compares all combinations of "A", "B", and "C" layer centroids to determine if they correspond to tracks above a certain $p_T$ threshold(typically 3 to 7 GeV/c). The address space for each combination exceeds the physical limits of available fast SRAM's, so instead each combination of "A", "B", and "C" centroids is used to generate two addresses to two different SRAM's containing combinations which correspond to tracks exceeding a given $p_T$ threshold. These two addresses were optimized to eliminate any overlap between tracks above the programmed $p_T$ threshold. Thus, a good Level 1.5 trigger would require a confirmation from both of these memories. A 4 x 4 array of these SRAM's allows the look-ups for the 16 combinations of 1 "A" centroid, 4 "B" centroids, and 4 "C" centroids to be carried out in parallel.

For each good trigger combination, the latched input centroid for that trigger is used as an address input for a second set of memories. These memories produce two 24 bit trigger words which are user defined and output to FIFO's for read out by the OTCMGR, described below. This information is then available for further processing on the OTCMGR and at Level 2. Processing times for the Level 1.5 trigger in WAMUS are typically less than 2 $\mu$s.

After each OTC's processing is complete, it's output FIFO is read by the OTCMGR (OTC Manager) card. The OTCMGR for each $\eta$ region processes all the trigger words for that region and sends 3 user defined bits of $p_T$, multiplicity, and/or geographic information to the TRGMON.

The TRGMON(Trigger Monitor) card receives two bits of Level 1 multiplicity and 3 bits of Level 1.5 information from each eta region. These Level 1 and Level 1.5 eta region bits are mapped into 16 Level 1 and 16 Level 1.5 physics bits (e.g.

two muons in $|\eta|$ <3.3) via downloadable RAM on the TRGMON. These 32 bits are sent to the AND-OR network of the trigger framework along with trigger information from other detector systems to determine if any of the programmed 32 specific Level 1 physics bits have fired.

### 4.3.3 Level 2 Trigger

The Level 2 trigger is a software based filter used to reduce the Level 1 rate from approximately 200 Hz down to 2 Hz, the rate at which events can be logged to tape.

Approximately 50 Vaxstation 4000/60's, called Level 2 nodes, house the Level 2 trigger code. When an event passes a Level 1 trigger, that information is digitized and read out on data cables to an idle Level 2 node. The Level 2 trigger then performs a partial reconstruction of the event using information from all subsystems of the detector. This includes digital information unavailable to the Level 1 trigger framework so that the full resolution of the detector can be utilized. Typical processing time from Level 2 triggers is 200 ms.

The Level 2 reconstruction is built around a series of filter "tools". Each tool has a specific function related to the identification of physics objects, such as muons, jets, EM calorimeter clusters, and missing $E_T$. These tools are called from any one of 128 "scripts", or output triggers. A script is comprised of a Level 1 trigger requirement and any combination of Level 2 tools, depending on what type of event characteristic is desired. Events that pass any script are subsequently written to tape for complete event reconstruction and analysis.

# Chapter 5

# Data Selection

This chapter describes the cuts which are applied to the data set in order to select good dimuon events, and in particular, cuts which enrich the sample originating from $b$-quark production. Several different trigger configurations are used to collect the data set, and each will be described in detail. In addition, the data processing and offline cuts applied to the data sample will be detailed. These cuts include "muon offline identification" cuts, used to select good dimuon events originating from the $p\overline{p}$ interaction, and "event selection criteria" which serve to enhance the fraction of dimuon events produced from $b$-quarks.

## 5.1 Data Collection and Processing

Data for this analysis was collected during the 1992-1993 collider run at Fermilab. Only data collected after the January 1993 shutdown was used, corresponding to global run numbers 60833 to 65429. The data is restricted to these runs because of an improvement in the dimuon trigger acceptance installed during the January shutdown. In addition, data from bad runs, where problems exist with

the detector(high-voltage), trigger, or data acquisition system, are removed from the sample[50].

### 5.1.1 Event Reconstruction

After the data is collected and written to tape, the hit information from each system of the detector is used to reconstruct the momenta and trajectories of the objects produced in the $p\overline{p}$ collisions. All data used in this analysis is processed with versions 11.17-11.19 of the DØ reconstruction program. As part of the event reconstruction, events are written to different output streams based on event characteristics. The "ALL" stream contains every event written to tape, while the "B2M" stream includes those events with event characteristics consistent with dimuon production, as described below.

In addition to the standard DØ reconstruction, two other programs are run on the data set. The first, is a fix to a known problem with the muon global fit code in the official V11 executable of the reconstruction. The second program, known as CAFIX[51], is run to adjust the jet, electron, and missing transverse energy scales.

### 5.1.2 *b*-physics Data Stream

The data used in this analysis is selected from the B2M stream, also known as the *b*-physics dimuon stream. This subset of the ALL stream data sample represents approximately 6% of the total post-shutdown data, as shown in Table 5-1. The B2M stream imposes a loose set of cuts based on the reconstructed muon information. Each event in the stream must have at least two reconstructed muon tracks in addition to satisfying the following three criteria:

- **Muon Track Quality**

  The muon track quality flag, IFW4, describes the character or goodness of the reconstructed muon track. The muon track quality flag is described in detail in Sec. 5.4.1. The B2M stream requires that the muon track quality flags of the two muons sum to two or less.

- **Calorimeter Energy**

  For each of the muon tracks, there must be an associated minimum ionizing energy deposited in the calorimeter. The energy in the calorimeter cells along the muon track plus the two nearest neighbor cells must be greater than 1.0 GeV.

- **Cosmic Ray Rejection**

  The three-dimensional opening angle is defined as the dot product of the direction cosines of the muon track segments outside the iron toroid. Only the muon tracking information is used in this calculation since it does not force the track to pass through the event vertex. The B2M stream requires that the three-dimensional opening angle be less than 160° or at least one muon track to have a floating time, $t_0^f$, less than 100 ns. The float time parameter is described in Sec. 8.2.1. This cut is also referred to as the MUCTAG (MUon Cosmic TAG) flag.

## 5.2 Trigger Requirements

Three independent trigger conditions are used to select events used in this analysis. They are known as MU_2_HIGH, MU_1_JET, and MU_JET_LOW. As with all of the

| Sample | Trigger Name | | |
|---|---|---|---|
| | MU_2_HIGH | MU_1_JET | MU_JET_LOW |
| Total Post-shutdown Data Sample | $6 \times 10^6$ | $6 \times 10^6$ | $6 \times 10^6$ |
| B2M Stream | $3.5 \times 10^5$ | $3.5 \times 10^5$ | $3.5 \times 10^5$ |
| B2M Stream w/ Bad Runs Removed | $3.1 \times 10^5$ | $3.1 \times 10^5$ | $3.1 \times 10^5$ |
| Satisfy Level 1 Trigger | $1.3 \times 10^5$ | $8.7 \times 10^4$ | $7.2 \times 10^4$ |
| Satisfy Level 2 Trigger | $4.8 \times 10^4$ | $7.9 \times 10^4$ | $6.9 \times 10^4$ |
| Final Candidate Sample | 192 | 277 | 397 |

Table 5-1: Number of events found in the selection of the $b\overline{b}$ candidate event sample for each trigger used.

DØ triggers, each of these consisted of a scintillator-based Level 0 component, a hardware-based Level 1 component, and a software-based Level 2 component.

The Level 0 trigger signals when a $p\overline{p}$ inelastic collision occurs (see Sec. 4.3.1). This condition is required on all three of the triggers used. The difference in the three trigger conditions is found in the Level 1 and Level 2 configurations. Each of these is explained in detail below. A summary of the three different trigger conditions is given in Table 5-2.

| Trigger Name | Level 1 | Level 2 |
|---|---|---|
| MU_2_HIGH | $\geq 2$ muons, $\lvert\eta^{\mu}\rvert < 1.7$ | $\geq 2$ muons, $\lvert\eta^{\mu}\rvert < 1.7$, $p_T^{\mu} \geq 3.0$ GeV/c |
| MU_1_JET | $\geq 1$ muon, $\lvert\eta^{\mu}\rvert < 1.7$<br>$\geq 1$ jet, $\lvert\eta^{jet}\rvert < 3.2$ | $\geq 1$ muon, $\lvert\eta^{\mu}\rvert < 1.7$, $p_T^{\mu} \geq 3.0$ GeV/c<br>$\geq 1$ jet, $E_T^{jet} \geq 10$ GeV |
| MU_JET_LOW | $\geq 1$ muon, $\lvert\eta^{\mu}\rvert < 2.4$<br>$\geq 2$ jets, $\lvert\eta^{jet}\rvert < 3.2$ | $\geq 1$ muon, $\lvert\eta^{\mu}\rvert < 2.4$, $p_T^{\mu} \geq 3.0$ GeV/c<br>$\geq 2$ jets, $E_T^{jet} \geq 10$ GeV |

Table 5-2: Level 1 and Level 2 trigger requirements.

### 5.2.1 MU_2_HIGH Trigger

The MU_2_HIGH trigger is a muon-only based trigger. The Level 1 trigger requires AND/OR terms corresponding to two Level 1 muon triggers with $|\eta^{\mu}| < 1.7$. The Level 1 muon trigger has a turn on efficiency of 50% at $p_T^{\mu} = 4.0$ GeV/c. In addition, the main ring vetoes MRBS_LOSS and MICRO_BLANK(see Sec. 4.3.2) are also required. The Level 2 filter requires two reconstructed muon tracks with $p_T^{\mu} \geq 3.0$ GeV/c and $|\eta^{\mu}| < 1.7$. The MU_2_HIGH Level 2 filter also includes a cut on opposite tracks or hits in Level 2 based on the MUCTAG flag, described in Sec. 5.1.2. In addition, as with all Level 2 muons, a cut is placed on the quality of the reconstructed muons. The two muon quality cuts found in Level 2 are "common" and "tight". These correspond to maximum values of the muon quality flag, IFW4, of one and zero respectively. This flag has the same definition in the offline reconstruction and is described in Sec. 5.4.1. The MU_2_HIGH Level 2 filter requires that both muons have a quality of "common" or better, and one muon to have a quality of "tight".

### 5.2.2 MU_1_JET Trigger

The MU_1_JET trigger incorporates information from both the muon system and the calorimeter. At Level 1, the muon portion of the trigger requires one muon with $|\eta^{\mu}| < 1.7$. In addition, the Level 1 MU_1_JET trigger requires one or more hadronic plus EM trigger towers with $E_T \geq 3$ GeV. The MRBS_LOSS and MICRO_BLANK veto terms are also included in the Level 1 definition. The Level 2 filter requires that there be at least one "tight" muon with $p_T^{\mu} \geq 3.0$ GeV/c and $|\eta^{\mu}| < 1.7$. The Level 2 jet section of the MU_1_JET trigger requires that there be at least one reconstructed jet with $E_T \geq 10.0$ GeV using a jet cone size of $R = 0.7$. A complete

description of the jet reconstruction is found in Sec. 5.5.6.

### 5.2.3 MU_JET_LOW Trigger

Like the MU_1_JET trigger, the MU_JET_LOW trigger also uses information from both the muon system and the calorimeter. The Level 1 muon trigger requires one muon with $|\eta^{\mu}| < 2.4$, while the jet portion of the Level 1 MU_JET_LOW trigger requires at least two hadronic plus EM trigger towers with $E_T \geq 3$ GeV each. Once again, the MRBS_LOSS and MICRO_BLANK veto terms are included. The Level 2 filter requires that there be at least one "common" muon with $p_T^{\mu} \geq 3.0$ GeV/c and $|\eta^{\mu}| < 2.4$, and that there be at least one reconstructed jet with $E_T \geq 10.0$ GeV.

### 5.2.4 Trigger List Versions

Three different versions(7.1, 7.2, 7.3) of the trigger definition menu were used to collect this data sample. Different versions of the trigger menu correspond to changes in the definition of specific trigger bits or changes in the Level 2 reconstruction code. A complete listing of the trigger versions, associated Level 2 executables, and STP[1] file versions is given in Table 5-3[52].

The only changes in trigger versions which affect this analysis occurred in the MU_1_JET and MU_JET_LOW trigger. Slight modifications to the Level 2 muon filter were made in each trigger version. Table 5-4 lists these changes for the MU_1_JET and MU_JET_LOW triggers and their associated trigger version.

[1]The STP files define the geometry of the detector. Access to the detector during the run required moving the detector from its original position.

| Effective Date [1993] | Trigger Menu | L2 EXE | L2 STP | Global Runs |
|---|---|---|---|---|
| Feb. 7 | 7.1.0 | 4.3 | 4.3 | 60369-60379 |
| | 7.1.1 | | | 60414-60420 |
| | 7.1.2 | | | 60473-60700 |
| | 7.1.2 | 4.4 | 4.4 | 60833-60834 |
| | | 4.5 | 4.5 | 60835-60978 |
| | | 4.6 | 4.6 | 60979-61617 |
| | | 4.7 | 4.7 | 61618-62149 |
| Mar. 10 | 7.2.0 | 4.8 | 4.8 | 62158-62199 |
| | 7.2.1 | | | 62200-63802 |
| | | | 4.9 | 63803-63866 |
| Apr. 21 | 7.3.0 | | | 64086-64094 |
| | 7.3.1 | | | 64096-64105 |
| | 7.3.2 | | | 64127-64278 |
| | | 4.9 | | 64425-64675 |
| | | 4.11 | 4.11 | 64676-65121 |
| | | 4.12 | 4.12 | 65122-65421 |
| | | 4.13 | 4.13 | 65422-65879 |

Table 5-3: Versions of trigger list, Level 2 executable, and Level 2 STP file and the corresponding global run numbers.

## 5.3 Luminosity Determination

In order to calculate the integrated luminosity sampled by each trigger, a determination of the total time-integrated luminosity sampled by the detector must be made. A complete discussion of this calculation may be found in[53].

The instantaneous luminosity, $\mathcal{L}$, is related to the counting rate, $R_{\mathrm{L}\emptyset}$, observed in the Level 0 trigger and the inelastic cross section, $\sigma_{\mathrm{L}\emptyset}$, sampled by the Level 0

| Trigger Menu | MU_1_JET | MU_JET_LOW |
|---|---|---|
| 7.1 | $\geq 1$ "common" muon | $\geq 1$ "tight" muon |
| 7.2 | $\geq 1$ "common" muon | $\geq 1$ "common" muon |
| 7.3 | $\geq 1$ "tight" muon | $\geq 1$ "common" muon |

Table 5-4: Level 2 muon definitions for the MU_1_JET and MU_JET_LOW triggers.

trigger:

$$\mathcal{L} = \frac{R_{\mathrm{L}\emptyset}}{\sigma_{\mathrm{L}\emptyset}}. \tag{5.1}$$

This is only true in the limit of low instantaneous luminosity, where the chance for more than one interaction in a bunch crossing is negligible. It also assumes that the rate observed in the Level 0 counters is equal to the interaction rate.

The inelastic scattering cross section can be separated into three parts: single diffractive, double diffractive, and the hard core scattering component. The world average cross sections for these processes are determined using data from E710[54] and the CDF Collaboration[55, 56, 57]. From this, the observable Level 0 cross section is

$$\sigma_{\mathrm{L}\emptyset} = \varepsilon_{\mathrm{L}\emptyset}(\varepsilon_{\mathrm{SD}}\sigma_{\mathrm{SD}} + \varepsilon_{\mathrm{DD}}\sigma_{\mathrm{DD}} + \varepsilon_{\mathrm{HC}}\sigma_{\mathrm{HC}}), \tag{5.2}$$

where the efficiencies for detecting each process, $\varepsilon_{\mathrm{SD}}, \varepsilon_{\mathrm{DD}}$, and $\varepsilon_{\mathrm{HC}}$, are determined using Monte Carlo. The overall efficiency of the Level 0 trigger, $\varepsilon_{\mathrm{L}\emptyset}$, is determined from the data. A summary of the input numbers used in this calculation and the resulting observable cross section is given in Table 5-5.

The effect of multiple interactions in a bunch crossing have to be taken into

| Inelastic Process | Acceptance [%] |
|---|---|
| SD Acceptance ($\varepsilon_{\rm SD}$) | $15.1 \pm 0.8$ (stat) $\pm 5.4$ (sys) |
| DD Acceptance ($\varepsilon_{\rm DD}$) | $71.6 \pm 1.1$ (stat) $\pm 3.1$ (sys) |
| HC Acceptance ($\varepsilon_{\rm HC}$) | $97.1 \pm 0.5$ (stat) $\pm 1.9$ (sys) |
| **Inelastic Process** | **Cross Section [mb]** |
| SD Cross Section ($\sigma_{\rm SD}$) | $9.54 \pm 0.43$ |
| DD Cross Section ($\sigma_{\rm DD}$) | $1.15 \pm 0.17$ |
| HC Cross Section ($\sigma_{\rm HC}$) | $48.25 \pm 2.23$ |
| Observable Cross Section ($\sigma_{\rm L\emptyset}$) | $46.7 \pm 2.5$ |

Table 5-5: Inputs to the calculation of the inelastic cross section observed by the Level 0 trigger.

account since the instantaneous luminosities delivered during the 1992-1993 run were high. In this case, the Level 0 counting rate is less than the interaction rate since multiple interactions get counted only once. Using Poisson statistics, the average number of interactions per crossing, $\overline{n}$, is given by

$$\overline{n} = \mathcal{L}_{meas} \tau \sigma_{\rm L\emptyset}, \tag{5.3}$$

where $\tau$ is the beam crossing time of 3.5 $\mu$s. The correction factor to account for multiple interactions is then given by

$$\frac{\mathcal{L}_{real}}{\mathcal{L}_{meas}} = \frac{\overline{n}}{1 - e^{-\overline{n}}} = \frac{-\ln(1 - \mathcal{L}_{meas} \tau \sigma_{\rm L\emptyset})}{\mathcal{L}_{meas} \tau \sigma_{\rm L\emptyset}}, \tag{5.4}$$

where (5.3) has been substituted into (5.4).

Now that the total integrated luminosity sampled by the detector is known, we must calculate what fraction of this luminosity is actually available to each of the triggers. Several factors affect this calculation. First, a prescale on each of the Level 1 triggers was imposed due to limitations in the available bandwidth in the Trigger Framework. The prescale depended on the instantaneous luminos-

ity delivered by the accelerator, typically about $5\times10^{30}\text{cm}^{-2}\text{s}^{-1}$. Second, dead time introduced by the Level 1 Trigger Framework resulted in the loss of the next bunch crossing after a good Level 1 trigger. Finally, dead times introduced by the MRBS_LOSS and MICRO_BLANK vetoes must also be accounted for. The instantaneous luminosity for each trigger is calculated using the offline luminosity utility[58], which accounts for prescales, multiple interactions, and any dead time caused by the Level 1 Trigger Framework and by the main ring vetoes. Table 5-6 lists the integrated luminosity and average prescale for each of the triggers used. The uncertainty in the integrated luminosity is 5.4%[53].

| Trigger Name | Average Prescale | $\int \mathcal{L}dt$ [$\text{nb}^{-1}$] |
|---|---|---|
| MU_2_HIGH | 5/3 | 6568.0 $\pm$ 354.7 |
| MU_1_JET | 3 | 3711.9 $\pm$ 200.4 |
| MU_JET_LOW | 5/3 | 6506.1 $\pm$ 351.3 |

Table 5-6: The average prescales and integrated luminosities for each of the triggers used.

## 5.4 Offline Muon Identification

Offline muon quality cuts are made to the data to ensure that the muons found in the B2M stream correspond to beam-produced muons. These cuts also help reduce backgrounds from cosmic ray muons and fake tracks produced from combinations of noise hits or hadronic punchthrough. Table 5-7 summarizes these cuts. Each of these cuts is described in detail below.

| Muon Selection Criteria | |
|---|---|
| Muon Track Quality Flag, IFW4 | IFW4 $\leq 1$ |
| Muon MIP Deposition | $\sum_{1NN} E_{cal} \geq 1.0$ GeV |

Table 5-7: Criteria used to select good quality muons from candidate tracks.

### 5.4.1 Muon Track Quality Flag, IFW4

The muon track reconstruction assigns a track quality flag, IFW4, to each muon based on certain attributes of the track determined from information from the proportional drift tubes. The flag word IFW4 is given a default value of zero, and is incremented by one for each of the following criteria that fail:

1. good track fit in the bend direction
2. good track fit in the non-bend direction
3. good track fit to the event vertex in the bend direction(within approximately 3-5 meters, depending on the angle and momentum of the muon)
4. good track fit to the event vertex in the non-bend direction(within approximately 3-5 meters, depending on the angle and momentum of the muon)

For muon tracks that are reconstructed using only two layers of muon chambers, the event vertex is also used as a point in the reconstruction. Therefore, these tracks will have a good fit to the event vertex by definition.

In the Level 2 filter, only muons with a track quality flag of less than or equal to two are considered to be candidate muons. For the offline muon selection, this

cut is further restricted to IFW4 $\leq 1$ for each muon.

### 5.4.2 Muon Minimum Ionizing Energy Deposition

Muons produced from beam interactions deposit a characteristic minimum energy in the calorimeter consistent with the passage of a minimum ionizing particle. Reconstructed tracks that do not point to the interaction region, such as cosmic ray muons, or tracks reconstructed from noise will not have associated energy in the calorimeter. For candidate muons, the energy in each calorimeter cell along the direction of the muon track is added with the energy of the nearest neighbor cell:

$$\sum_{1NN} E_{cal} \geq 1.0 \text{ GeV}.$$

Figure 5-1 shows the distribution of $\sum_{1NN} E_{cal}$ for muon tracks in cosmic ray events and for a sample of beam produced muons. Clearly seen is the minimum ionizing peak in the events where the muon originates from the hard scatter.

## 5.5 Event Selection Criteria

The final event selection cuts are based upon the overall event topology of $b\bar{b}$ events. These cuts are made to optimize $b\bar{b}$ acceptance while at the same time reduce background contributions to the final data sample. Table 5-8 summarizes the event selection criteria.

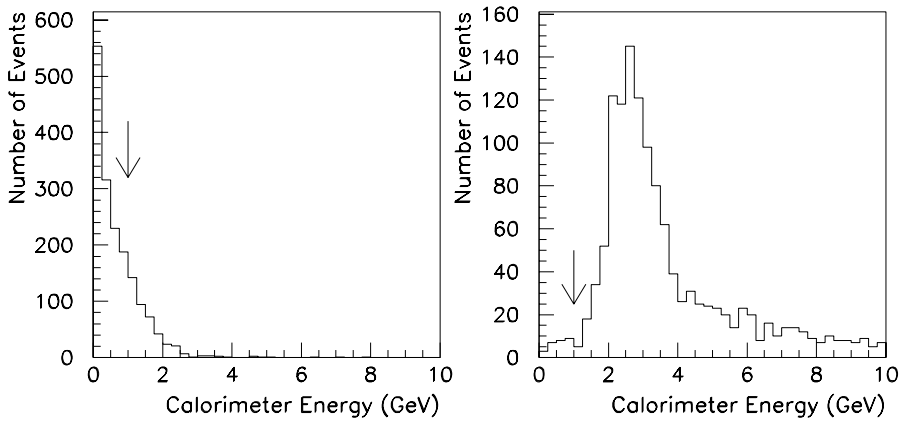


Figure 5-1: Calorimeter energy deposition in cells along the muon track plus their nearest neighbor cells for (a) muon tracks originating from cosmic rays and (b) muon tracks from the hard scatter.

| $b\bar{b}$ Event Selection | |
|---|---|
| Two Good Quality Muons | |
| Muon Pseudorapidity | $\|\eta^{\mu}\| \leq 0.8$ |
| Muon Transverse Momentum | $4 \leq p_T^{\mu} \leq 25$ GeV/c |
| Dimuon Invariant Mass | $6 \leq M^{\mu\mu} \leq 35$ GeV/c$^2$ |
| Dimuon 3-D Opening Angle | $\Delta\phi_{3D} \leq 165°$ |
| Fiducial Muon Phi | $\varphi^{\mu} \leq 80°$ or $\varphi^{\mu} \geq 110°$ |
| Associated Jet with the Muon | $\Delta R_{\mu-jet} \leq 0.8$ radians |
| Jet Transverse Energy | $E_T^{jet} \geq 12$ GeV |

Table 5-8: $b\bar{b}$ event selection criteria.

### 5.5.1 Muon Multiplicity and Quality

Each event is required to have two muons reconstructed within the pseudorapidity region $|\eta^{\mu}| \leq 0.8$. This corresponds to approximately the CF region of the DØ detector. In addition, both muons are required to be of good quality as defined by the muon selection criteria in Table 5-7.

### 5.5.2 Muon Transverse Momentum

In the CF region, due to the thickness of the calorimeter and iron toroid, muons must have a momentum of at least 3.0 GeV/c to make it through to the outer layers of the muon system. This translates into an effective cutoff of $p_T^{\mu} \geq 3.0$ GeV/c. The requirement of $p_T^{\mu} \geq 4.0$ GeV/c ensures that the muon momentum is well measured and that the momentum lies above the turn on point of the Level 1 muon trigger.

The upper cutoff of 25 GeV/c helps ensure proper sign determination and essentially eliminates the background from $W$ and $Z$ boson decays which turn on at higher transverse momentum of the muon[59, 60].

### 5.5.3 Dimuon Invariant Mass

The invariant mass of the dimuon system is required to be $6 \leq M^{\mu\mu} \leq 35$ GeV/c$^2$. The lower limit reduces backgrounds from $J/\psi$ production[2], low mass meson decays, and sequential heavy quark decays. This also ensures that the muons come primarily from different $b$-quarks. The upper limit excludes dimuons from $Z$ boson decays[59].

### 5.5.4 Dimuon Three-Dimensional Opening Angle

A three-dimensional opening angle cut, $\Delta\phi_{3D}$, has been applied to reduce the background from cosmic ray muons since these tracks tend to have a back-to-back topology. The opening angle is defined as

$$\Delta\phi_{3D} = \cos^{-1}\left[\frac{\vec{p_1}\cdot\vec{p_2}}{|\vec{p_1}||\vec{p_2}|}\right].$$

The momentum vector, $\vec{p}$, is measured using only the muon system. This is done since the global fit uses the vertex in the fit and cosmic rays need not point to the event vertex. From Fig. 5-2, we see that an opening angle cut of $\Delta\phi_{3D} \leq 165^\circ$ removes a large fraction of cosmic rays while removing very little of the $b$-quark signal.

[2] A study on the invariant mass of the $J/\psi$ decaying to two muons is performed in [61]. The dimuon invariant mass is found to be $M^{J/\psi} = 3.053 \pm 0.005$ GeV/c$^2$ with a width of $\sigma^{J/\psi} = 0.38$ GeV/c$^2$ using a full Monte Carlo simulation.

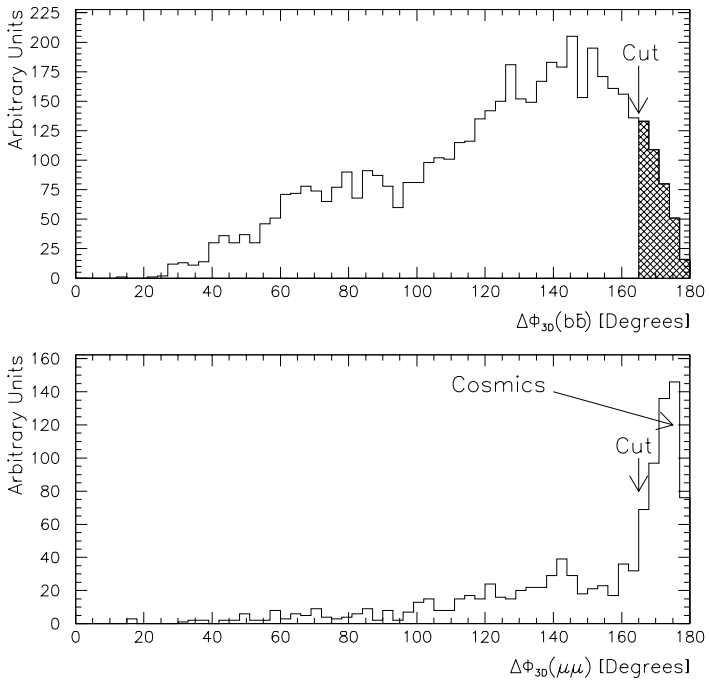


Figure 5-2: (top) The opening angle distribution for $b\bar{b} \rightarrow \mu\mu$. The cut is at $\Delta\phi_{3D}^{\mu\mu} < 165°$. (bottom) $\Delta\phi_{3D}$ distribution for dimuon data. Easily seen is the contribution from cosmic ray muons.

### 5.5.5 Fiducial Volume

The main ring of the Tevatron passes through the region of the detector located at approximately $\varphi = 90°$. Because of radiation leaks during main ring production cycles, the anode wires of the muon chambers adjacent to the main ring became contaminated. Figure 5-3 shows a deficit of muons in this $\varphi$-region relative to the Monte Carlo predictions. Since these chamber inefficiencies are not modeled in the Monte Carlo simulations, this portion of the detector is removed from the analysis to avoid large systematic uncertainties in the efficiencies:

$$\varphi^{\mu} \leq 80° \text{ or } \varphi^{\mu} \geq 110°.$$

### 5.5.6 Associated Jet with the Muon

In addition to cuts applied to the muon kinematic variables, the final event selection also include cuts on jet variables. Before describing these cuts, it is first essential to understand how jets are identified in the DØ detector.

- **Jet Finding**

  The jet definition most commonly used in hadron interactions is a "cone algorithm", where the jet energy is taken to be the energy inside a cone of fixed radius in $\eta$-$\phi$ space. A similar definition is used by UA1, UA2, and CDF. At DØ , jets are defined as the summation of the measured $E_T$ found in calorimeter cells within a cone in $\eta$-$\phi$ space of radius

  $$R = \sqrt{(\Delta\eta^2 + \Delta\phi^2)} = 0.7.$$

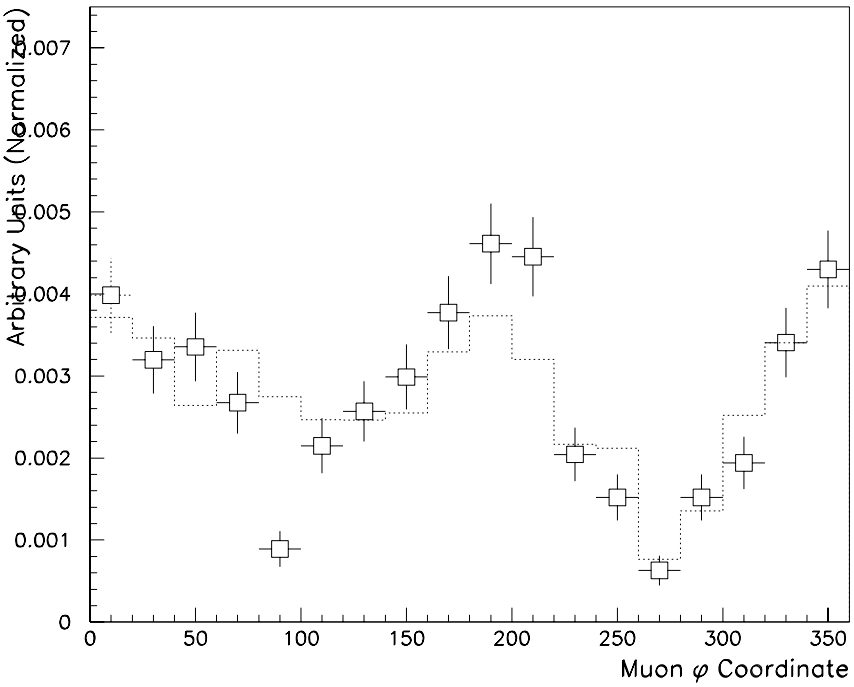


Figure 5-3: Distribution of $\varphi^{\mu}$ for $b\overline{b}$ and $c\overline{c}$ Monte Carlo processed through the detector simulation (dotted line) and a sample of data events (points). The deficit in data events around $\varphi^{\mu} = 90^{\circ}$ is due to chamber inefficiencies not modeled in the Monte Carlo.

The jet finding algorithm starts with a sorted list of the measured $E_T$ found in the calorimeter towers. The calorimeter towers have a width of $\Delta\eta \times \Delta\phi = 0.1 \times 0.1$ in the central region, while slightly wider towers are utilized in the forward region(see Sec. 4.2.2). The initial step of jet finding is to start with the highest $E_T$ calorimeter tower which has not yet been assigned to a precluster. A precluster is defined as a tower with $E_T > 1.0$ GeV in conjunction with all towers with $E_T > 1.0$ GeV within $|\Delta\eta| < 0.3$ and $|\Delta\phi| < 0.3$ of the original tower. This process continues until all towers have been assigned to a precluster. For each precluster found, the $E_T$ weighted center of all the towers in that precluster define the axis of the corresponding jet candidate. This axis is utilized as the starting point of a $R = 0.7$ jet cone.

Next, the $E_T$ weighted center of all calorimeter cells within $R = 0.7$ of the precluster position is calculated. If this new weighted center is found to be the same to that of the precluster, the jet position is considered stable. Otherwise, the process continues in an iterative manner with the axis of the cone redefined each time the new $E_T$ weighted center of the calorimeter towers is found. Eventually, the position of the cone axis will stabilize on the center of the calorimeter energy cluster. Once the position of the energy cluster is found, the summed $E_T$ within the $R = 0.7$ cone is required to be at least 8 GeV for the cluster to be identified as a jet.

One complication may arise if some calorimeter cells have been assigned to more than one jet. In this case, a decision must be made whether to split the jets or merge them into one. This decision is based on the amount of shared $E_T$ between the two jets. If the fraction of the total transverse energy of either jet shared with the other jet is more than 50%, the two jets are merged together, and the new jet axis is calculated from the centroids of all the calorimeter cells in the merged jet. Otherwise, the jets are split, and

each shared cell is assigned to the jet with the closer axis. In the case where two different preclusters produce jets whose axis lie within $\Delta R \leq 0.1$ of each other, the jets are assumed to be the same and the jet determined from the smaller precluster is deleted.

- **Jet Corrections**

  Ideally, the measured jet energy gives the energy of the original parton which produced the jet. This is generally not true because of systematic biases in measuring the jet energy. In addition to having to determine the jet energy scale, or overall energy normalization, several other effects must be accounted for. These include

  1. Soft particles($\leq$ 2 GeV) are also present in high $E_T$ jets. In this low $E_T$ region the calorimeter response is nonlinear, so simply summing the calorimeter responses for each particle will not produce the correct energy.
  2. Since hadronization is a statistical process, some fraction of this shower may extend beyond the jet cone.
  3. The underlying, or spectator event, as well as noise due to the natural radioactivity of the uranium absorber, will add extra energy to the calorimeter cells.
  4. The zero-suppression used in the calorimeter readout can also give a systematic shift in the cell energy.

  The method used to obtain the jet corrections is called the Missing Projection Fraction (MPF) method, and its application at DØ is described in [62].

- **Standard Jet Definition**

A standard set of jet cuts is used to eliminate fake jets from the data sample. Fake jets may be formed in the calorimeter from main ring losses, hot calorimeter cells, and cosmic ray bremsstrahlung. The cuts which define a good jet consist of the following three conditions.

1. **0.05 < EMFrac < 0.95** The fraction of the jet $E_T$ contained in the electromagnetic section of the calorimeter must be greater than 0.05 and less than 0.95. This cut is over 90% effective in removing fake jets associated with hot cells[63]. From Monte Carlo studies, the EMFrac cut is more than 99% efficient in retaining real jets except in the intercryostat region, where the efficiency is slightly lower[64]. This is because there is no EM coverage in the IC region(see Section 4.2.2).

2. **CHFrac < 0.40** The fraction of the jet $E_T$ in the coarse hadronic section of the calorimeter must be less than 0.40. This cut is designed to remove fake jets produced by losses in the main ring of the accelerator. Since the main ring passes directly through the coarse hadronic section of the calorimeter, it should be expected that any losses from the main ring be deposited there. This cut has been determined to be over 95% effective in removing fake jets associated with hot cells in the CH section. Monte Carlo studies show that the CHFrac cut is approximately 99% efficient in retaining good jets.

3. **Hot Cell Ratio < 10** The hot cell ratio is defined as the ratio of the highest $E_T$ cell in a jet to that of the second highest $E_T$ cell of the same jet. Real physics processes are unlikely to produce energy deposition in one calorimeter cell which is an order of magnitude larger than any other cell within a jet. Therefore, this cut is very efficient in removing fake jets due to noisy cells within the calorimeter.

The total efficiency of all these standard cuts has been studied and found to be between 96% for jets with $E_T = 11$ GeV and 91% for jets with $E_T = 400$ GeV. Therefore, since most of the jets considered in this analysis fall in the lower $E_T$ spectrum, it is assumed that there is almost no loss in jet finding efficiency associated with the standard jet definition.

- **Final Jet Cuts**

  Two jet cuts are imposed on the final data sample.

  1. **Associated Jet with the Muon** This analysis requires that each muon have an associated jet defined as

     $$\Delta R = \sqrt{(\Delta\eta^2_{\mu-jet} + \Delta\phi^2_{\mu-jet})} \leq 0.8$$

     where $\eta$ and $\phi$ are measured from the jet axis and muon momentum vector. For muons that are produced close together, the same jet may be shared between them. By requiring an associated jet with each muon, any contributions from $\Upsilon$ and Drell-Yan production to the final data sample are essentially eliminated. In addition, an associated jet is necessary in defining $p_T^{rel}$(see Sec. 8.2.2) which is used later in the analysis.

  2. **Jet Transverse Energy** A jet transverse energy, $E_T^{jet}$, cut of

     $$E_T^{jet} \geq 12 \text{ GeV}$$

     is used to ensure that the jet energy is well measured.

# Chapter 6

# Signal and Background Monte Carlo

Muons produced in hadronic collisions are produced by other sources in addition to decays of $b$-quarks. These non-$b$ sources of muons must be identified and removed from the data sample before a measurement of the $b$ cross section can be made.

This chapter describes the Monte Carlo samples used in determining the strengths of each of the physics processes that contribute to the dimuon signal. These samples are also used in determining the shapes of the input distributions to the maximum likelihood fits described in Chapter 8. In addition, these samples are also utilized in calculating the trigger efficiencies and some of the selection cut efficiencies described in Chapter 7. Finally, a discussion of additional sources of backgrounds to the $b$-quark signal is presented at the end of the chapter.

The Monte Carlo samples used are processed through the following chain of simulations:

- **CADFIX**

  The CADFIX software package is used to correct the format of the raw FULL_DØGEANT calorimeter banks so that they are compatible with the event

reconstruction package.

- **CAFIX**

  The CAFIX software package corrects the jet energy scale for reconstructed jets. The energy correction routines for jets found in Monte Carlo samples were developed to match the jet energy scale found in the Monte Carlo with that found in the data[51, 65]. For this analysis, the correction routine developed by the top quark analysis group with a jet cone size of $\Delta R = 0.7$ was chosen.

  A check on the effectiveness of these corrections is to compare an unbiased sample of jets found in data to those found in Monte Carlo[66]. Figure 6-1 shows how well the reconstructed jet $E_T$ distributions agree between data and Monte Carlo for two different samples: all jets and jets associated with muons. The jet spectrum obtained from data has a slight deficiency of jets in the lowest $E_T$ bins which can be attributed to small differences in the jet reconstruction efficiency for low $E_T$ jets in the data and Monte Carlo.

- **MU_SMEAR**

  The muon chamber efficiencies are properly simulated by running the MU_SMEAR[67] software package before the trigger simulation and reconstruction. MU_SMEAR simulates the muon chamber efficiency, pad latch efficiency, and uncertainties in the muon spatial resolution caused by the finite resolution and position uncertainties of the muon chambers. The version of MU_SMEAR used in this analysis includes an uncertainty of $\pm 3$ mm in the absolute positioning of the proportional drift tubes. The efficiencies used in MU_SMEAR are obtained directly from the data.

- **Trigger Simulator**

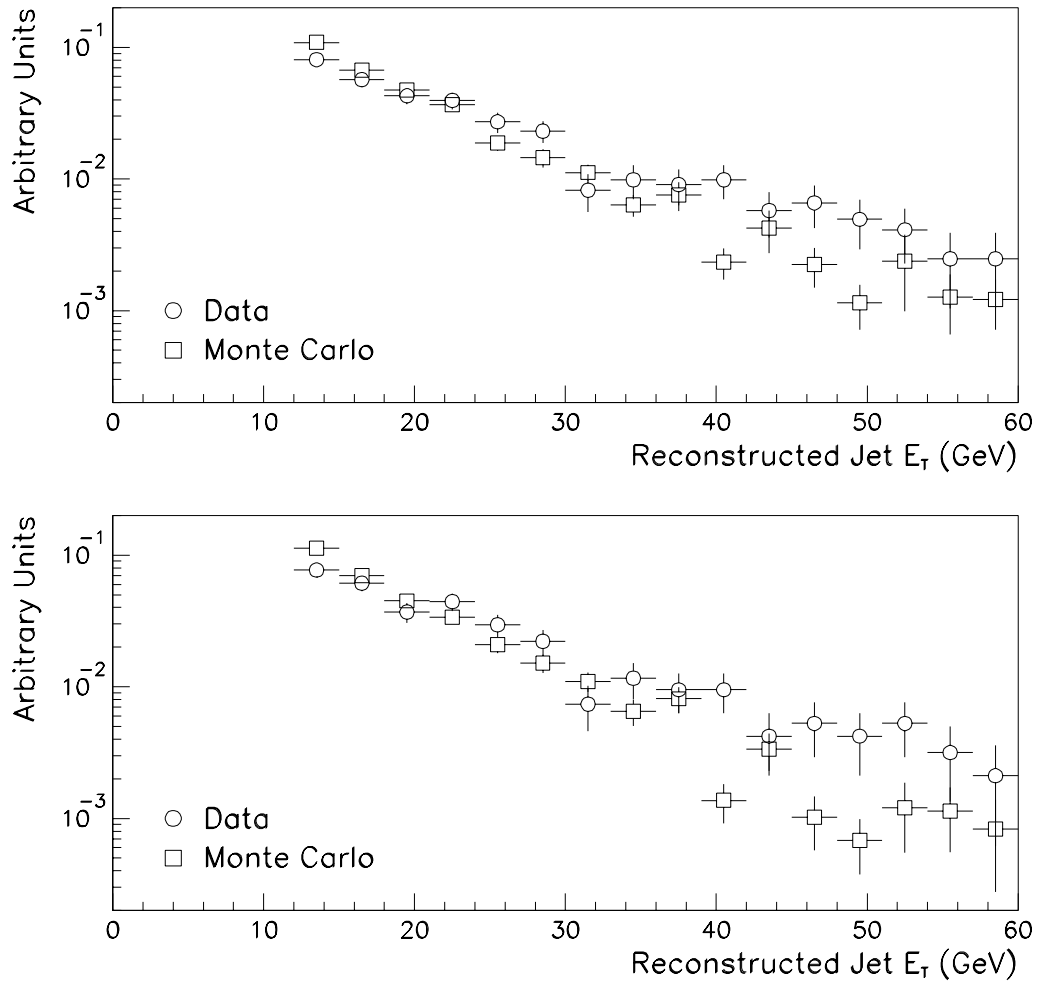


Figure 6-1: Comparison of jet $E_T$ spectrum for (a) all jets and (b) jets associated with muons in dimuon data and Monte Carlo.

The trigger simulator simulates the Level 1 hardware and Level 2 software triggers found in the detector.

- **Event reconstruction**

  Version 11.19 of the event reconstruction is used for the Monte Carlo samples.

- **Global Fit**

  This is a muon-only software package used to correct a known bug in the V11.19 reconstruction of the muon global fit code.

## 6.1 $b\bar{b}$ and $c\bar{c}$

As discussed in Chapter 3, the ISALEP Monte Carlo is used to provide an accurate description of the kinematic properties associated with dimuon events produced in the decays of $b\bar{b}$ and $c\bar{c}$ pairs. Although ISALEP does a good task of describing the fragmentation and decays of the hard scatter, the inclusive $b$-quark cross section calculated in ISALEP is found to disagree in both magnitude and shape with recent measurements of the same cross section[19, 60, 68]. Therefore, the cross section assigned to each dimuon event generated with ISALEP needs to be corrected based on differences between the predicted and measured production cross sections for heavy quark pairs.

It has been shown that the shape of the $b$-quark production cross section obtained from the NLO calculations of NDE are in close agreement with the shape measured in experiments[60, 68]. Therefore, the heavy quark cross sections calculated by NDE are used to normalize the heavy quark production cross sections in ISALEP. In order to calculate these normalizations, the shape of the inclusive $b$ and $c$-quark cross sections in ISALEP have to be determined from heavy quark samples

generated without any muon requirements. While generating these samples, it was discovered that the shape of the inclusive heavy quark cross sections calculated in ISALEP varies as a function of the input values of NEVOLVE and NHADRON, described in Chapter 3. Figure 6-2 shows an example of how the $b$-quark cross section given by ISALEP compares with the central NLO calculation of NDE as a function of two choices of the parameters NEVOLVE and NHADRON.

In addition, the inclusive muon cross sections calculated with ISALEP are also found to depend on these input values, but in a manner which is not consistent with that found for the inclusive heavy quark cross sections. That is, the ratio of the inclusive heavy quark cross sections underlying generated dimuon events to the total heavy quark cross sections varied for given sets of NEVOLVE and NHADRON.

To correct the cross sections supplied by ISALEP for the underlying heavy quark cross sections so that they are consistent with those calculated by NDE, a two step correction is applied. The first step involves normalizing the underlying heavy quark cross sections for single muon events generated with the ISALEP parameters NEVOLVE and NHADRON equal to 10 to that for muon events generated with these parameters set equal to 1. This normalization results in identical muon cross sections for both samples. Next, the total heavy quark cross sections for ISALEP events generated with NEVOLVE and NHADRON set equal to 1 are normalized to the calculation of NDE. The correction factors applied to the dimuon ISALEP events generated with NEVOLVE and NHADRON set equal to 10 are the product of the above two correction factors. These corrections are calculated as a function of the heavy quark $p_T$ which is taken as the average value of the generated quark and antiquark. Correction factors are calculated independently for $b\overline{b}$ and $c\overline{c}$ pairs. Figure 6-3 shows the form of these corrections as a function of $p_T^Q$. Note that

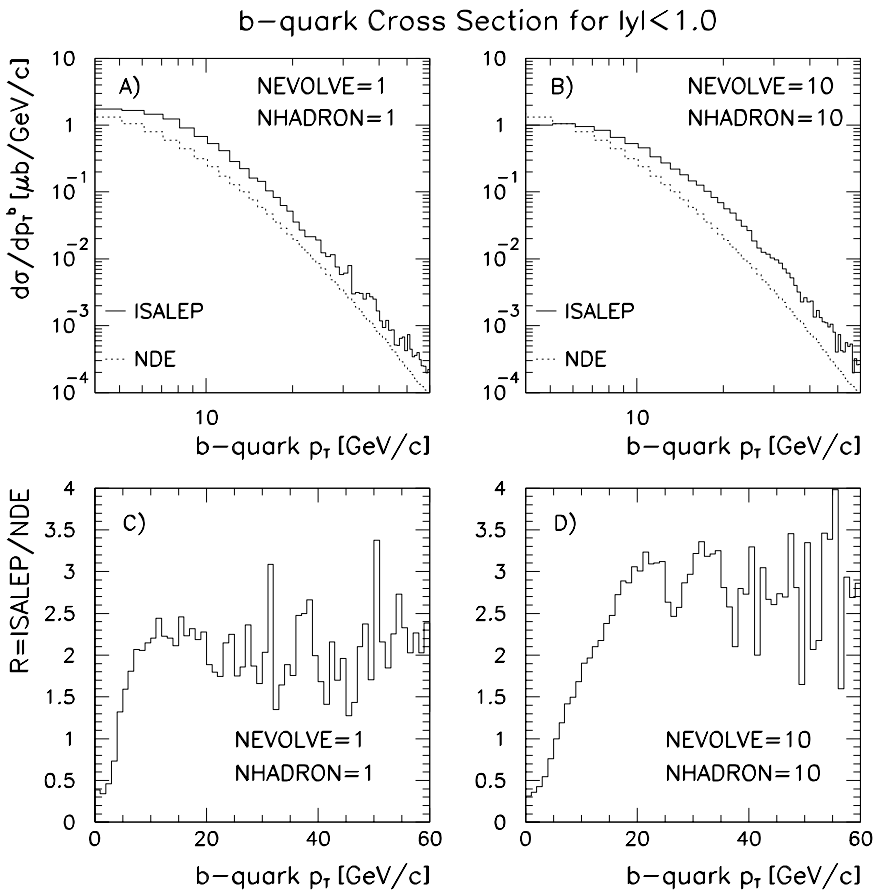


Figure 6-2: Comparison of the $b$-quark production cross section for $|y^b| < 1.0$ as given by ISALEP for two different sets of parameters NEVOLVE and NHADRON. A) and B) show the ISALEP cross section with the central NDE value, while C) and D) show the ratio, $R \equiv \frac{ISALEP}{NDE}$ for each set of ISALEP parameters.

we have assumed that the correction factors determined using the inclusive single muon samples are identical to those for dimuons.

Several general remarks can be made about the properties of muons from $b$-decays that can be used to distinguish them from other processes. First, the muons are expected to have relatively high $p_T$. This is because the muon's parent quark is expected to have $p_T^q \sim m_q$. Secondly, the muons from heavy quark decays are accompanied by a jet of hadronic energy from the decay fragments of the heavy quark. Finally, the transverse momentum of the muon with respect to the jet axis, referred to as $p_T^{rel}$, should increase as the mass of the heavy quark increases. This feature will be used later to distinguish $b$-quarks from lighter quark decays.

The production cross section for $c$-quarks is expected to be much larger than the $b$ cross section since the charm quarks are considerably lighter than $b$-quarks. However, in the semileptonic decay channel, $c$-quarks can be distinguished from $b$-quarks because the muons from $c$-decays tend to have lower $p_T$ than muons from $b$-decays. Also, the $p_T^{rel}$ from $c$-decays is softer than those from $b$-decays because of the parent quark mass.

## 6.2 Prompt Muon plus $\pi/K$ Decay

A significant number of charged pions and kaons are produced in each $p\overline{p}$ collision[68]. Although the decay lengths of charged pions and kaons are boosted in the lab frame due to the particles' momentum, a small fraction will still decay to muons in the central detector before interacting with the material in the calorimeter. Also, since the branching fraction for these particles to decay into muons is large, we expect some fraction of muons to originate from in-flight decays. When these

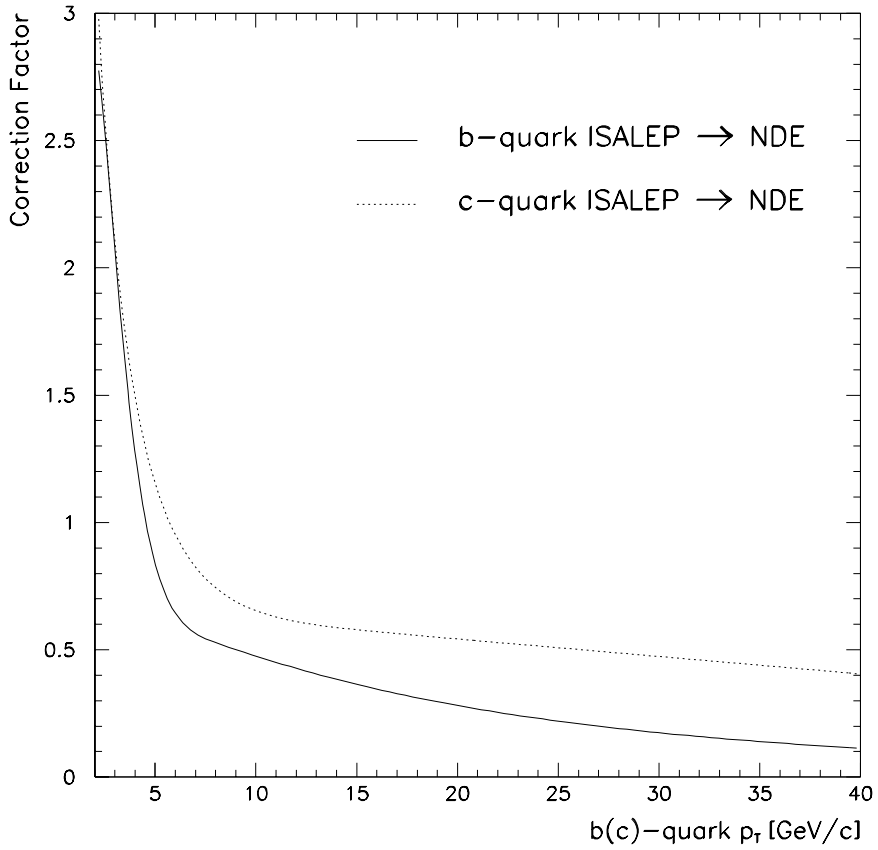


Figure 6-3: Correction factor for $b$ and $c$-quark production plotted as a function of the heavy quark $p_T$. This factor is used to normalize the ISALEP cross section to the NLO calculations of NDE.

in-flight decays occur in an event in conjunction with a prompt muon produced from either a $c$ or $b$-decay, it then becomes a contribution to the dimuon signal. In addition, the decay of two charged pions or kaons in a single event can also produce a dimuon pair. The contribution to the total dimuon cross section from these two sources are calculated in this section.

The measured cross section for prompt muons plus $\pi/K$ decay depends on the production cross section for the parent hadrons, the fraction of these hadrons decaying, and the decay kinematics. To determine the kinematic distributions for the prompt muon plus $\pi/K$ decay contribution to the dimuon sample, we start with a sample of unbiased, two-jet, ISALEP $c$ and $b$ events that decay semileptonically to single muons as the source of the prompt muons. This is chosen because single muon $b$ and $c$ decays dominate in the $p_T$ range we are interested in. From this ISALEP sample, a $\pi^{\pm}$, $K^{\pm}$, or $K_L^0$ is selected at random to decay into a muon and a neutrino within the radius of the central tracking volume. The probability of the 'forced' decay is calculated using the formula:

$$W_i = P_i \prod_{j=1}^{N-1} (1 - P_j), \tag{6.1}$$

where $N$ is the total number of pions and kaons, $P_i$ is the probability of decay for the pion or kaon that was selected to decay, and $P_j$ is the probability of decay for the remaining pions and kaons. Since we are interested in higher (>4 GeV/c) $p_T$ muons in the central ($|\eta| < 0.8$) region, only $\pi$'s and $K$'s with $p_T^{\pi/K} > 3$ GeV/c and $|\eta^{\pi/K}| < 0.9$ are considered. These cuts are found to be 100% efficient in producing all the decay muons in the kinematic region of interest. This greatly reduces the number of decay candidates to where $N$ is a small number and (6.1) can be approximated as:

$$W_i \approx N P_i. \tag{6.2}$$

The quantity $W_i$ is assigned as a weight to the event, and is multiplied by the two-jet ISALEP weight to get the total weight of the event. By forcing the decays of pions and kaons, we are able to avoid processing large amounts of Monte Carlo which contain no in-flight decays.

The decay probability, $P$, in (6.2), is a function of the particle lifetime and momentum:

$$P = BR(\pi/K \rightarrow \mu)\frac{rM_{had}}{c\tau_{had}}\frac{1}{p_T^{had}}, \tag{6.3}$$

where $BR(\pi/K \rightarrow \mu)$ is the branching ratio of the pion or kaon into a muon, $M_{had}$ is the mass of the parent $\pi$ or $K$, $c\tau_{had}$ is the decay length, and $p_T^{had}$ is the hadrons' transverse momentum. The radius of the decay volume, $r$, is approximately a cylinder of radius 84 cm. This small decay volume helps suppress these decays. The decay probability can then be approximated by:

$$P_\pi = 0.015/p_T^\pi \tag{6.4}$$

$$P_{K^\pm} = 0.074/p_T^{K^\pm} \tag{6.5}$$

$$P_{K_L} = 0.0073/p_T^{K_L}, \tag{6.6}$$

where the decay lengths for the $\pi$, $K^\pm$, and $K_L^0$ are 7.8, 15.5, and 3.7 m respectively. Figure 6-4 shows that the results of the decay Monte Carlo agree with this prediction for each of these mesons.

The Monte Carlo then decays the meson to create products with the correct 4-vectors. The decays included are

$$\pi^\pm \rightarrow \mu^\pm\nu_\mu, \tag{6.7}$$

$$K^\pm \rightarrow \mu^\pm\nu_\mu, \tag{6.8}$$

$$K^\pm \rightarrow \pi^\circ\mu^\pm\nu_\mu, \tag{6.9}$$

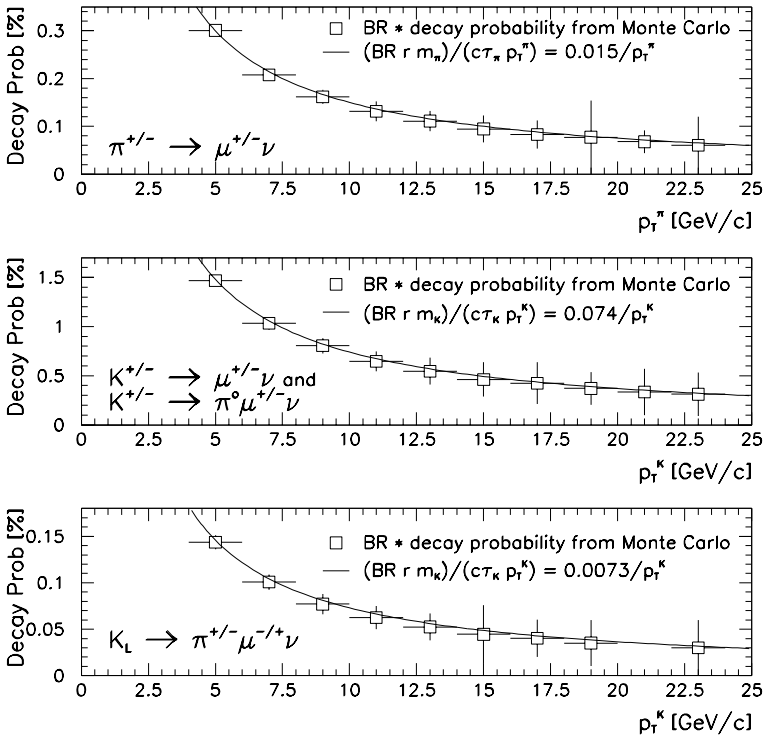


Figure 6-4: Probability of an individual pion or kaon to decay into a muon. The result of the detector simulation is compared to a calculation (solid line) assuming a cylindrical decay volume of radius $r = 84$ cm for each possible in-flight decay meson: $\pi^{\pm}$, $K^{\pm}$, and $K_L^0$.

and

$$K_L^0 \rightarrow \pi^{\pm}\mu^{\mp}\nu. \tag{6.10}$$

As a check to the validity of the decay package described above, a comparison is made to a calculation of the single muon cross section expected from $\pi$ and $K$ decays based on the charged particle cross section measured by CDF[68]. The input to the decay package for this test consisted of unbiased ISAJET events generated with the TWOJET utility with the transverse momentum of the jets restricted to the range of 3-100 GeV/c. One particle from the resulting candidate list is forced to decay into a muon within the tracking volume and an event weight is assigned in accordance to (6.2). A comparison with the single muon cross section from $\pi$ and $K$ decays as determined from this package and from our calculation above is shown in Fig. 6-5. Very good agreement is found over the entire $p_T^{\mu}$ range.

The background contribution to dimuon events where both muons are produced in the decay of charged pions or kaons (double decay events) is found to be more than a factor of 5 smaller than the contribution from a prompt muon plus a $\pi/K$ decay[66]. Given this small contribution to the total dimuon cross section, the double decay events are not processed through the full detector simulation. In addition, the kinematic properties of muons produced in $c$-quark decays are found to be similar to those for muons produced in the decay of charged pions or kaons. Therefore, the double decay contribution to the measured dimuon cross section, discussed in Chapter 9, are included in the $c\bar{c}$ contribution. Table 6-1 lists the cross sections obtained from the decay package for each of the processes described. These cross sections are for dimuon events with $|\eta^{\mu}| < 0.8$, $4 \leq p_T^{\mu} \leq 25$ GeV/c, $6 \leq M^{\mu\mu} \leq 35$ GeV/c$^2$, and $\Delta\phi_{3D} \leq 165°$.

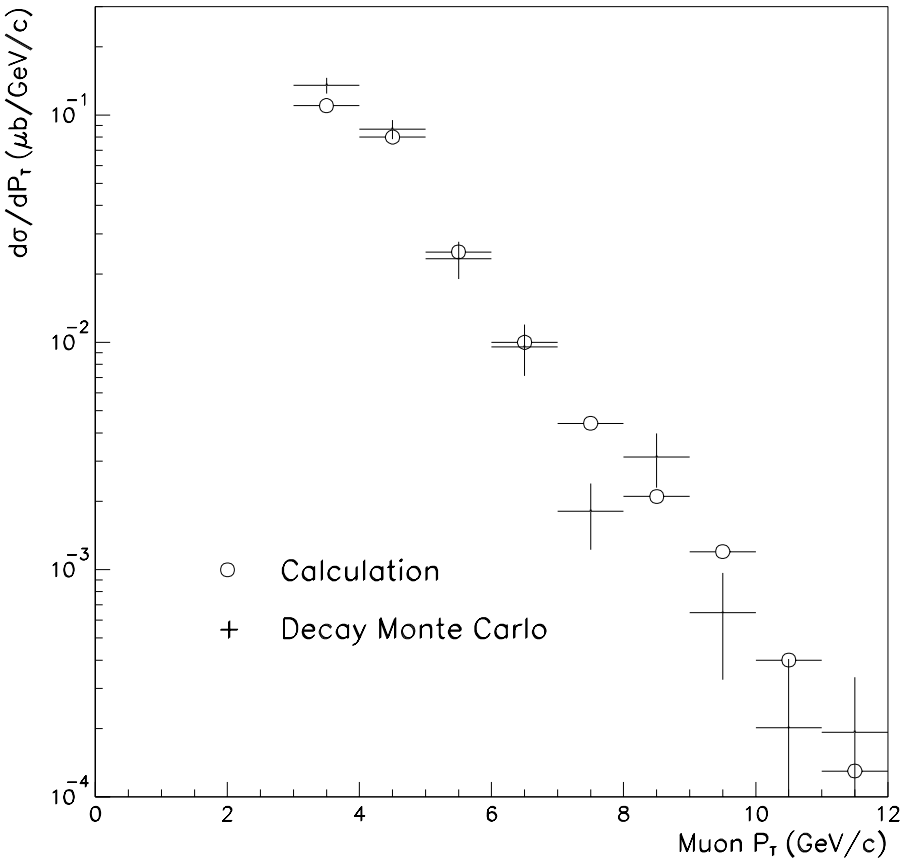


Figure 6-5: Comparison of inclusive single muon cross section from $\pi$ and $K$ decays obtained from decay package utilized in this analysis with the calculation based on charged particle cross section measured by the CDF experiment.

| Production Process | Dimuon Cross Section($\mu b$) |
|---|---|
| $b \to \mu + \pi/K \to \mu$ | $2.85\times10^{-5}$ |
| $c \to \mu + \pi/K \to \mu$ | $1.94\times10^{-5}$ |
| $\pi/K \to \mu + \pi/K \to \mu$ | $9.02\times10^{-6}$ |

Table 6-1: Decay event generator level cross sections for dimuon events which include muons produced in the decay of a charged pion or kaon. The dimuon cross sections are based on the following cuts: $|\eta^{\mu}| < 0.8$, $4 \leq p_T^{\mu} \leq 25$ GeV/c, $6 \leq M^{\mu\mu} \leq 35$ GeV/c$^2$, and $\Delta\phi_{3D} \leq 165°$.

## 6.3 Drell-Yan

The Drell-Yan mechanism can also produce $\mu^+\mu^-$ pairs. The Drell-Yan Monte Carlo sample is generated using the DRELLYAN utility of the ISAJET Monte Carlo. Drell-Yan production in ISAJET includes contributions from the leading order process

$$q\overline{q} \to \gamma^* \to \mu^+\mu^- \tag{6.11}$$

and from next-to-leading order processes

$$\begin{aligned} q(\overline{q})g &\to \gamma^* q(\overline{q}) \\ &\hookrightarrow \mu^+\mu^-. \end{aligned} \tag{6.12}$$

Approximately 5000 Monte Carlo events in the mass range of $4.0 \leq M^{\gamma^*} \leq 40.0$ GeV/c$^2$ were passed through the full detector simulator, and no events were found to pass the trigger and data cuts listed in Chapter 5. Since the measured inclusive Drell-Yan cross section agrees with the cross section given by the ISAJET Monte Carlo[52], the event weights supplied by ISAJET can be used to set a limit on the amount of Drell-Yan present in the data samples. From this, we set an upper limit

on the Drell-Yan cross section contributing to the data sample of

$$\frac{d\sigma(DY \rightarrow \mu^+\mu^-)}{dy} = 8.1 \text{ x } 10^{-5} \text{ nb} \tag{6.13}$$

at the 90% confidence level. This cross section is equivalent to approximately one-half of one event in the final data sample based on the recorded integrated luminosity. Thus, Drell-Yan is not considered to contribute to the final data samples.

## 6.4 Upsilon

The decay of $b\overline{b}$ bound states($\Upsilon(1S), \Upsilon(2S), \Upsilon(3S)$) to $\mu^+\mu^-$ pairs is also a source of dimuon pairs since the $\Upsilon$ mass($\sim$ 9.5 GeV/c$^2$) is centered in the mass region the data set spans. An $\Upsilon$ event generator written by Mangano[69] is used as the basis for a Monte Carlo. The Mangano Monte Carlo generator produces each of the nine known $\Upsilon$ and $\chi_b$ states correctly to $\mathcal{O}(\alpha_s^3)$. These states are produced through two types of processes: direct production through gluon-gluon fusion

$$gg \rightarrow \Upsilon g, \tag{6.14}$$

and indirect production through the radiative decays of $\chi_b$

$$\begin{aligned} q\overline{q}, gg &\rightarrow \chi_b \\ &\hookrightarrow \Upsilon\gamma \\ q\overline{q}, gg &\rightarrow \chi_b g \\ &\hookrightarrow \Upsilon\gamma \\ q(\overline{q})g &\rightarrow \chi_b q(\overline{q}) \\ &\hookrightarrow \Upsilon\gamma. \end{aligned} \tag{6.15}$$

An additional program written by A. Smith[52] is used to simulate decays between these states and to decay these states to $\mu^+\mu^-$ pairs. This Monte Carlo does not include a package to fragment quarks and gluons, so any variables relating to hadronic activity are taken to be the same as from the Drell-Yan Monte Carlo. This is a reasonable assumption since in both cases, the $\mu^+\mu^-$ pair are the only decay products and we expect the muons to be generally isolated.

A total of approximately 85000 events were passed through the full detector and trigger simulator, and no events passed all the data selection cuts from Chapter 5. Using the recent measurement of $\Upsilon \rightarrow \mu^+\mu^-$ production at the Tevatron[52, 70],

$$\frac{d\sigma\left[\Upsilon(1S,2S,3S) \rightarrow \mu^+\mu^-\right]}{dy} \approx 1 \text{ nb}, \tag{6.16}$$

we set an upper limit on the $\Upsilon$ cross section passing the data cuts of

$$\frac{d\sigma\left[\Upsilon(1S,2S,3S) \rightarrow \mu^+\mu^-\right]}{dy} = 2.3 \text{ x } 10^{-5} \text{ nb} \tag{6.17}$$

at the 90% confidence level, which is equivalent to less than one-half of one event. Given this fact, $\Upsilon$ decays are not considered to contribute to the final data samples.

## 6.5 Other Backgrounds

All other sources of dimuon events are considered to have negligible contributions to the dimuon data sample. These include :

- $\boldsymbol{W \rightarrow \mu\nu}$ **plus prompt muon** $W$ boson decays produce high $p_T$ muons[59, 60] above the $p_T^\mu$ cutoff of 25 GeV/c applied to this data sample.
- $\boldsymbol{Z \rightarrow \mu\mu}$ The mass of the $Z$ boson, $M_Z = 91.19$ GeV/c$^2$[71], is well above the invariant mass cutoff of $M^{\mu\mu} \leq 35$ GeV/c$^2$ employed in the data selection.

In addition, the muons produced from $Z$-decays are expected to be isolated and not associated with jet activity.

- **Hadronic Punchthrough** The thickness of the calorimeter and iron toroid in the central region, $\approx 14$ interaction lengths[37], removes all of the hadronic punchthrough[72].

- ***J/ψ* decay** The invariant mass of two muons originating from $J/\psi$ production is studied in [61] using the full detector simulation. The reconstructed mass and associated width is found to be well below the lower limit of $M^{\mu\mu} \geq 6$ GeV/c$^2$.

- **Top decay** An analysis of $t\bar{t} \rightarrow \mu\mu$ production is studied in [1]. Contributions from this decay channel should contribute less than 0.01 events to this data sample based on the $t\bar{t}$ cross section and acceptance for these events.

# Chapter 7

# Efficiency Determination

The cuts described in Chapter 5 are made to select good dimuon events and enhance the contribution from $b\bar{b}$ production in the final data sample. Each of these cuts has an effect on the number of signal events that reach the final data sample and on the kinematic distributions we ultimately observe. The efficiencies for these cuts as well as the trigger efficiencies must be determined in order to extract a cross section.

This chapter will quantify the effects of the trigger and offline cuts on the data sample by using the $b\bar{b}$ and $c\bar{c}$ Monte Carlo samples described in Chapter 6. A calculation of the efficiencies using the prompt muon plus decay Monte Carlo sample gives similar results within statistical uncertainty, so these efficiencies are considered to be the same. Whenever possible, a comparison of results from the Monte Carlo simulations is made with data. As we will see in Sec. 7.2, this comparison discloses inefficiencies in the trigger that are not simulated in the Monte Carlo.

The uncertainties in the efficiencies, $\epsilon$, due to statistics of the sample is calcu-

lated using the expression for a binomial distribution,

$$\sigma_\epsilon = \sqrt{\frac{\epsilon(1-\epsilon)}{N}}, \tag{7.1}$$

where $N$ is the total number of events used in determining the efficiency. This formula is only true if there are large statistics in the sample and if the true efficiency, $\epsilon$, is known.

## 7.1 Simulator Corrections

Three corrections are added to the detector simulation in order to model the detector response more precisely. The first is a modeling of muon chamber efficiencies and positions. The second is a correction to the Level 1 jet trigger tower thresholds, and the third accounts for the Level 2 jet trigger efficiency.

### 7.1.1 MU_SMEAR

As discussed in Chapter 6, MU_SMEAR simulates the muon chamber efficiencies. Since triggers are formed based on the chamber pad latch information, properly simulating these efficiencies is essential in determining the trigger efficiency with Monte Carlo. Uncertainties in the pad latch efficiency and in the muon spatial resolution used in MU_SMEAR will have the largest effect on the Level 1 trigger efficiency. The systematic uncertainty in the trigger efficiencies determined using the Monte Carlo processed with MU_SMEAR is determined to be 10% per muon from the $W$ boson analysis[52, 73]. This result is confirmed in Sec. 7.2.1 below.

### 7.1.2 Level 1 Jet Tower Trigger

After a careful study of low $E_T$ jets, it is determined that the simulator does not reproduce the correct structure of the Level 1 jet trigger efficiency at low jet $E_T$[66]. In this study, a sample of jets is collected in the dimuon data samples using the MU_2_HIGH trigger and compared with those jets found in the Monte Carlo using the same trigger requirement. Since there are no jet requirements in the MU_2_HIGH trigger, the reconstructed jets found in these events are unbiased with respect to the calorimeter trigger. From Fig. 7-1, we see that the full trigger simulator finds a higher Level 1 trigger efficiency for low $E_T$ jets than that found in the real detector and trigger hardware. This is true for all jets and for jets with an associated muon. This suggests that jets are not modeled properly in the Monte Carlo. A correction is made where the calorimeter trigger tower thresholds vary in the Monte Carlo as a function of the reconstructed jet $E_T$. These corrections are made separately in the $|\eta| < 0.8$ and $0.8 < |\eta| < 1.2$ regions due to different performance features of the calorimeter. Figure 7-2 shows the corrections applied to the calorimeter trigger tower thresholds as a function of reconstructed jet $E_T$.

After applying the corrections from Fig. 7-2, we find good agreement between the Monte Carlo and data Level 1 jet trigger efficiency for all jets and for jets with an associated muon, as shown in Fig. 7-3.

### 7.1.3 Level 2 Jet Trigger Efficiency

The Level 2 jet trigger efficiency is also checked using the same unbiased sample described above. For each reconstructed jet with an associated Level 1 calorimeter trigger tower above the required threshold, a search is performed in a $\Delta R = 0.5$ cone around the jet axis to find the associated Level 2 jet with $E_T^{jet} \geq 10$ GeV.

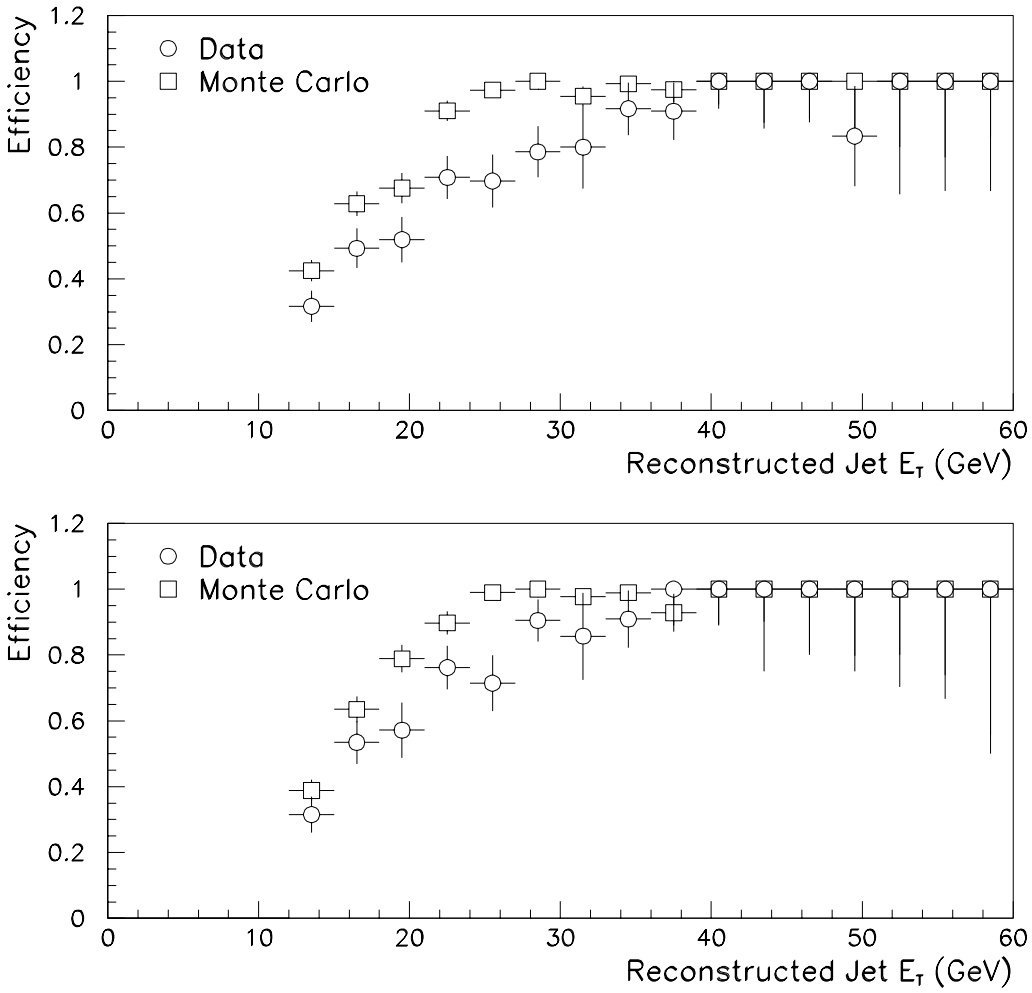


Figure 7-1: Uncorrected Level 1 jet trigger efficiency for (top) all jets and (bottom) for jets with an associated muon.

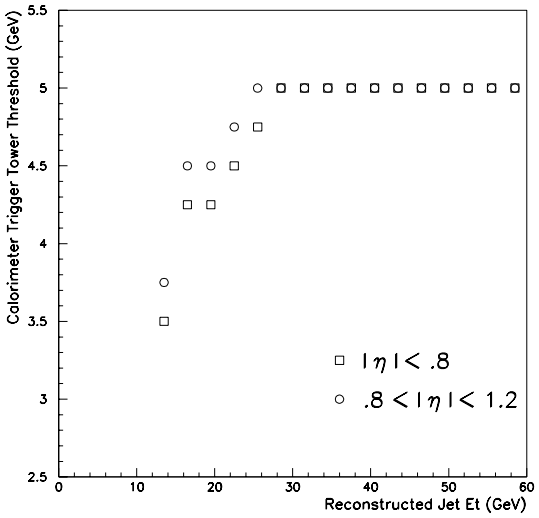


Figure 7-2: Jet trigger tower threshold corrections based on the reconstructed jet $E_T$.

The 10 GeV threshold for Level 2 jets is chosen to match the Level 2 jet trigger conditions found in the detector. Figure 7-4 shows the Level 2 jet trigger efficiency for data and Monte Carlo as a function of reconstructed $E_T^{jet}$ for all jets and for jets associated with muons. In the case of the Monte Carlo, the modified Level 1 calorimeter trigger tower thresholds are used to define a good Level 1 jet. The data efficiency curves show that the DØ detector is approximately 100% efficient for triggering on Level 2 jets given a good Level 1 jet. The inefficiency in the lowest $E_T^{jet}$ bin in the Monte Carlo is attributed to the fact that the information regarding energy deposition in the calorimeter which is used at the trigger simulation level does not include the corrections to the energy scale provided by CAFIX. Therefore, a Level 2 jet trigger efficiency correction is made to the Monte Carlo samples for jets with $12 \leq E_T^{jet} \leq 15$ GeV to match the data efficiency. This is accomplished by assuming that all jets in the Monte Carlo which are found to have an associated Level 1 trigger tower above the required energy deposition threshold and a

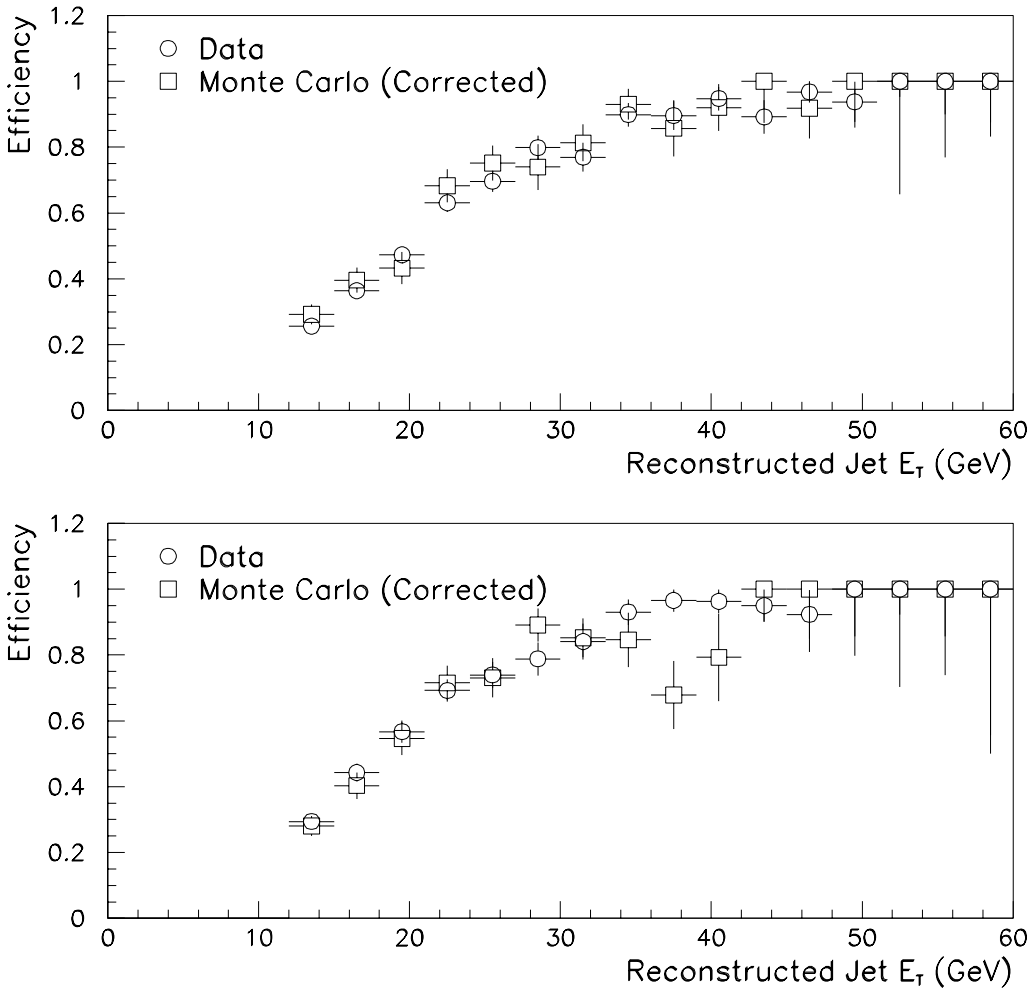


Figure 7-3: Corrected Level 1 jet trigger efficiency for (top) all jets and (bottom) for jets with an associated muon.

reconstructed jet energy between $12 \leq E_T^{jet} \leq 15$ GeV have a Level 2 jet trigger efficiency of 100%.

## 7.2 Level 1 and Level 2 Trigger Efficiencies

The Level 1 and Level 2 trigger efficiencies are determined using the $b\overline{b}$ and $c\overline{c}$ Monte Carlo events processed with FULL_DØGEANT, MU_SMEAR, and simulation of trigger conditions used during the V7.3 trigger menu. These events are first subjected to the following kinematic cuts before they are used in the calculation of efficiencies:

- $4 \leq p_T^{\mu} \leq 25$ GeV/c
- $|\eta^{\mu}| \leq 0.8$
- $6 \leq M^{\mu\mu} \leq 35$ GeV/c$^2$
- $\Delta\phi_{3D} \leq 165°$.

The effect of these kinematic cuts will be included in Chapter 9 when the inclusive $b$-quark production cross section is calculated.

The Level 1 trigger efficiency is calculated to be the number of these events passing the Level 1 trigger requirements divided by the total number of events presented to the trigger:

$$\epsilon_{L1} = \frac{N_{L1}}{N_{kin\ cut}}. \tag{7.2}$$

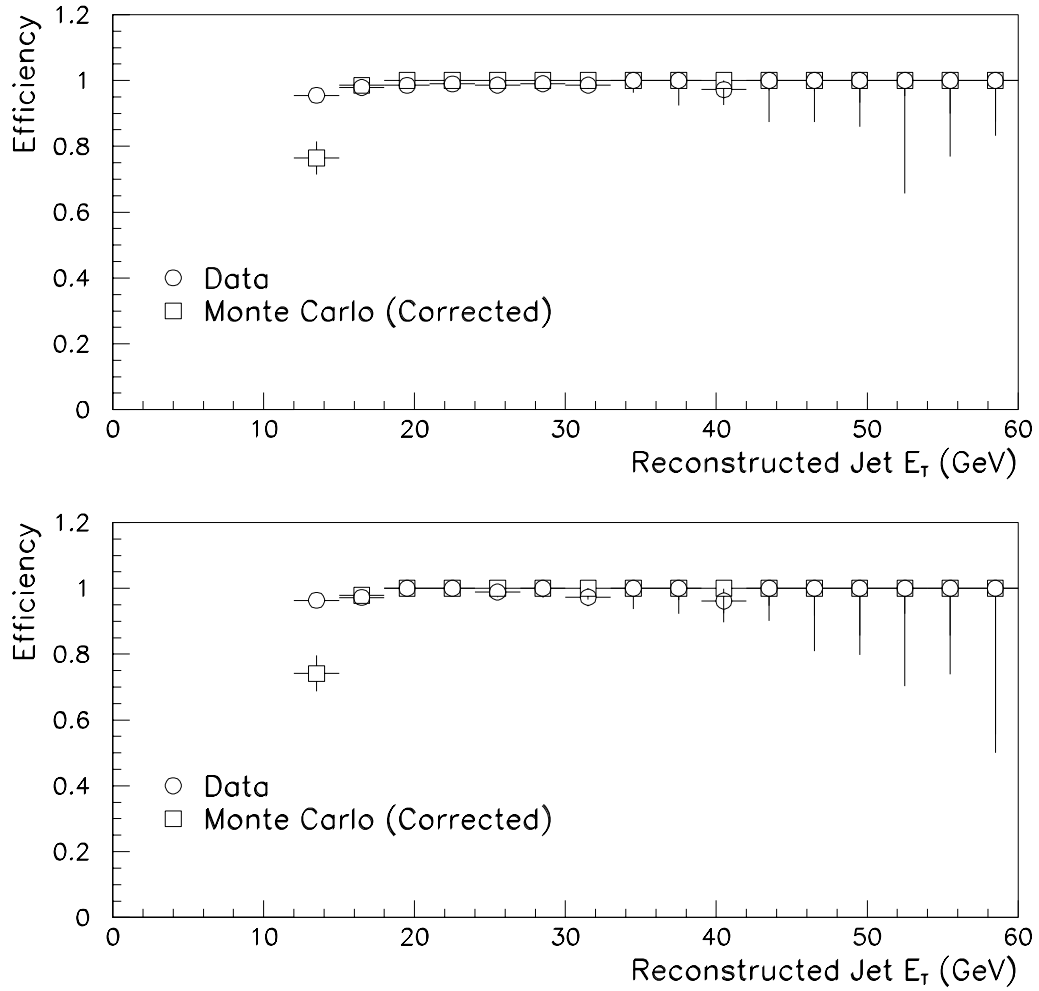


Figure 7-4: The Level 2 jet trigger efficiency for (top) all jets and (bottom) for jets with an associated muon. A correction is made to the Monte Carlo in the lowest $E_T^{jet}$ bin to match the efficiency with the data.

Similarly, the Level 2 trigger efficiency is the number of events satisfying the Level 2 requirements divided by the number of events passing the Level 1 trigger condition:

$$\epsilon_{L2} = \frac{N_{L2}}{N_{L1}}. \tag{7.3}$$

Figures 7-5 and 7-6 show the Level 1 trigger efficiencies for each trigger bit used as a function of unsmeared $p_T^{\mu}$(leading) and $\Delta\phi^{\mu\mu}$. $p_T^{\mu}$(leading) is defined as the muon with the greater measured value of transverse momentum. The slow turn-on in the MU_1_JET and MU_JET_LOW triggers of Fig. 7-5 is due to the fact that the jet trigger towers are considerably smaller than the size of the jets. Therefore, only a fraction of the jets energy is detected in any given jet trigger tower. The Level 2 trigger efficiencies are shown in Figs. 7-7 and 7-8. The effect of the cosmic ray cut in the Level 2 MU_2_HIGH trigger can be seen as the lower efficiency in the upper $\Delta\phi^{\mu\mu}$ bins in Fig. 7-8(a).

### 7.2.1 Calibration of Monte Carlo Muon Trigger Efficiencies using Data

Even after the corrections described in Sec. 7.1, there are still two significant differences between the data events and the Monte Carlo events processed with the V7.3 trigger simulation that need to be accounted for. The first difference includes effects in the muon detector hardware that are not simulated in the Monte Carlo. Distributions such as the drift times or delta-times which determine the position of a cell hit in the proportional drift tubes have non-Gaussian tails due to occasional poor measurements of these quantities by the hardware. This results in a position measurement that is so far off the reconstructed muon track that the hit is not assigned to the muon track. This in turn may cause the reconstruction

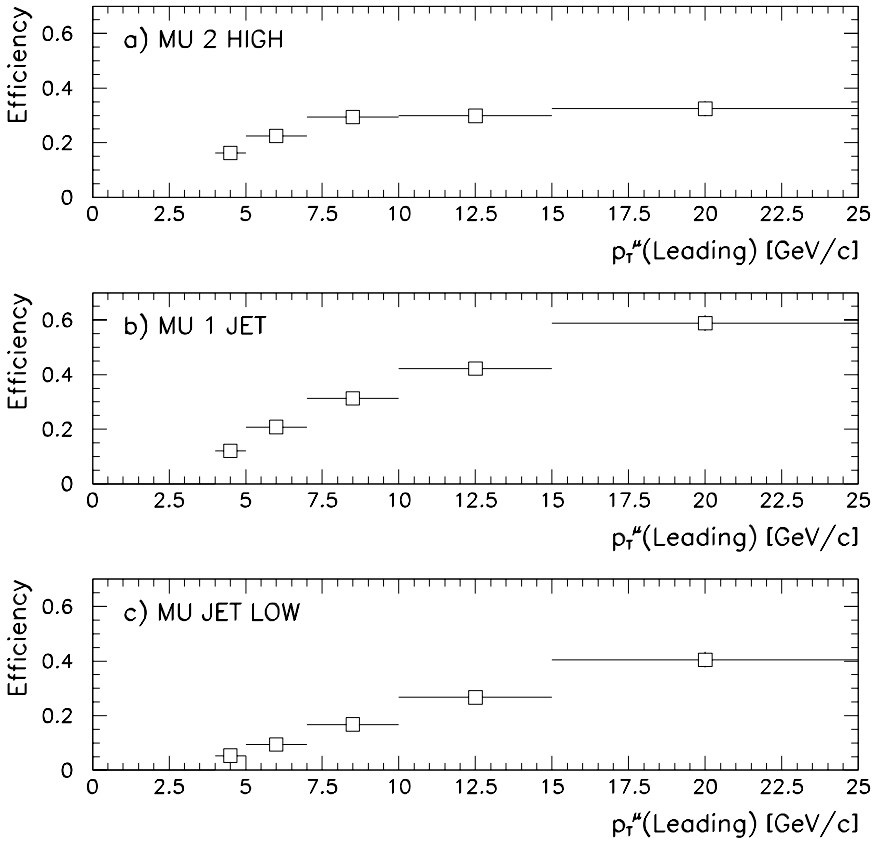


Figure 7-5: Level 1 efficiency as a function of unsmeared $p_T^{\mu}$(leading) for a) MU_2_HIGH, b) MU_1_JET, and c) MU_JET_LOW.

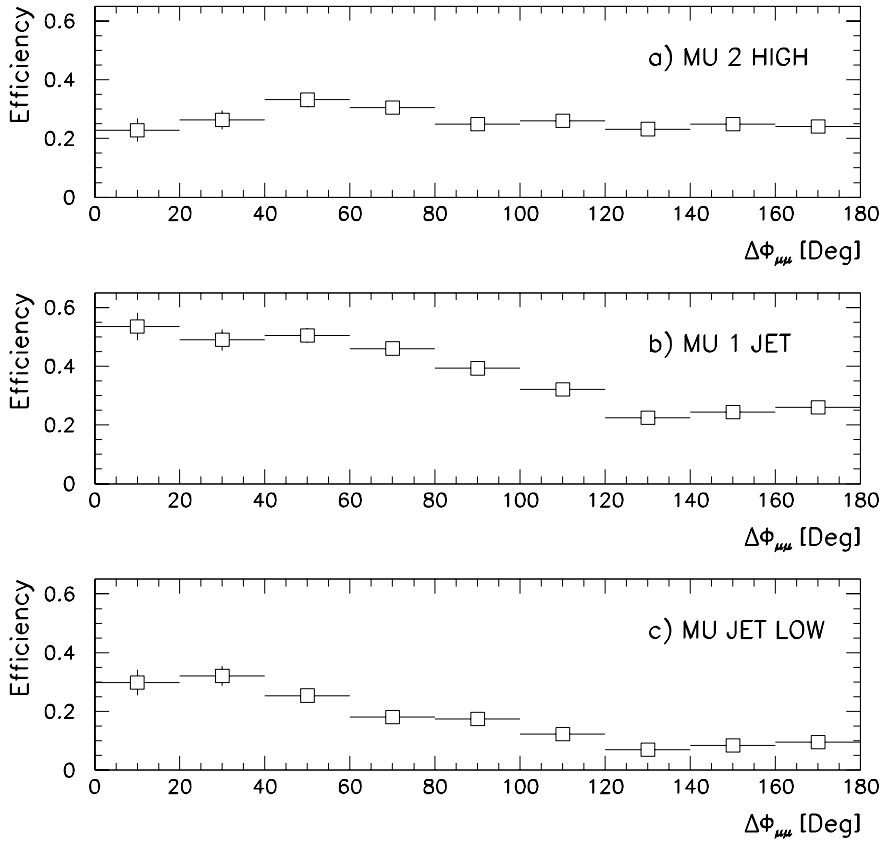


Figure 7-6: Level 1 efficiency as a function of unsmeared $\Delta\phi^{\mu\mu}$ for a) MU_2_HIGH, b) MU_1_JET, and c) MU_JET_LOW.

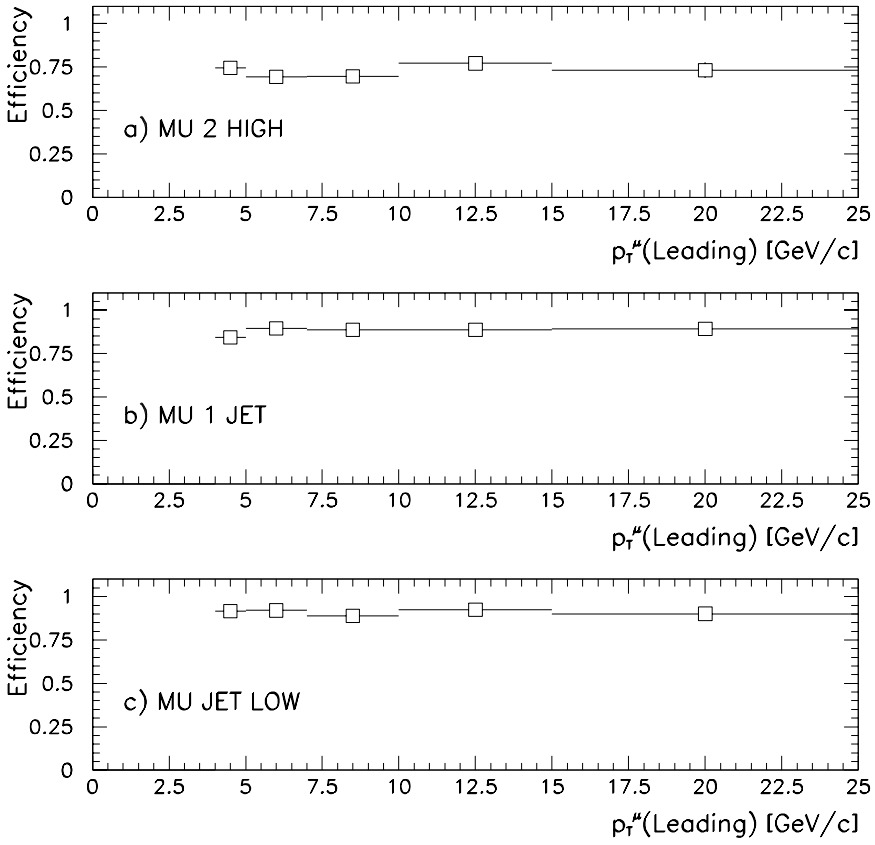


Figure 7-7: Level 2 efficiency as a function of unsmeared $p_T^\mu$(leading) for a) MU_2_HIGH, b) MU_1_JET, and c) MU_JET_LOW.

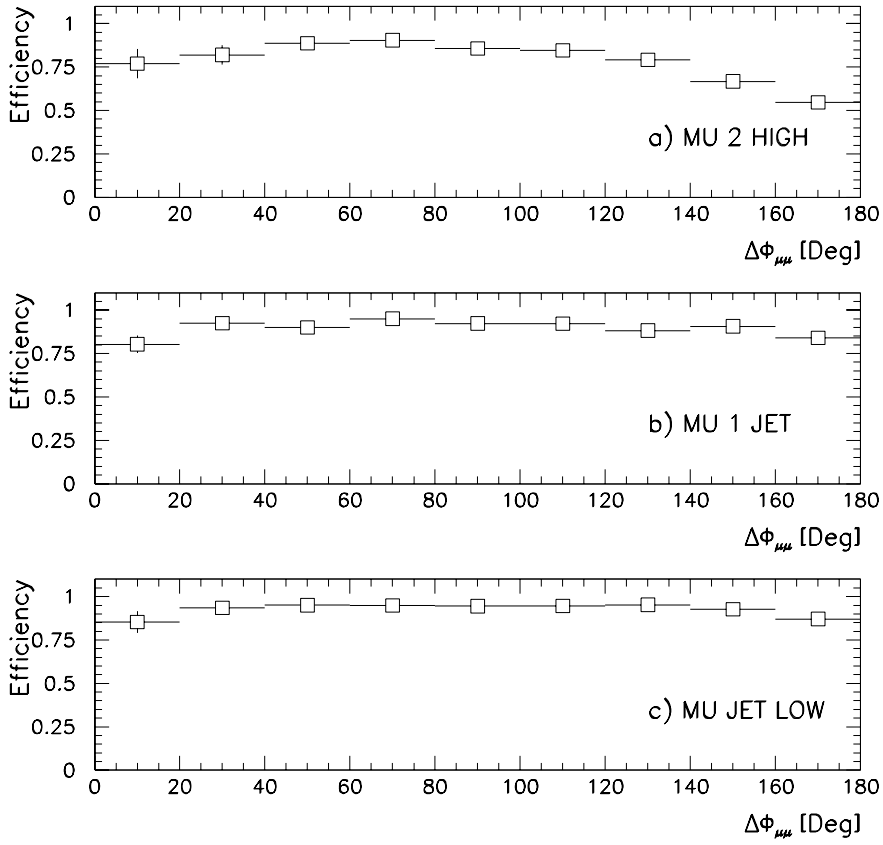


Figure 7-8: Level 2 efficiency as a function of unsmeared $\Delta\varphi^{\mu\mu}$ for a) MU_2_HIGH, b) MU_1_JET, and c) MU_JET_LOW.

to increment the IFW4 flag, described in Sec. 5.4. The effect of this is that tracks found in the data that should have a "tight" quality are found to be "common" by the Level 2 reconstruction and tracks that should have a "common" flag get thrown out since tracks with IFW4$\geq$2 are not saved. See Sec. 5.2.1 for the definitions of "tight" and "common". Since these effect are not modeled in the Monte Carlo, the Level 2 trigger efficiency for muons should be over estimated in the Monte Carlo.

The second difference between the data and the Monte Carlo is that only the V7.3 trigger conditions are simulated in the Monte Carlo. The Level 1 muon trigger hardware remained unchanged during trigger menu versions 7.1, 7.2, and 7.3. Therefore, any differences observed between the Level 1 muon efficiency in Monte Carlo and data are due to uncertainties in the MU_SMEAR determination of the pad latch efficiencies and chamber positions. For the Level 2 muon trigger, Table 5-4 shows that the Level 2 muon definitions changed between each version of the trigger menu. Therefore, a correction factor is determined to take into account the changes in the Level 2 muon trigger based on the amount of recorded luminosity taken during each trigger menu.

In order to calibrate the trigger efficiencies obtained using the fully simulated Monte Carlo sample, a comparison is made between the trigger efficiencies for reconstructed muons in the Monte Carlo and data. Ideally, one would like to use dimuon events collected using a non-muon trigger so that the effects of the muon trigger can be calculated using unbiased events. While this is theoretically possible, the statistics from run 1A using this method prove to be too small to be useful. Instead, a sample of dimuon events collected on the single muon plus jets triggers(MU_1_JET and MU_JET_LOW) are used. Because these triggers require only one muon, this sample contains at least one unbiased muon in each event, and single muon efficiencies can be calculated. The differences in efficiencies in

Monte Carlo and this data sample are used to confirm the uncertainty in the Level 1 efficiency from MU_SMEAR and to correct the Level 2 efficiency for the effects described above.

### Level 1 Single Muon Efficiency Study

The cuts applied to both the data and Monte Carlo events for the Level 1 single muon efficiency study are summarized in Table 7-1. In each event, if one muon passes the Level 1 trigger requirement, the other muon is considered unbiased for trigger studies. Thus, it is possible that both muons in an event can be used in the study. The efficiency is taken to be the number of unbiased muons which have a Level 1 trigger in the same $\varphi$-octant as the reconstructed muon divided by the total number of unbiased muons. Figure 7-9 shows the results for both the data and Monte Carlo samples. Both samples are consistent within the statistical uncertainty and are within the 10% systematic uncertainty associated with the MU_SMEAR simulation.

### Level 2 Single Muon Efficiency Corrections

A similar study is done to find the Level 2 single muon trigger efficiency. This study is complicated by the fact that there are two different muon track quality requirements in the Level 2 filters. These requirements, referred to as "common" and "tight", correspond to maximum values of the muon track quality flag of one and zero respectively, as described in Sec. 5.2.1. This study utilizes the Level 2 trigger information stored in the ESUM banks of the data and Monte Carlo events. To account for correlations between the Level 1 and Level 2 muon triggers, candidate events are required to have Level 1 triggers in the same trigger octant as

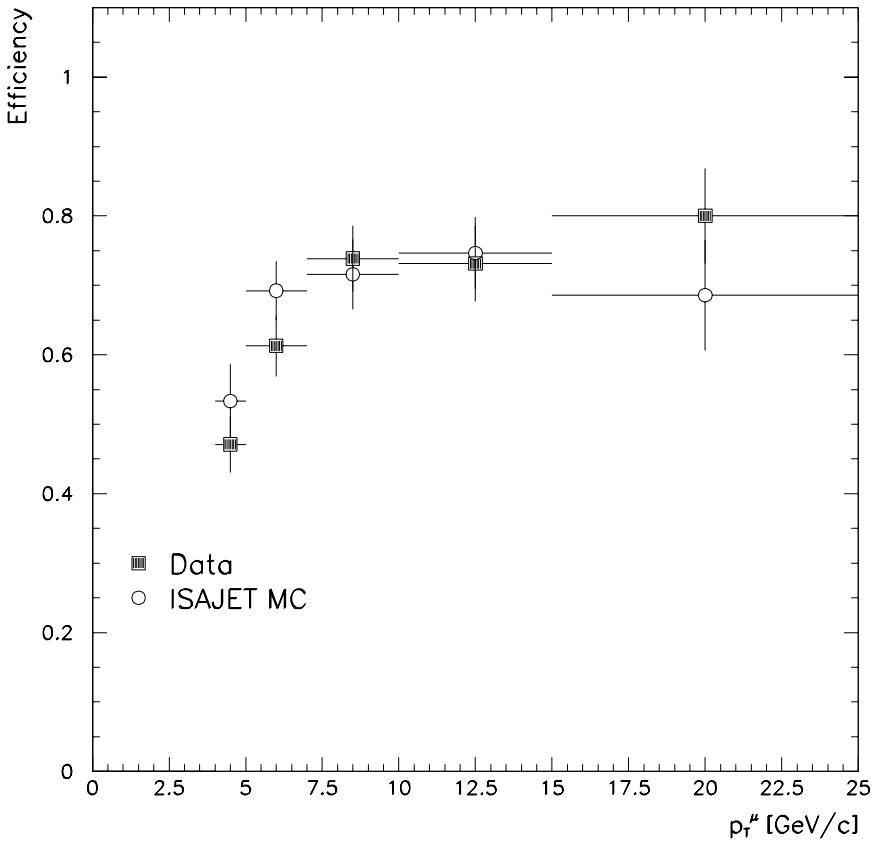


Figure 7-9: Comparison of the Level 1 single muon trigger efficiency for reconstructed muons in data and Monte Carlo as a function of reconstructed $p_T^\mu$.

| Selection of Events for the Level 1 Efficiency Study |
|---|
| Event Satisfies MU_1_JET or MU_JET_LOW Level 2 Filter |
| Two Reconstructed Muons with $\|\eta^{\mu}\| \leq 0.8$ |
| $\varphi^{\mu} \leq 80^{\circ}$ or $\varphi^{\mu} \geq 110^{\circ}$ |
| $\Delta R_{\mu-jet} \leq 0.8$ radians |
| $E_T^{jet} \geq 12$ GeV |
| $\sum_{1NN} E_{Cal} \geq 1.0$ GeV |
| IFW4 $\leq 1$ |
| $6 \leq M^{\mu\mu} \leq 35$ GeV/c$^2$ |
| $\Delta\phi_{3D} \leq 165^{\circ}$ |
| Reconstructed Muons in Different Level 1 Trigger Octants |

Table 7-1: Criteria used to select events to determine the Level 1 single muon trigger efficiency.

the reconstructed muons. In addition, both muons are required to have passed the Level 1 muon trigger requirements. Table 7-2 summarizes the cuts used to select both data and Monte Carlo events for the Level 2 single muon efficiency study.

An unbiased muon sample is found by requiring one muon in the event to pass the "common" filter requirement. This ensures that the second muon in the event is unbiased with respect to the muon trigger. As in the Level 1 muon trigger study, it is possible for both muons in an event to be used in this study. The Level 2 "common" efficiency for reconstructed muons is calculated by dividing the number of unbiased Level 2 "common" tracks by the total number of unbiased muons:

$$\epsilon_{com} = \frac{N_{com}}{N_{unbiased}}. \tag{7.4}$$

The efficiency for both the data and Monte Carlo samples is shown in Fig. 7-10. Note that the agreement is very good over the entire $p_T^{\mu}$ range.

| Selection of Events for the Level 2 Efficiency Study |
|---|
| Event Satisfies MU_1_JET or MU_JET_LOW Level 2 Filter |
| Two Reconstructed Muons with $\|\eta^{\mu}\| \leq 0.8$ |
| $\varphi^{\mu} \leq 80^{\circ}$ or $\varphi^{\mu} \geq 110^{\circ}$ |
| $\Delta R_{\mu-jet} \leq 0.8$ radians |
| $E_T^{jet} \geq 12$ GeV |
| $\sum_{1NN} E_{Cal} \geq 1.0$ GeV |
| IFW4 $\leq 1$ |
| $6 \leq M^{\mu\mu} \leq 35$ GeV/c$^2$ |
| $\Delta\phi_{3D} \leq 165^{\circ}$ |
| Reconstructed Muons in Different Level 1 Trigger Octants |
| Both Muons Have a Matching Level 1 Trigger |

Table 7-2: Criteria used to select events to determine the Level 2 single muon trigger efficiency. See Table 5-2 for a description of the MU_1_JET and MU_JET_LOW Level 2 filter requirements.

The data efficiency shown in Fig. 7-10 utilizes data collected in each of the trigger menu versions 7.1, 7.2, and 7.3, while the Monte Carlo efficiency is calculated using only V7.3 of the trigger menu. If only V7.1 and V7.2 of the trigger menus are used to calculate the Level 2 "common" muon efficiency, the result is unchanged.

To determine the Level 2 "tight" muon efficiency, the number of "tight" unbiased muons is divided by the number of "common" unbiased muons:

$$\epsilon_{tig} = \frac{N_{tig}}{N_{com,unbiased}}. \tag{7.5}$$

The efficiency for Level 2 "tight" muon tracks is shown in Fig. 7-11. As with the Level 2 "common" muon efficiency, no differences are found in the data between the different trigger menu versions. The differences in the efficiencies between the data and Monte Carlo distributions are due to the non-Gaussian drift time and

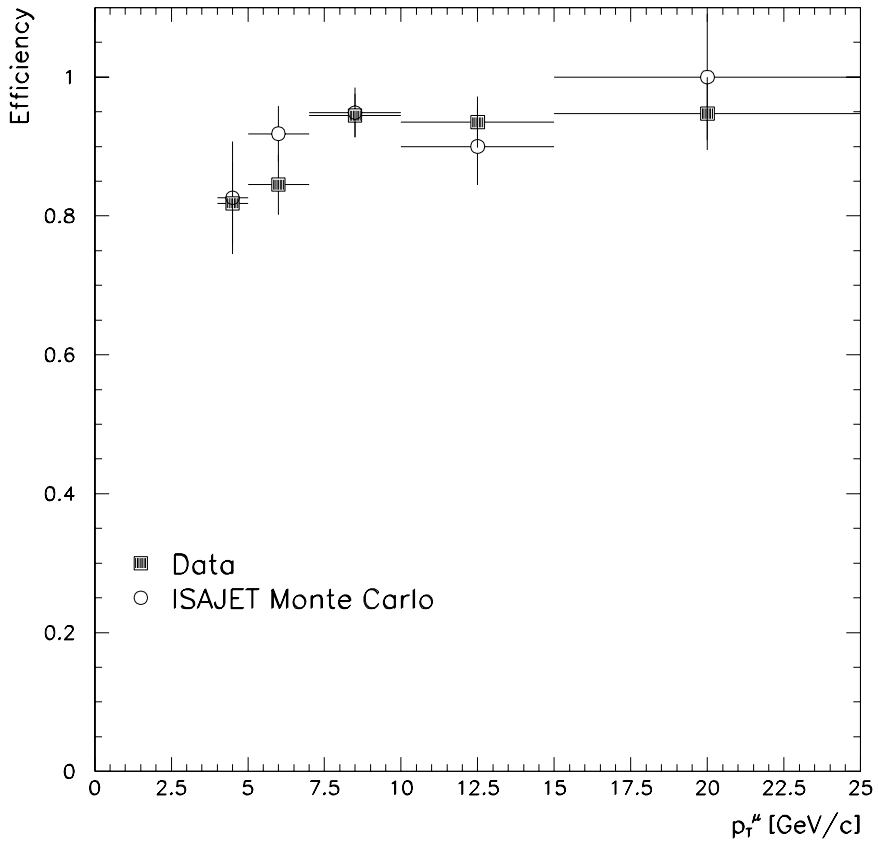


Figure 7-10: Comparison of the Level 2 "common" muon efficiency for reconstructed tracks, $\epsilon_{com}$, in data and Monte Carlo as a function of reconstructed $p_T^\mu$.

$\Delta t$ distributions in the data, which may degrade the quality flag of the muon from "tight" to "common".

These effects may also result in an additional IFW4 flag being counted against a muon track of "common" quality, thus degrading the track to a quality of IFW4$\geq 2$. These tracks are not saved by the Level 2 reconstruction. Since these effects are not simulated in the Monte Carlo, no muons are lost due to the miscalculation of drift time or $\Delta t$:

$$[\epsilon_{RECO}]_{MC} = 100\%. \tag{7.6}$$

To calculate this efficiency in the data, events where a Level 1 muon trigger occurred in the same detector octant as a reconstructed jet are used. These events are then scanned by eye to see if there is a good muon and if it is reconstructed[74]. From this study, a reconstruction efficiency for data is determined to be

$$[\epsilon_{RECO}]_{data} = 0.95 \pm 0.03. \tag{7.7}$$

This efficiency is assumed to be independent of $p_T^\mu$ within the quoted uncertainty.

### 7.2.2 Corrections to Trigger Efficiencies

The efficiencies calculated in the previous section are used to correct the Monte Carlo trigger efficiency for each of the three triggers used in this analysis: MU_2_HIGH, MU_1_JET, and MU_JET_LOW. This is done on an event-by-event basis by weighting those events which pass both the Level 1 trigger and Level 2 filter by the correction factors for each requirement:

$$W^{MU\_2\_HIGH} = w_{tig}^{MU\_2\_HIGH} w_{RECO} w_{com}$$

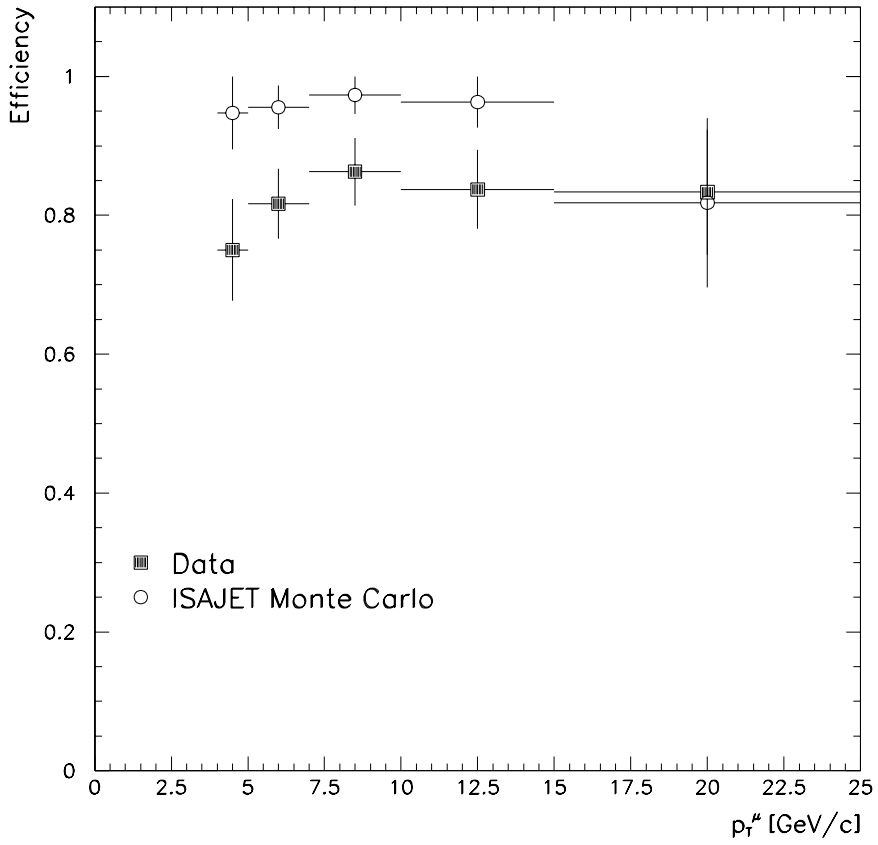


Figure 7-11: Comparison of the Level 2 "tight" muon efficiency for reconstructed tracks, $\epsilon_{tig}$, in data and Monte Carlo as a function of reconstructed $p_T^\mu$.

$$W^{MU\_1\_JET} = w_{tig}^{MU\_1\_JET} w_{RECO} w_{com} \tag{7.8}$$
$$W^{MU\_JET\_LOW} = w_{tig}^{MU\_JET\_LOW} w_{RECO} w_{com}.$$

The weighting is performed using the reconstructed $p_T^\mu$, since this is the variable the correction factors are defined for. In (7.8), $w_{tig}$ is the correction factor for requiring a "tight" muon with $p_T^\mu \geq 3.0$ GeV/c in the Level 2 filter, and $w_{RECO}$ accounts for the reconstruction inefficiencies due to the non-Gaussian tails of the drift time and $\Delta t$ distributions not simulated in the Monte Carlo. $w_{tig}$ is different for each of the triggers due to the different Level 2 filter requirements imposed. A complete description of the Level 2 filter requirements for each trigger used can be found in Secs. 5.2.1 through 5.2.3. The correction factor for requiring a "common" muon in the Level 2 filter, $w_{com}$, is assumed to be one, since both the efficiencies obtained from the Monte Carlo and data samples agreed, as shown in Fig. 7-10.

### MU_2_HIGH Trigger Efficiency Correction

Since only one of the two Level 2 "common" muons is required to pass the Level 2 "tight" condition, the correction factor for the "tight" efficiency is not simply the ratio between the data and Monte Carlo efficiencies shown in Fig. 7-11. For two "common" muons, the efficiency of requiring that one muon be "tight" is given by

$$\epsilon_{tig}^{MU\_2\_HIGH} = \epsilon_{tig}^1 + \epsilon_{tig}^2(1 - \epsilon_{tig}^1), \tag{7.9}$$

where the efficiency for a muon to pass the "tight" quality, $\epsilon_{tig}^i$, is obtained from Fig. 7-11. Thus, the correction factor corresponding to the Level 2 "tight" muon filter requirement is

$$w_{tig}^{MU\_2\_HIGH} = \frac{[\epsilon_{tig}^{MU\_2\_HIGH}]_{data}}{[\epsilon_{tig}^{MU\_2\_HIGH}]_{MC}}. \tag{7.10}$$

### MU_1_JET and MU_JET_LOW Trigger Efficiency Corrections

For both the MU_1_JET and MU_JET_LOW triggers, the Level 2 filter requiring a "tight" muon was only imposed during part of the data collection. Table 5-4 shows that the Level 2 "tight" requirement was in place during V7.3 of the trigger menu for the MU_1_JET trigger and during V7.1 of the trigger menu for the MU_JET_LOW trigger. V7.1 of the trigger menu was utilized during 15.2% of the data collection based on integrated luminosity, and V7.3 was in place for 20.9% of the data collection. The correction factor for requiring one Level 2 "tight" muon is then calculated as

$$w_{tig}^{MU\_1\_JET,MU\_JET\_LOW} = \frac{[\epsilon_{tig}^{1}]_{data}}{[\epsilon_{tig}^{1}]_{MC}} f_{tig}^{MU\_1\_JET,MU\_JET\_LOW} + (1 - f_{tig}^{MU\_1\_JET,MU\_JET\_LOW}), \quad (7.11)$$

where

$$f_{tig}^{MU\_1\_JET} = 0.152$$
$$f_{tig}^{MU\_JET\_LOW} = 0.209.$$

Finally, the correction factor corresponding to the muons lost in the Level 2 reconstruction due to the unphysical drift time and $\Delta$times distributions is calculated using

$$w_{RECO} = \frac{[\epsilon_{RECO}]_{data}^{2}}{[\epsilon_{RECO}]_{MC}^{2}} = 0.90 \pm 0.04. \quad (7.12)$$

This value is used for each of the three triggers since we require two reconstructed muons in each sample.

Each Monte Carlo event which passes the trigger requirements is weighted by the product of these corrections, (7.8), calculated using the reconstructed $p_T$ of each

muon. This procedure is followed to determine the corrected trigger efficiencies for each of the three trigger bits as a function of measured $p_T^\mu$(leading) and $\Delta\phi^{\mu\mu}$. The corrected trigger efficiencies are shown along with the uncorrected trigger efficiencies in Figs. 7-12 through 7-14 as a function of unsmeared $p_T^\mu$(leading) and $\Delta\phi^{\mu\mu}$.

The corrected efficiencies are translated from measured $p_T^\mu$ to unsmeared $p_T^\mu$ using the same Monte Carlo samples that are used in determining the efficiencies. The first step is to calculate the correction factor in terms of the smeared, or measured, variable. Since we know what the unsmeared value of $p_T^\mu$ is for these Monte Carlo events, the corrected efficiencies can be determined in terms of the unsmeared variable.

The systematic uncertainties due to the various trigger efficiencies, not shown in Figs. 7-12, 7-13, and 7-14, are listed in Table 7-3. For the jet triggers, a 10% fractional uncertainty is used for the Level 1 jet trigger efficiency which is taken as the average difference between the Monte Carlo corrected and data Level 1 jet trigger efficiencies, shown in Fig. 7-3. A 5% fractional uncertainty is assigned to the Level 2 jet trigger efficiency. This is determined from the small differences between the Monte Carlo corrected and data Level 2 jet trigger efficiencies shown in Fig. 7-4. A 10% fractional uncertainty in the Level 1 single muon efficiency is calculated using the uncertainty in MU_SMEAR, which is confirmed by the Level 1 muon efficiency study described above. The uncertainty in the Level 2 "common" efficiency for single muons is taken to be 4%, the overall $1\sigma$ uncertainty between the data and Monte Carlo from Fig. 7-9. For the Level 2 "tight" efficiency for single muons, a fractional uncertainty is taken to be 5%. Finally, the uncertainty in the muon reconstruction efficiency is the statistical uncertainty from the scanned data sample. The total systematic uncertainty in the trigger efficiencies for the

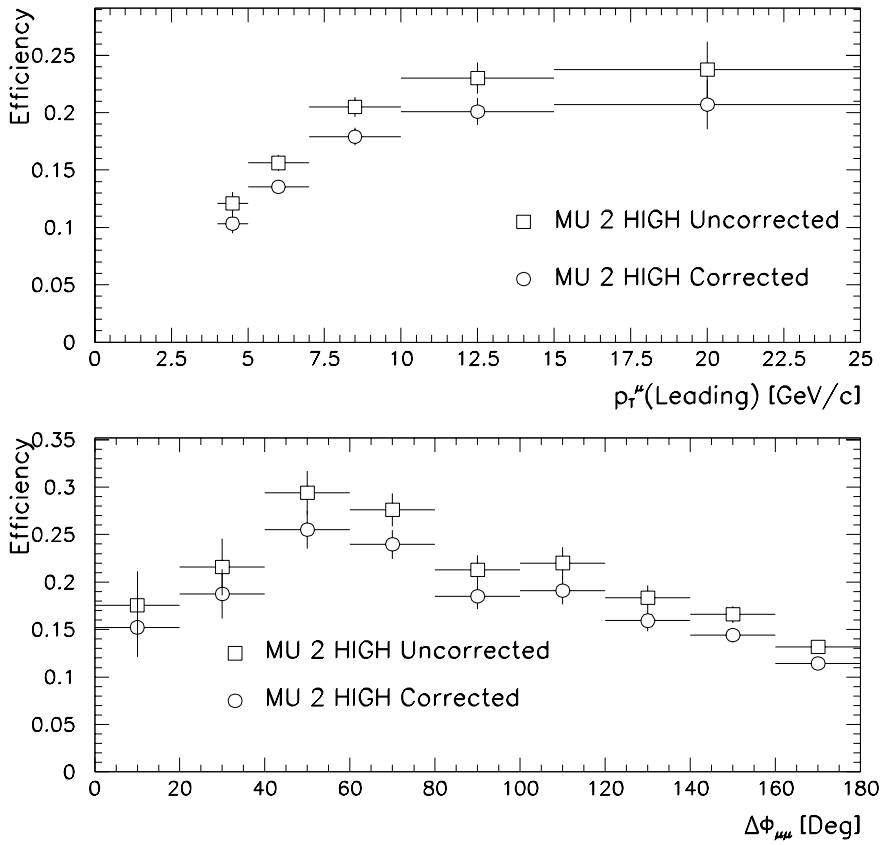


Figure 7-12: Corrected and uncorrected Level 1∗Level 2 trigger efficiencies for the MU_2_HIGH trigger as a function of unsmeared $p_T^{\mu}$(leading) and $\Delta\phi^{\mu\mu}$. The uncertainties are due to Monte Carlo statistics only.

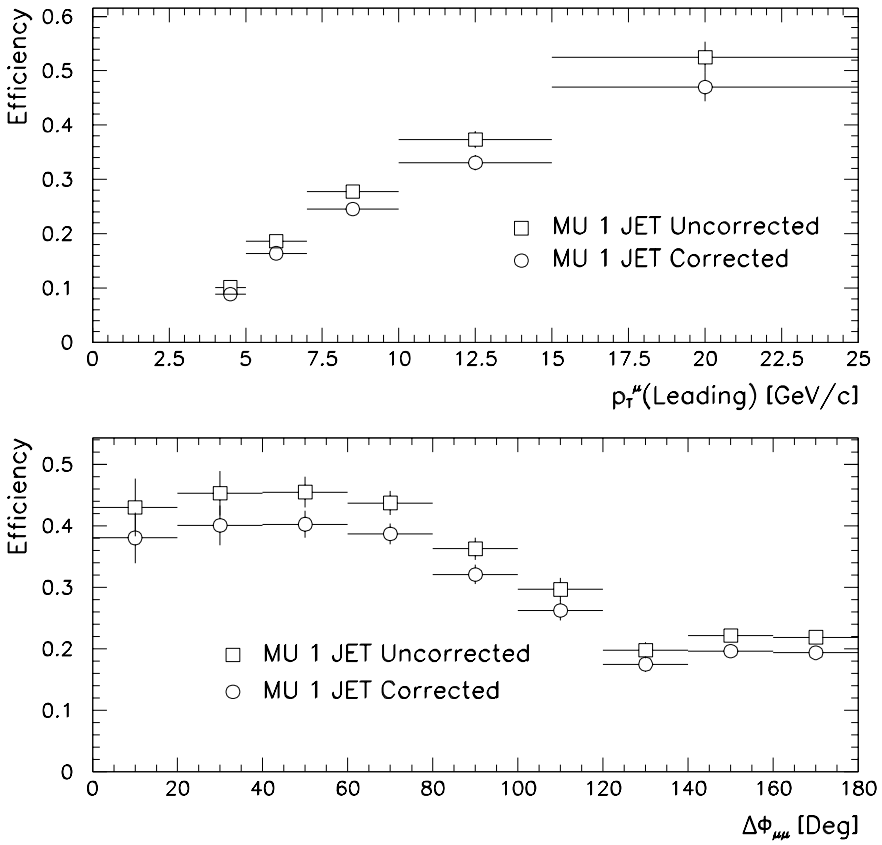


Figure 7-13: Corrected and uncorrected Level 1∗Level 2 trigger efficiencies for the MU_1_JET trigger as a function of unsmeared $p_T^\mu$(leading) and $\Delta\phi^{\mu\mu}$. The uncertainties are due to Monte Carlo statistics only.

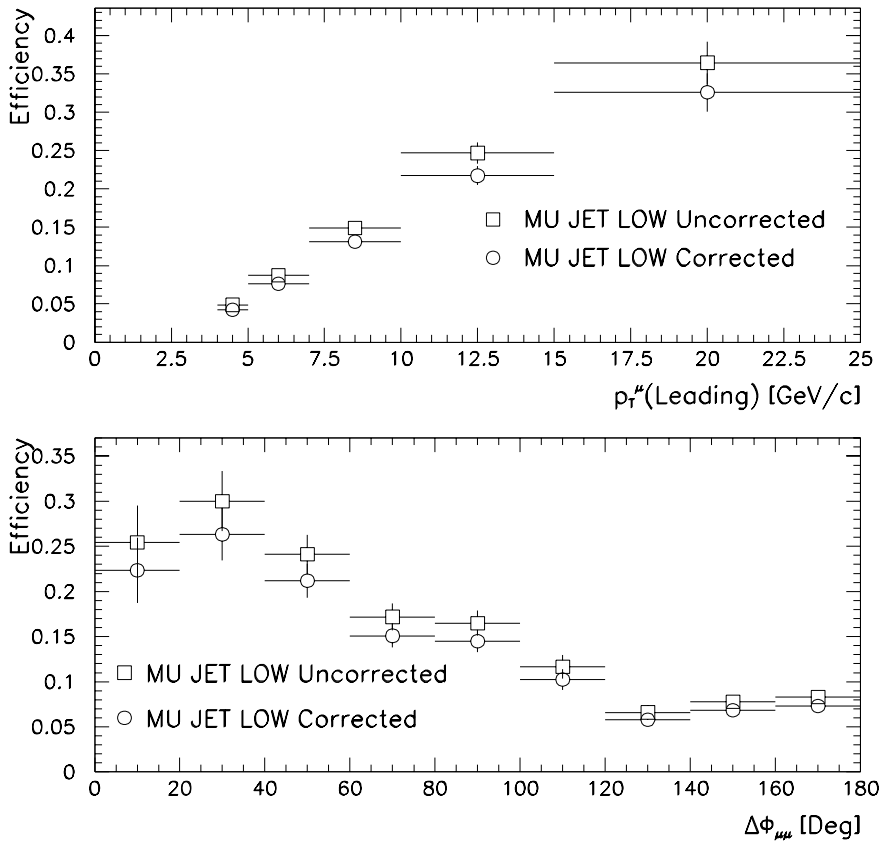


Figure 7-14: Corrected and uncorrected Level 1∗Level 2 trigger efficiencies for the MU_JET_LOW trigger as a function of unsmeared $p_T^{\mu}$(leading) and $\Delta\phi^{\mu\mu}$. The uncertainties are due to Monte Carlo statistics only.

MU_2_HIGH, MU_1_JET, and MU_JET_LOW triggers are 17%, 16%, and 19%, respectively.

| Source | Fractional Uncertainty | | |
|---|---|---|---|
| | MU_2_HIGH | MU_1_JET | MU_JET_LOW |
| Level 1 Jet Efficiency | - | 10% | 14% |
| Level 2 Jet Efficiency | - | 5% | 5% |
| Level 1 Muon Efficiency | 14% | 10% | 10% |
| Level 2 "common" Muon Efficiency | 6% | 4% | 4% |
| Level 2 "tight" Muon Efficiency | 5% | - | - |
| Level 2 Muon RECO Efficiency | 4% | 4% | 4% |
| Total Systematic Uncertainty | 17% | 16% | 19% |

Table 7-3: Sources of systematic uncertainties in the trigger efficiencies.

## 7.3 Offline Muon Identification Efficiency

### 7.3.1 Muon Track Quality Flag, IFW4

Because each of the Level 2 triggers require muons to have a track quality of at least "common" quality(IFW4=1), we expect this offline cut to be nearly 100% efficient. This efficiency is confirmed using the $b\bar{b}$ Monte Carlo sample with the full detector simulation. A value of 100% with negligible uncertainties is used for this analysis.

### 7.3.2 Muon Minimum Ionizing Energy Deposition

To determine the efficiency of the minimum ionizing energy deposition cut, a sample of good quality muons is selected from the data. This sample has the same cuts as the regular data sample, listed in Table 5-8, but with the following two changes. First, a tighter cut on the muon track quality flag, IFW4, is applied. Only muons with IFW4=0 are accepted. Second, the minimum ionizing energy cut is only applied to the biased muon in the event. Of the 819 unbiased muon passing these cuts, 796 satisfy the minimum ionizing energy confirmation. This gives

$$\epsilon_{MIP} = 97 \pm 1\%.$$

Figure 7-15 shows the $\sum_{1NN} E_{Cal}$ distribution for these events.

## 7.4 Offline Dimuon Event Selection Efficiency

The final event selection cut efficiencies are determined using the Monte Carlo samples described in Chapter 6. The efficiencies are calculated by applying all the data cuts listed in Table 5-8 to the Monte Carlo sample with unsmeared variables and then relaxing the cut which is under investigation. The ratio between these two values gives the efficiency of that selection cut.

### 7.4.1 Muon Pseudorapidity

Requiring two reconstructed muons to be within the CF region ($|\eta| \leq 0.8$) of the detector has very little effect since the detector smearing in this variable is negligible. Figure 7-16(A) shows the efficiency of requiring two reconstructed muons in

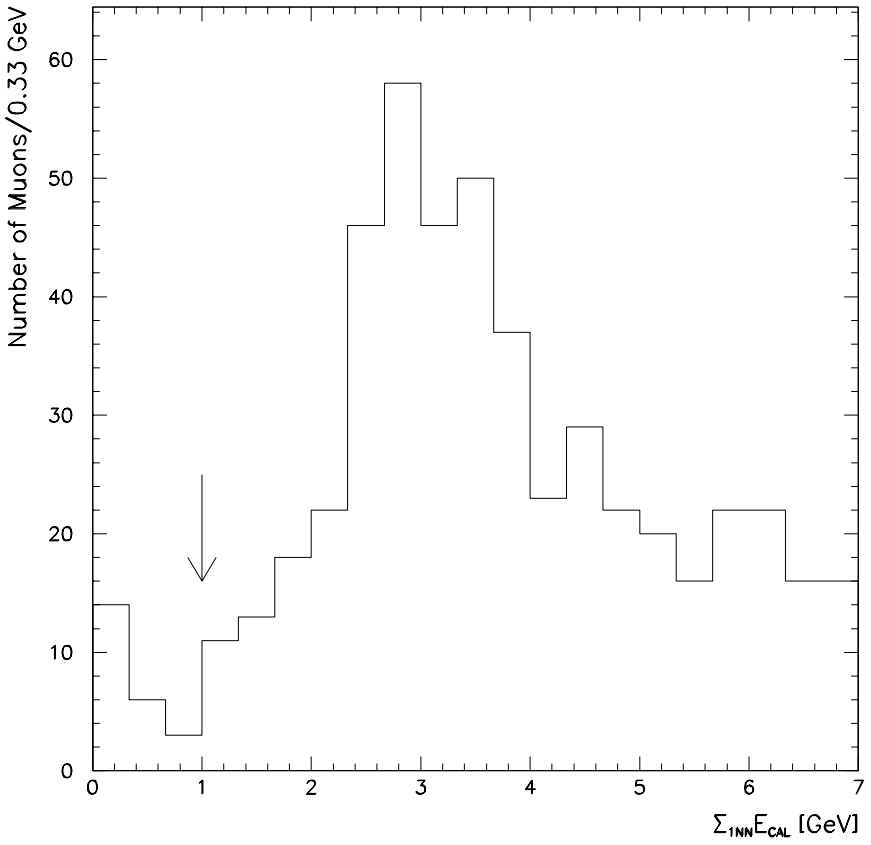


Figure 7-15: Distribution of the minimum ionizing energy ($\sum_{1NN} E_{Cal}$) for unbiased muons. The cut made in the data is indicated by the arrow.

$|\eta^{\mu}| \leq 0.8$ as a function of the unsmeared $p_T$ of the leading muon.

### 7.4.2 Muon Transverse Momentum

Since the DØ detector has a finite momentum resolution (see Sec. 9.1), the effect of requiring both muons to have a reconstructed transverse momentum in the range $4 \leq p_T^{\mu} \leq 25$ GeV/c will be larger than the effect of the pseudorapidity cut. Figure 7-16(B) shows the efficiency of the reconstructed $p_T^{\mu}$ cut as a function of the unsmeared $p_T^{\mu}$(leading) in the event. The overall loss in efficiency is due to the fact that the non-leading muon $p_T$ spectrum is heavily weighted towards the lower $p_T^{\mu}$ cutoff of 4 GeV/c. When these muons are reconstructed, some will fall out of the required reconstructed muon $p_T$ region due to the detector smearing. The low efficiencies in the first and last bins of Fig. 7-16(B) reflect additional losses due to the leading muon being reconstructed out of the accepted $p_T^{\mu}$ range.

### 7.4.3 Dimuon Invariant Mass

A loss in efficiency also occurs when reconstructing the dimuon invariant mass. This loss is also caused by the finite momentum resolution of the detector since the muon momentum vector is used in the calculation of the reconstructed invariant mass. Figure 7-16(C) shows this efficiency as a function of the dimuon opening angle, $\Delta\phi^{\mu\mu}$. The effect is most pronounced at smaller opening angles since these events have an unsmeared invariant mass already near the lower threshold of 6 GeV/$c^2$.

### 7.4.4 Dimuon Three-Dimensional Opening Angle

The three-dimensional opening angle cut has very little effect on the data sample. This cut is almost 100% efficient due to the good position measurement of muons in the DØ detector, with only a small loss occurring in the largest $\Delta\phi^{\mu\mu}$ bin, as shown in Fig. 7-16(D).

### 7.4.5 Muon Fiducial Volume

The efficiency of the fiducial volume cut, $\varphi^{\mu} \leq 80^{\circ}$ or $\varphi^{\mu} \geq 110^{\circ}$, is determined using the fully reconstructed Monte Carlo samples. For a given dimuon opening angle, $\Delta\phi^{\mu\mu}$, we expect the efficiency of events with one muon in a given $\varphi$-region of the detector to depend upon the acceptance in the $\varphi$-region where the other muon is detected. Since the acceptance of the detector is very non-uniform in $\varphi$, particularly in the bottom portion of the detector where there are gaps in the muon coverage, we expect to see a dependence of this efficiency in both $p_T^{\mu}$(leading) and $\Delta\phi^{\mu\mu}$. The efficiency of this cut as a function of unsmeared $p_T^{\mu}$(leading) and $\Delta\phi^{\mu\mu}$ is shown in Fig. 7-17.

### 7.4.6 Associated Jet with the Muon

The efficiency of finding an associated jet of $E_T^{jet} \geq 12$ GeV with each muon is obtained from the reconstructed Monte Carlo. Figure 7-18 shows the $\Delta R_{\mu-jet}$ distribution for events with reconstructed jets. Clearly seen is the peak at $\Delta R_{\mu-jet} = 0$ indicating the production of a muon associated with hadronic activity. The cut of $\Delta R_{\mu-jet} \leq 0.8$, indicated by the arrow in Fig. 7-18, is made to ensure that the

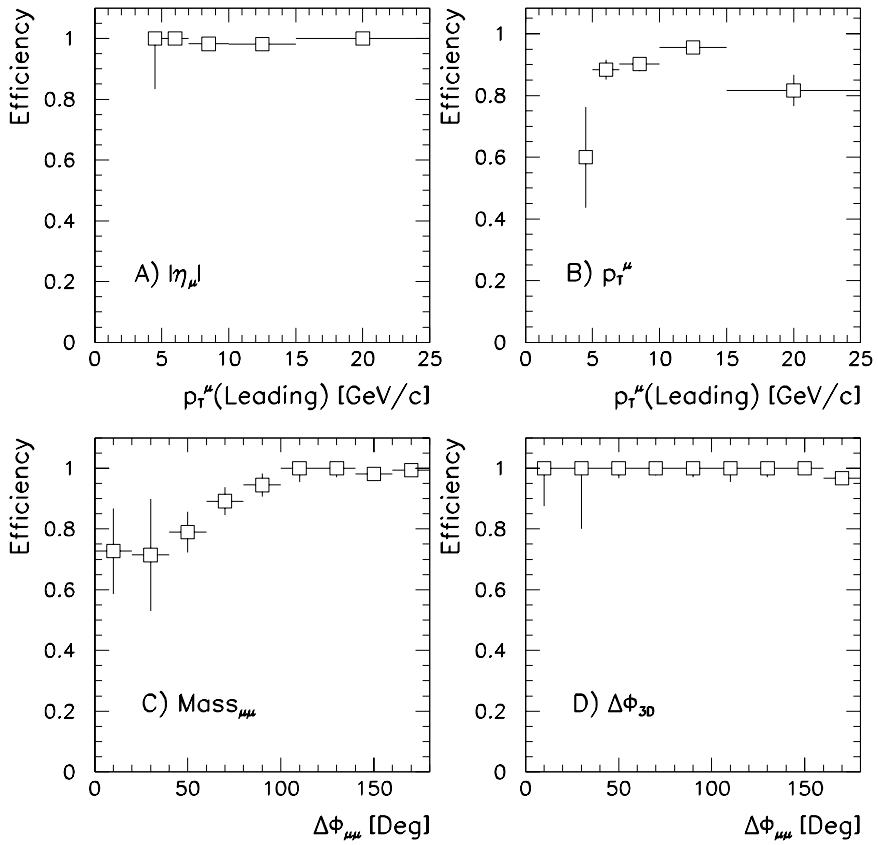


Figure 7-16: Monte Carlo efficiency calculations for various kinematic cuts: (A) $|\eta^\mu|$, (B) $p_T^\mu$, (C) Invariant Mass, and (D) $\Delta\phi_{3D}$, plotted as a function of unsmeared $p_T^\mu$(leading) and $\Delta\phi^{\mu\mu}$. The errors shown are due to Monte Carlo statistics.

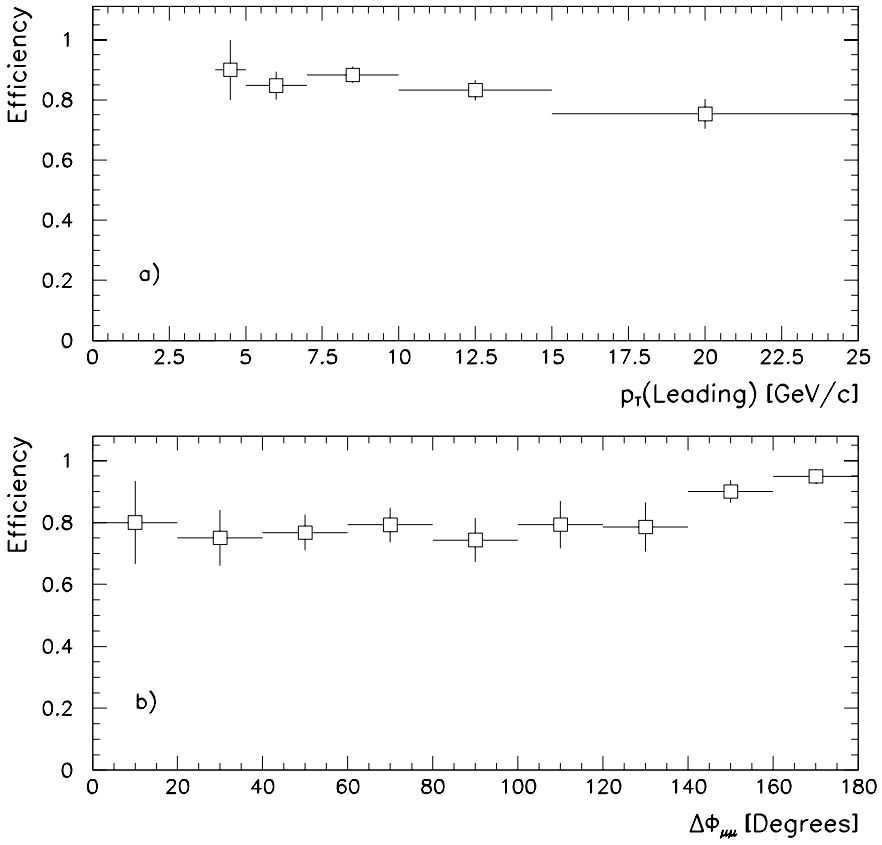


Figure 7-17: Efficiency of the fiducial muon phi cut as a function of a) unsmeared $p_T^{\mu}$(leading) and b) $\Delta\phi^{\mu\mu}$. The errors shown are due to Monte Carlo statistics.

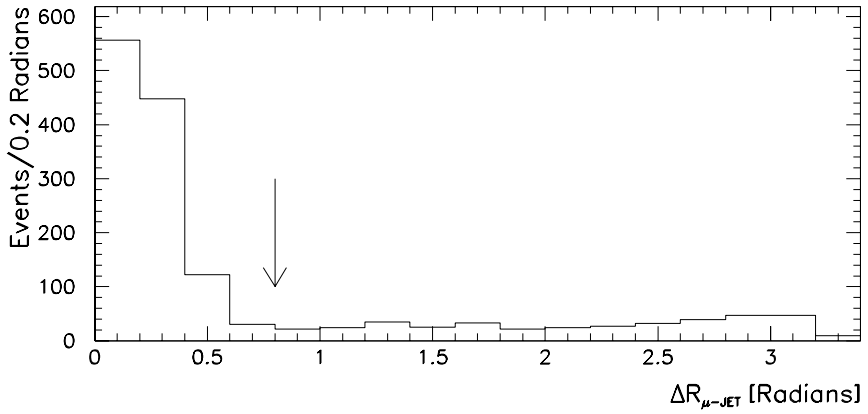


Figure 7-18: The distribution of $\Delta R_{\mu-jet}$ for events that contain reconstructed jets. The arrow indicates where the cut is made in the data.

muons are closely associated with each jet and that the variable $p_T^{rel}$ is well defined.

Since each of the triggers used require different trigger conditions on the jets, MU_2_HIGH having no jet requirement at all, we expect that the efficiency for requiring each muon to have an associated jet of $E_T^{jet} \geq 12$ GeV be different for each trigger. Figure 7-19 shows this efficiency as a function of the unsmeared leading muon $p_T$ for each of the triggers. As expected, the efficiency of the MU_2_HIGH trigger (Fig. 7-19(A)) is considerably less than those triggers which already contain jet requirements. A possible additional source of systematic error not included here may be introduced by the choice of Monte Carlo used to calculate this efficiency.

The total offline selection efficiencies, including the muon identification efficiencies, are shown in Figs. 7-20 and 7-21. These efficiencies include correlations between offline cuts, such as the dimuon invariant mass, $M^{\mu\mu}$, and $\Delta\phi_{3D}$.

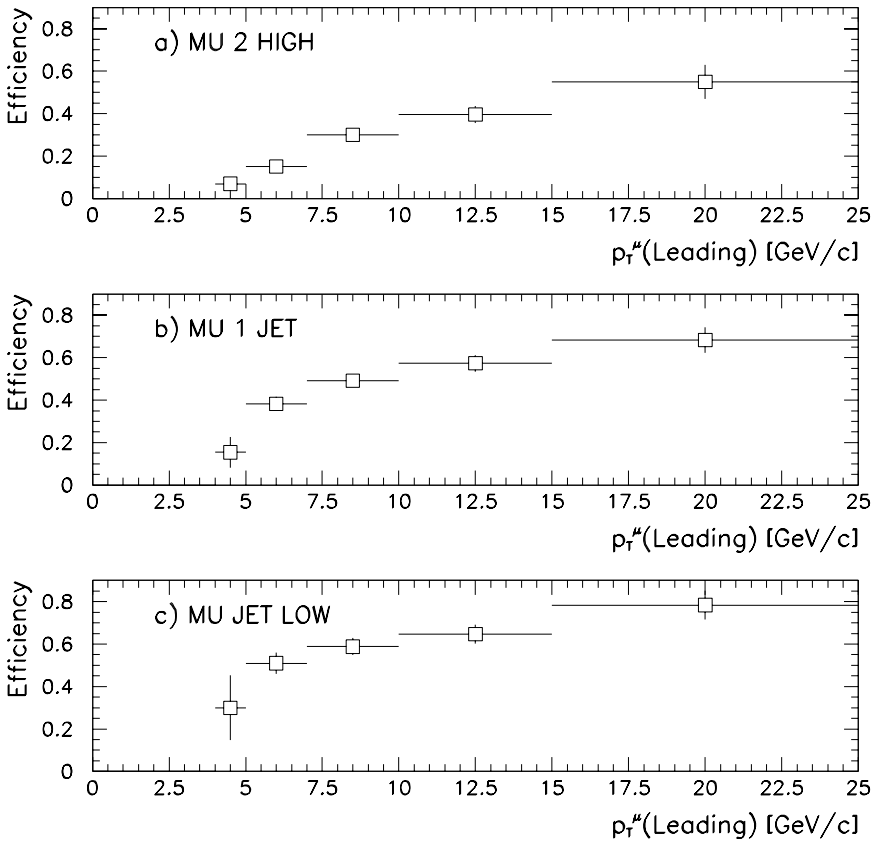


Figure 7-19: Efficiency for requiring an associated jet of $E_T^{jet} \geq 12$ GeV with each muon as a function of the unsmeared $p_T^\mu$(leading) for each trigger: a) MU_2_HIGH, b) MU_1_JET, and c) MU_JET_LOW.

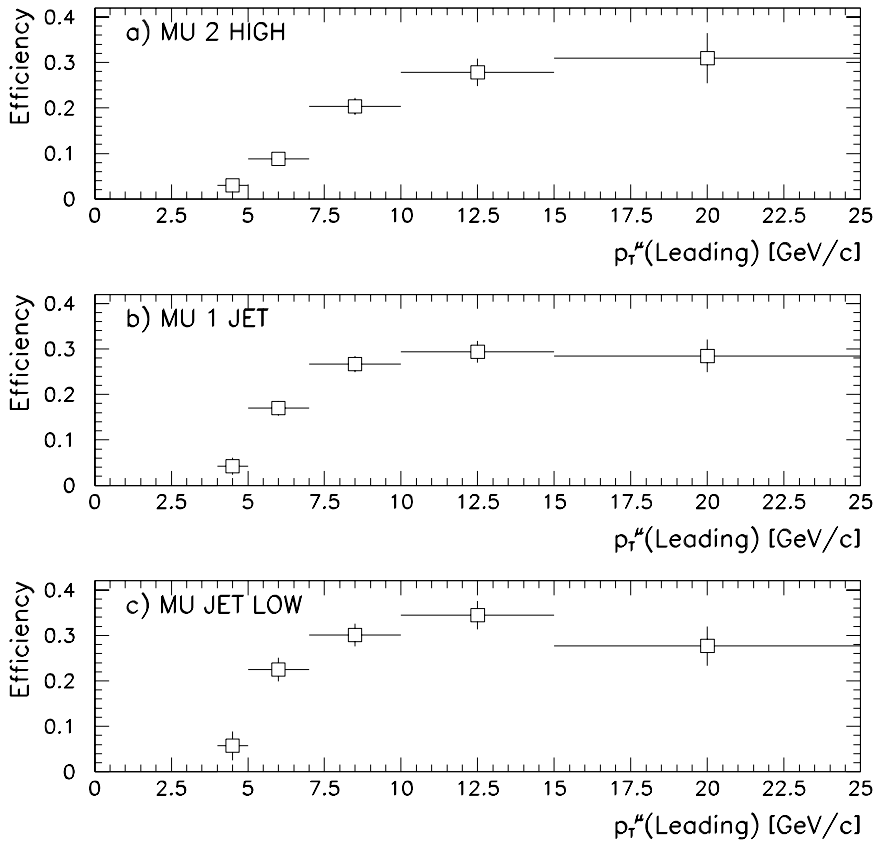


Figure 7-20: Offline efficiency as a function of unsmeared $p_T^{\mu}$(leading) for a) MU_2_HIGH, b) MU_1_JET, and c) MU_JET_LOW. The errors are due to Monte Carlo statistics.

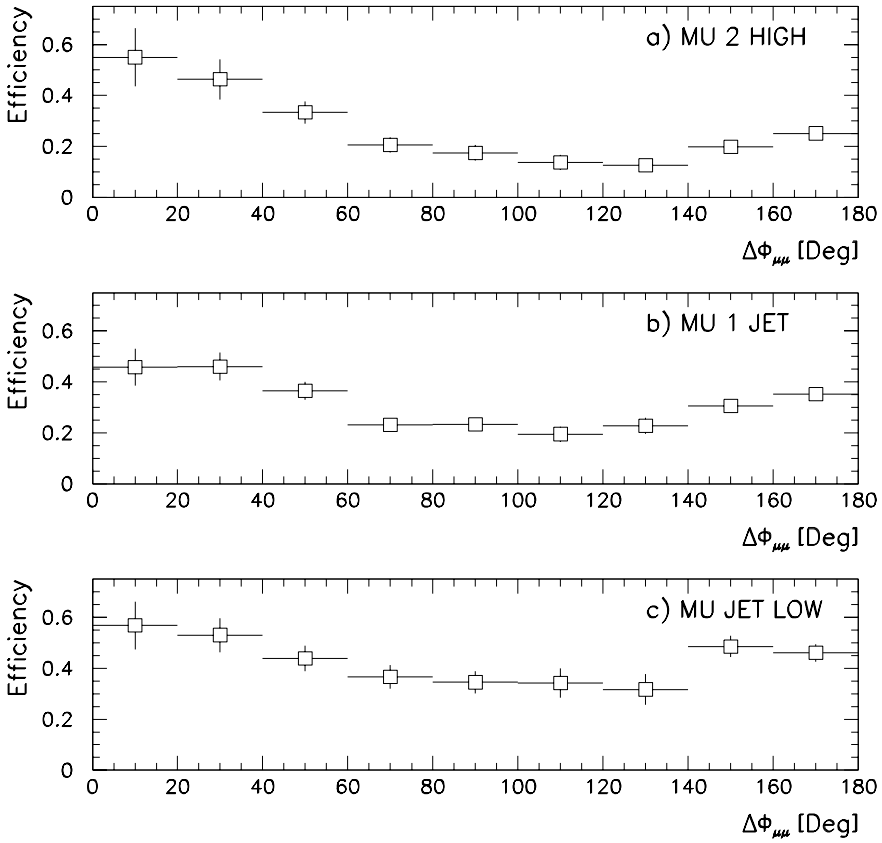


Figure 7-21: Offline efficiency as a function of $\Delta\phi^{\mu\mu}$ for a) MU_2_HIGH, b) MU_1_JET, and c) MU_JET_LOW. The errors are due to Monte Carlo statistics.

### 7.4.7 Total Efficiency

By combining the trigger efficiencies of Sec. 7.2 with the offline selection efficiencies shown in Sec. 7.4, we obtain the total efficiencies for detecting dimuon events. Figures 7-22 and 7-23 show the total efficiencies for each trigger as a function of unsmeared $p_T^{\mu}$(leading) and $\Delta\phi^{\mu\mu}$. These efficiencies are used in the calculation of the total dimuon and $b\overline{b} \rightarrow \mu\mu$ cross sections of Chapter 9.

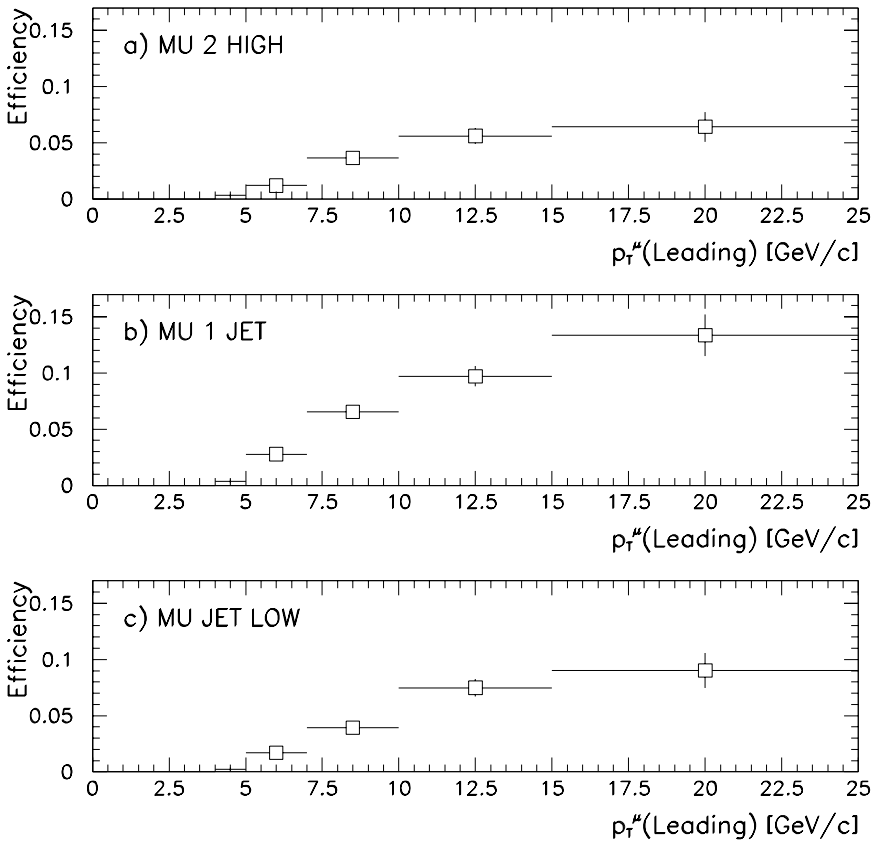


Figure 7-22: Total efficiency as a function of unsmeared $p_T^\mu$(leading) for a) MU_2_HIGH, b) MU_1_JET, and c) MU_JET_LOW. The errors are due to Monte Carlo statistics.

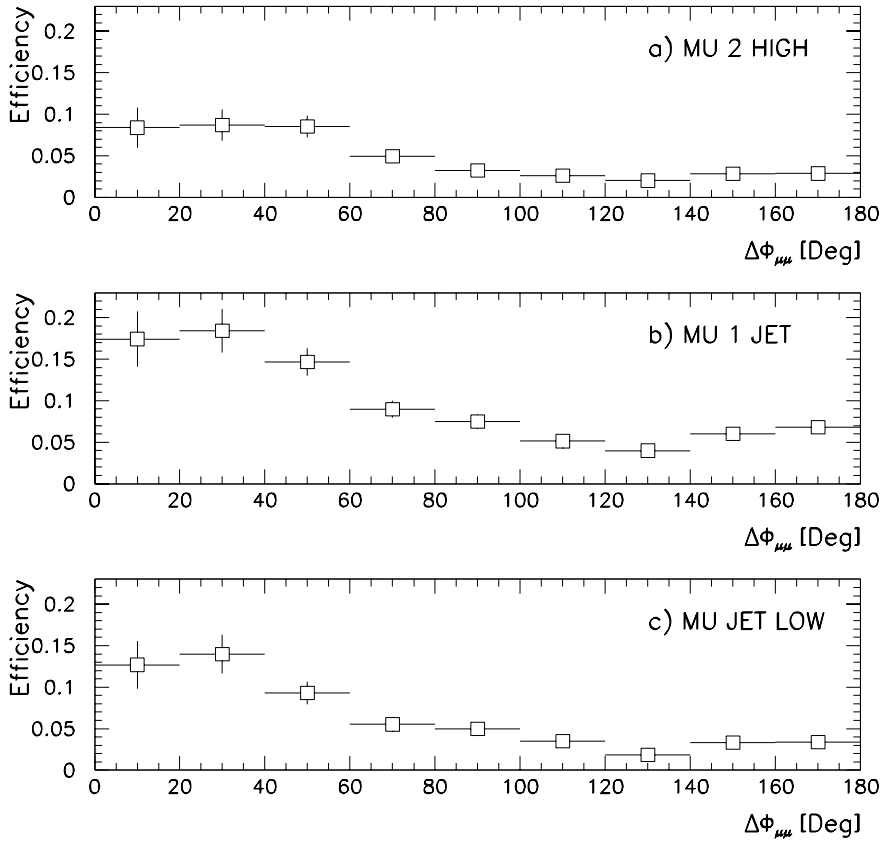


Figure 7-23: Total efficiency as a function of $\Delta\phi^{\mu\mu}$ for a) MU_2_HIGH, b) MU_1_JET, and c) MU_JET_LOW. The errors are due to Monte Carlo statistics.

# Chapter 8

# Determination of Signal and Background

As discussed in Chapter 6, the events in the final data samples contain contributions from the following physics processes: $b\bar{b}$ production, $c\bar{c}$ production, events where one muon is from the semileptonic decay of a heavy quark and the other muon is from the decay-in-flight of a $\pi$ or $K$, and double decay events where both muons originate from in-flight decays of a $\pi$ or $K$. There is an additional source of background events from cosmic ray muons. This chapter discusses the technique used to separate the $b\bar{b}$ signal from the other processes that contribute to the dimuon signal.

## 8.1 The Maximum Likelihood Fit

An event-by-event maximum likelihood fit is used to extract the $b\bar{b}$ and background contributions to the dimuon data. This method is chosen so as to avoid any loss of information due to binning. In order to determine the fraction of the sample,

$A_j$, from each of the contributing processes, $j$, $j = 1, \ldots, N_j$, it is necessary to maximize the log-likelihood function

$$L = \ln \mathcal{L} \tag{8.1}$$

with respect to the variables $A_j$. The likelihood function, $\mathcal{L}$, is a measure of the probability that a set of measured quantities, $x_k$, are distributed according to a probability density function, $p(x_k)$. The likelihood function, $\mathcal{L}$, is given by

$$\mathcal{L} = \prod_{i=1}^{N_i} \left[ \sum_{j=1}^{N_j} A_j \prod_{k=1}^{N_k} p_k^j(x_k^i) \right], \tag{8.2}$$

where the functions $p_k^j(x_k)$ are the normalized probability density functions for each variable $x_k$, where the variables $x_k$ are the floating time, $t_0^f$, $p_T^{rel}$ of the leading muon, $p_T^{rel}$ of the trailing muon, and $z'$, the fraction of the jet momentum carried by the muon divided by the jet $E_T$. The product over $i$ in (8.2) is taken over all $N_i$ events in the data set. As discussed in Chapter 6, only $b\overline{b}$, $c\overline{c}$, prompt muon plus $\pi/K$ decay, and cosmic rays are considered to contribute to the signal so that $N_j = 4$. The double decay events are included with the $c\overline{c}$ contribution. Thus, the four parameters, $A_j$, are subject to the normalization constraint

$$\sum_{j=1}^{N_j} A_j = 1. \tag{8.3}$$

Because of this condition, the $A_j$'s can be transformed into a set of $N_j$ - 1 independent parameters, $\alpha_j$, where $0 < \alpha_j < 1$. Thus, the four contributing processes to the dimuon sample can be written as functions of the three independent parameters, $\alpha_j$:

$$\begin{aligned} A_1 &= \alpha_1 \\ A_2 &= (1-\alpha_1)\cdot\alpha_2 \\ A_3 &= (1-\alpha_1)\cdot(1-\alpha_2)\cdot\alpha_3 \end{aligned} \tag{8.4}$$

$$A_4 \;=\; (1-\alpha_1)\cdot(1-\alpha_2)\cdot(1-\alpha_3).$$

These equations satisfy the normalization condition (8.3).

The minimum of the log-likelihood is found by satisfying the set of conditions

$$\frac{\partial(-2\cdot\ln L)}{\partial\alpha_j}=0, \quad j=1,\ldots,N_j-1. \tag{8.5}$$

The CERNLIB package MINUIT [75] is used to perform this minimization. The minus sign in (8.5) is necessary because MINUIT finds the minimum, not the maximum of the function. The factor of 2 is included so that a change of $\Delta(-2\cdot\ln L)=+1$ in the minimum value of the log-likelihood function corresponds to a $1\sigma$ error on $\alpha_j$. The MINOS error analysis package used in MINUIT finds the contours of equal likelihood in $(N_j-1)$-dimensional space. These generally turn out to be hyperbolic-like functions. A change in $+1$ above the minimum in this function gives the $1\sigma$ error. Since this function is not necessarily symmetric around the minimum, the upper and lower errors found on $\alpha_j$ will often be asymmetric.

## 8.2 Inputs to the Likelihood Equation

The input distributions used in the maximum likelihood fit are selected on the basis that they are qualitatively different for the each of the contributing processes to the dimuon signal. The success of the fit depends on how well these input distributions represent the distributions in the data. Whenever possible, distributions are obtained from different sources to reduce the systematic errors. Uncertainties due to the input distributions are discussed at the end of the chapter. Three variables are used in this fit: floating time shift, $t_0^f$ , the transverse momentum of the muon with respect to the associated jet, $p_T^{rel}$, and $z'$, the fraction of the associated jet

momentum carried by the muon divided by the transverse energy of the jet.

### 8.2.1 Floating Time Shift, $t_0^f$

Figure 8-1 shows a depiction of a muon track traversing a chamber. The position of the track within each drift cell in the bend view is proportional to the difference between the time of the beam crossing, $t_0$, and the arrival time of the charge at the anode wire, $t_i$:

$$d_i = \frac{|t_i - t_0|}{v_{drift}}.$$

The floating time shift, $t_0^f$, is defined as the difference between the $t_0$ which gives the best fit to the muon track and the $t_0$ which corresponds to the ADC value corresponding to a hit on the wire at the time of the beam crossing. The floating $t_0$ is obtained by allowing the $t_0$ used in calculating the muon drift distances on a track to float in the muon track fit. Beam produced muons give a $t_0^f$ distribution which peaks at zero since they are produced in coincidence with the beam crossing. Cosmic rays should arrive randomly, thus producing a $t_0^f$ distribution which is flat.

The $t_0^f$ distribution for the data signal is obtained from two different samples. Both samples are extracted from the data sample using the same quality cuts used to select the final data sample except for the requirement of two associated jets. Instead, there is the additional requirement that the global fit $\chi^2$ on the muon fit be less than 50. The global fit $\chi^2$ is a measure of how well the reconstructed muon track matches up with tracks in the central detector and the event vertex. The

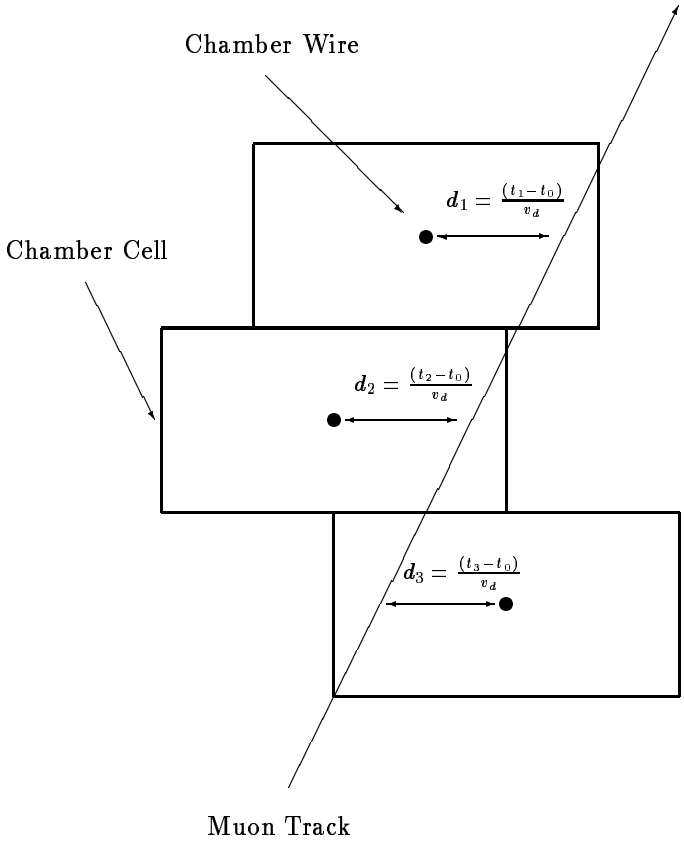


Figure 8-1: The floating time is calculated by allowing the beam crossing time, $t_0$, to be a free parameter in the refit of the muon track.

first sample requires that at least one muon be non-isolated, as defined by

$$E_{cal}(R = 0.6) - E_{cal}(R = 0.2) \geq 5.0 \text{ GeV},$$

where $E_{cal}(R = 0.6(0.2))$ is the amount of energy found in a cone of radius, $R = 0.6(0.2)$, around the muon track. This cut ensures that there is appreciable hadronic activity around the muon, thus eliminating muons from cosmic rays. Additionally, the first sample requires that the mass be in the range of the $J/\psi$,

$$2.0 \text{ GeV/c}^2 \leq M^{\mu\mu} \leq 4.0 \text{ GeV/c}^2.$$

The second sample also requires a non-isolated muon, but a mass range of

$$6.0 \text{ GeV/c}^2 \leq M^{\mu\mu} \leq 25.0 \text{ GeV/c}^2$$

is used. Figure 8-2 shows good agreement between the two distributions from the independent samples. The agreement gives us confidence that the true distribution for beam-produced muons was found.

The shoulder on the positive side of the $t_0^f$ distribution for beam produced muons in Fig. 8-2 is an artifact of the floating time fitting algorithm. The algorithm prefers to include as many hits on the track as possible. Consequently, it may choose a larger value of $t_0^f$ to include more hits on a muon track[76].

A sample of cosmic ray muons obtained during special cosmic ray runs is used to determine the $t_0^f$ distribution for cosmic ray muons. The special cosmic ray runs were taken under normal collider running conditions except for the fact that there was no beam in the Tevatron of Main Ring. This guaranteed that any reconstructed muon track originated from cosmic rays. The cuts used to select events from these special runs are summarized in Table 8-1. As a check to this distribution, an independent sample of cosmic ray muons is selected from the data

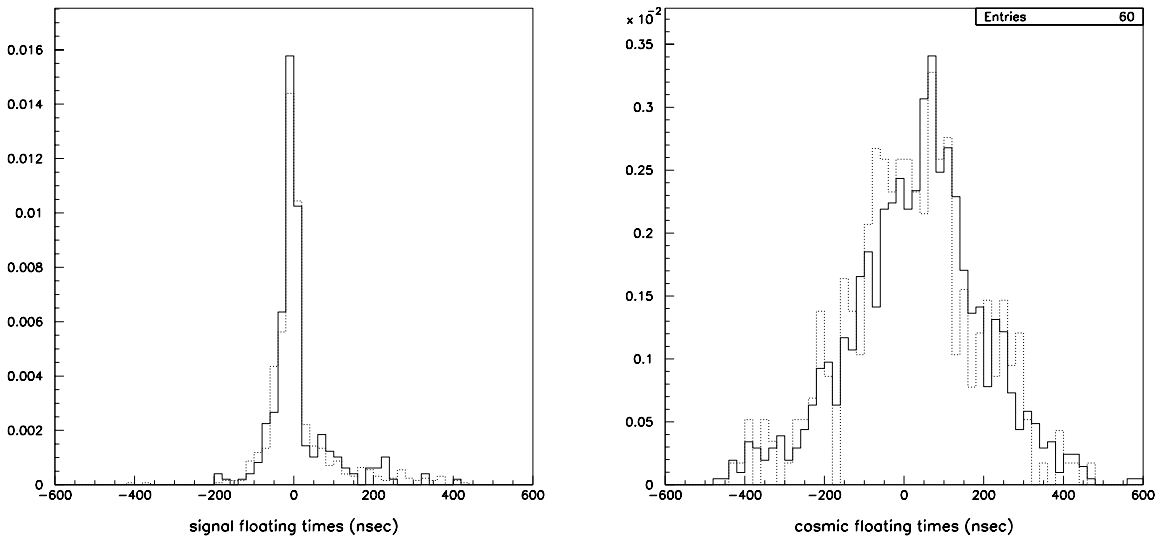


Figure 8-2: (left) $t_0^f$ distributions for beam produced muons. The solid line is from the $J/\psi$ data sample and the dashed line is from the QCD data sample. (right) $t_0^f$ distributions for cosmic rays taken from the cosmic ray runs(solid line) and from the scanned data sample(dashed line).

| Event Selection for Cosmic Ray Runs |
|---|
| Two Muon Tracks of Opposite Sign |
| $6 \leq M^{\mu\mu} \leq 40$ GeV/c$^2$ |
| Muon Track Quality Flag, IFW4 $= 0$ |
| $\lvert\eta^{\mu}\rvert \leq 0.8$ |
| $p_T^{\mu} \geq 4.0$ GeV/c |
| $\varphi^{\mu} \leq 80^{\circ}$ or $\varphi^{\mu} \geq 110^{\circ}$ |

Table 8-1: Selection cuts used to obtain the cosmic ray muon $t_0^f$ distribution.

by eye-scanning. Cosmic ray muons are easily identified by hits in the central detector and calorimeter which do not project to the event vertex in the bend and non-bend views. Both of these distributions are also shown in Fig. 8-2. Again, there is very good agreement between these two samples.

The $t_0^f$ distribution for cosmic ray muons turns out not to be flat for the following reasons. First, hits in the muon chambers are only recorded if the ionizing charge in the cells drifts to the wire inside an approximate 800 ns gate which is used to record events in coincidence with the beam crossings. In addition, the closer in time to the beam crossing that a cosmic ray muon traverses the detector, the more likely it is that its ionization drifts to the wire within the gate, so that "in-time" cosmic ray muons tend to have more hits. These tracks thus have a higher probability of triggering the detector and reconstructing. Finally, the pad latch circuits which flag a cell as being hit have a fairly slow rise time ($\approx$50 ns). This feature gives a survival advantage to those cosmic ray muons which arrive early with respect to the beam crossing. This accounts for the positive offset in the $t_0^f$ distribution for cosmic ray muons[76]. Figure 8-3 shows the unnormalized input fit distributions for the beam-produced muon sample and the cosmic ray

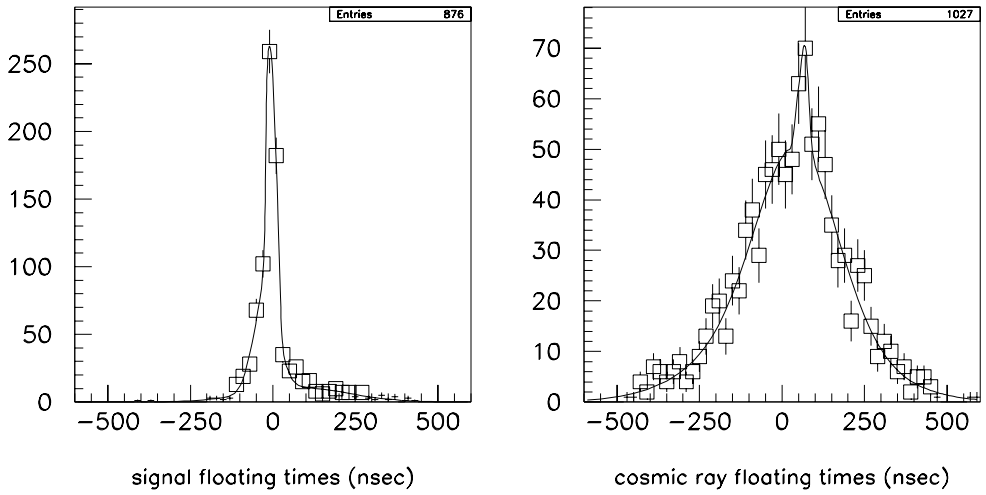


Figure 8-3: Fits to the floating time distributions for beam-produced muons and cosmic rays.

muon sample.

### 8.2.2 $p_T^{rel}$

The transverse momentum of the muon with respect to the associated jet, $p_T^{rel}$, is defined as

$$p_T^{rel} = |\vec{p}_\mu| \sin \theta^{rel}, \tag{8.6}$$

where $\theta^{rel}$ is the angle between the muon momentum vector and the momentum vector of the jet of which the muon is a part. Figure 8-4 shows a schematic representation of the variable $p_T^{rel}$.

This variable is useful in distinguishing between $b$-quark decays, $c$-quark decays, and other backgrounds. The value of $p_T^{rel}$ depends on the mass of the de-

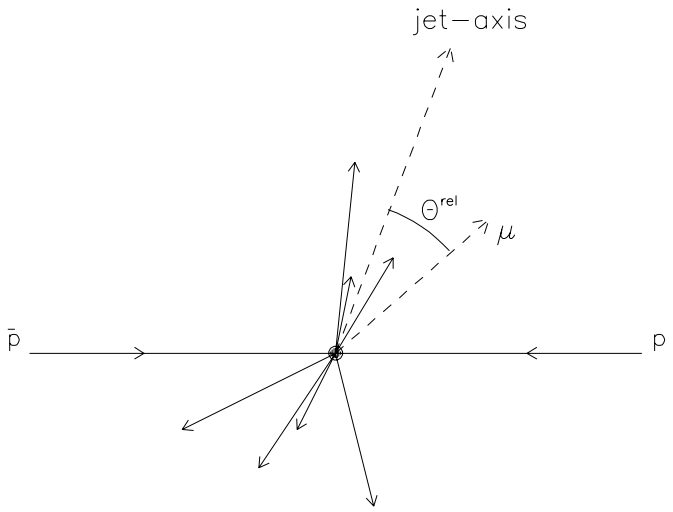


Figure 8-4: Schematic representation of how the variable $p_T^{rel}$ is defined.

caying particle which produces the muon. It is this mass which gives the decay products extra kicks of momentum which may have a component perpendicular to the original parent particle, and thus perpendicular to the jet direction.

The value of $p_T^{rel}$ will also depend on how the jet is defined. In the standard jet definition used at DØ the muon is not included in the definition of the jet energy or the jet-axis. To better reproduce the originating quarks direction and energy, we have included the muon in the jet definition when calculating $p_T^{rel}$. Because of this, an additional correction has to be made because the muon minimum ionizing energy has already been measured in the calorimeter, so this energy must be subtracted. This leads to the new jet definition

$$\vec{p}'_{jet} = \vec{p}_{jet} + \vec{p}_{\mu} - \vec{p}_{\mu}^{expected}$$

and

$$E'_{jet} = E_{jet} + E_{\mu} - E_{\mu}^{expected},$$

where $E_{\mu}^{expected}$ is the energy loss of the muon expected in the calorimeter. The value of $p_T^{rel}$ is calculated for both the leading and trailing muon in the event.

The full Monte Carlo simulation is used in determining the shapes of the $p_T^{rel}$ distributions. All cuts that are applied to the data sample are also applied to the Monte Carlo with the exception of the trigger requirement. Here, we require that the events pass *any* one of the three triggers used: MU_2_HIGH, MU_1_JET, or MU_JET_LOW. It is found that the different trigger conditions have little effect on the shape of the $p_T^{rel}$ distributions. Separate distributions are found for $b\overline{b}$ production, $c\overline{c}$ production, and for a prompt muon from a $b$-quark decay plus a muon from a $\pi/K$ decay. The distributions for a prompt muon from a $c$-quark decay plus a $\pi/K$ decay are found to be very similar to those from $c\overline{c}$ production

as discussed in Chapter 6. Thus, the contribution from a prompt muon from a $c$-quark decay plus a $\pi/K$ decay are included in the $c\overline{c}$ production contribution. Figures 8-5 to 8-7 show the $p_T^{rel}$ distributions for each of the physics processes.

The cosmic ray muon $p_T^{rel}$ distributions are obtained from the data. Once again, the same data cuts are applied as above except that the three-dimensional opening angle cut is changed to

$$\Delta\phi_{3D} > 140^\circ,$$

and the MIP deposition cut is only applied to the muon in the event that is not being fit. This is done so that the sample is heavily contaminated with cosmic ray muons and so the general event characteristics still resemble those of the final data set. An event-by-event log-likelihood fit, as described in Sec. 8.1, is performed on this sample using only the $t_0^f$ distribution as the input. Figure 8-8 shows the $t_0^f$ fit to this sample and Table 8-2 lists the relative amounts of beam-produced and cosmic ray muons determined from the fit. The errors listed are from the fit only.

| *Muon Type* | *# of Events* | *% Cosmic Ray Muons* | *% Beam Muons* |
|---|---|---|---|
| Leading Muon | 1137 | 82.1±2.3 | 17.9±2.3 |
| Trailing Muon | 1101 | 68.6±2.5 | 31.4±2.5 |

Table 8-2: Floating $t_0$ fit to the cosmic ray muon sample.

From this fit we extract the $p_T^{rel}$ distribution for the leading and trailing muons using the method outlined in Sec. 8.5. The results are shown in Fig. 8-9. Notice how broad the $p_T^{rel}$ distributions are for cosmic ray muons as compared to the beam-produced muons.

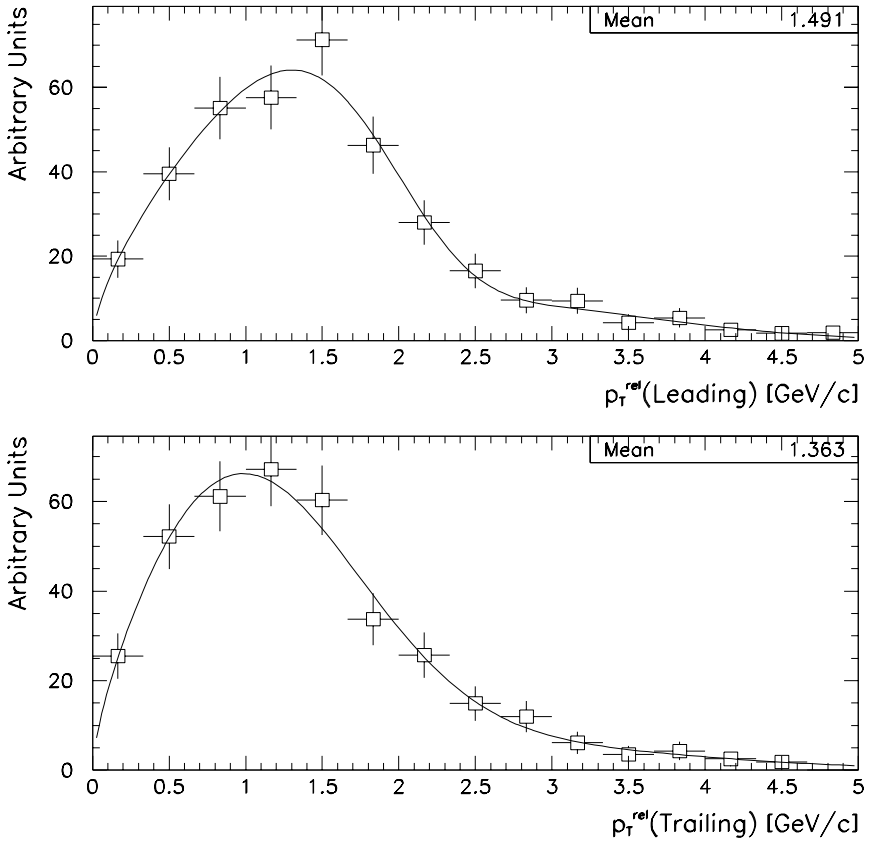


Figure 8-5: Fit to the $p_T^{rel}$ distribution for the (top) leading and (bottom) trailing muon from $b\overline{b}$ production.

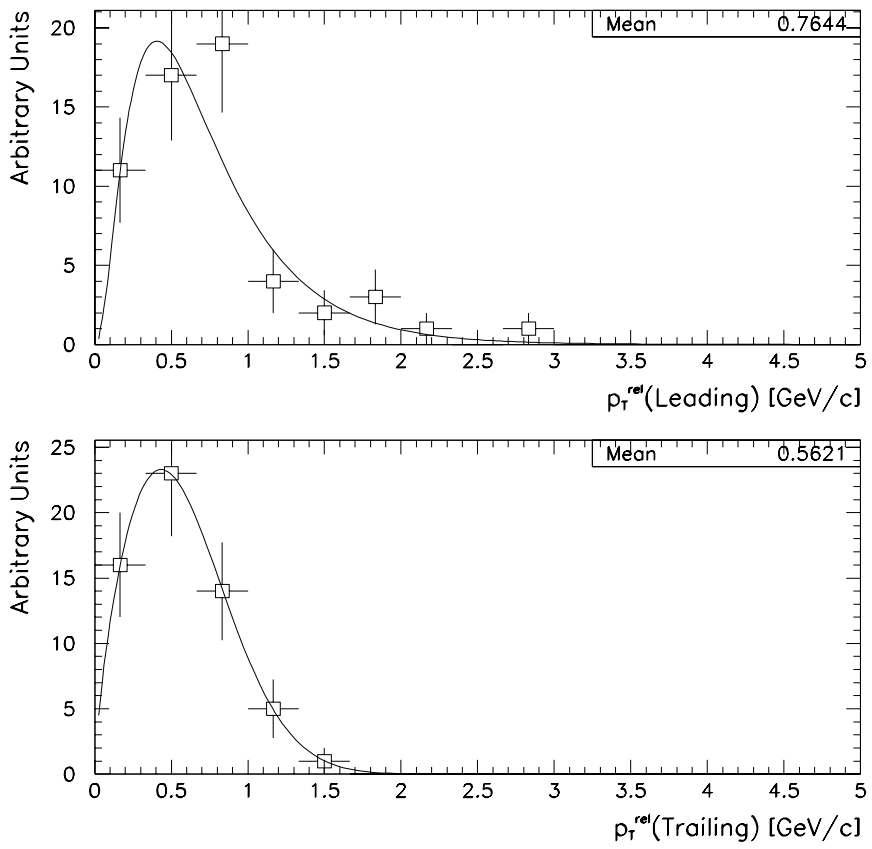


Figure 8-6: Fit to the $p_T^{rel}$ distribution for the (top) leading and (bottom) trailing muon from $c\bar{c}$ production.

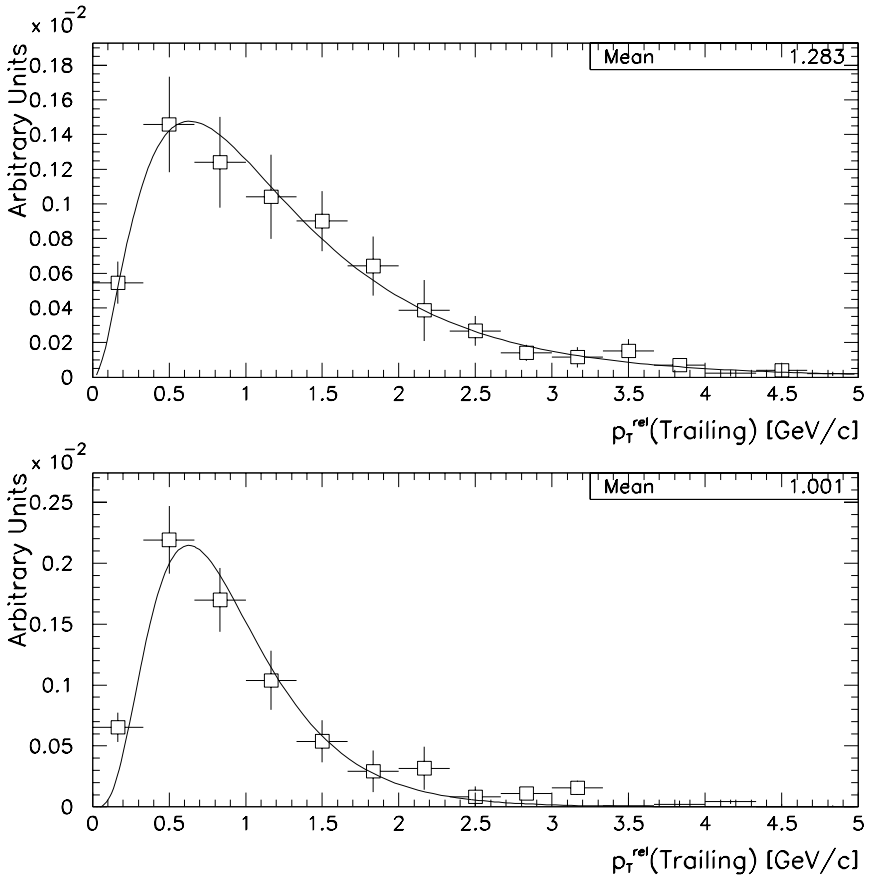


Figure 8-7: Fit to the $p_T^{rel}$ distribution for the (top) leading and (bottom) trailing muon from a prompt muon from a $b$-decay plus a muon from a $\pi/K$ decay.

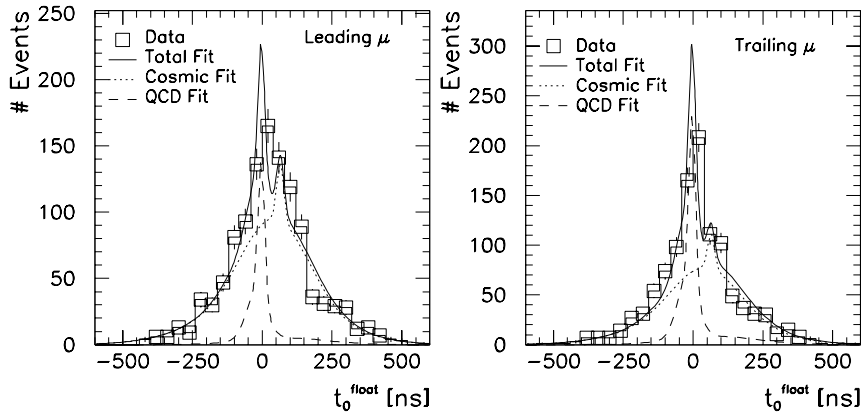


Figure 8-8: Floating $t_0$ distributions for the cosmic ray muon sample: (left) leading muon, (right) trailing muon.

### 8.2.3 $z'$

Another variable helpful in distinguishing between $b\bar{b}$ production and the other contributing physics processes is $z'$, defined as

$$z' \equiv \frac{z}{E_T^{jet}} = \frac{|\vec{p}_\mu| \cos\theta^{rel}}{|\vec{p}_{jet}|} \frac{1}{E_T^{jet}}, \tag{8.7}$$

where $\theta^{rel}$ is the angle between the muon momentum vector and the momentum vector of the associated jet (again corrected for the muon momentum and expected energy loss), and $\vec{p}_\mu$ is the momentum vector of the leading muon in the event. The fraction of the jet momentum in the longitudinal direction carried by the muon, $z$, is directly related to the fragmentation functions, shown in Fig. 3-6. These differences are accentuated by dividing $z$ by the transverse momentum of the jet, since muons with the same value of $z$, but originating from different types of jets, are likely to have different values of $E_T^{jet}$ depending on whether or not there is a

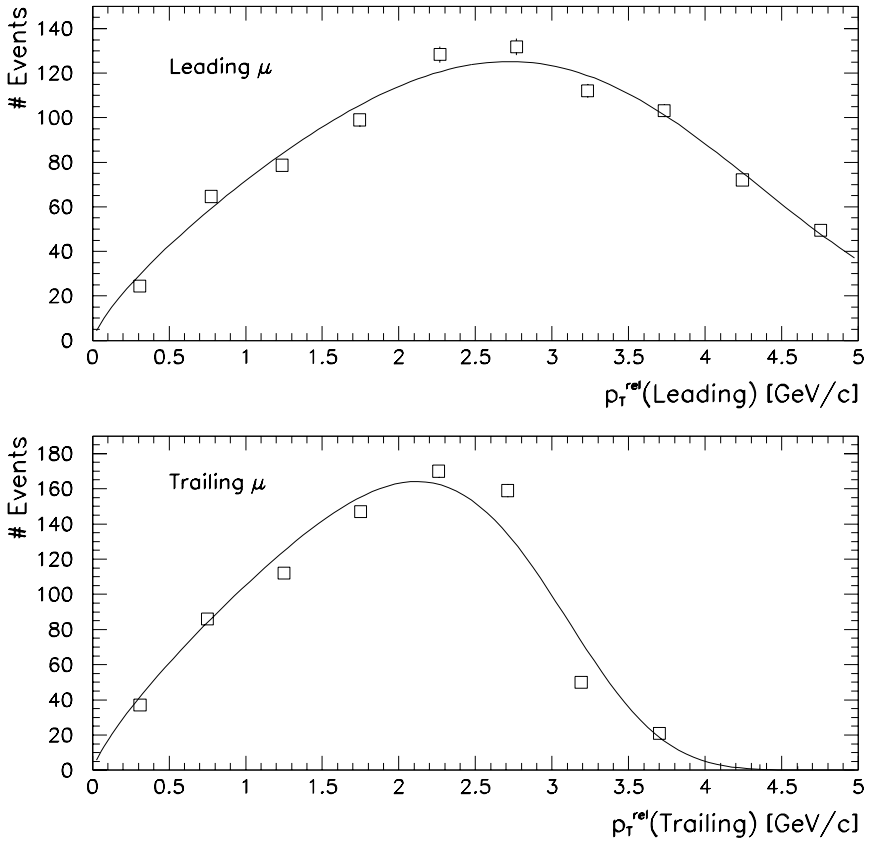


Figure 8-9: Fit to the $p_T^{rel}$ distribution for the (top) leading and (bottom) trailing muon from cosmic ray muons.

heavy quark in the jet. The width of the $b\overline{b}$ $z'$ distribution, along with its longer tail, is what helps distinguish this distribution from the others. Only the leading muon $z'$ is used in the fit.

The same method is used in determining the shapes of the $z'$ distributions for the physics processes as is used in determining the $p_T^{rel}$ distributions, described in the previous section. Figure 8-10 shows the $z'$ distributions for $b\overline{b}$ production, $c\overline{c}$ production, and for events with a muon from a $b$-decay plus a muon from a $\pi/K$ decay.

The cosmic ray muon $z'$ distribution is obtained from the data. In addition to the standard cuts described in Chapter 5, the following cuts are employed to ensure the sample contains a large fraction of cosmic ray muons:

- Trigger on MU_2_HIGH , MU_1_JET , *or* MU_JET_LOW
- Associated jet with the leading muon only
- $\Delta\phi_{3D} > 140^\circ$
- $\sum_{1NN} E_{Cal} \leq 1.0$ GeV/c$^2$ on one muon.

These cuts are very similar to the ones employed to determine the $p_T^{rel}$ distributions for cosmic ray muons. In this case, we need to require an associated jet with the leading muon in the event, so the sample size is reduced. Applying these cuts yields 564 events. An event-by-event log-likelihood fit is performed on this sample using only the $t_0^f$ distribution as input to determine the fraction of cosmic ray muons. From the fit, we find that 91.3$\pm$14.6% of the events are from cosmic ray muons. The $z'$ distribution is then extracted from this fit in the same manner as the $p_T^{rel}$ distributions were derived and is shown in Fig. 8-11.

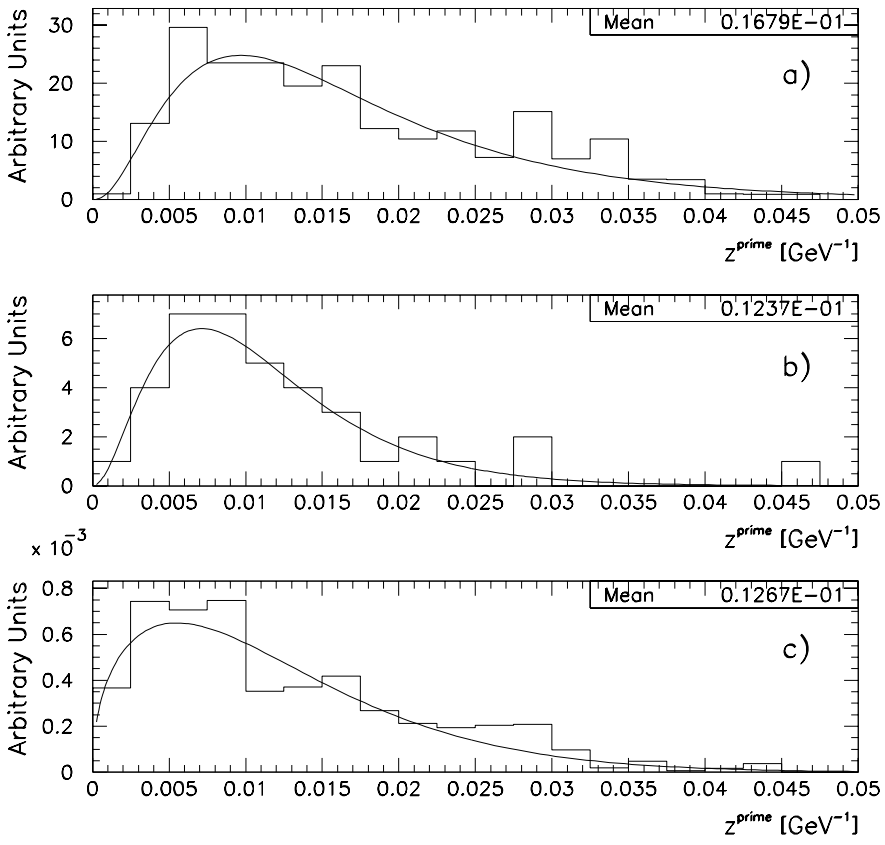


Figure 8-10: Fit to the $z'$ distributions for a) $b\bar{b}$ production, b) $c\bar{c}$ production, and c) prompt muon from a $b$-decay plus a muon from a $\pi/K$ decay.

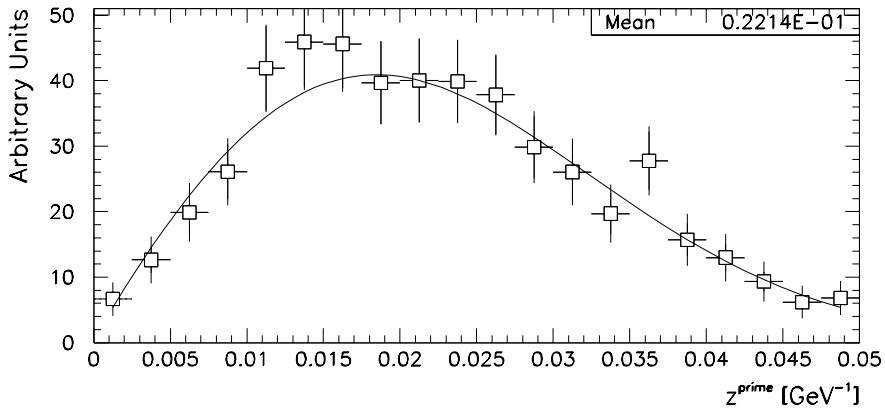


Figure 8-11: Fit to the $z'$ distribution for the cosmic ray muon sample.

## 8.3 Results of the Fit

### 8.3.1 Fit to the Monte Carlo

To establish the effectiveness of the maximum likelihood fit in determining the correct fraction of events originating from each physics process, the fit is first performed on a sample of Monte Carlo events. The Monte Carlo sample chosen included events from $b\overline{b}$ production, $c\overline{c}$ production, and events where one muon originates from a semileptonic decay of a $b$-quark, and the other muon is from a $\pi/K$ decay.

Slight modifications are made to the input $p_T^{rel}$ and $z'$ distributions for these events. Because we want these input distributions to correctly model the sample being fit, no correction is made to the branching ratio used for $b$-quark decays in ISAJET. This correction, as discussed in Chapter 3, is made for the input distribu-

tions representing the data sample. In addition, the $t_0^f$ distribution is not used in this fit because the $t_0^f$ parameter is meaningless for Monte Carlo events. Table 8-3 summarizes the results of the simultaneous fit to the Monte Carlo sample. The errors shown are from the fit only. Note that the fit is very effective in determining the correct fraction of input processes for this particular mixture of events. Figures 8-12 to 8-14 show the results of this fit for the $p_T^{rel}$ and $z'$ distributions. The Monte Carlo event sample is chosen in such a way as to represent the data samples as closely as possible. The Monte Carlo events are selected from samples of $b\overline{b}$, $c\overline{c}$, and $b \rightarrow \mu + \pi/K$ decay events so that the relative amount of each process approximates that found in the data samples. A total of 400 Monte Carlo events are utilized in this sample.

| | $\% \; b\overline{b}$ | $\% \; b \rightarrow \mu + \pi/K \; Decay$ | $\% \; c\overline{c}$ |
|---|---|---|---|
| Sample A<br>Input Monte Carlo<br>Results of Fit | 61.3<br>$62.3^{+7.2}_{-7.5}$ | 29.2<br>$23.1^{+4.7}_{-5.9}$ | 9.5<br>$14.6^{+5.9}_{-4.7}$ |
| Sample B<br>Input Monte Carlo<br>Results of Fit | 45.7<br>$45.1^{+7.3}_{-7.3}$ | 45.7<br>$43.9^{+4.7}_{-4.1}$ | 8.6<br>$11.0^{+4.1}_{-4.7}$ |

Table 8-3: Summary of simultaneous fit results to the Monte Carlo samples. Each sample contains different fractions of the contributing processes to the dimuon Monte Carlo sample. The fit performs well in both cases.

As a cross check to this fit, a different sample of Monte Carlo events is chosen so that the relative fractions of each contributing process are different from the

| *Trigger Name* | *% $b\bar{b}$* | *% $b \to \mu + \pi/K$ Decay* | *% $c\bar{c}$* | *% Cosmic Rays* |
|---|---|---|---|---|
| MU_2_HIGH | $68.0^{+8.6}_{-9.0}$ | $22.1^{+7.9}_{-8.4}$ | $6.5^{+5.0}_{-4.6}$ | $3.4^{+3.4}_{-3.2}$ |
| MU_1_JET | $55.4^{+7.1}_{-7.2}$ | $26.2^{+6.4}_{-6.9}$ | $13.4^{+4.9}_{-4.6}$ | $5.0^{+2.7}_{-2.4}$ |
| MU_JET_LOW | $45.3^{+5.8}_{-5.8}$ | $37.9^{+5.5}_{-5.7}$ | $14.0^{+3.9}_{-3.7}$ | $2.8^{+1.7}_{-1.5}$ |

Table 8-4: Summary of simultaneous fit to each of the trigger samples.

sample above. A total of 438 Monte Carlo events are in this sample. Since the shapes of the input distributions to the fit are different in this sample, a good fit to this Monte Carlo sample of events should give us confidence that the fit is performing well. The results of this fit are also shown in Table 8-3 and show again that the Monte Carlo samples are fit very well.

The log-likelihood function is plotted near the minimum for the two independent variables, $\alpha_1$ and $\alpha_2$, in Fig. 8-15. These plots are determined by varying the parameters, $\alpha_i$, one at a time, while fixing the other variable at its minimum. These plots show that a clear minimum is found for each independent variable.

### 8.3.2 Fit to the Data

The results of the simultaneous fit to each of the three triggers are summarized in Table 8-4. The errors are from the fit only. Table 8-5 lists the total number of data events for each trigger. Figures 8-16 to 8-17 show the fit to the $t_0^f$ , $z'$, and

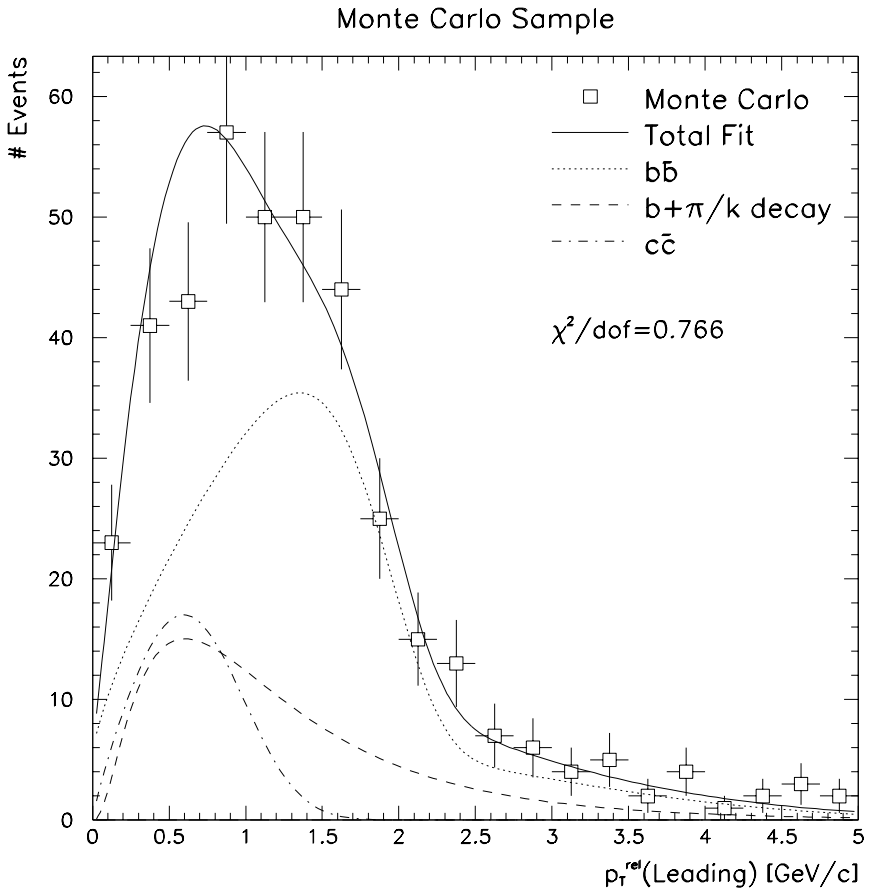


Figure 8-12: Result of simultaneous fit to $p_T^{rel}$(leading) for the Monte Carlo sample.

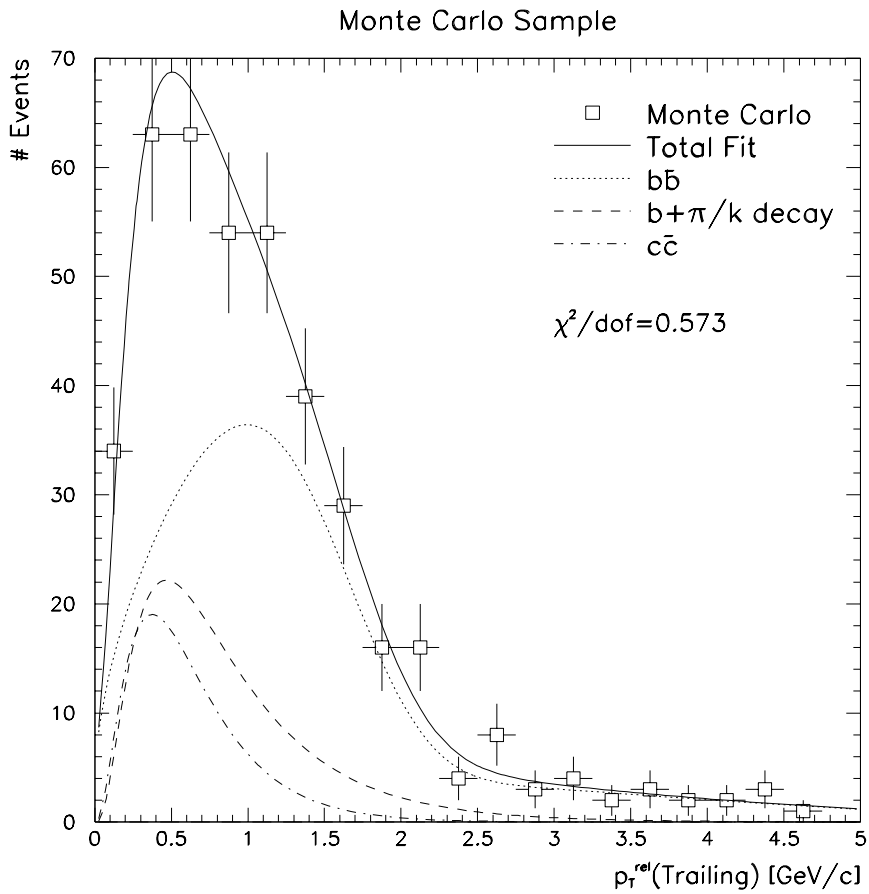


Figure 8-13: Result of simultaneous fit to $p_T^{rel}$(trailing) for the Monte Carlo sample.

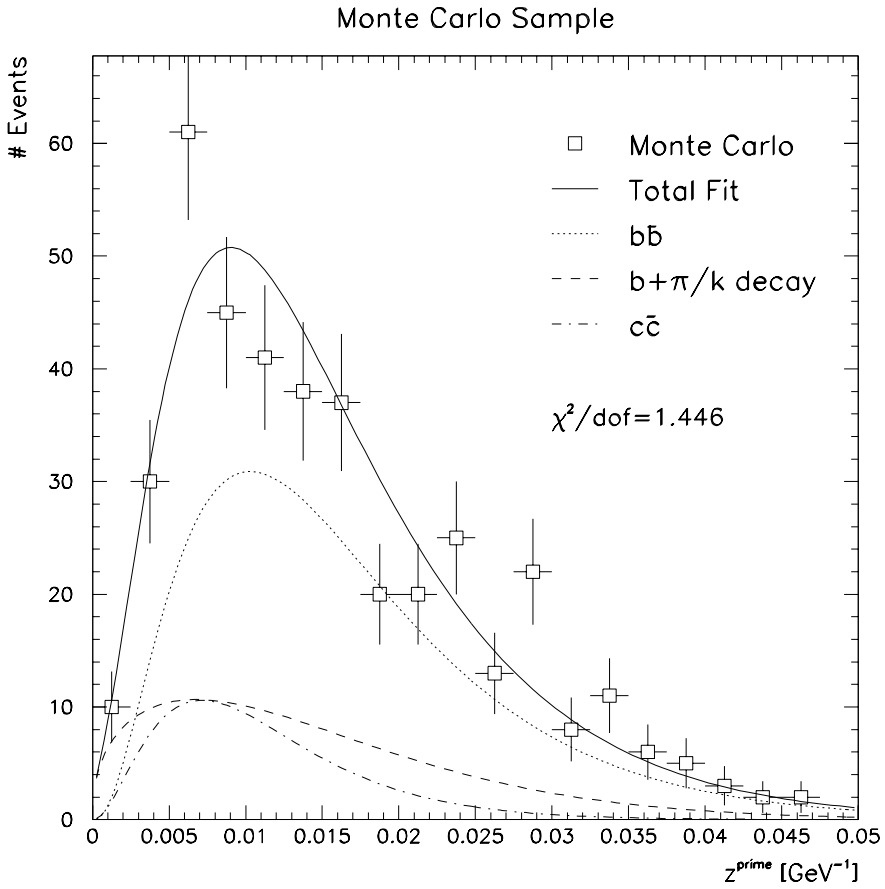


Figure 8-14: Result of simultaneous fit to $z'$ for the Monte Carlo sample.

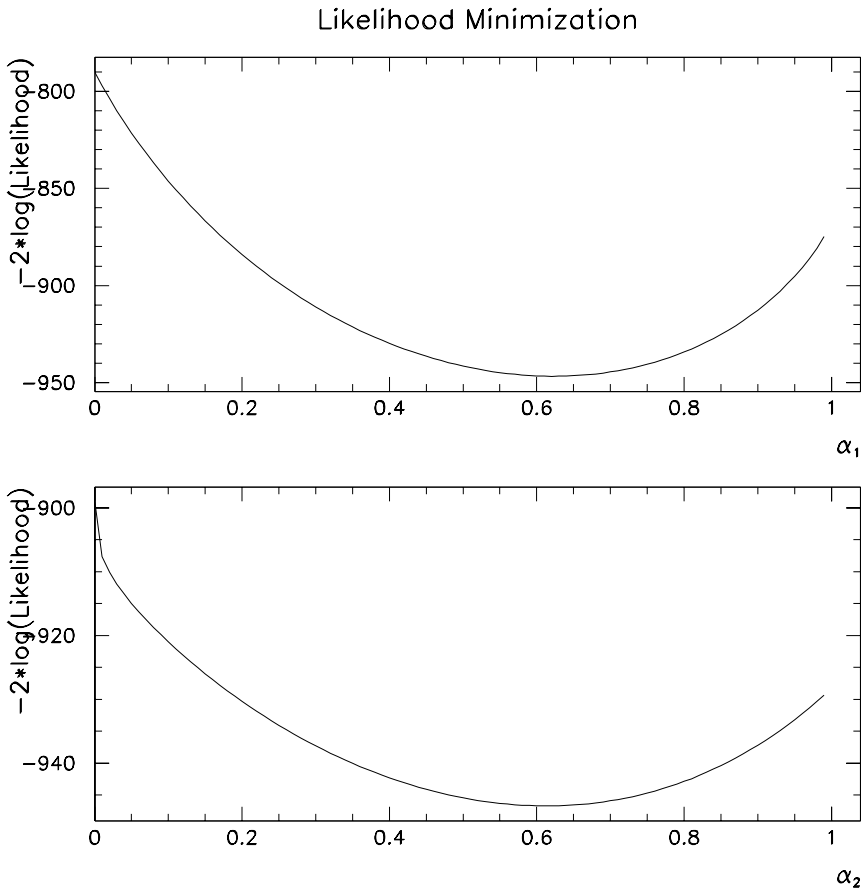


Figure 8-15: Plots of the log-likelihood function centered around the minimum for the two variables to the fit to the Monte Carlo sample. Note that the functions are well behaved.

| *Trigger Name* | *# of Events* |
|---|---|
| MU_2_HIGH | 192 |
| MU_1_JET | 277 |
| MU_JET_LOW | 397 |

Table 8-5: Number of data events for each trigger.

$p_T^{rel}$ distributions for the MU_2_HIGH trigger, Figs. 8-19 to 8-20 for MU_1_JET, and Figs. 8-22 to 8-23 for MU_JET_LOW. The log-likelihood function is plotted near the minimum for each of the independent variables, $\alpha_i$, in Figs. 8-18, 8-21, and 8-24. Once again, it is clear that correct minimum for the functions are found.

## 8.4 Systematic Uncertainties in the Maximum Likelihood Fit

As discussed in Sec. 8.1, the uncertainties in the maximum likelihood fit are determined using the MINOS error analysis package supplied in MINUIT. The uncertainties reflect the width of the minimum of the log-likelihood function in each $\alpha_i$. The errors listed in Table 8-4 include these uncertainties.

In addition, there are systematic uncertainties due to differences in the shapes of the distributions used as input to the fit. These uncertainties are not represented in

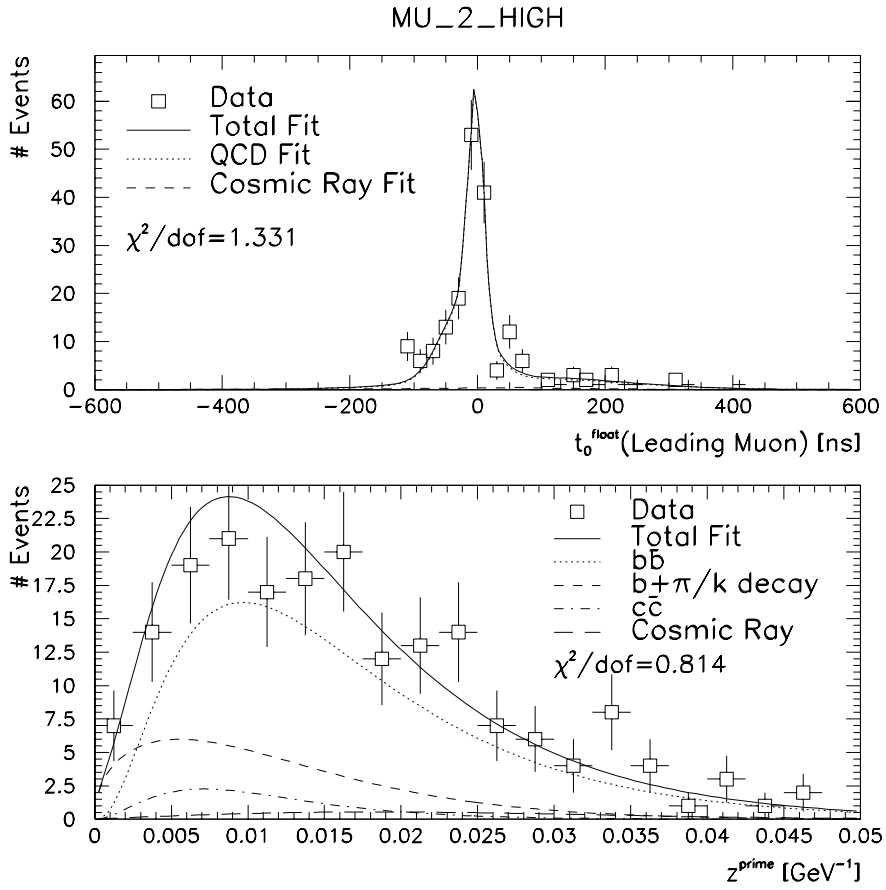


Figure 8-16: Result of simultaneous fit to: (upper) $t_0^f$ and (lower) $z'$ for the MU_2-_HIGH trigger.

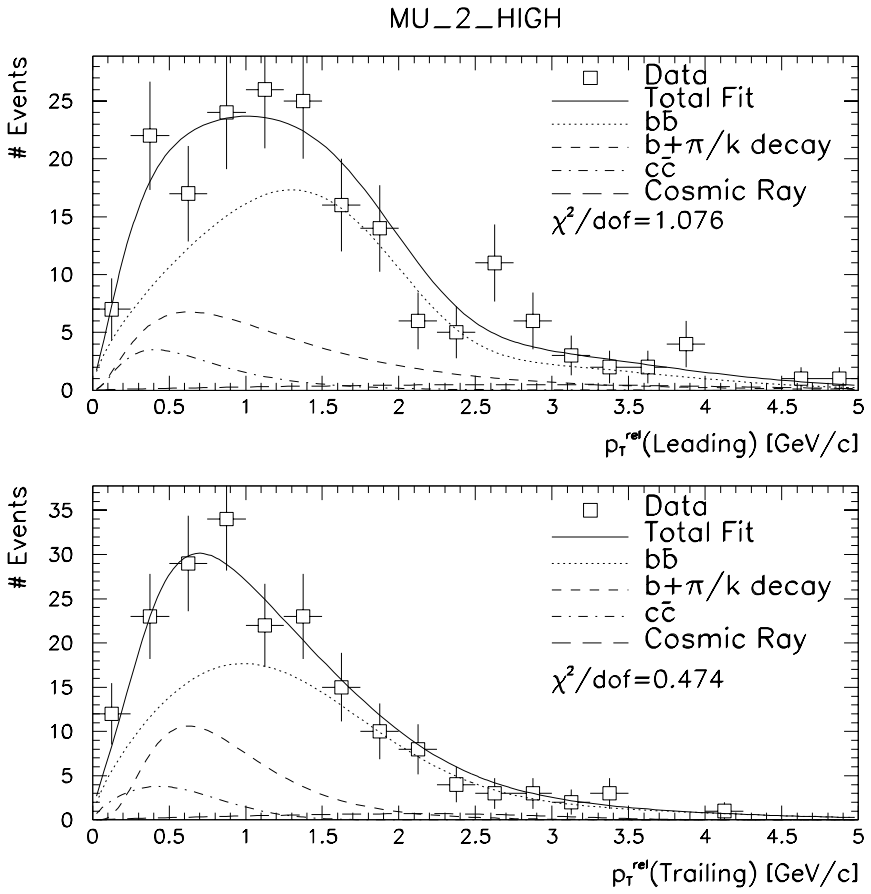


Figure 8-17: Result of simultaneous fit to: (upper) $p_T^{rel}$(leading) and (lower) $p_T^{rel}$-(trailing) for the MU_2_HIGH trigger.

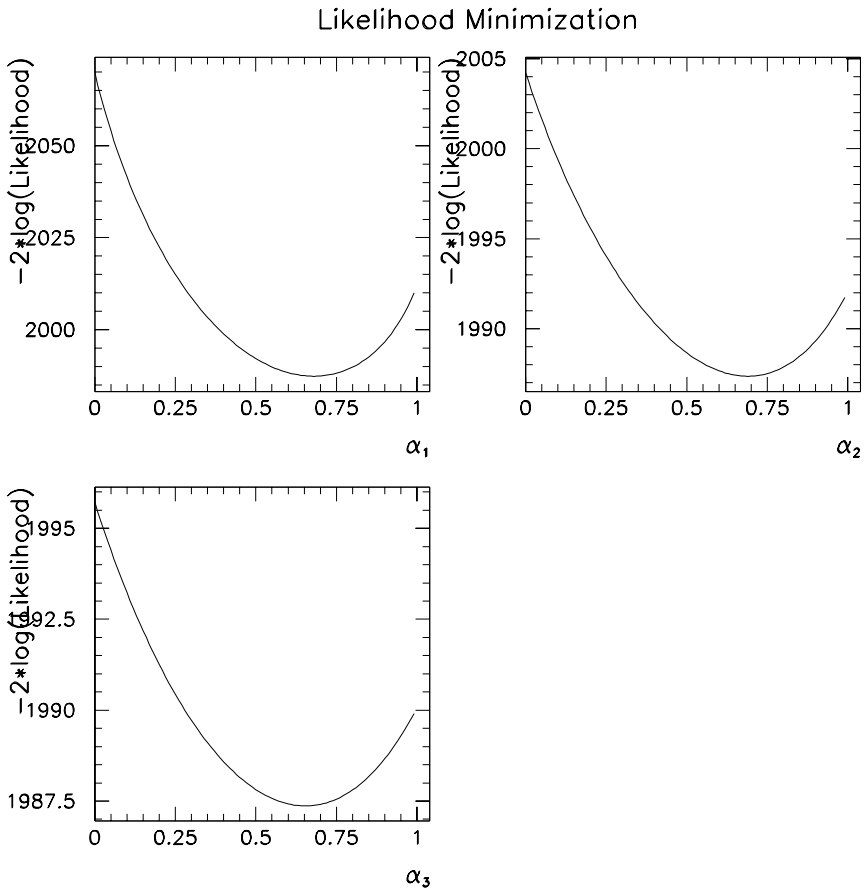


Figure 8-18: Plots of the log-likelihood function centered around the minimum for the variables in the fit to the MU_2_HIGH sample. Note that the functions are well behaved.

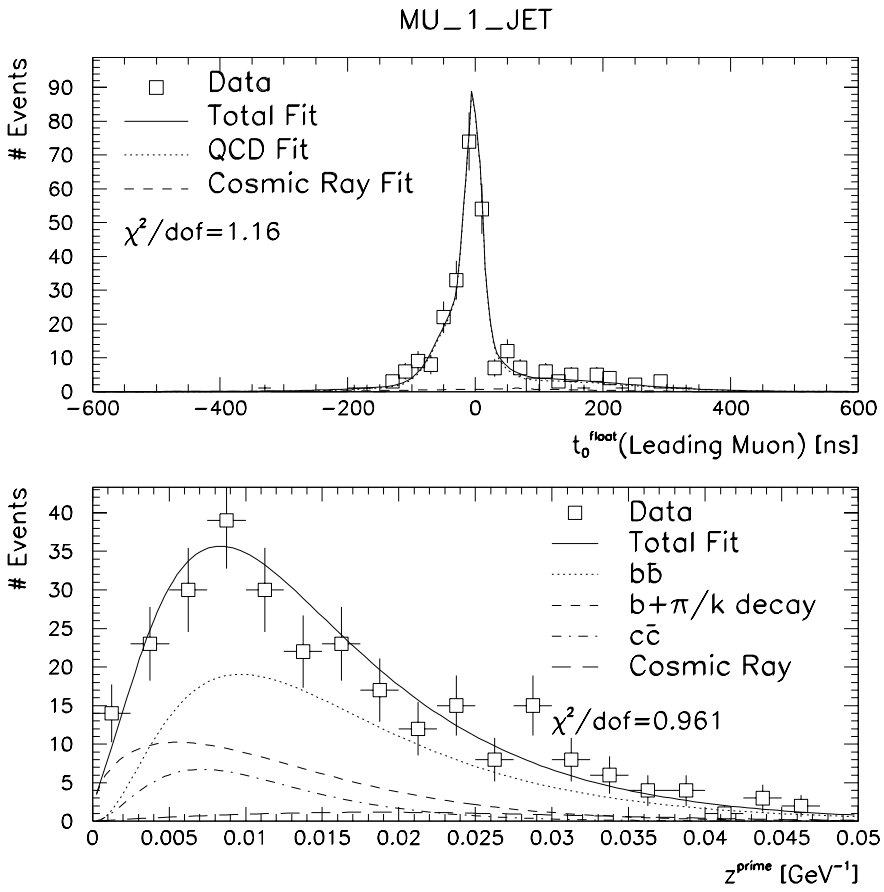


Figure 8-19: Result of simultaneous fit to: (upper) $t_0^f$ and (lower) $z'$ for the MU_1-_JET trigger.

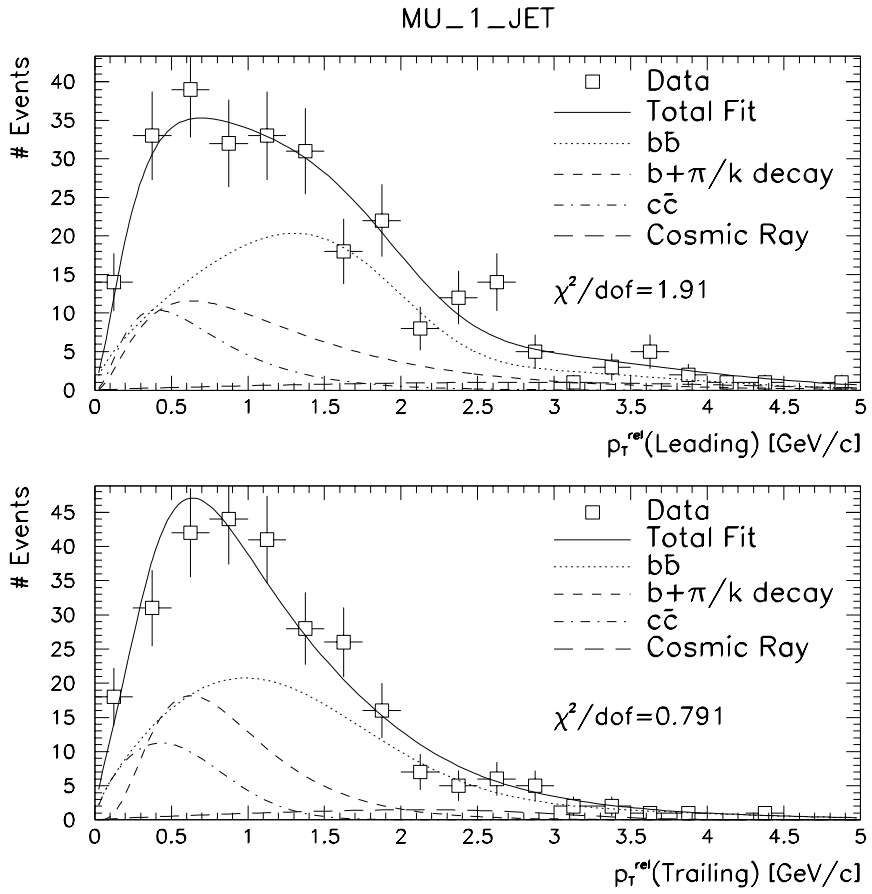


Figure 8-20: Result of simultaneous fit to: (upper) $p_T^{rel}$(leading) and (lower) $p_T^{rel}$-(trailing) for the MU_1_JET trigger.

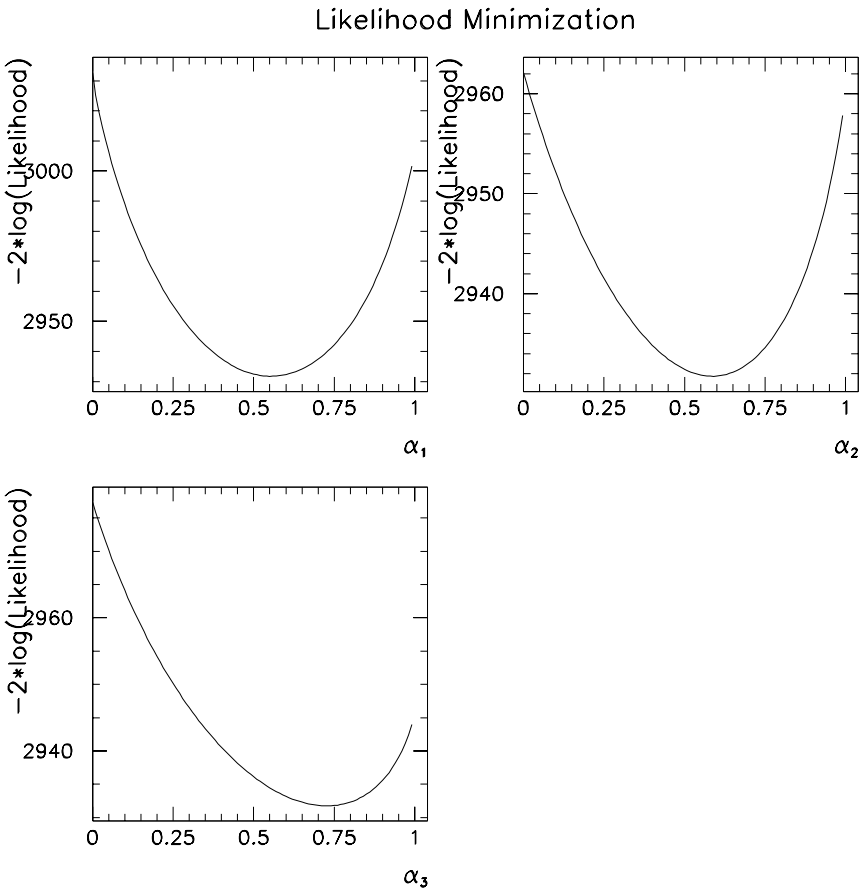


Figure 8-21: Plots of the log-likelihood function centered around the minimum for the variables in the fit to the MU_1_JET sample. Note that the functions are well behaved.

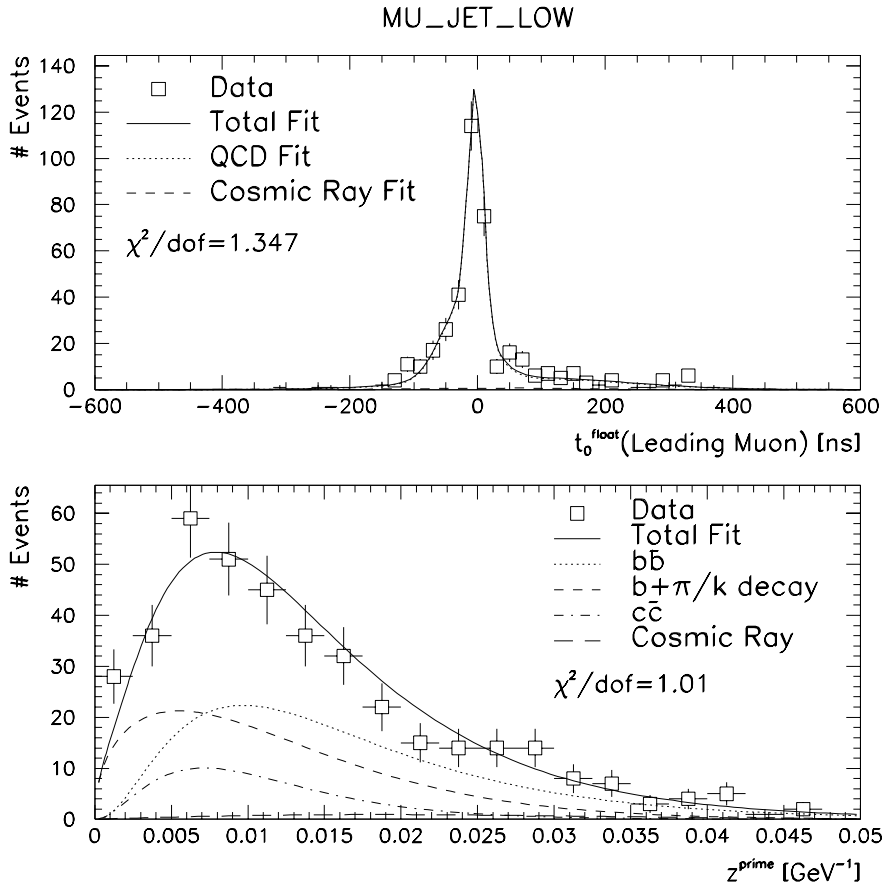


Figure 8-22: Result of simultaneous fit to: (upper) $t_0^f$ and (lower) $z'$ for the MU_JET_LOW trigger.

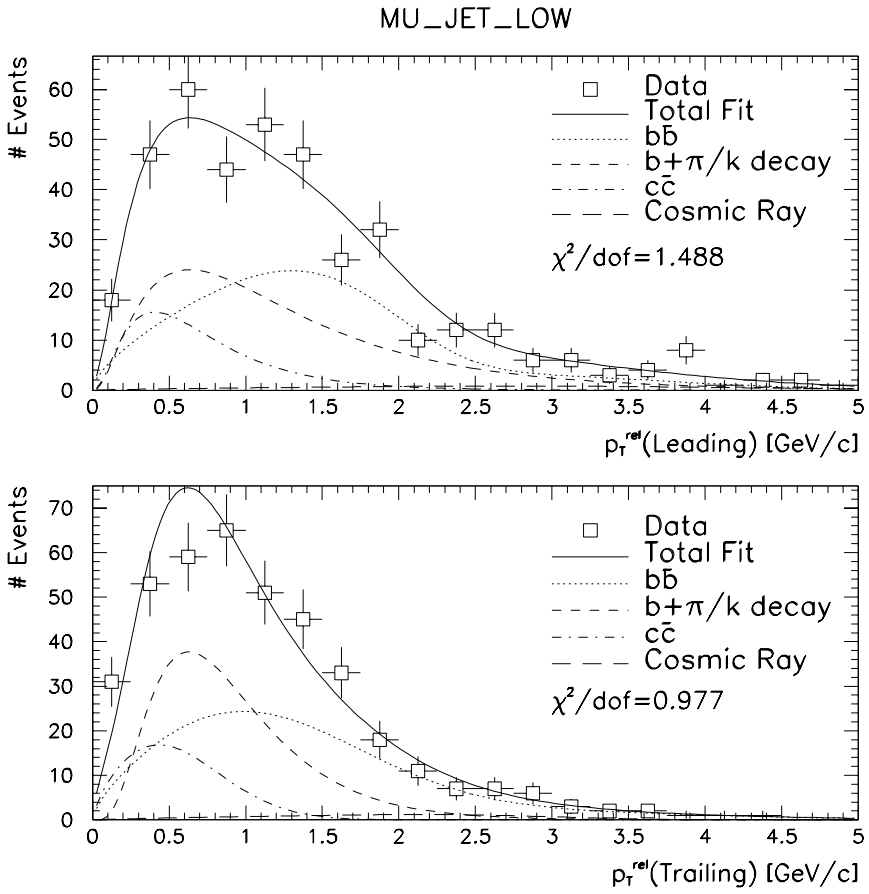


Figure 8-23: Result of simultaneous fit to: (upper) $p_T^{rel}$(leading) and (lower) $p_T^{rel}$-(trailing) for the MU_JET_LOW trigger.

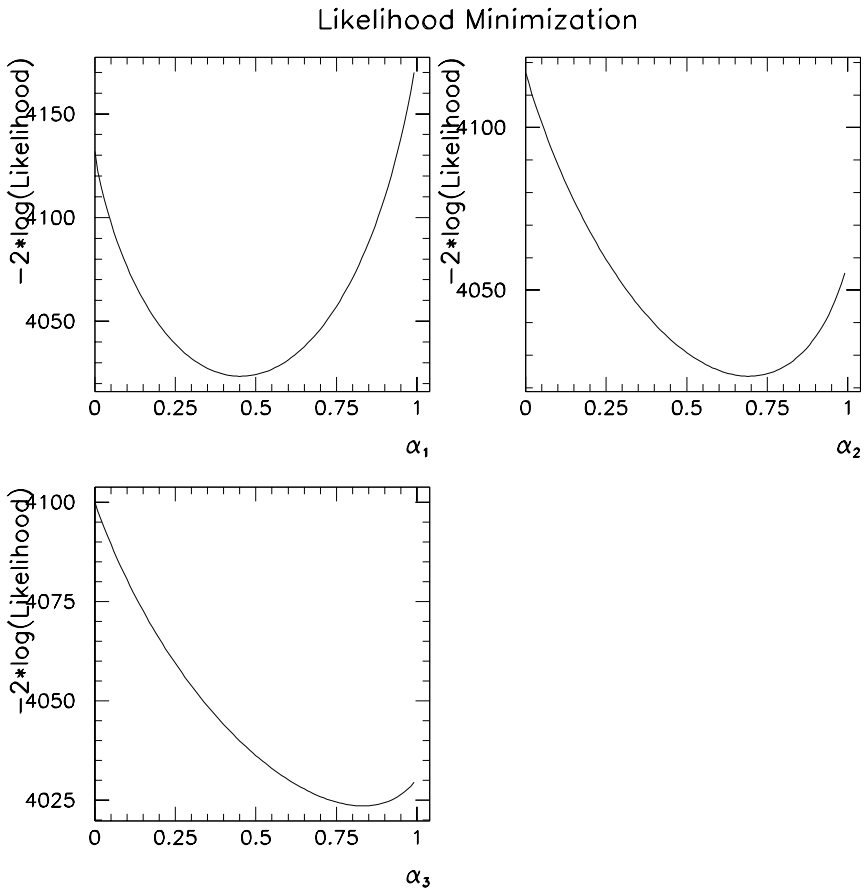


Figure 8-24: Plots of the log-likelihood function centered around the minimum for the variables in the fit to the MU_JET_LOW sample. Note that the functions are well behaved.

Table 8-4. An estimate of these uncertainties is obtained by selecting distributions from other reasonable sources and by systematically varying the parameters used to define the input distributions. Then, by comparing how the fit number of $b\overline{b}$ events changes with each of the new distributions, an error can be assigned to the input distribution shape.

The uncertainties associated with the cosmic ray muon floating time distribution are estimated using the scanned cosmic ray events and the sample collected during the special cosmic ray runs. These samples are discussed in Sec. 8.2.1. Similarly, the $J/\psi$ and high mass dimuon samples discussed in that section are used to estimate the uncertainty due to the beam produced floating time distribution.

The uncertainties due to the choice of the $p_T^{rel}$ distributions are determined by using a set of independently fit distributions. This new set of fits utilizes the same ISAJET Monte Carlo events but applies different selection criteria[77]. The differences found with these new input distributions is taken to be the $1\sigma$ systematic error. In addition, the uncertainties associated with the $b\overline{b}$ $p_T^{rel}$ distributions are cross checked with the results obtained using distributions determined from the Monte Carlo but with the gluon splitting contribution to the $b\overline{b}$ cross section reduced by a factor of two. Similar uncertainties are found when fitting the data samples with these new distributions. A further check is performed by fitting the $b\overline{b}$ $p_T^{rel}$ distributions with all of the gluon splitting contribution removed. Again, similar errors in the data distributions are found with these new fits. This correction is a better estimate of the reduced fraction of gluon splitting found in the final data sample in Sec. 9.3.4.

To determine the uncertainties associated with the $z'$ distributions, the original fit parameters are allowed to vary within 2.5% of their mean value to produce new fits to the $z'$ distributions. The differences in the fit number of $b\overline{b}$ events using

these new input distributions is taken to be the $3\sigma$ systematic uncertainty. As with the $b\bar{b}$ $p_T^{rel}$ distributions, the $b\bar{b}$ $z'$ distributions are also cross checked with a sample of Monte Carlo events with the gluon splitting contribution reduced by a factor of two. Once again, the uncertainties in the fit number of $b\bar{b}$ events in the data remain unchanged.

Variations in the cosmic ray muon $p_T^{rel}$ and $z'$ distributions have little effect on the number of $b\bar{b}$ events found in the fit. This is a reasonable expectation since the contribution from cosmic ray muons to the final data set is small. Thus, any changes in cosmic ray muon distributions should have little effect. A 1% uncertainty is assigned to each of these errors.

The results of these studies are summarized in Table 8-6.

## 8.5 Determination of the Differential Distributions

The dimuon differential cross sections, $d\sigma/dp_T$ and $d\sigma/d\Delta\phi^{\mu\mu}$, for both inclusive dimuon production and dimuons from $b$-quarks, are extracted using an event-by-event fit from the log-likelihood fits of Sec. 8.3. The number of events in each bin for process $j$ is determined by summing over all events, $N_i$, in the sample weighted by the probability that the event originated from the physics process $j$. Therefore, the total number of events coming from process $j$ is

$$N_j = \sum_{i=1}^{N_i} w_{ij},$$

| | | $\sigma_{N_{b\bar{b}}}/N_{b\bar{b}}$ | | |
|---|---|---|---|---|
| Distribution | Source | MU_2_HIGH | MU_1_JET | MU_JET_LOW |
| $t_0^f$ | Beam | 1% | 1% | 1% |
| | Cosmic Ray | 1% | 1% | 1% |
| $p_T^{rel}$ | $b\bar{b}$ | 1% | 1% | 1% |
| | $b$ plus $\pi/K$ Decay | 1% | 3% | 6% |
| | $c\bar{c}$ | 2% | 3% | 3% |
| | Cosmic Ray | 1% | 1% | 1% |
| $z'$ | $b\bar{b}$ | 1% | 3% | 4% |
| | $b$ plus $\pi/K$ Decay | 3% | 2% | 2% |
| | $c\bar{c}$ | 1% | 1% | 1% |
| | Cosmic Ray | 1% | 1% | 1% |
| Total Fit Input Uncertainty | | 5% | 6% | 8% |

Table 8-6: Systematic uncertainties in the number of $b\bar{b}$ events found in the fit due to variations in the input distributions.

where $w_{ij}$ is the probability that event $i$ comes from physics process $j$. The probabilities are defined as

$$w_{ij} = \frac{A_j \cdot \prod_{k=1}^{N_k} p_k^j(x_k^i)}{\sum_{j=1}^{N_j} \left[ A_j \cdot \prod_{k=1}^{N_k} p_k^j(x_k^i) \right]}. \tag{8.8}$$

As in (8.2), the functions $p_k^j(x_k)$ are the normalized probability density functions for the four variables $x_k$, and the coefficient $A_j$ in (8.8) is the total fraction of events in the sample from contribution $j$. These coefficients are determined using the maximum likelihood fit described in Sec. 8.3 and are listed in Table 8-4.

In Section 8.4, the systematic uncertainties in the maximum likelihood fit due to variations in the input distributions were calculated. For the differential distributions, $d\sigma/dp_T$ and $d\sigma/d\Delta\phi^{\mu\mu}$, it is necessary to convert the uncertainties in the total number of events into uncertainties in the number in each bin $i$, $\sigma_{N_i}/N_i$. The fractional uncertainty in the total number of events is related to the fractional uncertainty in the number in each bin by

$$\frac{\sigma_{N_{Tot}}}{N_{Tot}} = \frac{1}{N_{Tot}} \left[ \sum_{i=1}^{n} \left( \frac{\sigma_{N_i}}{N_i} \right)^2 N_i^2 \right]^{\frac{1}{2}} \tag{8.9}$$

where $n$ is the number of bins in the distribution and $N_i$ is the number of events in each bin $i$. Assuming the fractional uncertainty in each bin is approximately the same,

$$\left( \frac{\sigma_{N_1}}{N_1} \right) \approx \left( \frac{\sigma_{N_2}}{N_2} \right) \approx \cdots \approx \left( \frac{\sigma_{N_n}}{N_n} \right) \equiv \left( \frac{\sigma_N}{N} \right), \tag{8.10}$$

(8.9) can then be solved for the uncertainty in each bin

$$\left( \frac{\sigma_N}{N} \right) = \left( \frac{\sigma_{N_{Tot}}}{N_{Tot}} \right) \frac{N_{Tot}}{[\sum_{i=1}^{n} N_i^2]^{\frac{1}{2}}}. \tag{8.11}$$

Table 8-7 lists the systematic uncertainties in the number of events in each bin for dimuon production from $b$-quarks. The uncertainties are calculated for both of the

| Trigger Name | Systematic Uncertainty, $\left(\frac{\sigma_N}{N}\right)_{b\bar{b}\to\mu\mu}$ | |
|---|---|---|
| | $d\sigma/dp_T$ | $d\sigma/d\Delta\phi^{\mu\mu}$ |
| MU_2_HIGH | 0.10 | 0.10 |
| MU_1_JET | 0.12 | 0.11 |
| MU_JET_LOW | 0.16 | 0.16 |

Table 8-7: Systematic uncertainties in each bin from the maximum likelihood fit for $b\bar{b} \to \mu\mu$ production.

differential distributions and are approximately twice as large as the uncertainties in the total number of events. These results will be used in the next chapter.

# Chapter 9

# Cross Section Results

## 9.1 Unfolding the Detector Resolution

Before calculating the differential cross sections, the finite resolution of the DØ detector must be unfolded from the measured muon spectrums. The effects of the detector resolution on the observed muon spectrums can be broken down into two categories:

1. The effect of reconstructing events that lie outside the allowed kinematic ranges into the final data sample, and
2. The effect of the muon momentum resolution on the observed final data sample.

The first effect accounts for events where the unsmeared kinematic variables lie outside the accepted true muon kinematic range,

- $4 \leq p_T^{\mu}(\text{trailing}) \leq 25$ GeV/c

- $|\eta^{\mu}| \leq 0.8$
- $6 \leq M^{\mu\mu} \leq 35$ GeV/c$^2$
- $\Delta\phi_{3D} \leq 165°$,

but get reconstructed into the measured kinematic range of the final data sample. These events should not contribute to the true variable cross section measurement. For example, an event that contains two muons with true $p_T^{\mu} > 4$ GeV/c and true $M^{\mu\mu} < 6$ GeV/c$^2$ may get reconstructed with measured $M^{\mu\mu} > 6$ GeV/c$^2$ due to the muon momentum smearing. These effects are accounted for by using the fully reconstructed $b\bar{b}$, $c\bar{c}$, and prompt muon plus decay muon Monte Carlo that includes events covering the entire invariant mass range and muon transverse momentum range down to 3 GeV/c. From this Monte Carlo sample, it is determined what fraction of events which reconstruct into the final data sample originate from outside the accepted true muon kinematic ranges for invariant mass of the dimuon system and $p_T^{\mu}$(trailing). There is little smearing of $|\eta^{\mu}|$ and $\Delta\phi_{3D}$. These corrections are applied on a bin-by-bin basis. These values vary from about 5-40% depending on $p_T^{\mu}$(leading), $\Delta\phi^{\mu\mu}$, and trigger bit. Appendix B gives a summary of these unfolding factors.

The second effect takes into account the limited muon momentum resolution of the detector. The limitation on the $p_T^{\mu}$ resolution is from multiple scattering of the muon in the calorimeter and toroid and from limitations in the position resolution of the WAMUS PDT's. The smearing of the azimuthal angle of the muon, $\phi^{\mu}$, is very small. Figure 9-1 shows the difference between the reconstructed $\Delta\phi^{\mu\mu}$ spectrum and the ISAJET $\Delta\phi^{\mu\mu}$ spectrum for $b\bar{b}$ Monte Carlo passed through the full detector simulation. The central peak has a width of less than 1° which is much less than the 20° binning used in the $d\sigma/d\Delta\phi^{\mu\mu}$ distributions. Therefore, no

smearing correction is applied when unfolding the measured $\Delta\phi^{\mu\mu}$ spectrum to the true $\Delta\phi^{\mu\mu}$ spectrum.

The unfolding of the muon $p_T$ spectrum is more complicated. Figure 9-2 shows the muon momentum resolution plotted as a function of muon momentum. The dotted curve is the resolution determined from the $Z$ boson data sample with uncertainties indicated by the dashed curves[78]. The solid curve is the momentum resolution determined from a Monte Carlo sample of $b\overline{b}$ and $c\overline{c}$ events processed through the full detector simulation. Figure 9-2 shows good agreement between the Monte Carlo simulation of the detector resolution and the data.

With this in mind, the fully reconstructed Monte Carlo is then used to determine how the $p_T^{\mu}$ spectrum is smeared. The unfolding of the smeared $p_T^{\mu}$ spectrum is accomplished using a method based on Bayes' Theorem[79]. One advantage of the Bayesian approach is that it does not depend on the theoretical shape of the distribution being unfolded. In fact, a uniform theoretical distribution is assumed at the start of the unfolding. The program uses a smearing matrix determined from the Monte Carlo and the data distribution as input. The smearing matrix is calculated using a Monte Carlo sample which passes all trigger and offline selection cuts. It is then determined how the true values of the muon transverse momentum get reconstructed into different bins of measured $p_T^{\mu}$ using this sample. The Bayes' Theorem program also performs an error analysis based on the input smearing distribution and the number of events in the input distribution to give bin-by-bin uncertainties of the number of events. Figure 9-3 shows the effect of the unfolding for each data sample where the cosmic ray contribution to each sample has been subtracted prior to unfolding. The uncertainties associated with the unfolding are on the order 5-10%.

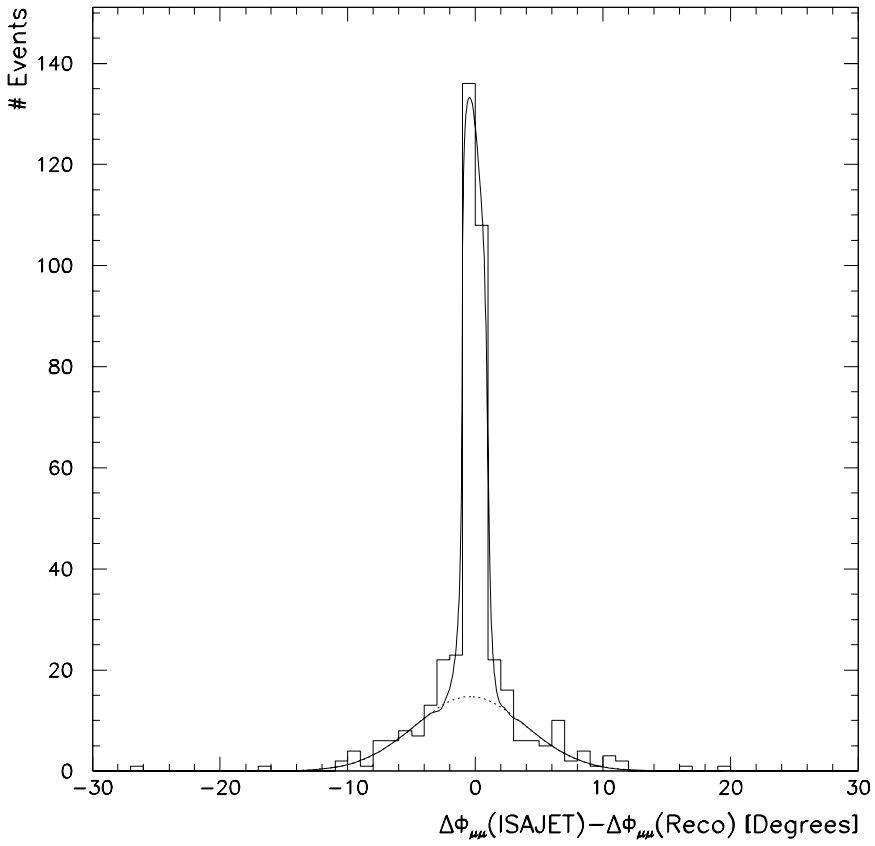


Figure 9-1: Difference between the calculated $\Delta\phi^{\mu\mu}$ spectrum from fully reconstructed $b\bar{b}$ Monte Carlo and the $\Delta\phi^{\mu\mu}$ spectrum from ISAJET. The central peak has a width of less than 1°.

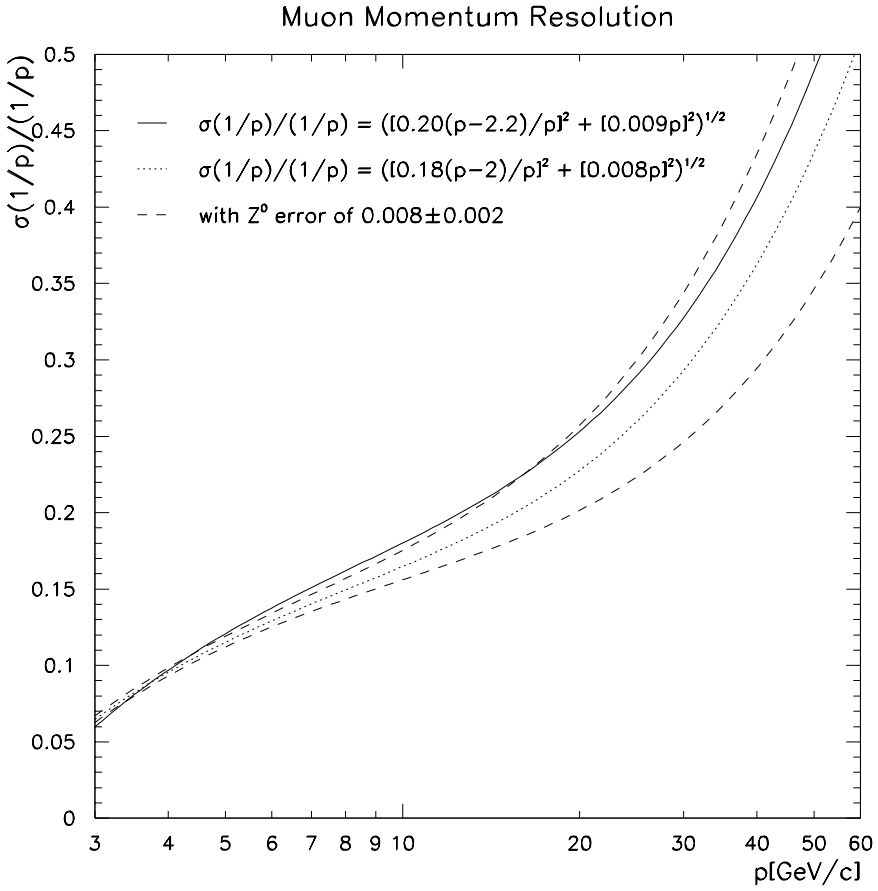


Figure 9-2: Muon momentum resolution functions obtained from the $Z$ boson data sample(dotted curve) and from the $b/c$ Monte Carlo sample processed through the detector simulation(solid curve). The resolution determined from the Monte Carlo is consistent with the errors determined from the $Z$ boson data sample(dashed curves).

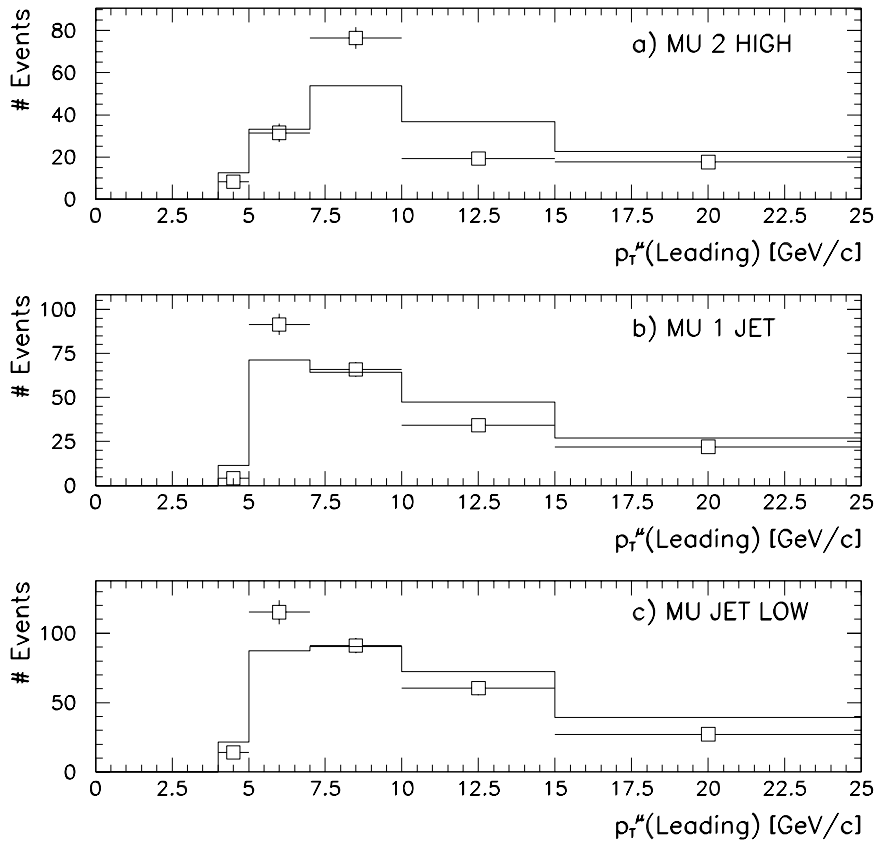


Figure 9-3: Number of events per bin in $p_T^\mu$(leading) for a) MU_2_HIGH, b) MU_1_JET, and c) MU_JET_LOW from the maximum likelihood fit before (solid line) and after (points) unfolding. Only the errors due to unfolding are shown.

As a check to the Bayesian approach to unfolding, a sample of fully reconstructed $b\bar{b}$ Monte Carlo events is used as the input to the unfolding program. As shown in Fig. 9-4, the Bayes' Theorem method does a good job in reproducing the original unsmeared distribution.

## 9.2 Dimuon Production

Using the method outlined above, the unfolded number of dimuon events is determined for the two differential distributions, $dN/dp_T$ and $dN/d\Delta\phi^{\mu\mu}$. The inclusive dimuon cross section is quoted for dimuons from heavy flavor production associated with the following true kinematic cuts:

- $4 \leq p_T^{\mu} \leq 25$ GeV/c
- $|\eta^{\mu}| \leq 0.8$
- $6 \leq M^{\mu\mu} \leq 35$ GeV/c$^2$
- $\Delta\phi_{3D} \leq 165°$.

In order to translate the measured number of events into a cross section, the number of events in each bin must first be corrected for any cosmic ray muons fit in that bin, and then divided by the trigger efficiency, $\epsilon_{Trig}$, the efficiency of the offline event selection, $\epsilon_{Sel}$, the integrated luminosity, and the width of the bin:

$$\frac{d\sigma(p\overline{p} \rightarrow \mu\mu)}{dp_T} = \frac{N_{Data} - N_{Cosmic}}{\epsilon_{Trig}\epsilon_{Sel} \int \mathcal{L}dt \ \Delta p_T} \tag{9.1}$$

and

$$\frac{d\sigma(p\overline{p} \rightarrow \mu\mu)}{d\Delta\phi^{\mu\mu}} = \frac{N_{Data} - N_{Cosmic}}{\epsilon_{Trig}\epsilon_{Sel} \int \mathcal{L}dt \ \Delta\phi^{\mu\mu}}. \tag{9.2}$$

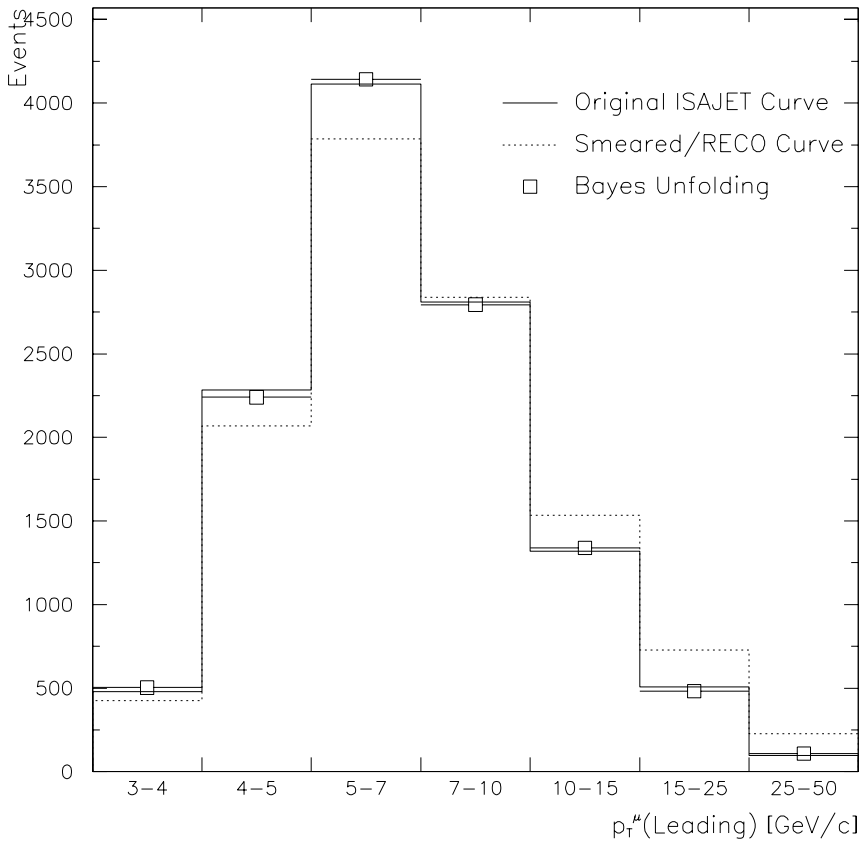


Figure 9-4: Unfolding spectrum results from Bayes Theorem. The solid line is the original unsmeared ISAJET distribution while the dashed line shows the distribution after detector smearing. The points show the unfolded distribution given by the Bayes' method.

| Source | Uncertainty |
|---|---|
| Luminosity | 5% |
| Cosmic Ray Muon Subtraction | 5% |
| Efficiency From Monte Carlo | 16-19% |
| Unfolding Spectrum | 5-43% |
| Total | 18-48% |

Table 9-1: Systematic uncertainties in the dimuon cross section.

Here, $N_{Data} - N_{Cosmic}$ is the total number of unfolded events after cosmic ray muon subtraction. Figure 9-5 through Fig. 9-10 show the inclusive dimuon differential cross section plotted as a function of the true $p_T^{\mu}$(leading) and $\Delta\phi^{\mu\mu}$ for each trigger. The ISAJET Monte Carlo predictions normalized to the NDE calculation for the various processes which contribute to the dimuon cross section, as discussed in Chapter 6, are shown for comparison. Both statistical and total errors are included with the data points. Table 9-1 summarizes the systematic uncertainties in the inclusive dimuon cross section. The range in the uncertainty associated with unfolding the muon spectrum, shown in Table 9-1, is due to differences in systematic uncertainties that are $p_T^{\mu}$(leading) and $\Delta\phi^{\mu\mu}$ dependent. All inputs to the calculation of the inclusive dimuon cross section are listed in Appendix C for reference.

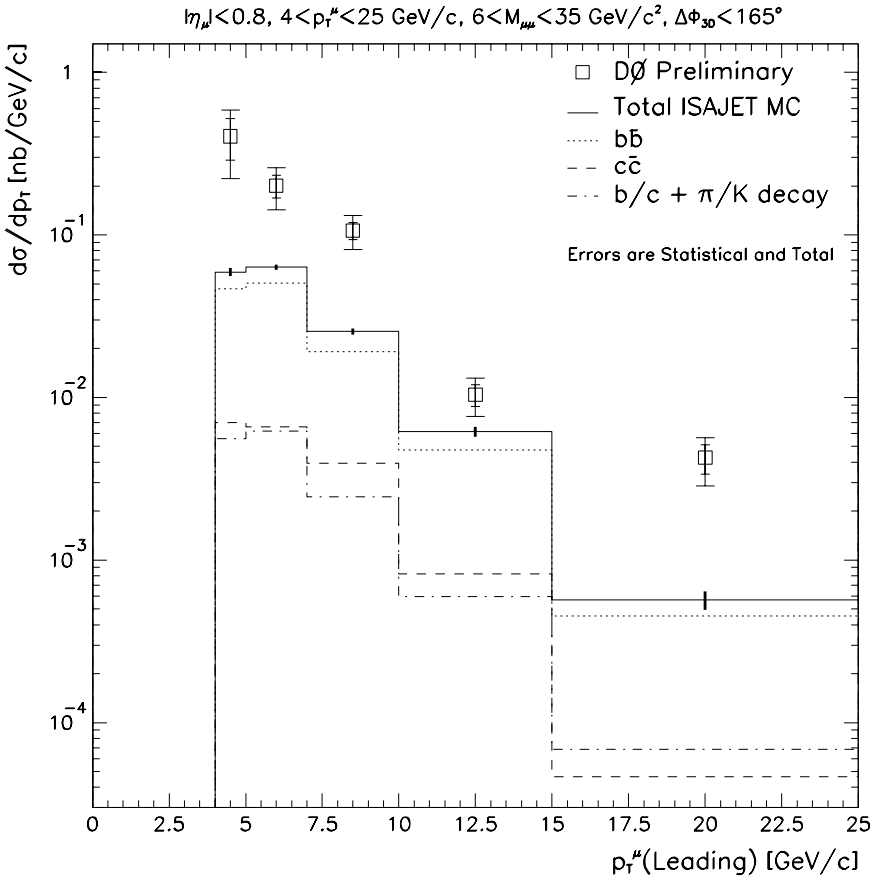


Figure 9-5: Dimuon cross section as a function of $p_T^\mu$(leading) for the MU_2_HIGH trigger. Also shown are the ISAJET Monte Carlo estimates of the various contributing processes to the cross section. The heavy dash represents the statistical error in the Monte Carlo.

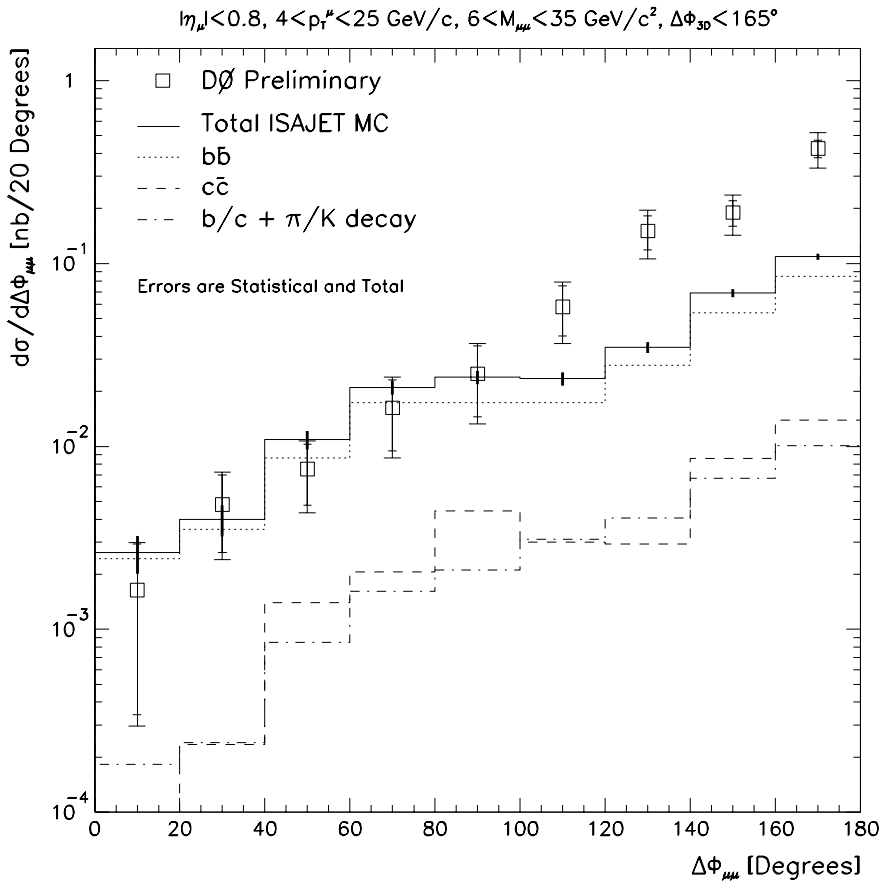


Figure 9-6: Dimuon cross section as a function of $\Delta\phi^{\mu\mu}$ for the MU_2_HIGH trigger. Also shown are the ISAJET Monte Carlo estimates of the various contributing processes to the cross section. The heavy dash represents the statistical error in the Monte Carlo.

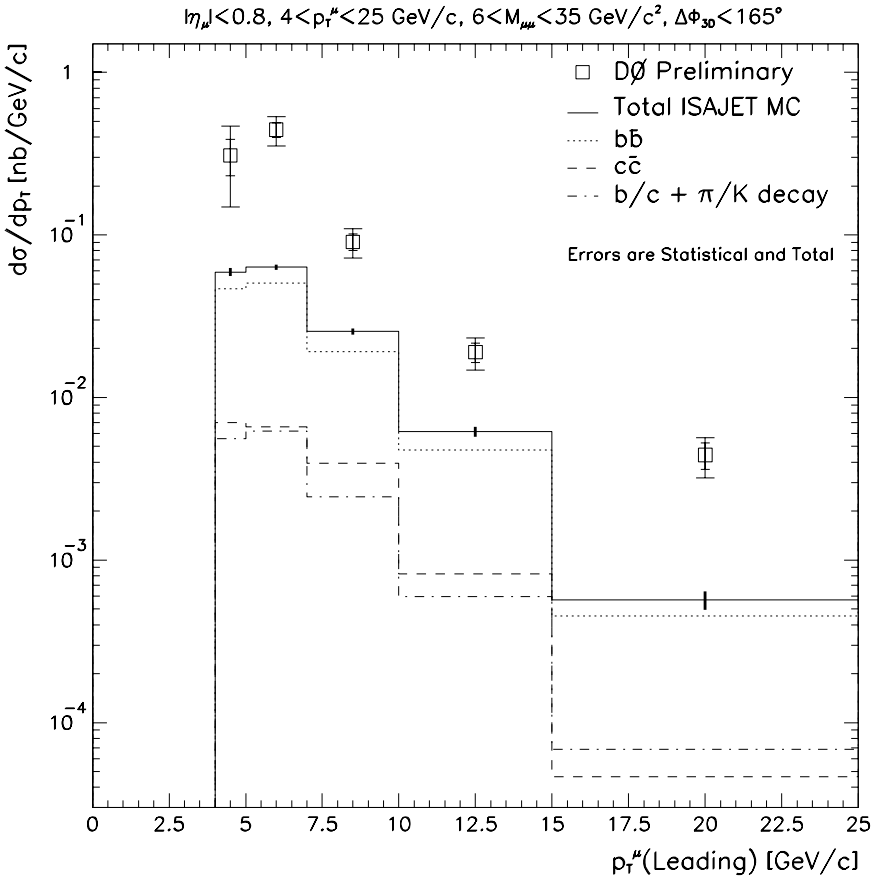


Figure 9-7: Dimuon cross section as a function of $p_T^\mu$(leading) for the MU_1_JET trigger. Also shown are the ISAJET Monte Carlo estimates of the various contributing processes to the cross section. The heavy dash represents the statistical error in the Monte Carlo.

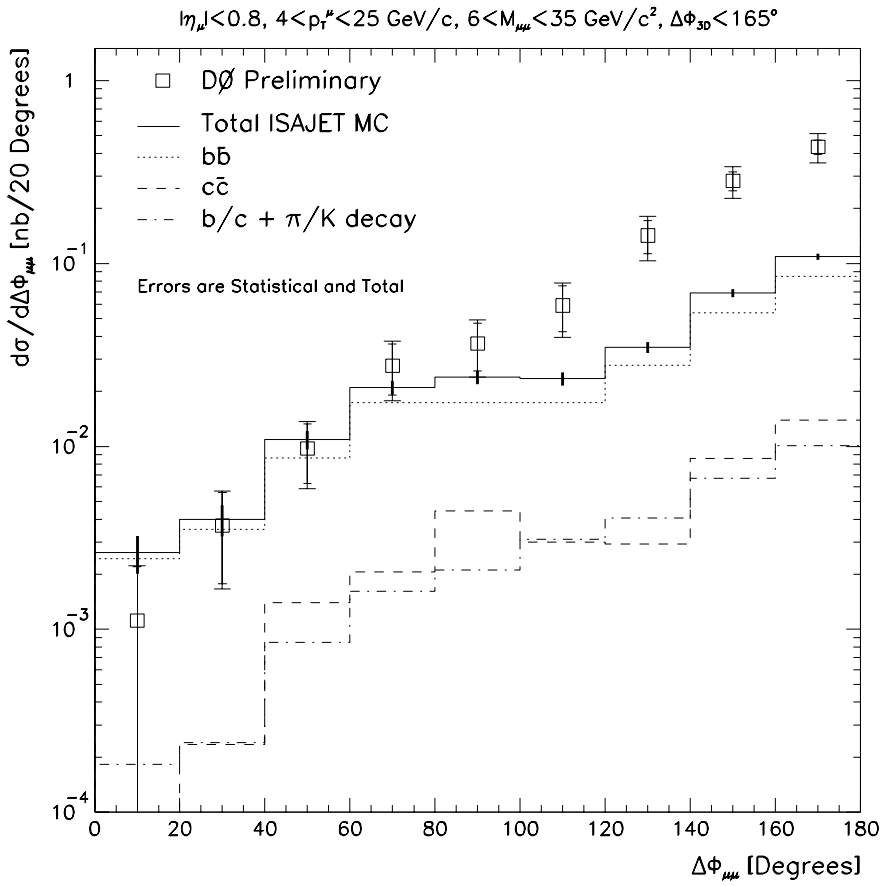


Figure 9-8: Dimuon cross section as a function of $\Delta\phi^{\mu\mu}$ for the MU_1_JET trigger. Also shown are the ISAJET Monte Carlo estimates of the various contributing processes to the cross section. The heavy dash represents the statistical error in the Monte Carlo.

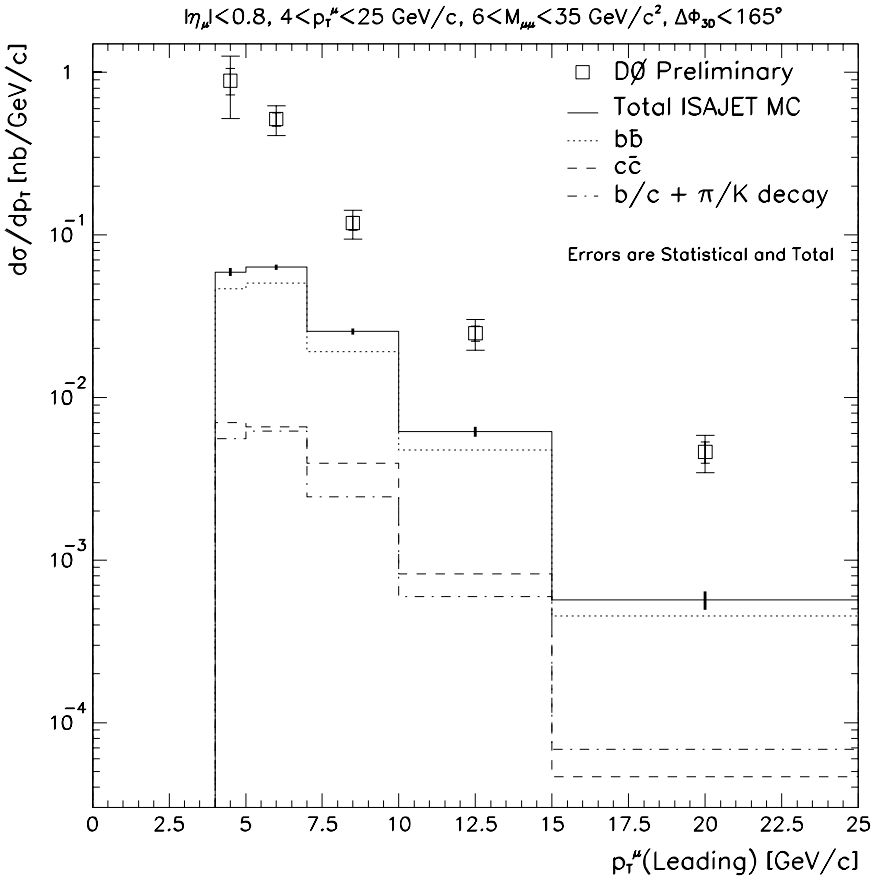


Figure 9-9: Dimuon cross section as a function of $p_T^\mu$(leading) for the MU_JET_LOW trigger. Also shown are the ISAJET Monte Carlo estimates of the various contributing processes to the cross section. The heavy dash represents the statistical error in the Monte Carlo.

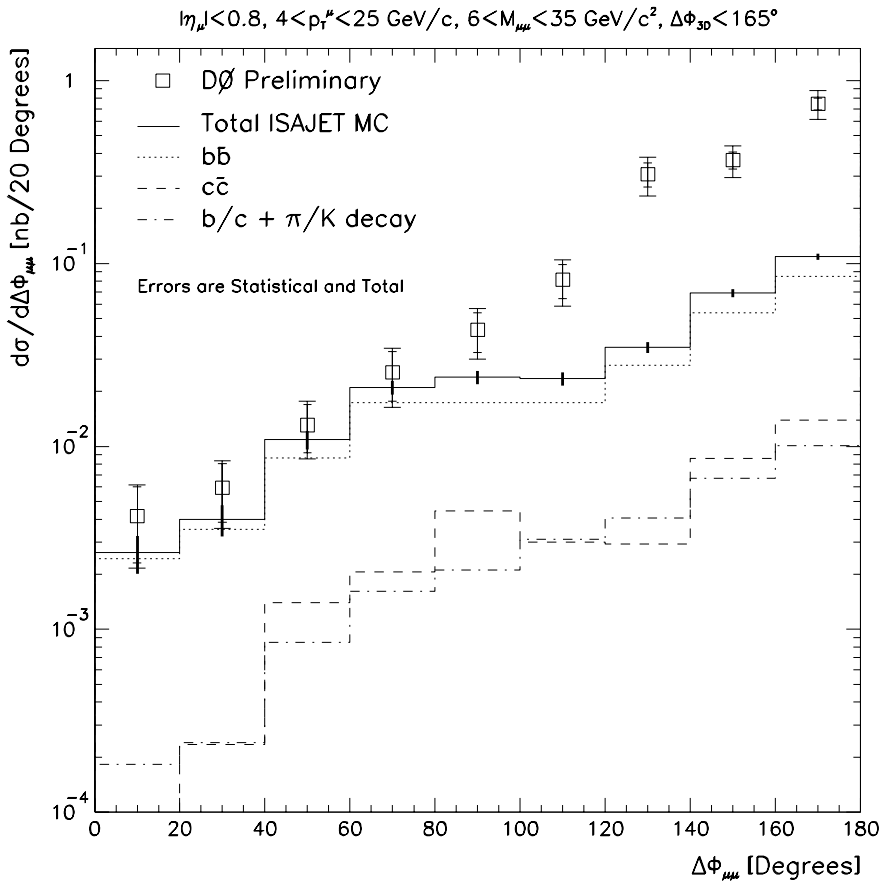


Figure 9-10: Dimuon cross section as a function of $\Delta\phi^{\mu\mu}$ for the MU_JET_LOW trigger. Also shown are the ISAJET Monte Carlo estimates of the various contributing processes to the cross section. The heavy dash represents the statistical error in the Monte Carlo.

## 9.3 $b$-quark Production

In order to extract a $b$-quark cross section from the dimuon data, several steps are involved. First, we find what portion of the dimuon data originates from $b\overline{b}$ production. This is already done using the event-by-event fit from Chapter 8. Unfolding this spectrum according to the procedure described in the first part of this chapter leads us to the $b\overline{b} \rightarrow \mu\mu$ cross section. To calculate the total $b$-quark cross section, the effects of the $b$ decay-chain, $b \rightarrow B \rightarrow \mu$, must be unfolded. These include:

- The effect of the muon-level kinematic cuts must be removed to give the full differential cross section for muons from $b$'s
- The differential muon cross section must be related to its parent $B$-hadron by taking into account the branching ratio and decay kinematics of the $B$-hadron
- The effect of fragmentation of the $b$-quark must be unfolded.

Each of the unfolding steps is modeled using ISAJET Monte Carlo $b\overline{b}$ events as described in Sec. 9.3.3.

### 9.3.1 Determination of $f_b$

As a cross check on the results of the maximum likelihood fit, the fraction of dimuon events originating from $b\overline{b}$ production, $f_b$, is determined using estimates from the ISAJET Monte Carlo. These estimates are compared to the fit of the $b\overline{b}$ fraction found in the data from Chapter 8.

### Monte Carlo

The ISAJET Monte Carlo described in Chapter 6 is used as an estimate of $f_b$ in the final data samples. This event sample consists of Monte Carlo events after processing through the full detector simulation with all data cuts applied. The renormalized ISAJET cross sections (see Secs. 6.1 through 6.2) are used as a better estimate of the relative contributions to the total dimuon cross section. The fraction of $b\overline{b}$ events is then calculated bin-by-bin according to the formula

$$f_b = \frac{b\overline{b}}{b\overline{b} + c\overline{c} + (\mu + decay)}, \tag{9.3}$$

where $b\overline{b}(c\overline{c})$ is the Monte Carlo prediction for $b\overline{b}(c\overline{c}) \rightarrow \mu\mu$ production and $(\mu + decay)$ is the Monte Carlo prediction for a prompt muon plus a $\pi$ or K decay. The diamonds in Figs 9-11 through 9-13 show the Monte Carlo estimates of $f_b$ for each trigger as a function of measured $p_T^{\mu}$(leading) and $\Delta\phi^{\mu\mu}$. The errors on the Monte Carlo estimates are from Monte Carlo statistics only.

### Maximum Likelihood Fit

As described in Chapter 8 and Sec. 8.5, the results of the event-by-event maximum likelihood fit yield the fraction of $b\overline{b}$ events found in the data. These results are shown in Figs 9-11 through 9-13 along with the Monte Carlo estimates. The errors on $f_b$ are from the fit only. These figures show that there is good agreement between the fit number of $b\overline{b}$ events found in the data and the estimates given by the Monte Carlo, except for the results from the MU_2_HIGH trigger which show the Monte Carlo estimates are slightly below those found in the data for small $p_T^{\mu}$.

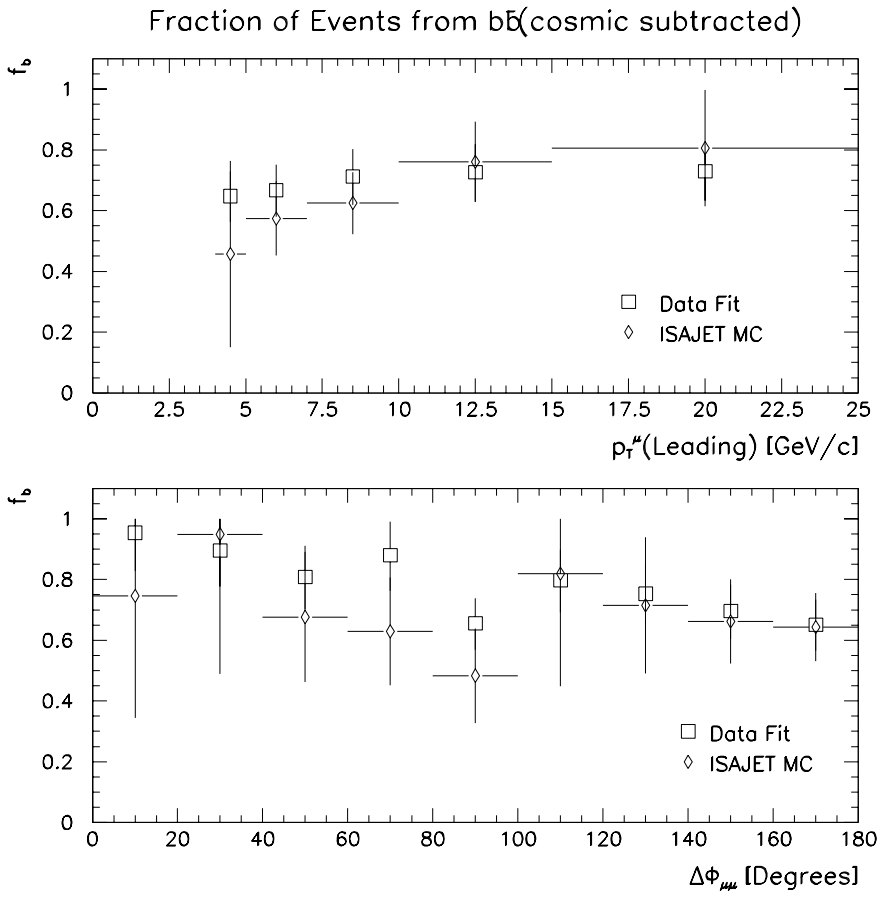


Figure 9-11: Fraction of $b\bar{b}$ events found from the data for MU_2_HIGH. Also shown is the Monte Carlo prediction.

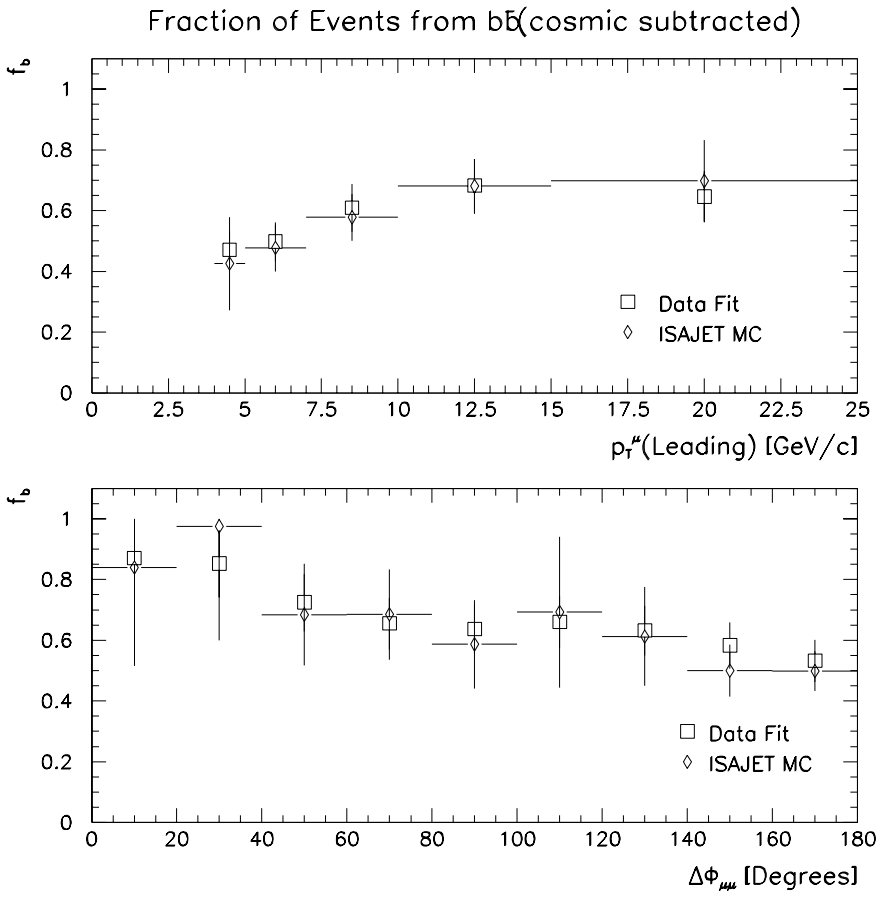


Figure 9-12: Fraction of $b\bar{b}$ events found from the data for MU_1_JET. Also shown is the Monte Carlo prediction.

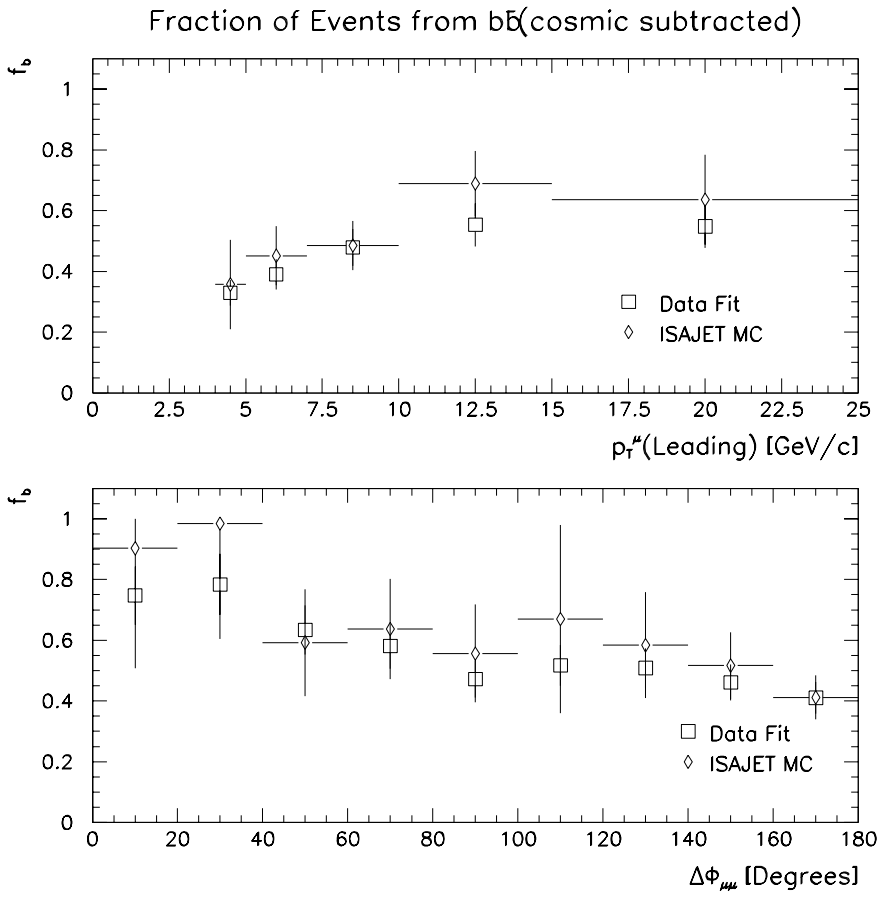


Figure 9-13: Fraction of $b\bar{b}$ events found from the data for MU_JET_LOW. Also shown is the Monte Carlo prediction.

### 9.3.2 $b\bar{b} \rightarrow \mu\mu$ Production

To obtain the $b\bar{b} \rightarrow \mu\mu$ production cross section, the fit number of $b\bar{b}$ events from Chapter 8 are unfolded according to the procedure described in the beginning of this chapter. We have confidence in these results since the total fits from the maximum likelihood method look reasonable and the Monte Carlo estimates of $f_b$ agree reasonably well with those obtained from the fits. In addition, a similar study performed on an inclusive single muon sample[60] using a fit to $p_T^{rel}$, found good agreement between the fit fraction of $b$-events in the data and the fraction of $b$-events predicted by a Monte Carlo sample. The $b\bar{b} \rightarrow \mu\mu$ production cross section is then calculated in the same way as the total dimuon cross section is calculated:

$$\frac{d\sigma(p\overline{p} \rightarrow b\overline{b} \rightarrow \mu\mu)}{dp_T} = \frac{N_{b\bar{b}}}{\epsilon_{Trig}\epsilon_{Sel}\int \mathcal{L}dt\ \Delta p_T} \tag{9.4}$$

and

$$\frac{d\sigma(p\overline{p} \rightarrow b\overline{b} \rightarrow \mu\mu)}{d\Delta\phi^{\mu\mu}} = \frac{N_{b\bar{b}}}{\epsilon_{Trig}\epsilon_{Sel}\int \mathcal{L}dt\ \Delta\phi^{\mu\mu}}. \tag{9.5}$$

Here, $N_{b\bar{b}}$ is the unfolded number of $b\bar{b}$ events found in the data. Figures 9-14 through 9-19 show the $b\bar{b} \rightarrow \mu\mu$ production cross section as a function of true $p_T^{\mu}$(leading) and $\Delta\phi^{\mu\mu}$ for each trigger. Also shown in each figure is the ISAJET Monte Carlo estimate of $b\bar{b}$ production normalized to the NDE calculation. Appendix C gives the inputs to this calculation along with the fit number of $b\bar{b}$ events before detector resolution is accounted for.

Two additional errors are incurred when using the fraction of $b\bar{b}$ production from the maximum likelihood fits. The first is the systematic uncertainty in each bin due to the variation in the input distributions. These are described in Sec.8.4 and listed in Table 8-7. The second error is due to the uncertainty in the number

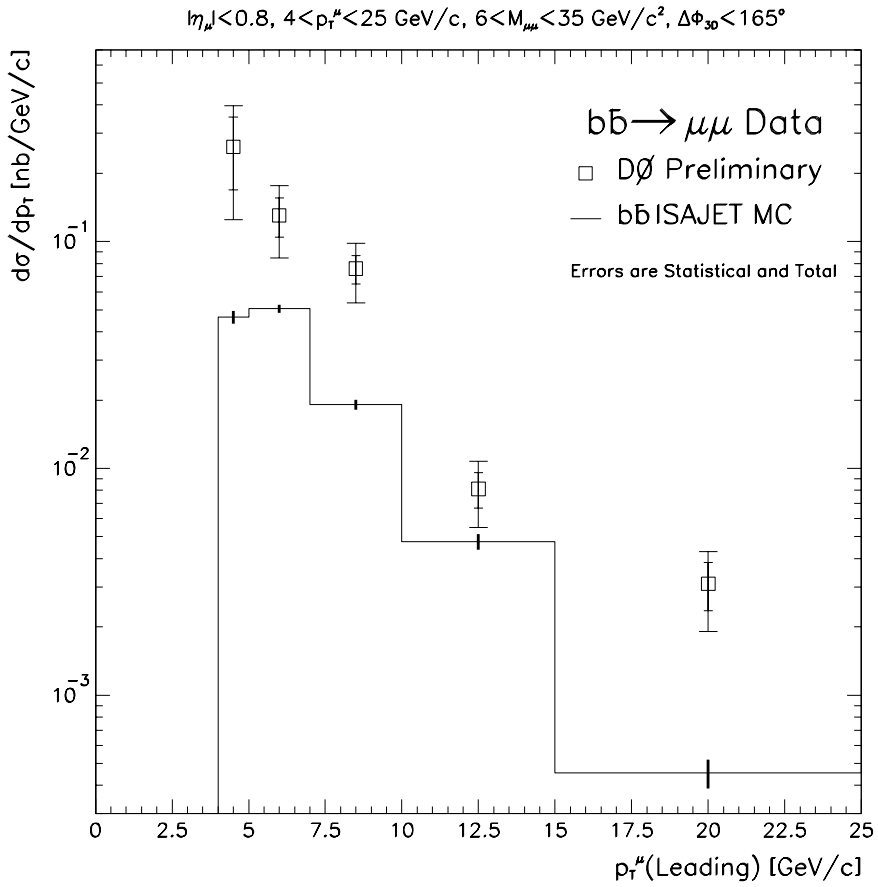


Figure 9-14: Dimuon cross section from $b\bar{b}$ production as a function of $p_T^\mu$(leading) for the MU_2_HIGH trigger. Also shown is the Monte Carlo estimate of $b\bar{b}$ production. Errors on the data are statistical and total. The heavy dash represents the statistical error in the Monte Carlo.

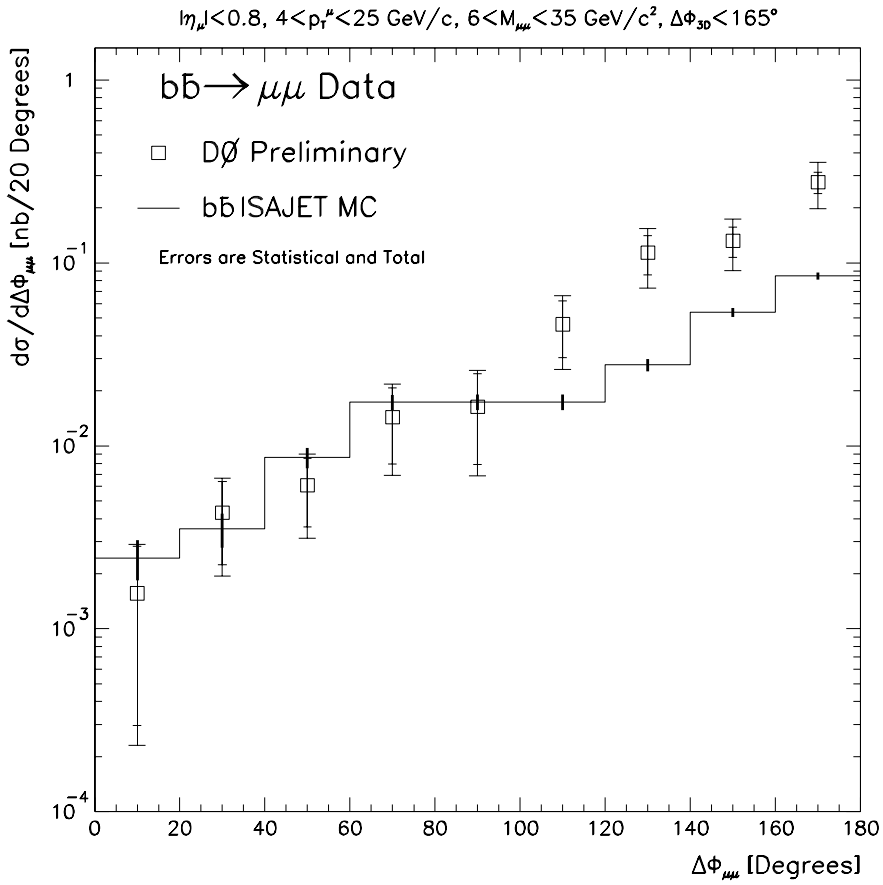


Figure 9-15: Dimuon cross section from $b\bar{b}$ production as a function of $\Delta\phi^{\mu\mu}$ for the MU_2_HIGH trigger. Also shown is the Monte Carlo estimate of $b\bar{b}$ production. Errors on the data are statistical and total. The heavy dash represents the statistical error in the Monte Carlo.

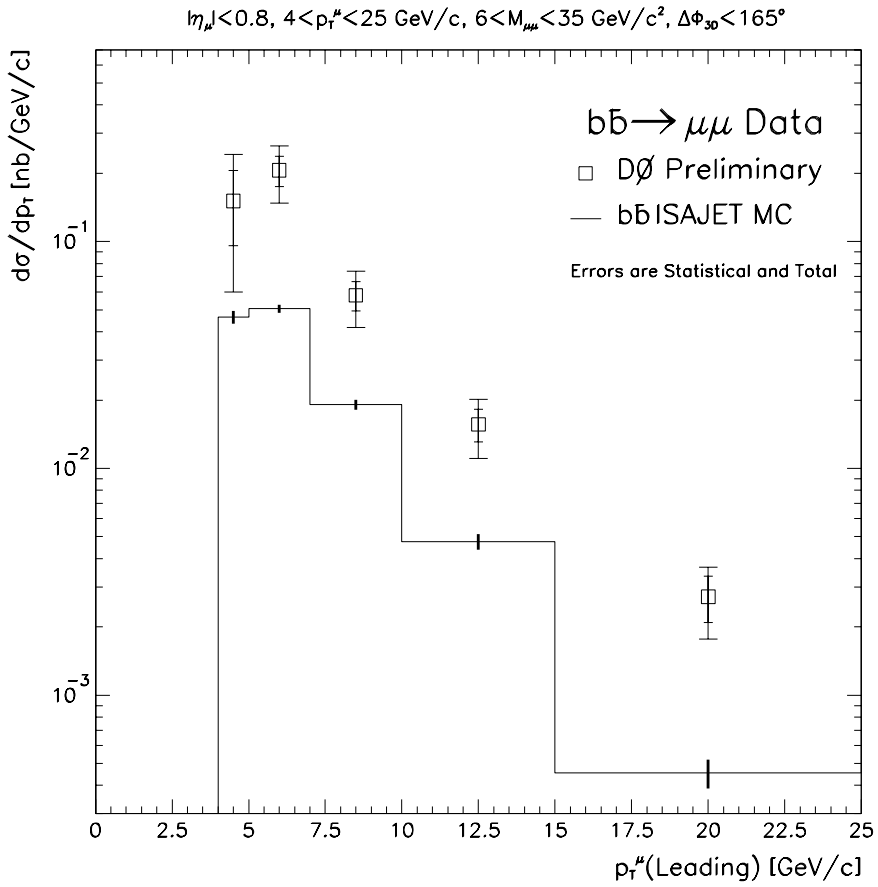


Figure 9-16: Dimuon cross section from $b\bar{b}$ production as a function of $p_T^\mu$(leading) for the MU_1_JET trigger. Also shown is the Monte Carlo estimate of $b\bar{b}$ production. Errors on the data are statistical and total. The heavy dash represents the statistical error in the Monte Carlo.

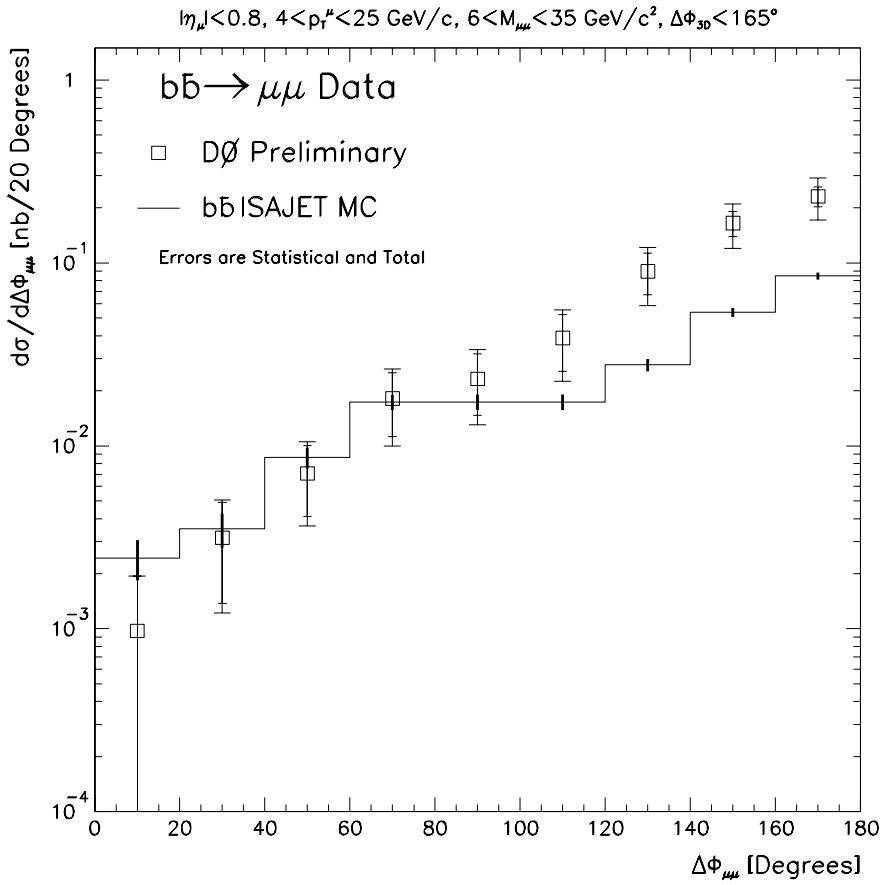


Figure 9-17: Dimuon cross section from $b\bar{b}$ production as a function of $\Delta\phi^{\mu\mu}$ for the MU_1_JET trigger. Also shown is the Monte Carlo estimate of $b\bar{b}$ production. Errors on the data are statistical and total. The heavy dash represents the statistical error in the Monte Carlo.

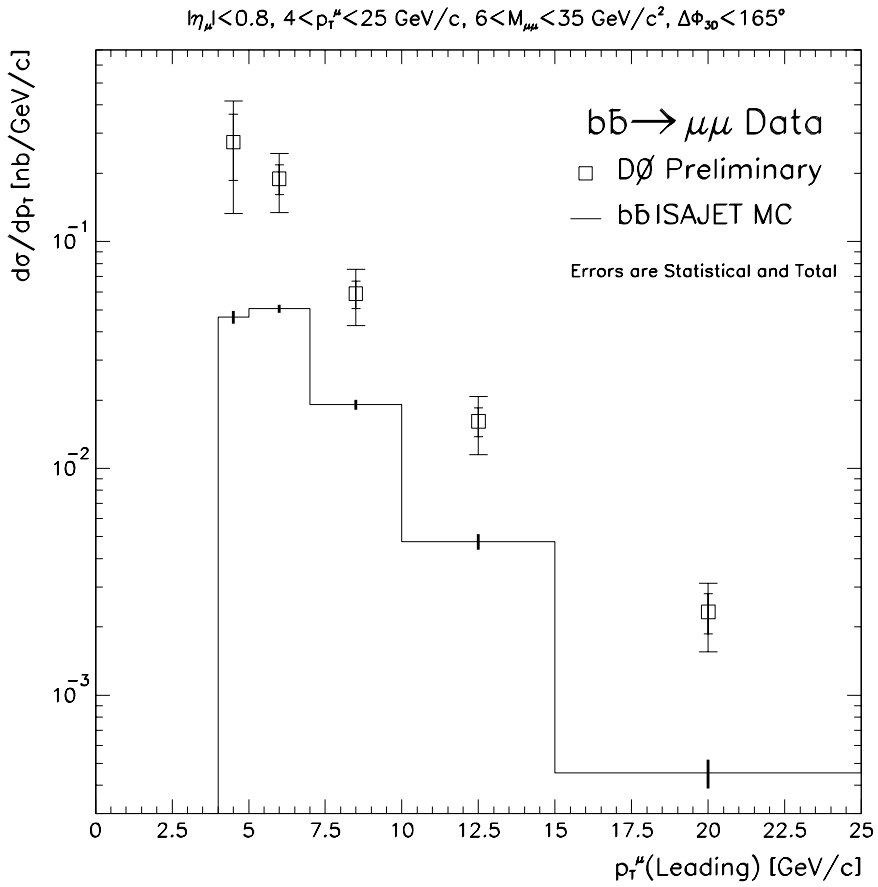


Figure 9-18: Dimuon cross section from $b\bar{b}$ production as a function of $p_T^\mu$(leading) for the MU_JET_LOW trigger. Also shown is the Monte Carlo estimate of $b\bar{b}$ production. Errors on the data are statistical and total. The heavy dash represents the statistical error in the Monte Carlo.

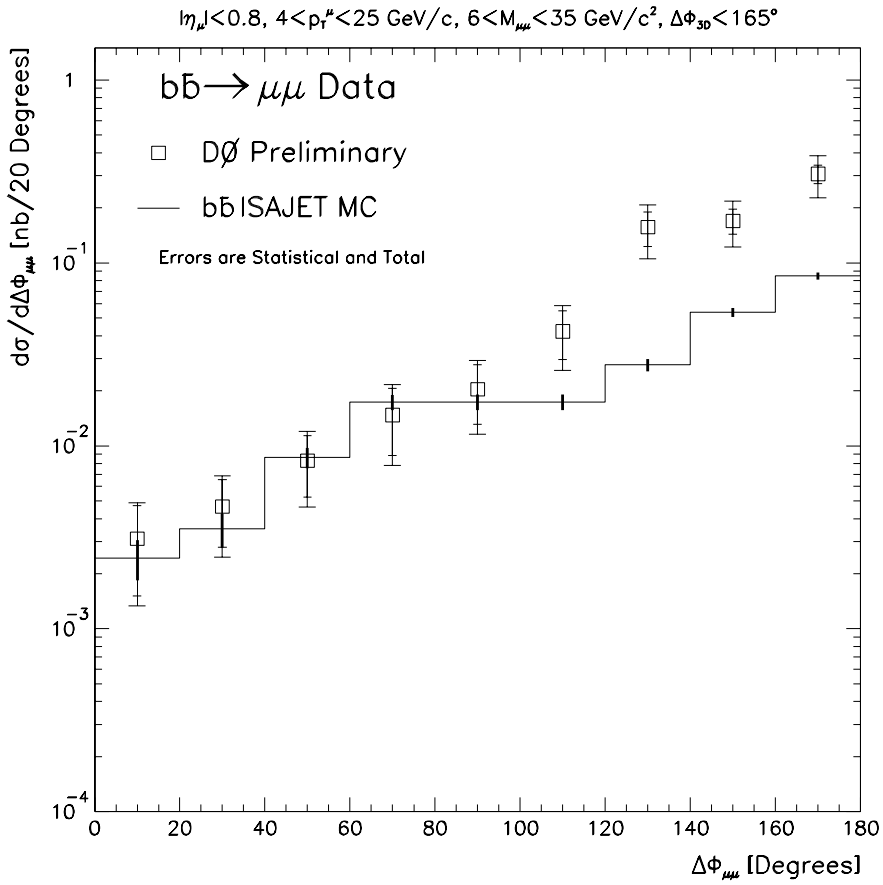


Figure 9-19: Dimuon cross section from $b\bar{b}$ production as a function of $\Delta\phi^{\mu\mu}$ for the MU_JET_LOW trigger. Also shown is the Monte Carlo estimate of $b\bar{b}$ production. Errors on the data are statistical and total. The heavy dash represents the statistical error in the Monte Carlo.

of $b\bar{b}$ events fit in each bin. This is the error from the fit. These errors are 12.6%, 12.8%, and 12.8% for MU_2_HIGH, MU_JET_LOW, and MU_1_JET respectively. Figures 9-14 through 9-19 reflect these additional systematic uncertainties.

### 9.3.3 Inclusive $b$-quark Production Cross Section

In order to translate the muon spectrum into a $b$-quark spectrum, the effects of the muon-level kinematic cuts, the $B$-hadron decay kinematics, and $b$-quark fragmentation must be taken into account. We use a Monte Carlo method to extrapolate the muon-level cross section into a $b$-quark level cross section. This method was developed by UA1[17] and is commonly used in hadron collider analysis[80, 61, 68].

Figure 9-20 illustrates this method. The figure shows the transverse momentum spectrum for $b$-quarks with a rapidity of $|y^b| < 1$ and for $b$-quarks that decay into muons that satisfy the required kinematic cuts (bottom histogram):

- $4 \leq p_T^\mu \leq 25$ GeV/c
- $|\eta^\mu| \leq 0.8$
- $6 \leq M^{\mu\mu} \leq 35$ GeV/c$^2$
- $\Delta\phi_{3D} \leq 165°$.

This histogram represents a threshold value of the $b$-quark $p_T$ which is determined by the fragmentation and decay kinematics in order for the $b$-quark to decay into a muon. Since muons produced from $b$-quarks have $p_T^\mu \leq p_T^b$, the muon $p_T$ cuts in the data are effectively $b$-quark $p_T$ cuts. For a set of cuts on the muon $p_T$'s, we define $p_T^{min}$ as that value of the $b$-quark $p_T$ for which 90% of the accepted $b$-quarks

have their transverse momentum greater than $p_T^{min}$. This value is illustrated in Fig. 9-20. The $b$-quark cross section can then be derived using the formula

$$\sigma_b(p_T^b > p_T^{min}, |y^b| < 1.0) = \sigma_{b\bar{b}\to\mu\mu}^{Data} \cdot \frac{\sigma_b^{MC}}{\sigma_{b\bar{b}\to\mu\mu}^{MC}}, \tag{9.6}$$

where $\sigma_{b\bar{b}\to\mu\mu}^{Data}$ is the measured integrated $b\bar{b} \to \mu\mu$ cross section, $\sigma_b^{MC}$ is the integrated Monte Carlo cross section for $b$-quark production above $p_T^{min}$, and $\sigma_{b\bar{b}\to\mu\mu}^{MC}$ is the integrated Monte Carlo production cross section for dimuons coming from $b\bar{b}$ . The exact value of $p_T^{min}$ is determined by the $p_T^{\mu}$ cuts applied in the data.

Results for the inclusive $b$-quark production cross section are presented in Table 9-2 and Figs. 9-21 through 9-23 for each of the triggers. Table 9-3 and Fig. 9-24 show the weighted average of the three triggers taking into account correlations between the data events and systematic errors. Also shown in each figure is the $\mathcal{O}(\alpha_s^3)$ calculation[15] for inclusive $b$-quark production.

| $p_T^{\mu_1}$ [GeV/c] | $p_T^{\mu_2}$ [GeV/c] | $p_T^{min}$ [GeV/c] | $\sigma_b(p_T^b > p_T^{min})$[nb] | | |
|---|---|---|---|---|---|
| | | | MU_2_HIGH | MU_1_JET | MU_JET_LOW |
| 4 | 4 | 8.0 | $3839 \pm 336 \pm 1774$ | $3935 \pm 318 \pm 2139$ | $4365 \pm 326 \pm 2073$ |
| 5 | 4 | 9.0 | $2464 \pm 223 \pm 952$ | $3040 \pm 252 \pm 1062$ | $2899 \pm 222 \pm 1027$ |
| 7 | 4 | 12.5 | $1071 \pm 109 \pm 392$ | $998 \pm 99 \pm 350$ | $1004 \pm 90 \pm 353$ |
| 10 | 4 | 17.0 | $325 \pm 47 \pm 126$ | $477 \pm 64 \pm 174$ | $471 \pm 55 \pm 171$ |
| 15 | 4 | 25.5 | $130 \pm 31 \pm 59$ | $113 \pm 26 \pm 48$ | $97 \pm 20 \pm 40$ |

Table 9-2: The inclusive $b$-quark cross section $\sigma_b(p_T^b > p_T^{min}, |y^b| < 1.0)$, where the error on the cross sections are statistical and systematic for each of the triggers.

The additional systematic uncertainties in the extraction of the $b$-quark cross section are due to the choice of the fragmentation function, the $BR(b \to \mu X)$, and

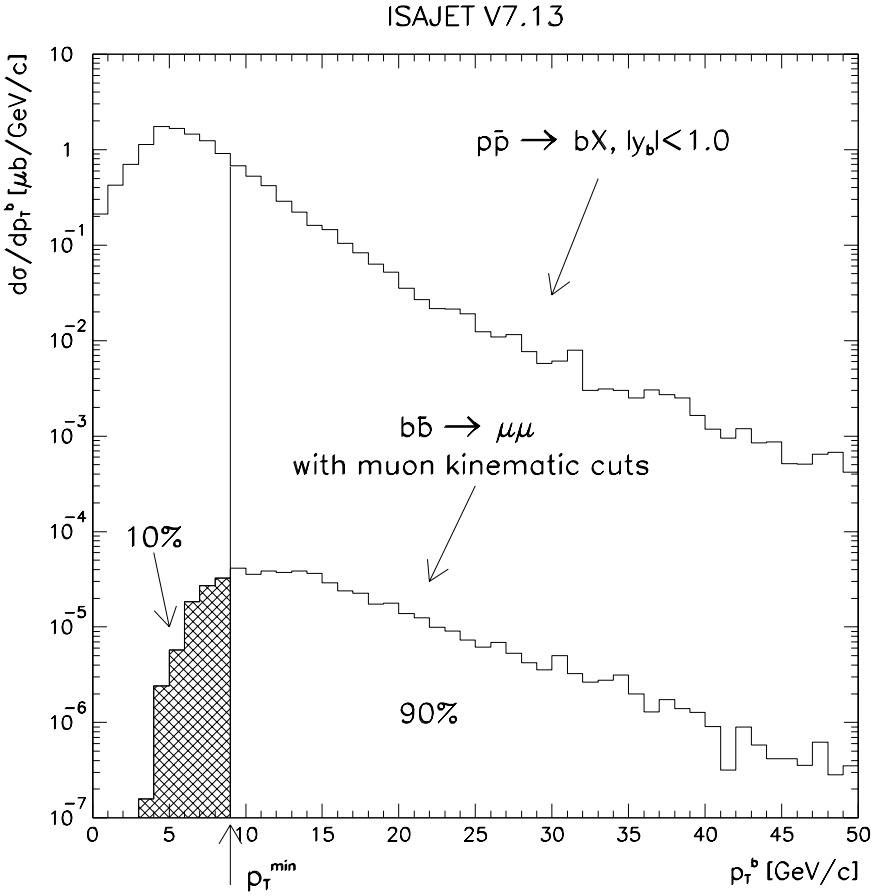


Figure 9-20: The differential cross section for inclusive $b$-quark production(top curve) and for those events which yield dimuons with kinematic cuts(bottom curve). Also shown is the value of $p_T^{min}$ for a given set of kinematic cuts.

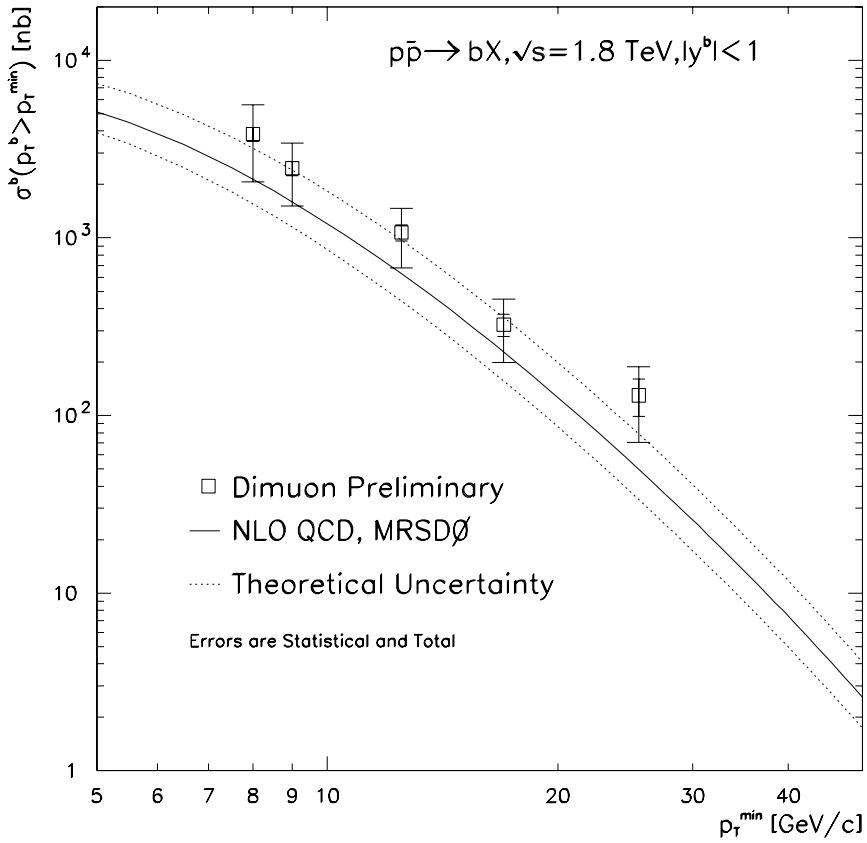


Figure 9-21: The inclusive $b$-quark cross section for $|y^b| < 1.0$ as a function of $p_T^{min}$ for the MU_2_HIGH trigger. Also shown is the $\mathcal{O}(\alpha_s^3)$ calculation(solid line) and its error bands(dashed lines).

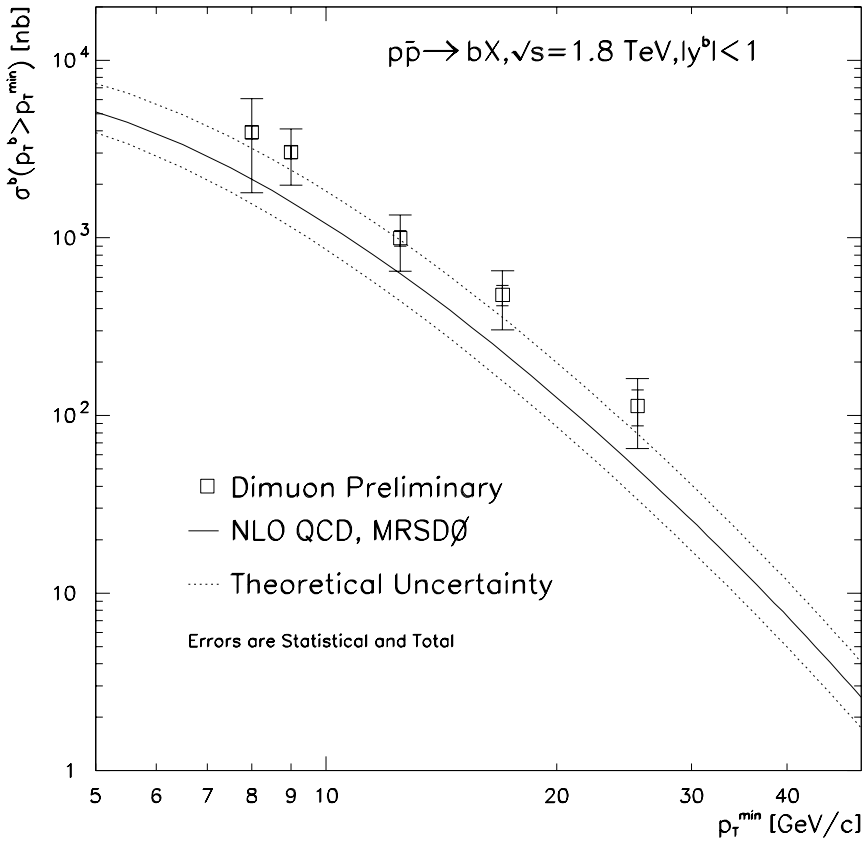


Figure 9-22: The inclusive $b$-quark cross section for $|y^b| < 1.0$ as a function of $p_T^{min}$ for the MU_1_JET trigger. Also shown is the $\mathcal{O}(\alpha_s^3)$ calculation(solid line) and its error bands(dashed lines).

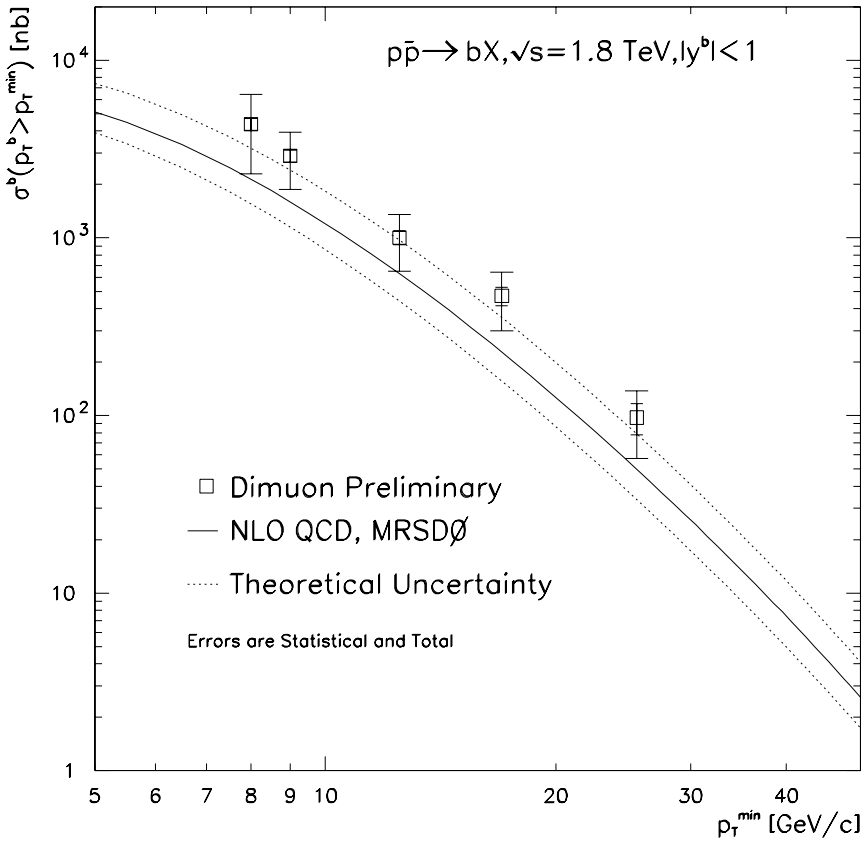


Figure 9-23: The inclusive $b$-quark cross section for $|y^b| < 1.0$ as a function of $p_T^{min}$ for the MU_JET_LOW trigger. Also shown is the $\mathcal{O}(\alpha_s^3)$ calculation(solid line) and its error bands(dashed lines).

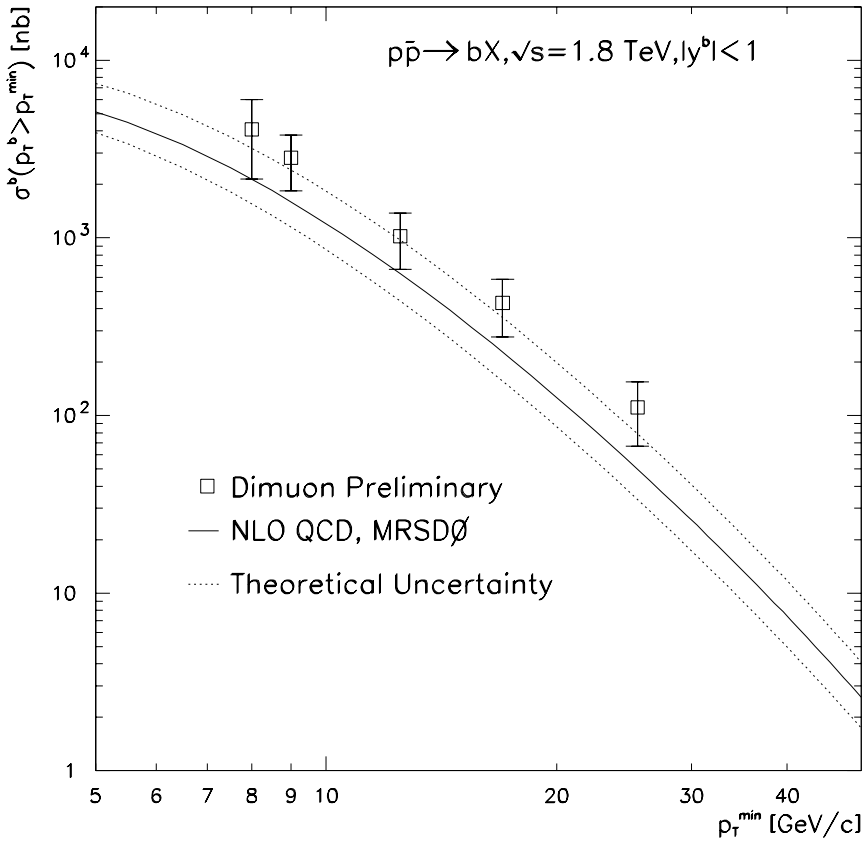


Figure 9-24: The inclusive $b$-quark cross section for $|y^b| < 1.0$ as a function of $p_T^{min}$. The errors on the data are combined statistical and systematic. Also shown is the $\mathcal{O}(\alpha_s^3)$ calculation(solid line) and its error bands(dashed lines).

| $p_T^{\mu_1}$ [GeV/c] | $p_T^{\mu_2}$ [GeV/c] | $p_T^{min}$ [GeV/c] | $\sigma_b(p_T^b > p_T^{min})[\mu\text{b}]$ Weighted Average |
|---|---|---|---|
| 4 | 4 | 8.0 | $4.08 \pm 1.93$ |
| 5 | 4 | 9.0 | $2.82 \pm 0.98$ |
| 7 | 4 | 12.5 | $1.02 \pm 0.36$ |
| 10 | 4 | 17.0 | $0.43 \pm 0.15$ |
| 15 | 4 | 25.5 | $0.11 \pm 0.04$ |

Table 9-3: The inclusive $b$-quark cross section $\sigma_b(p_T^b > p_T^{min}, |y^b| < 1.0)$, where the error on the cross sections is the combined statistical and systematic. Correlations between the three data sets have been taken into account.

uncertainties in the assumed muon spectrum from $b$-quarks. The uncertainty due to the fragmentation function is estimated by varying the Peterson parameter by 50% and recalculating the ratio $\frac{\sigma_b^{MC}}{\sigma_{b\bar{b}\to\mu\mu}^{MC}}$ in (9.6). This changes this ratio by about 14% for single muon events[68]. Since we require two muons in the final data sample, this error must be doubled. Errors associated with changing the structure function have little effect on this ratio since it effects both $\sigma_b^{MC}$ and $\sigma_{b\bar{b}\to\mu\mu}^{MC}$ equally.

An error of 5% for each muon is assigned to the uncertainty in the inclusive branching ratio of $b$ decays to muons. Finally, the uncertainty due to the assumed muon spectrum from $b$-quark decays is 8% for each muon[81]. Table 9-4 summarizes the additional uncertainties incurred when converting from the muon to $b$-quark cross section.

Figs 9-21 through 9-24 show the data compared to the NLO QCD theory prediction of Nason *et al.* described in Sec. 2.4. The central theory prediction is obtained using the MRSD0 structure function with $\mu = \mu_0$ and $\Lambda_4 = 140$ MeV.

| Source | Uncertainty |
|---|---|
| Parameterization of Fragmentation(14%) | 20% |
| $BR$ for $b \rightarrow \mu + X$ Decay(5%) | 7% |
| Spectrum for $b \rightarrow \mu + X$ Decay(8%) | 11% |
| Total | 24% |

Table 9-4: Systematic uncertainties in converting from the muon to $b$-quark cross section. The errors in parenthesis are for single $b$-quarks.

The error bands correspond to variations in $\Lambda_4$, $\mu$, and $m_b$ of 280 MeV, $\mu_0/2$, and 4.50 GeV/c$^2$ for the upper curve and 160 MeV, $2\mu_0$, and 5.00 GeV/c$^2$ for the lower curve.

### 9.3.4 $b\bar{b}$ Correlations

The differential $b\bar{b}$ cross sections calculated in Sec. 9.3 give us further information on the underlying QCD production mechanisms by looking at the correlations between the two $b$-quarks. This study is motivated by the event topology of the $b\bar{b}$ pair which allows us to differentiate between the contributing QCD production mechanisms, as discussed in Chapter 3. In addition, comparisons to theoretical calculations may enable us to determine whether a particular production mechanism is incorrectly modeled.

The $b\bar{b}$ correlation study uses the results from the data sample collected on the MU_JET_LOW trigger only. The reasons for this are twofold. The MU_JET_LOW trigger contains the largest number of events of the three data samples collected,

and the $b\bar{b}$ fraction of this sample given by the maximum likelihood fit of Chapter 8 has the smallest errors.

The ISAJET Monte Carlo is used as the basis for determining the shapes of the $\Delta\phi^{\mu\mu}$ distributions for the different heavy flavor contributions. This is only a phenomenological model since it doesn't take interference effects into account. These contributions include:

- gluon splitting
- flavor excitation
- flavor creation.

Figure 9-25 shows these distributions for each of the contributing processes with the listed kinematic cuts.

Before performing the fit, the results of Fig. 9-19 are first acceptance corrected for the three-dimensional opening angle cut. The efficiency for this cut is determined from the fully reconstructed $b\bar{b}$ Monte Carlo sample. The results are shown in Fig. 9-26. As expected, the three-dimensional opening angle cut only affects events in the largest $\Delta\phi^{\mu\mu}$ bin and has an efficiency of $0.77\pm0.02$.

Once this acceptance is applied, the $\Delta\phi^{\mu\mu}$ spectrum is fit with each of the heavy flavor contributions, separately and without constraint. The results of this fit are shown in Fig. 9-27 and listed in Table 9-5. Also shown in Fig. 9-27 is the ISAJET $b\bar{b}$ cross section normalized to the prediction of NDE.

Table 9-5 also includes the estimates of each of the three heavy flavor contributions to the $b\bar{b}$ cross section as given by ISAJET with the NDE normalization. A comparison between the leading order contribution obtained from the data fit

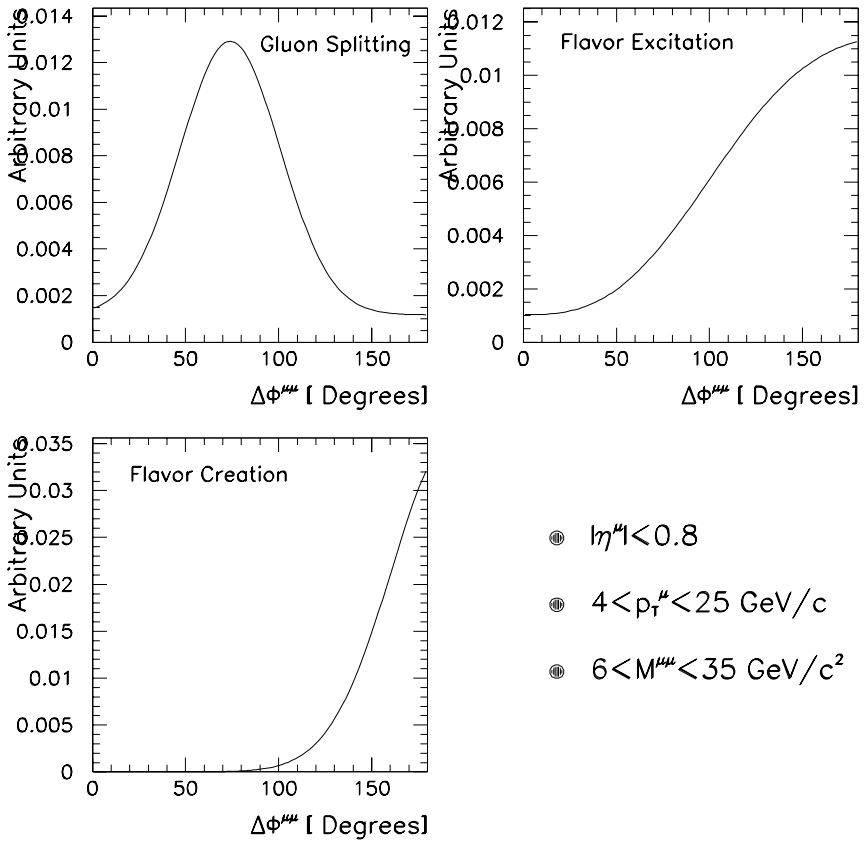


Figure 9-25: The $\Delta\phi^{\mu\mu}$ distributions for the three different contributions to the $b\bar{b}$ cross section: gluon splitting, flavor excitation, and flavor creation. The distributions are determined from ISAJET with the listed cuts.

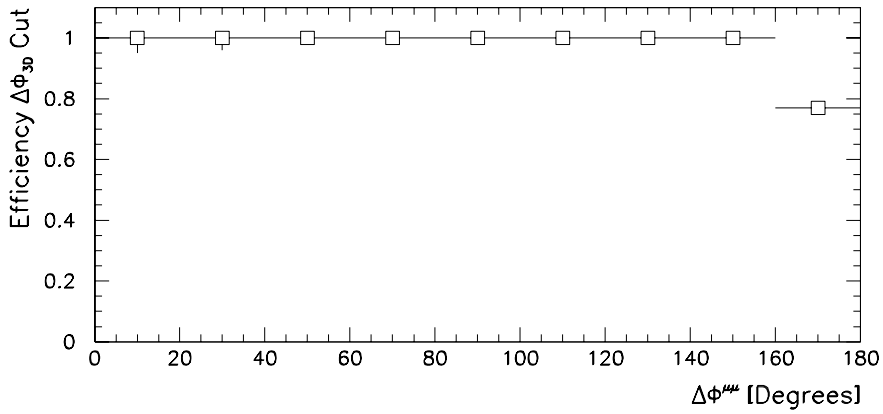


Figure 9-26: Efficiency of the three-dimensional opening angle cut on the $\Delta\phi^{\mu\mu}$ distribution. Only events in the largest $\Delta\phi$ bin are effected.

| Production Mechanism | Fit From Data | ISAJET |
|---|---|---|
| Gluon Splitting | 1.7±1.7% | 20.3% |
| Flavor Excitation | 19.7±4.6% | 16.0% |
| Total Higher Order(GS+FX) | 21.4±5.0% | 36.3% |
| Flavor Creation | 78.6±18.5% | 63.7% |

Table 9-5: Fractions of heavy flavor production mechanisms fit to the data and predicted by ISAJET. Errors are from the fit only.

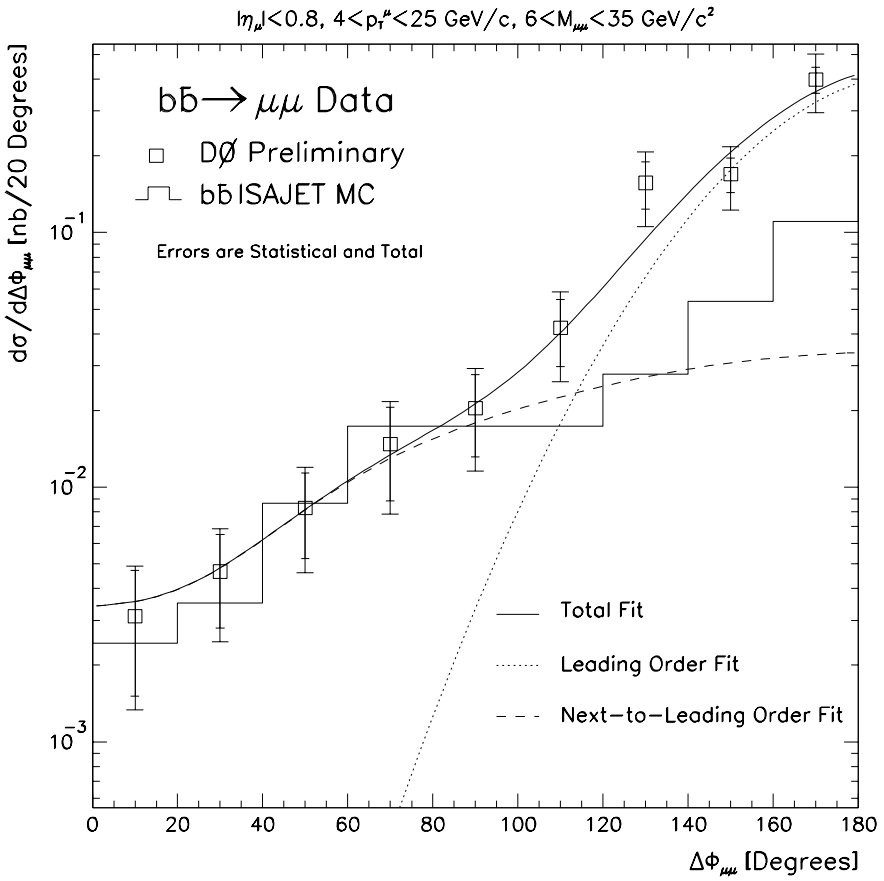


Figure 9-27: Fit of the leading order and higher order contributions to the $\Delta\phi^{\mu\mu}$ spectrum. Also shown is the ISAJET $b\bar{b}$ production cross section normalized to the prediction of NDE.

and the estimate from ISAJET show that there is fairly good agreement. Likewise, the total higher order fraction (gluon splitting plus flavor excitation) shows fairly good agreement between the data and Monte Carlo.

It is interesting that while the total higher order contribution is estimated fairly well by the Monte Carlo, the amount of gluon splitting predicted by the Monte Carlo is greatly over estimated. This is not entirely unexpected since the higher order ISAJET predictions for $p_T^b < 10$ GeV/c should be unreliable due to the internal mass threshold in producing $b\bar{b}$ pairs.

The NLO calculation of MNR[20] are also compared with the results of Fig. 9-27. Since no decay package for use with the MNR parton level event generator is available at this time, we use the ISAJET Monte Carlo to estimate the effects of the hadronization and decay of these partons into muons. Figure 9-28(top) shows the ISAJET prediction and the NLO calculation of MNR for the $\Delta\phi^{b\bar{b}}$ distribution for $p_T^b > 8$ GeV/c and $|y^b| < 0.8$. The effect of the muon kinematic cuts, $4 \leq p_T^\mu \leq 25$ GeV/c, $6 \leq M^{\mu\mu} \leq 35$ GeV/c$^2$, and $|\eta^\mu| \leq 0.8$, on the differential $\Delta\phi^{b\bar{b}}$ distribution are shown in Fig. 9-28(bottom). The ratio between these two ISAJET distributions is used to estimate the effects of hadronization and the subsequent applied cuts on the $\Delta\phi^{b\bar{b}}$ distribution. It is then applied to the $\Delta\phi^{b\bar{b}}$ calculation of MNR.

We are able to translate from $\Delta\phi^{b\bar{b}} \rightarrow \Delta\phi^{\mu\mu}$ since a strong correlation is expected to exist between the muons and the parent $b$-quark. Figure 9-29 shows this correlation for a sample of $b\bar{b}$ ISAJET Monte Carlo events. The average difference between the azimuthal difference of these events is characterized by a Gaussian distribution with $\sigma = 13.5°$. The bin size of $\Delta\phi = 20°$ has been selected to represent this uncertainty.

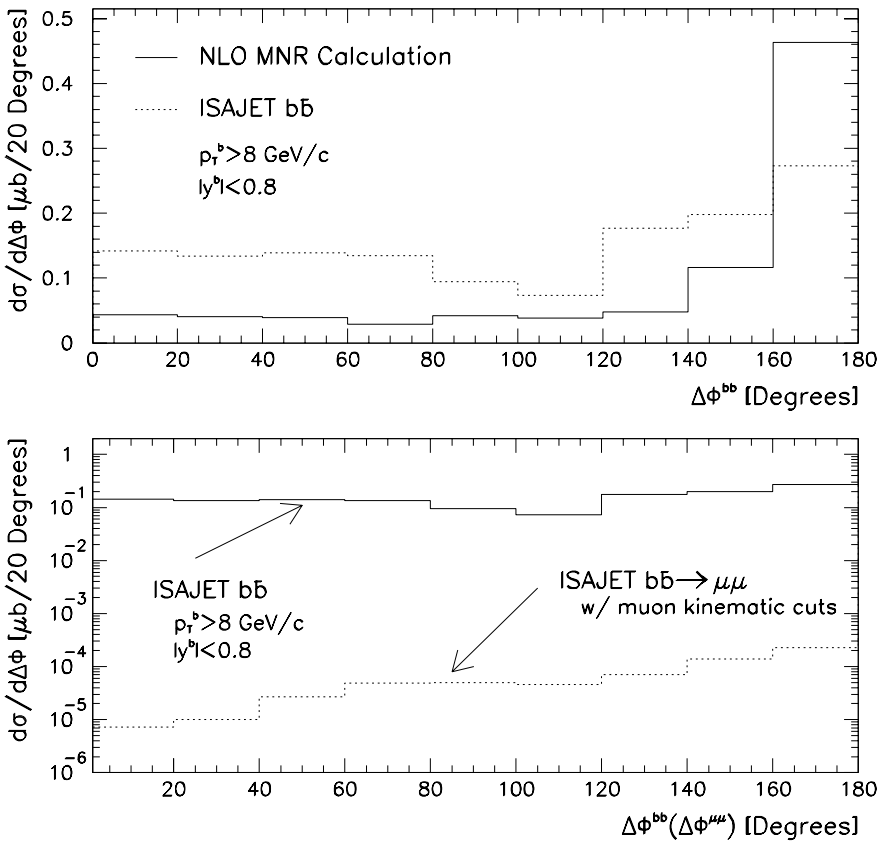


Figure 9-28: The difference between the ISAJET prediction and the NLO calculation of MNR for the $\Delta\phi^{b\bar{b}}$ distribution (top) and the effects of applying the muon kinematic cuts listed in the text to the ISAJET $b\bar{b}$ sample (bottom).

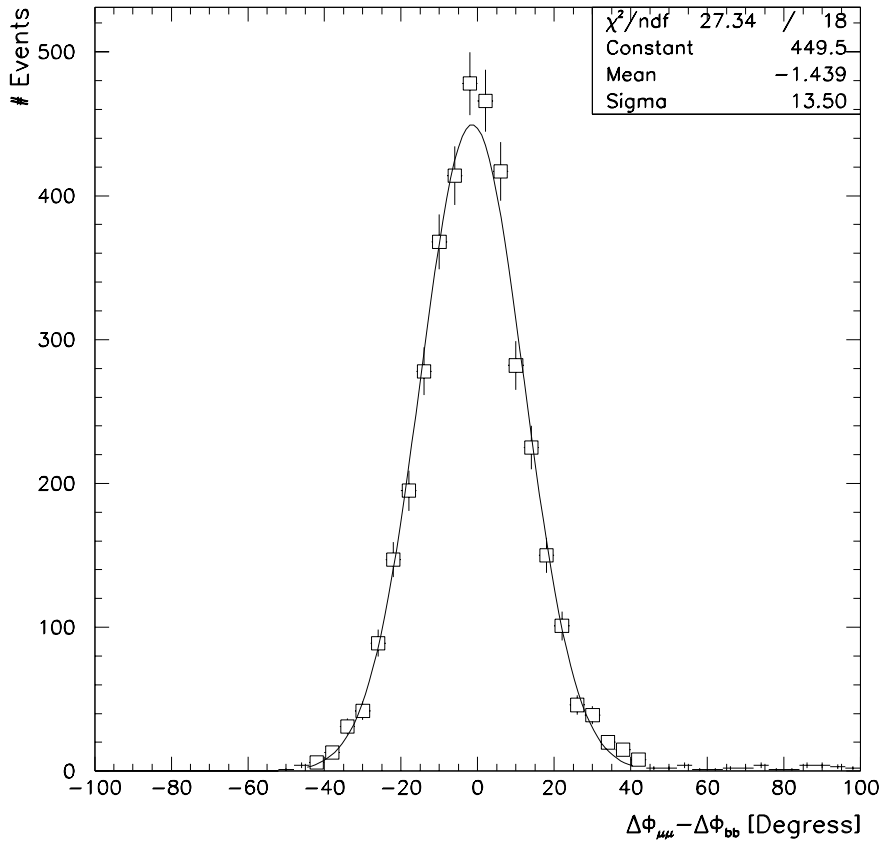


Figure 9-29: The difference between the azimuthal differences of muons from $b$-quarks and the $b$-quarks themselves. The fit is centered about zero and has a width of $\sigma = 13.5°$.

The estimate of the MNR $\Delta\phi^{\mu\mu}$ distribution can be written as

$$\Delta\phi^{\mu\mu}_{MNR} = \Delta\phi^{b\bar{b}}_{MNR}(p_T^b > 8, |y^b| < 0.8)\frac{\Delta\phi^{\mu\mu}_{ISAJET}(\text{w/ muon kinematic cuts})}{\Delta\phi^{b\bar{b}}_{ISAJET}(p_T^b > 8, |y^b| < 0.8)}. \tag{9.7}$$

In addition, an overall normalization is applied to $\Delta\phi^{\mu\mu}_{MNR}$ so that the total cross section agrees with the NLO normalized ISAJET cross section, shown in Fig. 9-27.

The MNR calculated $\Delta\phi^{\mu\mu}_{MNR}$ differential $b\bar{b}$ cross section is compared to the data in Fig. 9-30. The ISAJET estimation is included for reference. The implications of these results, as well as those of the inclusive $b$-quark cross section, are reserved for the next chapter.

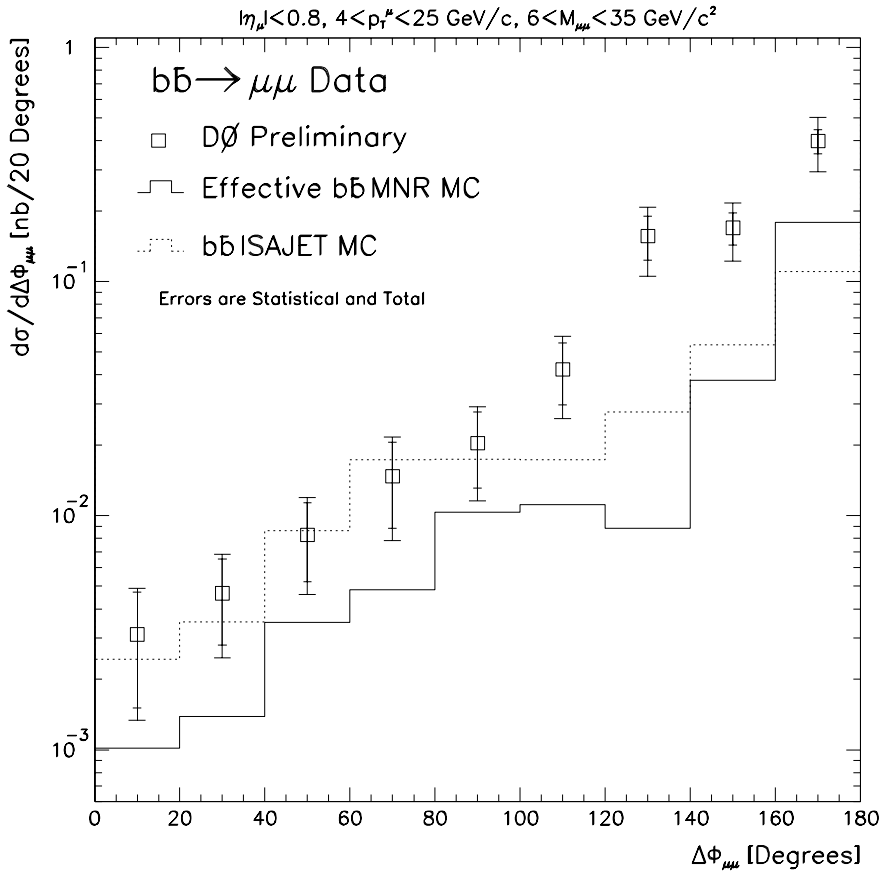


Figure 9-30: Comparison of the MNR calculated $\Delta\phi^{\mu\mu}$ $b\bar{b}$ cross section with the data and the NDE normalized ISAJET estimate.

# Chapter 10

# Discussion of Results

This analysis describes the measurement of the $b$-quark production cross section as well as the study of $b\bar{b}$ correlations using dimuon events collected at a center of mass energy of $\sqrt{s} = 1.8$ TeV using the DØ detector at the Tevatron $p\overline{p}$ collider at Fermilab.

The dimuon event sample used in this analysis is collected using three different triggers. The first trigger is a muon only based trigger which requires two muons with $p_T^\mu \geq 3$ GeV/c and $|\eta^\mu| \leq 1.7$. The other two triggers utilize the DØ calorimeter to identify jets associated with heavy quark production. The first of these triggers requires at least one muon with $p_T^\mu \geq 3$ GeV/c and $|\eta^\mu| \leq 1.7$ plus a jet with $E_T^{jet} \geq 10$ GeV. The last trigger requires a muon with $p_T^\mu \geq 3$ GeV/c and $|\eta^\mu| \leq 2.4$ as well as at least two jets with $E_T^{jet} \geq 10$ GeV.

In addition to these trigger requirements, each event is also subjected to a series of offline selection criteria designed to enhance the fraction of events produced from $b\bar{b}$ production. The dimuon invariant mass range is restricted to $6 \leq M^{\mu\mu} \leq 35$ GeV/c$^2$ in order to reduce contributions of events from $J/\psi$ decays and $Z^\circ$ decays. In addition, each muon is required to have an associated jet with

$E_T^{jet} \geq 12$ GeV. This cut essentially removes any contributions from $\Upsilon$ decay and Drell-Yan production which generally produce isolated muons. To reduce the contribution from events originating from semileptonic decays of $c$-quarks and in-flight $\pi/K$ decays, each muon is required to have $p_T^{\mu} \geq 4$ GeV/c. This cut is quite effective in reducing these backgrounds since the average muon transverse momentum is higher for muons produced in the semileptonic decay of $b$-quarks than those associated with $c$-quark and in-flight $\pi/K$ decays. In addition, a three-dimensional opening angle cut between the two muons is made at $\Delta\phi_{3D} \leq 165^{\circ}$ to reduce the background from cosmic ray muons.

After these cuts and additional muon track quality cuts are applied to the collected data, a total of 192, 277, and 397 events survive for each of the three triggers described above.

A maximum likelihood fit is employed to separate the $b\overline{b}$ signal from the background sources which include a small number of events from cosmic ray muons. The contribution from each source of dimuon events is determined by performing a simultaneous fit to several variables available in the data. The first variable, $t_0^f$, is used to determine which events are out of time with the $p\overline{p}$ collision . This variable helps identify those events originating from cosmic ray muons. Since they are not associated with the hard collision, their arrival time should be random with respect to the hard collision. Next, the transverse momentum of the muon with respect to the jet axis, $p_T^{rel}$, is used to help separate the contribution from heavy quark production. The average value of $p_T^{rel}$ depends on the mass of the decaying particle which produces the muon. Therefore, muons originating from $b$-quark production should have larger values of $p_T^{rel}$. Finally, $z'$, which is related to the fraction of the jet momentum carried by the muon, is used to help distinguish between different contributions to the dimuon sample.

As a check, the ISAJET Monte Carlo and the $\pi/K$ event generator are also used to estimate the fractions of each contributing process to the dimuon sample. Good agreement is found between the data fits and the Monte Carlo predictions.

A two step correction is then applied to the background subtracted muon spectrums to translate the spectrums measured in terms of the reconstructed variables to the spectrums in terms of the true $p_T$ of the muon and true $\Delta\phi^{\mu\mu}$. This leaves us with both the inclusive dimuon cross section and the $b\bar{b} \rightarrow \mu\mu$ cross section after accounting for the efficiencies of the trigger and offline selection cuts and the integrated luminosity of the data.

## 10.1 *b*-quark Production Cross Section

To obtain the $b$-quark production cross section, a Monte Carlo based method is used to convert the differential dimuon cross section from $b\bar{b}$ production to the $b$-quark cross section, $\sigma(p_T^b > p_T^{min})$, for the rapidity region $|y^b| \leq 1$. The quantity $p_T^{min}$ is defined as that value of the $b$-quark $p_T$ for which 90% of the accepted $b$-quarks have their transverse momentum greater than $p_T^{min}$. The combined $b$-quark cross section from the three trigger bits used in the data collection is listed in Table 10-1 and shown in Fig. 10-1. The experimental results are compared to the theoretical prediction of Nason *et al.*[15, 18]. The central theory curve is for $\Lambda_4 = 215$ MeV, $\mu = \mu_0$, and MRSD0 structure functions. The error bands on the theoretical calculation are obtained by varying $\Lambda_4$, $\mu$, and $m_b$ to 280 MeV, $\mu_0/2$, and 4.50 GeV/c$^2$ for the upper curve and 160 MeV, $2\mu_0$, and 5.00 GeV/c$^2$ for the lower curve.

In addition to extracting the $b$-quark cross section using dimuon events, DØ has

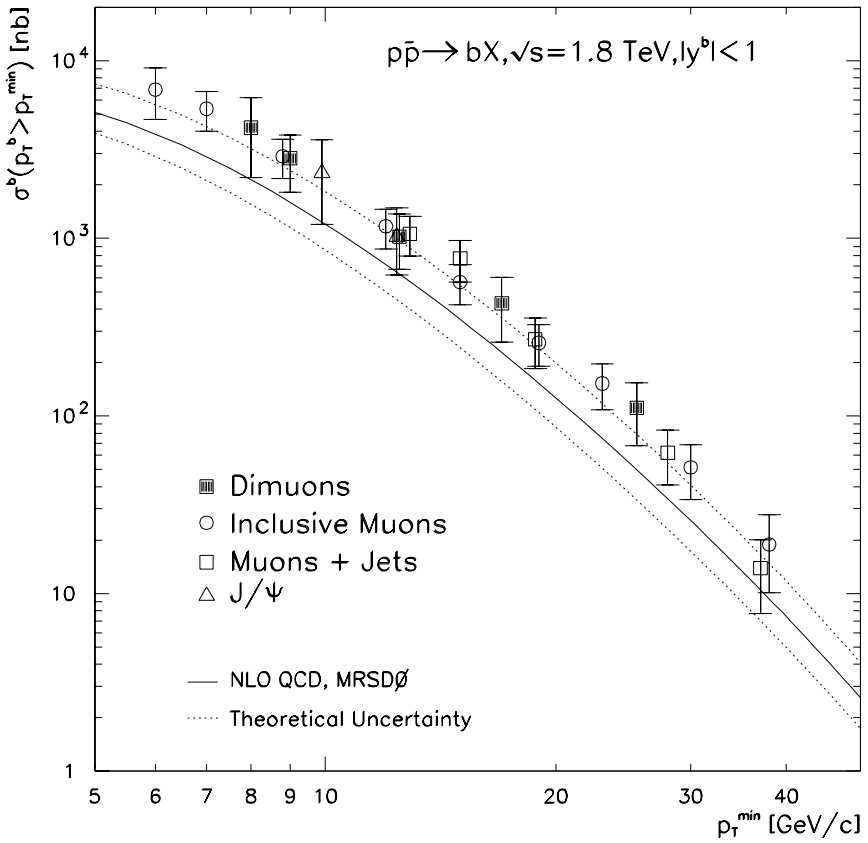


Figure 10-1: $b$-quark production cross section for $|y^b| < 1.0$ as a function of $p_T^{min}$ for this measurement and other measurements made using the DØ detector. Also shown is the $\mathcal{O}(\alpha_s^3)$ calculation(solid line) and its error bands(dashed lines). The values of the central theory prediction and its errors is described in the text.

| $p_T^{\mu_1}$ [GeV/c] | $p_T^{\mu_2}$ [GeV/c] | $p_T^{min}$ [GeV/c] | $\sigma_b(p_T^b > p_T^{min})[\mu\text{b}]$ Weighted Average |
|---|---|---|---|
| 4 | 4 | 8.0 | $4.08 \pm 1.93$ |
| 5 | 4 | 9.0 | $2.82 \pm 0.98$ |
| 7 | 4 | 12.5 | $1.02 \pm 0.36$ |
| 10 | 4 | 17.0 | $0.43 \pm 0.15$ |
| 15 | 4 | 25.5 | $0.11 \pm 0.04$ |

Table 10-1: The inclusive $b$-quark cross section $\sigma_b(p_T^b > p_T^{min}, |y^b| < 1.0)$, where the error on the cross sections are statistical and systematic. Correlations between the three data sets have been taken into account.

made other measurements of this cross section using other data samples. These include an inclusive single muon sample[60] and an inclusive single muon plus jet sample[68]. Both of these samples collected data which are independent of the data samples used in this analysis and are subject to different backgrounds and efficiencies. The results from both of these measurements are included in Fig. 10-1, and are consistent with the measurements of this analysis. In addition, a measurement of the $b$-quark cross section is extracted from a sample of $J/\psi$ decays[82], also shown in Fig. 10-1.

All of the DØ measurements lie on the upper error bands of the theoretical prediction and agree fairly well in shape with the prediction over several orders of magnitude in cross section.

Other measurements of the $b$-quark cross section at $\sqrt{s} = 1.8$ TeV have been made using the CDF detector[36] and are shown in Fig. 10-2. The CDF results include measurements from inclusive muon and inclusive electron data samples,

as well as from $J/\psi$ and $\psi(2S)$ data[19]. Once again, Fig. 10-2 shows that the measured $b$-quark cross section agrees with the shape of the NLO calculation but lies above the central theory prediction.

Measurements of the $b$-quark cross section by the UA1 detector at CERN have yielded similar results. They have measured the $b$-quark cross section for $|y^b| < 1.5$ using a sample of dimuons[83] and muons plus jet[17] collected at a center of mass energy of $\sqrt{s} = 630$ GeV. Figure 10-3[68] shows these results along with the same theoretical prediction calculated at $\sqrt{s} = 630$ GeV and for $|y^b| < 1.5$.

The measurement of the $b$-quark cross section presented in this analysis agrees quite well with existing measurements. All of the presented data agree in shape with the NLO calculation and only differ in overall normalization. Different choices in the sets of structure functions used in the NLO calculation and new choices in the parameters $\Lambda_4$ and $\mu_0$ all effect the overall normalization of the theoretical calculations. This may account for the differences between the theory and data. It has been shown[84] that by choosing the more recent MRSA[85] structure functions, $m_b = 4.5$ GeV/c$^2$, $\mu = \mu_0/2$, and $\Lambda_5 = 300$ MeV resolves the differences between the theoretical calculation and the data at both center of mass energies, $\sqrt{s} = 630$ GeV and $\sqrt{s} = 1.8$ TeV.

Including higher orders of $\alpha_s$ ($\mathcal{O}(\alpha_s^4)$) does not necessarily mean that large contributions to the $b$-quark cross section will be calculated. The large contributions, like the ones from the $gg \rightarrow gg$ process at $\mathcal{O}(\alpha_s^3)$ do not exist at the next higher order. This implies that the expectation of $\mathcal{O}(\alpha_s)$ corrections to the NLO calculations should prevail. Preliminary calculations[15] of some of the most important $\mathcal{O}(\alpha_s^4)$ terms show that this expectation seems to hold.

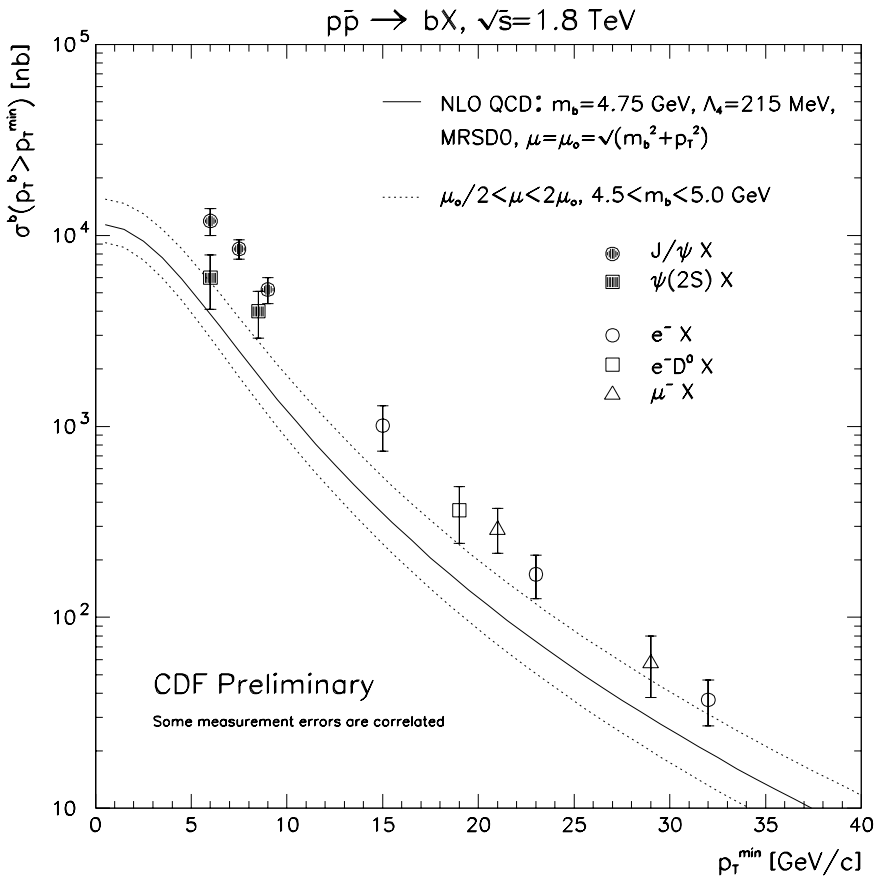


Figure 10-2: The $b$-quark production cross sections from the CDF experiment.

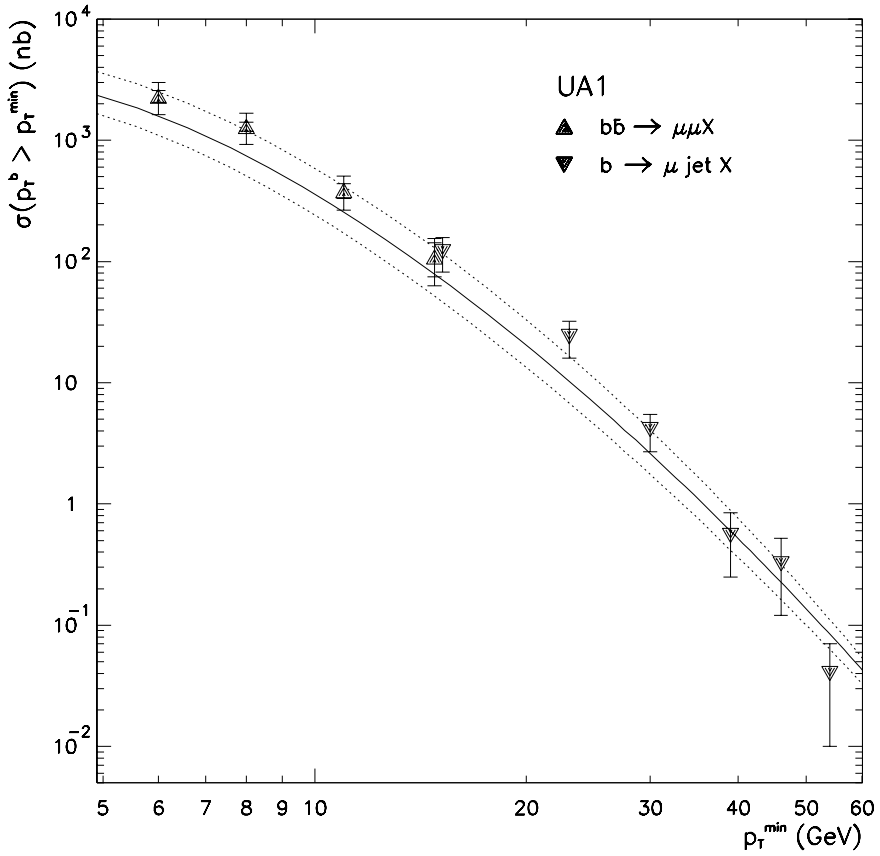


Figure 10-3: The $b$-quark production cross sections from the UA1 experiment measured at a center of mass energy of 630 GeV and for $|y^b| < 1.5$. The theoretical curve is explained in the text.

## 10.2 $b\bar{b}$ Correlations

The differential $b\bar{b}$ correlation distribution, shown in Fig. 10-4, displays a clear excess of data above the NLO MNR calculated $\Delta\phi^{\mu\mu}_{MNR}$ distribution. The results of this measurement are divided by the $\Delta\phi^{\mu\mu}_{MNR}$ calculation and are shown in Fig. 10-5. The measurement for the bin from $120^\circ < \Delta\phi^{\mu\mu} < 140^\circ$ has been omitted for clarity. This figure shows that the data differs from the NLO theoretical calculation by a overall constant of $2.6 \pm 0.4$.

The MNR calculation has been scaled by this constant and is shown with the data in Fig. 10-6. Good agreement is now found between the NLO calculation and the data. The ISAJET prediction has also been scaled by the same factor and is shown in Fig. 10-6. A clear overestimation is seen in the region around $60^\circ < \Delta\phi^{\mu\mu} < 100^\circ$, precisely where the production from gluon splitting is expected to contribute. The overestimation of gluon splitting by the ISAJET Monte Carlo is in agreement with the calculation from the fit to the data of the three heavy flavor contributions. These fits are summarized in Table 9-5 and shown in Fig. 9-27.

A similar measurement has been made by the UA1 detector at a center of mass energy of $\sqrt{s} = 630$ GeV. The results for high mass, non-isolated muon pairs from $b\bar{b}$ semileptonic decays[83] are shown in Fig. 10-7. The NLO theoretical calculation show in this figure uses the values $\Lambda_4 = 260$ MeV and DFLM[86] structure functions. Once again, the data show a systematic shift above the NLO calculation.

More recently, the CDF collaboration has measured the correlated $\mu$ - $\bar{b}$ jet cross section[87] at the Tevatron. In this measurement, the first $b$ is identified through the semileptonic decay to a muon and the other $b$-quark, referred to as $\bar{b}$, is identified using precision track reconstruction of particles in jets to measure

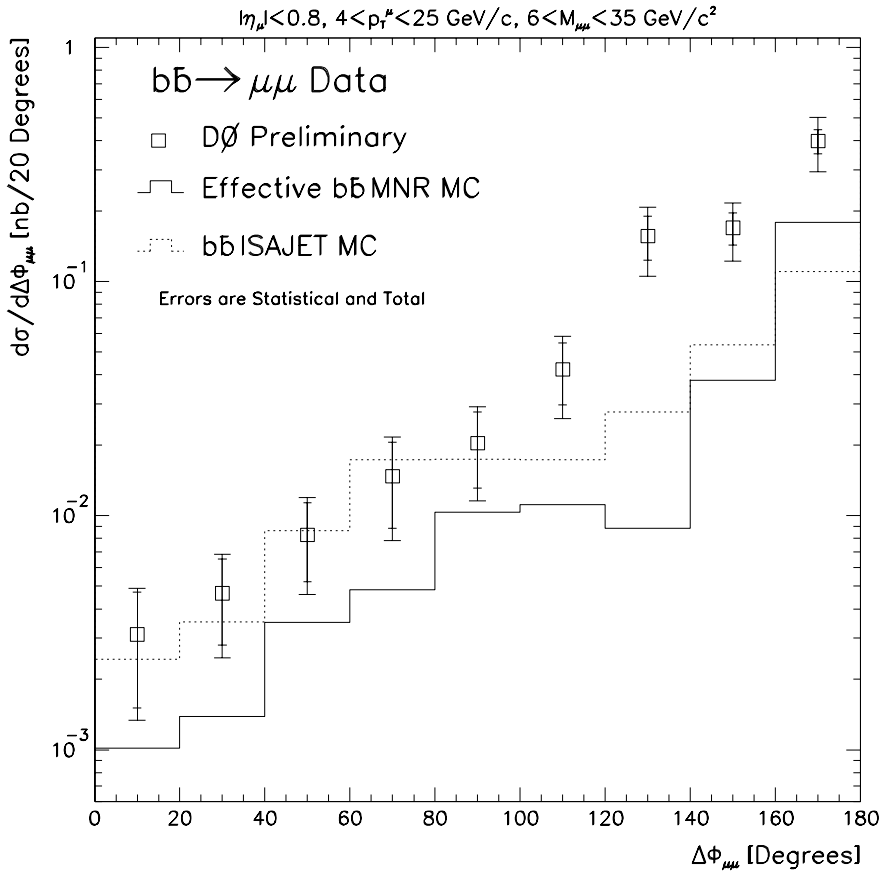


Figure 10-4: Comparison of the MNR calculated $\Delta\phi^{\mu\mu}$ $b\bar{b}$ cross section with the data and the NDE normalized ISAJET estimate.

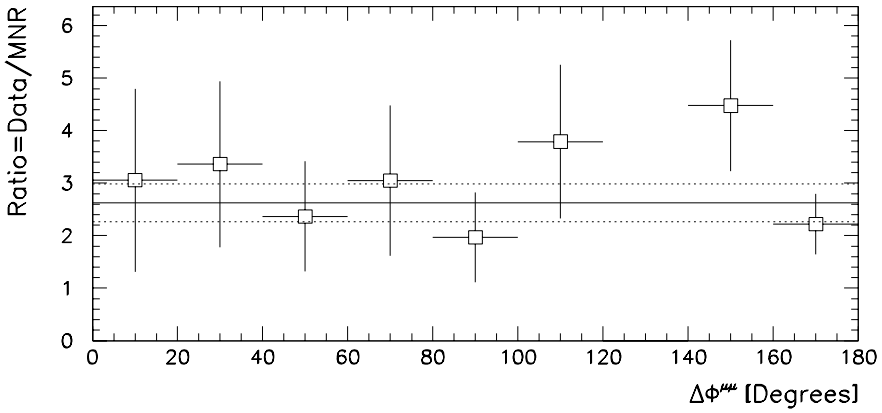


Figure 10-5: Ratio of the data to the MNR calculation. The data bin from 120° < $\Delta\phi^{\mu\mu}$ <140° has been omitted from the fit. The solid line is the mean value of the fit, $R = 2.6$, and the dashed lines are the errors, $\sigma_R = \pm 0.4$

displaced particles from the $\overline{b}$ decay. The muon is required to have $p_T^{\mu} > 9$ GeV/c and $|\eta^{\mu}| \leq 0.6$, while the jet is required to have $E_T^{\overline{b}} > 10$ GeV and $|\eta^{\overline{b}}| < 1.5$. Figure 10-8 shows these results compared to the NLO calculation of MNR using $\mu_0 = \sqrt{m_b^2 + (p_T^{b^2} + p_T^{\overline{b}^2})/2}$, MRSD0 structure functions, and the Peterson parameter of $\epsilon = 0.006$. The $B$-hadrons are decayed according to a CLEO Monte Carlo package. The data show agreement with the shape of the NLO calculation but again lie above the central theoretical prediction.

In addition, the CDF collaboration has measured the azimuth angle between two muons associated with $b\overline{b}$ production[88]. The measurement utilizes low $p_T$ muons, $3 < p_{T_2}^{\mu} < 7$ GeV/c and $p_{T_1}^{\mu} > 3$ GeV/c, with invariant mass, $M^{\mu\mu} > 5$ GeV/c$^2$. The $b\overline{b}$ signal is extracted by using differences in the impact parameter between the contributing processes to the total dimuon sample. The results of this preliminary measurement are shown in Fig. 10-9 along with the NLO calculation

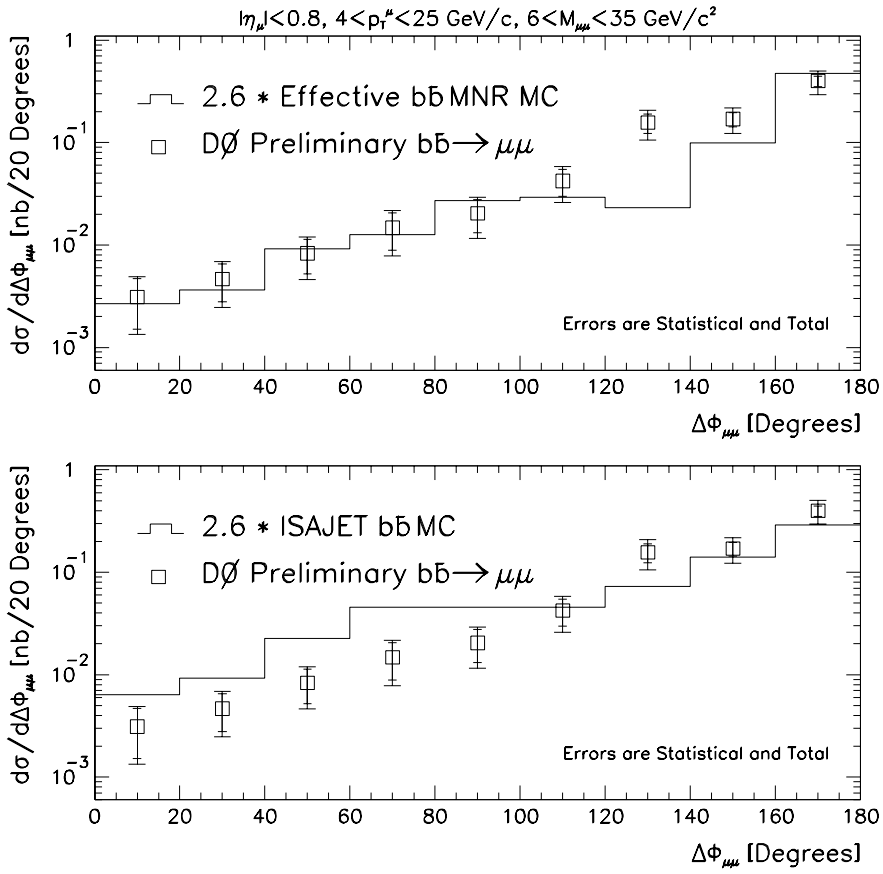


Figure 10-6: (top) Scaled MNR calculation compared to the data and (bottom) scaled ISAJET estimate. The scale factors are the same for both plots.

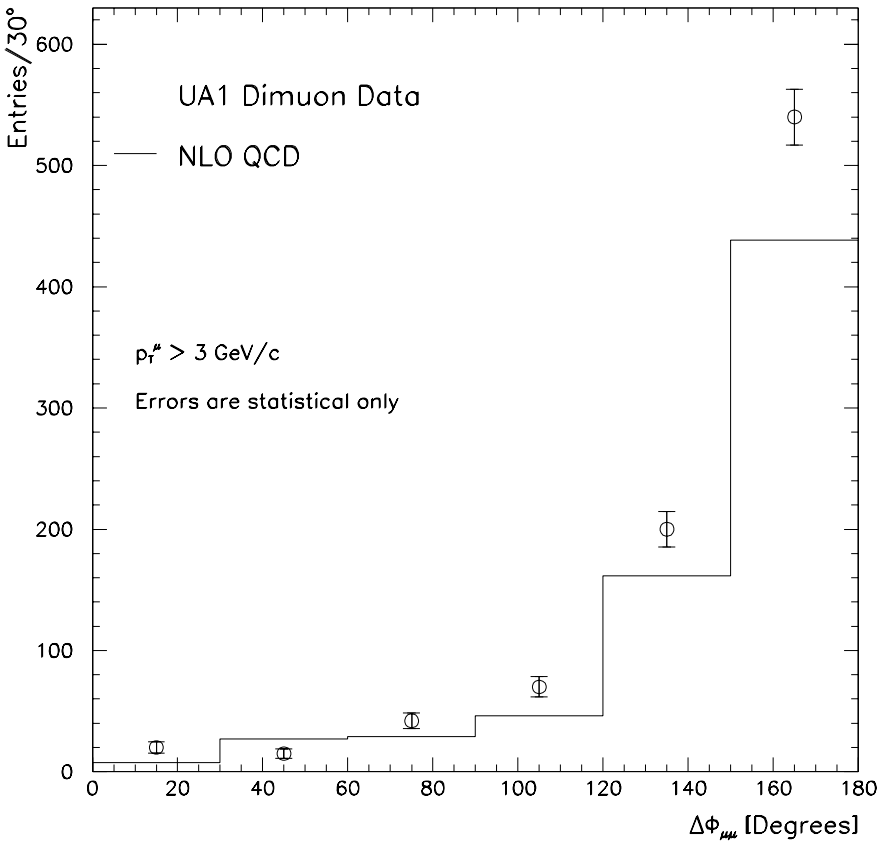


Figure 10-7: Results of the UA1 analysis for $b\bar{b}$ correlations.

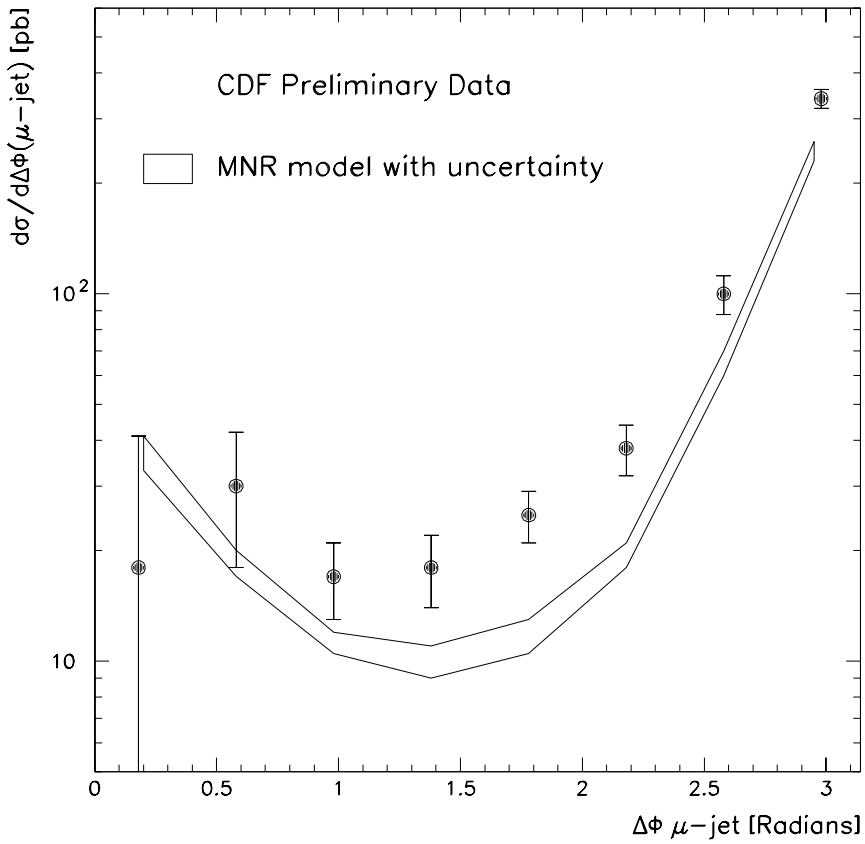


Figure 10-8: $\mu$ - $\overline{b}$ jet correlation distribution from the CDF experiment. The uncertainty in the theory is from the muonic branching fraction and fragmentation model.

with decay and detector simulation added on. Once again, the shape of the measured cross section agrees with the theoretical calculation but with the a higher normalization for the data.

The $b\bar{b}$ correlation measurement made in this analysis shows good qualitative agreement with the NLO calculations of MNR and are consistent with other measurements of correlated $b\bar{b}$ production. It has also been shown that while the ISAJET Monte Carlo overestimates the contribution of gluon splitting to the $b$-quark cross section, there clearly exists a sizeable higher order contribution. This presence of higher order contributions is shown in Fig. 9-27 where the populated small $\Delta\phi^{\mu\mu}$ bins can not be explained by the leading order contribution alone.

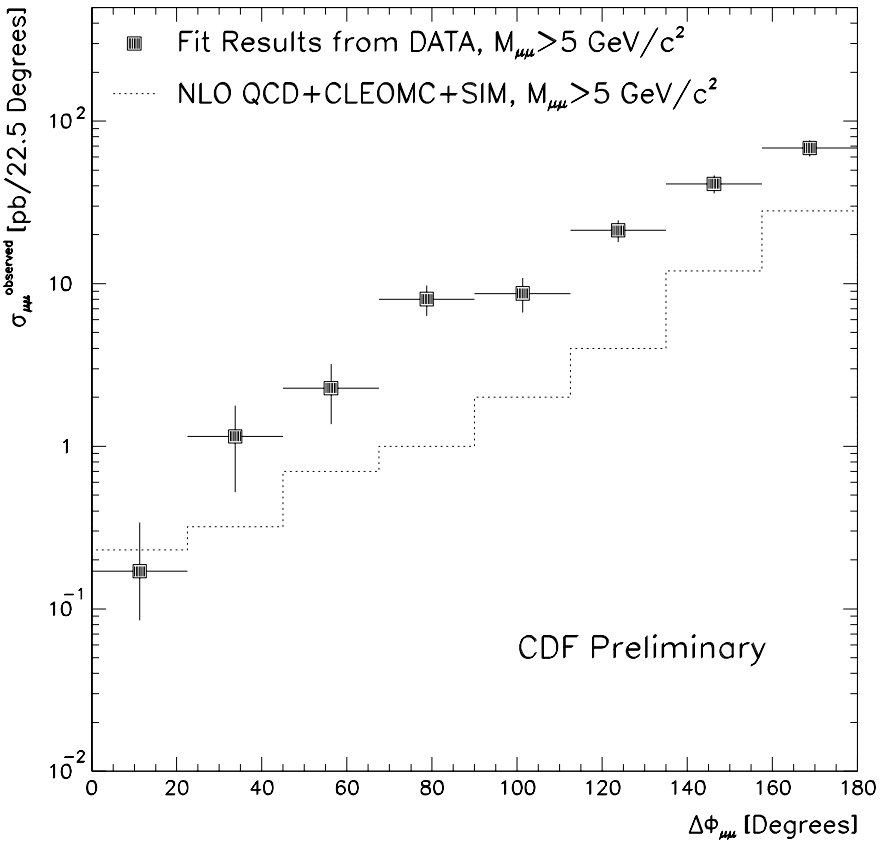


Figure 10-9: $\Delta\phi^{\mu\mu}$ correlation distribution from $b\bar{b}$ production measured by the CDF experiment. The NLO theoretical calculation with a decay and trigger simulation added on is shown for comparison.

# Appendix A

# The DØ Coordinate System

The DØ experiment uses a right-handed coordinate system where:

- the $+x$-axis lies in the plane of the Tevatron ring and points outward
- the $+y$-axis is perpendicular to the ring and points upward
- the $+z$-axis is along the proton direction.

The center of the coordinate system $(x, y, z) = (0, 0, 0)$ is located at the center of the detector.

Two common angle definitions used at DØ are: $\phi$, which is the azimuthal angle about the $z$-axis with $\phi = 0$ along the positive $x$-axis, and $\theta$, the polar angle, with $\theta = 0$ along the proton beam direction($+z$-axis). Another useful variable is the pseudo-rapidity $\eta$, which is defined as:

$$\eta = -\ln \tan \frac{\theta}{2}. \tag{A.1}$$

The pseudo-rapidity approximates the true rapidity, $y$,

$$y = \frac{1}{2}\ln(\frac{E + p_z}{E - p_z}),$$

for finite angles in the limit that $(m/E) \rightarrow 0$. Rapidity is used as a substitute for polar angles because differences in rapidity are Lorentz-invariant quantities.

# Appendix B

# Unfolding Factors Associated with Kinematic Cuts

Tables B-1 and B-2 summarize the unfolding factors used to determine the effect of events that lie outside the accepted true muon kinematic range,

- $4 \leq p_T^{\mu}(\text{trailing}) \leq 25$ GeV/c
- $|\eta^{\mu}| \leq 0.8$
- $6 \leq M^{\mu\mu} \leq 35$ GeV/c$^2$
- $\Delta\phi_{3D} \leq 165°$,

but get reconstructed into the measured final data sample. Since these events should not contribute to the true variable cross section measurement, they need to be removed from the data sample.

| | Unfolding Factor | | |
|---|---|---|---|
| $p_T^\mu$(leading) [GeV/c] | MU_2_HIGH | MU_1_JET | MU_JET_LOW |
| 4-5 | 0.75 | 0.71 | 0.78 |
| 5-7 | 0.86 | 0.81 | 0.75 |
| 7-10 | 0.78 | 0.86 | 0.83 |
| 10-15 | 0.86 | 0.88 | 0.86 |
| 15-25 | 0.95 | 0.94 | 0.93 |

Table B-1: Unfolding factors associated with making cuts in the measured muon kinematic spectrum calculated as a function of $p_T^\mu$(leading) for each of the three trigger bits.

| | Unfolding Factor | | |
|---|---|---|---|
| $\Delta\phi^{\mu\mu}$ [Degrees] | MU_2_HIGH | MU_1_JET | MU_JET_LOW |
| 0-60 | 0.57 | 0.68 | 0.68 |
| 60-120 | 0.92 | 0.88 | 0.84 |
| 120-140 | 0.89 | 0.87 | 0.85 |
| 140-160 | 0.88 | 0.90 | 0.89 |
| 160-180 | 0.92 | 0.91 | 0.91 |

Table B-2: Unfolding factors associated with making cuts in the measured muon kinematic spectrum calculated as a function of $\Delta\phi^{\mu\mu}$ for each of the three trigger bits.

# Appendix C

# Inputs to the Inclusive Dimuon Cross Section

Tables C-1 through C-3 summarize the inputs to the inclusive heavy quark dimuon and $b\bar{b} \rightarrow \mu\mu$ cross section calculations. The uncertainties in the number of events in each bin of $N_{Cosmic}$ and $N_{b\bar{b}}$ reflect those due to the minimization of the log-likelihood function. The $p_T^{\mu}$ and $\Delta\phi^{\mu\mu}$ centroid for each bin is calculated by taking the weighted average of data points in that bin. Detector resolution and smearing, as described in Sec. 9.1, are not included here.

| Variable | Value | | | | |
|---|---|---|---|---|---|
| $p_T^\mu$ Bin [GeV/c] | 4-5 | 5-7 | 7-10 | 10-15 | 15-25 |
| $p_T^\mu$ [GeV/c] | 4.6 | 6.1 | 8.4 | 12.2 | 18.3 |
| $N_{Data}$ | 13 | 39 | 70 | 45 | 25 |
| $N_{Cosmic}$ | 0.6±0.6 | 0.5±0.5 | 2.5±2.4 | 1.7±1.7 | 1.3±1.2 |
| $N_{b\bar{b}}$ | 8.0±1.0 | 25.7±3.3 | 48.1±6.2 | 31.4±4.1 | 17.7±2.2 |
| $\epsilon_{Trig}$[%] | 10.3±1.8 | 13.5±2.3 | 17.9±3.0 | 20.1±3.4 | 20.7±3.5 |
| $\epsilon_{Sel}$[%] | 3.0±0.2 | 8.8±0.7 | 20.4±1.6 | 27.9±2.2 | 31.0±2.5 |
| $\int \mathcal{L}dt$ [pb$^{-1}$] | | | 6.6±0.4 | | |
| $\Delta p_T^\mu$ [GeV/c] | 1 | 2 | 3 | 5 | 10 |

| Variable | Value | | | | | | | | |
|---|---|---|---|---|---|---|---|---|---|
| $\Delta\phi^{\mu\mu}$ Bin [Deg] | 0-20 | 20-40 | 40-60 | 60-80 | 80-100 | 100-120 | 120-140 | 140-160 | 160-180 |
| $\Delta\phi^{\mu\mu}$ [Deg] | 11 | 31 | 51 | 71 | 87 | 110 | 131 | 152 | 170 |
| $N_{Data}$ | 2 | 5 | 8 | 6 | 6 | 12 | 23 | 41 | 89 |
| $N_{Cosmic}$ | 0.4±0.4 | 0.1±0.1 | 0.6±0.6 | 0.3±0.3 | 0.3±0.3 | 1.2±1.2 | 0.7±0.7 | 0.7±0.7 | 2.3±2.3 |
| $N_{b\bar{b}}$ | 1.5±0.2 | 4.3±0.6 | 6.0±0.8 | 5.0±0.6 | 3.8±0.5 | 8.6±1.1 | 16.8±2.2 | 28.1±3.6 | 56.4±7.3 |
| $\epsilon_{Trig}$[%] | 15.2±2.6 | 18.7±3.2 | 25.5±4.3 | 24.0±4.1 | 18.5±3.1 | 19.1±3.2 | 15.9±2.7 | 14.4±2.4 | 11.4±1.9 |
| $\epsilon_{Sel}$[%] | 55.0±4.4 | 46.3±3.7 | 33.3±2.7 | 20.6±1.6 | 17.4±1.4 | 13.6±1.1 | 12.6±1.0 | 19.7±1.6 | 25.1±2.0 |
| $\int \mathcal{L}dt$ [pb$^{-1}$] | | | | | 6.6±0.4 | | | | |

Table C-1: Input numbers for the inclusive heavy quark dimuon and $b\bar{b} \to \mu\mu$ cross sections as a function of $p_T^\mu$(leading) and $\Delta\phi^{\mu\mu}$ for MU_2_HIGH.

| Variable | Value | | | | |
|---|---|---|---|---|---|
| $p_T^\mu$ Bin [GeV/c] | 4-5 | 5-7 | 7-10 | 10-15 | 15-25 |
| $p_T^\mu$ [GeV/c] | 4.7 | 6.0 | 8.3 | 12.0 | 18.4 |
| $N_{Data}$ | 17 | 89 | 81 | 59 | 31 |
| $N_{Cosmic}$ | 1.0±1.0 | 0.9±0.9 | 5.7±5.7 | 4.5±4.5 | 1.8±1.8 |
| $N_{b\bar{b}}$ | 7.5±1.0 | 43.9±5.7 | 45.9±6.0 | 37.2±4.8 | 18.8±2.4 |
| $\epsilon_{Trig}$[%] | 8.8±1.1 | 16.4±2.1 | 24.5±3.2 | 33.0±4.2 | 47.0±6.1 |
| $\epsilon_{Sel}$[%] | 4.2±0.3 | 17.0±1.4 | 26.6±2.1 | 29.4±2.4 | 28.5±2.3 |
| $\int \mathcal{L}dt$ [pb$^{-1}$] | | | 3.7±0.2 | | |
| $\Delta p_T^\mu$ [GeV/c] | 1 | 2 | 3 | 5 | 10 |

| Variable | Value | | | | | | | | |
|---|---|---|---|---|---|---|---|---|---|
| $\Delta\phi^{\mu\mu}$ Bin [Deg] | 0-20 | 20-40 | 40-60 | 60-80 | 80-100 | 100-120 | 120-140 | 140-160 | 160-180 |
| $\Delta\phi^{\mu\mu}$ [Deg] | 15 | 30 | 50 | 70 | 87 | 112 | 131 | 152 | 170 |
| $N_{Data}$ | 2 | 4 | 10 | 11 | 12 | 14 | 26 | 72 | 126 |
| $N_{Cosmic}$ | 0.9±0.9 | 0.3±0.3 | 2.2±2.2 | 0.5±0.5 | 0.4±0.4 | 1.2±1.2 | 1.7±1.7 | 1.7±1.7 | 5.1±5.1 |
| $N_{b\bar{b}}$ | 0.9±0.1 | 3.2±0.4 | 5.7±0.7 | 6.9±0.9 | 7.4±1.0 | 8.4±1.1 | 15.3±2.0 | 41.0±5.3 | 64.5±8.3 |
| $\epsilon_{Trig}$[%] | 38.0±4.9 | 40.0±5.2 | 40.2±5.2 | 38.7±5.0 | 32.1±4.2 | 26.3±3.4 | 17.5±2.3 | 19.6±2.5 | 19.4±2.5 |
| $\epsilon_{Sel}$[%] | 45.8±3.7 | 46.0±3.7 | 36.5±2.9 | 23.2±1.9 | 23.4±1.9 | 19.5±1.6 | 22.8±1.8 | 30.6±2.4 | 35.1±2.8 |
| $\int \mathcal{L}dt$ [pb$^{-1}$] | | | | | 3.7±0.2 | | | | |

Table C-2: Input numbers for the inclusive heavy quark dimuon and $b\bar{b} \to \mu\mu$ cross sections as a function of $p_T^\mu$(leading) and $\Delta\phi^{\mu\mu}$ for MU_1_JET.

| Variable | Value | | | | |
|---|---|---|---|---|---|
| $p_T^\mu$ Bin [GeV/c] | 4-5 | 5-7 | 7-10 | 10-15 | 15-25 |
| $p_T^\mu$ [GeV/c] | 4.7 | 6.0 | 8.3 | 12.1 | 18.1 |
| $N_{Data}$ | 29 | 117 | 113 | 90 | 48 |
| $N_{Cosmic}$ | 0.1±0.1 | 1.3±0.6 | 3.7±1.9 | 3.2±1.6 | 2.9±1.5 |
| $N_{b\bar{b}}$ | 9.5±1.2 | 45.2±5.8 | 52.3±6.7 | 48.0±6.1 | 24.7±3.2 |
| $\epsilon_{Trig}[\%]$ | 4.2±0.6 | 7.6±1.1 | 13.1±1.8 | 21.7±3.0 | 32.6±4.6 |
| $\epsilon_{Sel}[\%]$ | 5.7±0.5 | 22.5±2.8 | 30.1±2.4 | 34.5±2.8 | 27.7±2.2 |
| $\int \mathcal{L}dt$ [pb$^{-1}$] | | | 6.5±0.4 | | |
| $\Delta p_T^\mu$ [GeV/c] | 1 | 2 | 3 | 5 | 10 |

| Variable | Value | | | | | | | | |
|---|---|---|---|---|---|---|---|---|---|
| $\Delta\phi^{\mu\mu}$ Bin [Deg] | 0-20 | 20-40 | 40-60 | 60-80 | 80-100 | 100-120 | 120-140 | 140-160 | 160-180 |
| $\Delta\phi^{\mu\mu}$ [Deg] | 13 | 29 | 51 | 71 | 88 | 110 | 131 | 152 | 170 |
| $N_{Data}$ | 7 | 9 | 13 | 11 | 17 | 23 | 45 | 90 | 182 |
| $N_{Cosmic}$ | 1.9±1.0 | 1.0±0.5 | 1.4±0.7 | 0.2±0.1 | 0.3±0.2 | 0.9±0.5 | 1.5±0.8 | 1.1±0.6 | 2.8±1.4 |
| $N_{b\bar{b}}$ | 3.8±0.5 | 6.2±0.8 | 7.4±0.9 | 6.3±0.8 | 7.9±1.0 | 11.4±1.5 | 22.1±2.8 | 41.0±5.3 | 73.6±9.4 |
| $\epsilon_{Trig}[\%]$ | 22.3±3.1 | 26.3±3.7 | 21.2±3.0 | 15.1±2.1 | 14.5±2.0 | 10.2±1.4 | 5.8±0.8 | 6.8±1.0 | 7.3±1.0 |
| $\epsilon_{Sel}[\%]$ | 56.8±4.5 | 53.1±4.2 | 43.9±3.5 | 36.6±2.9 | 34.5±2.8 | 34.3±2.7 | 31.7±2.5 | 48.6±3.9 | 46.1±3.7 |
| $\int \mathcal{L}dt$ [pb$^{-1}$] | | | | | 6.5±0.4 | | | | |

Table C-3: Input numbers for the inclusive heavy quark dimuon and $b\bar{b} \to \mu\mu$ cross section as a function of $p_T^\mu$(leading) and $\Delta\phi^{\mu\mu}$ for MU_JET_LOW.

# REFERENCES

[1] DØ Collaboration, S. Abachi *et al.*, Phys. Rev. Lett. **74**, 2632 (1995).

[2] CDF Collaboration, F. Abe *et al.*, Phys. Rev. Lett. **74**, 2626 (1995).

[3] J. C. Street and E. C. Stevenson, Phys. Rev. **52**, 1003 (1937).

[4] M. L. Perl *et al.*, Phys. Rev. Lett. **35**, 1489 (1975); Phys. Lett. B **63**, 466 (1976).

[5] L. Montanet *et al.*, Phys. Rev. D **50**, 1173 (1994).

[6] E. Fermi, Zeit. Phys. **88**, 161 (1934).

[7] J. Bernstein, M. Ruderman, and G. Feinberg, Phys. Rev. **132**, 1227 (1963), and references therein.

[8] Richard C. Henry and P. D. Feldman, Phys. Rev. Lett. **47**, 618 (1981), and references therein.

[9] M. Gell-Mann, Phys. Lett. **8**, 214 (1964).

[10] J. J. Aubert *et al.*, Phys. Rev. Lett. **33**, 1404 (1974).
J.-E. Augustin *et al.*, Phys. Rev. Lett. **33**, 1406 (1974).

[11] S. W. Herb *et al.*, Phys. Rev. Lett. **39**, 252 (1977).
W. R. Innes *et al.*, Phys. Rev. Lett. **39**, 1240 (1977).

[12] Vernon D. Barger and Roger J. N. Phillips, *Collider Physics*, Addison-Wesley, 1987.

[13] S. L. Glashow, Nucl. Phys. **10**, 107 (1959).
S. Weinberg, Phys. Rev. Lett. **19**, 1264 (1967).
A. Salam and J. C. Ward, Nuovo Cimento **11**, 568 (1959).
A. Salam, *Proc. 8th Nobel Symposium, Aspenäsgarden, Sweden: Elementary Particle Theory*, N. Svartholm (ed.), Almquist and Wiksell, Stokholm, 1968, p. 367.

[14] P. W. Higgs, Phys. Lett. **12**, 132 (1964).

[15] P. Nason, S. Dawson, and R.K. Ellis, Nucl. Phys. **B327**, 49 (1989).

[16] W. Beenakker, *et al.*, Phys. Rev. D **40**, 54 (1989).

[17] UA1 Collaboration, C. Albajar *et al.*, Phys. Lett. B **213**, 405 (1988), **256**, 121 (1991).

[18] P. Nason, S. Dawson, and R.K. Ellis, Nucl. Phys. **B303**, 607 (1988).

[19] CDF Collaboration, F. Abe *et al.*, Phys. Rev. Lett. **68**, 3403 (1992), **69**, 3704 (1992), **71**, 500, 2396, 2537 (1993); Phys. Rev. D **50**, 4258 (1994).

[20] M. Mangano, P. Nason, G. Ridolfi, Nucl. Phys. **B373**, 295 (1992).

[21] W.A. Bardeen, A.J. Buras, D.W. Duke, and T. Muta, Phys. Rev. D **18**, 3998 (1978).

[22] E. Eichten, I. Hinchliffe, K. Lane, and C. Quigg, Rev. Mod. Phys. **56**, 579 (1984), **58**, 1065 (1986).

[23] Lai, Botts, Huston, Morfin, Owens, Qin, Tung, and Weerts, Phys. Rev. D **51**, 4763 (1995).

[24] A.D. Martin, R.G. Roberts, and W.J. Stirling, Phys. Rev. D **37**, 1161 (1988).

[25] H. Plothow-Besch, *PDFLIB: Structure Functions and $\alpha_s$ Calculations User's Manual, Version 3.00*, CERN program library entry W5051, 1992.

[26] A.D. Martin, R.G. Roberts, and W.J. Stirling, Phys. Rev. D **43**, 3648 (1991).

[27] F. Paige and S. Protopopescu, BNL Report No. BNL38034, 1986 (unpublished), release v 6.48.

[28] G.C. Fox and S. Wolfram, Nucl. Phys. **B168**, 285 (1980).

[29] R.D. Field and R.P. Feynman, Nucl. Phys. **B136**, 1 (1978).

[30] C. Peterson, *et al.*, Phys. Rev. D **27**, 105 (1986).

[31] S. Squarcia, "Heavy Flavor Physics at LEP", CERN-PPE/94-69 (1994).

[32] Torbjörn Sjöstrand, International Journal of Modern Physics A, Vol. 3, No. 4, 751-823 (1988).

[33] H.-U. Bengtsson, Computer Phys. Comm. **31**, 323 (1984).

[34] B. Andersson, G. Gustafson, and C. Peterson, Zeit. Phys. C **1**, 105 (1979).

[35] G. Marchesini and B.R. Webber, Nucl. Phys. **B310**, 461 (1988).

[36] CDF Collaboration, F. Abe *et al.*, Nucl. Instr. Meth. A **271**, 387 (1988).

[37] DØ Collaboration, S. Abachi *et al.*, Nucl. Instr. Meth. A **338**, 185 (1994).

[38] A.R. Clark *et al.*, Nucl. Instr. Meth. A **315**, 193 (1992).

[39] NiCoTin is an alloy of C0, Cr, Ni, Fe, Mo in respective fractions of 38.8%, 19.3%, 15.6%, 13.3%, and 11.4%.

[40] J. Kadyk, Nucl. Instr. Meth. A **300**, 436 (1991).

[41] V.L. Ginzberg and I.M. Frank, JETP **16**, 15 (1946).

[42] "Etude d'un Detecteur a Rayonnement de Transition pour l'Experience DØ au FNAL", Fabrice Feinstein, Ph.D Thesis, A l'Universite de Paris-Sud, Centre d'Orsay, December 1987 (unpublished).

[43] Thomas Ferbel, *Experimental Techniques in High Energy Physics*, Addison-Wesley (1987), p.391.

[44] A.R. Clark *et al.*, Nucl. Instr. Meth. A **279**, 243 (1989).

[45] R. Avery *et al.*, "Results from a Beam Test of the DØ Forward Drift Chamber", IEEE Trans. Nucl. Science (1992).

[46] D. Green *et al.*, Nucl. Instr. Meth. A **244**, 356 (1986).

[47] R. Yamada *et al.*, IEEE Transactions on Magnetics **28**, 520 (1992).

[48] R. Yamada *et al.*, "Field Calculation of DØ Toroids and Comparison with Measurement", Fermilab TM-1786 (1992).

[49] Yu. M. Antipov *et al.*, Nucl. Instr. Meth. A **297**, 121 (1990).

[50] UAZHEP::USR$ ROOT2:[FEIN.DST]BAD_RUN.LST.

[51] CAFIX, DØLIBRARY program package.

[52] "Measurement of the $\Upsilon$ and Drell-Yan Production Cross Sections at $\sqrt{s}$ = 1.8 TeV Using Dimuons", Alex B. Smith, Ph.D Thesis, University of Arizona, 1995 (unpublished).

[53] J. Bantly, A. Brandt, R. Partridge, J. Perkins, D. Puseljic, DØ Internal Note # 2544, Report No. FERMILAB-TM-1930 (1995).

[54] N. Amos *et al.*, Phys. Lett. B **243**, 158 (1990).

[55] CDF Collaboration, F. Abe *et al.*, Phys. Rev. D **50**, 5550 (1994).

[56] CDF Collaboration, F. Abe *et al.*, Phys. Rev. D **50**, 5518 (1994).

[57] CDF Collaboration, F. Abe *et al.*, Phys. Rev. D **50**, 5535 (1994).

[58] LUMIN_UTIL, DØLIBRARY program package.

[59] DØ Collaboration, S. Abachi *et al.*, Phys. Rev. Lett. **75**, 1456 (1995).

[60] DØ Collaboration, S. Abachi *et al.*, Phys. Rev. Lett. **74**, 3548 (1995).

[61] "Inclusive $J/\psi$ Production at DØ ", Christopher R. Murphy, Ph.D Thesis, Indiana University, April 1995 (unpublished).

[62] "Dijet Angular Distributionsat $\sqrt{s}$ = 1800 GeV Using the DØ Detector", Andrew J. Milder, Ph.D Thesis, University of Arizona, 1993.

"Measurement of the Inclusive Jet Cross Sections at $\sqrt{s}$ = 1.8 TeV with the DØ Detector", Victor D. Elvira, Ph.D Thesis, Universidad de Buenos Aries, Argentina, 1994.

Bob Kehoe, "Resolution Bias in Jet Response Measurement", DØ Internal Note #2052 (1994).

[63] R. Astur, "A Study of Fake Jets in the DØ Detector", DØ Internal Note #1662 (1993).

[64] R. Astur, J. Blazey, and D. Elvira, "A Study of Standard Jet Cuts and their Efficiencies using DØ Collider Data", DØ Internal Note #1763 (1993).

[65] T. Joffe-Minor and R. Astur, "A Study of the Effects of the CAFIX Energy Scale Corrections", DØ Internal Note #2211 (1994).

[66] "Measurement of the $B^{\circ}$-$\overline{B}^{\circ}$ Mixing Parameter using Dimuon Events Collected with the DØ Detector", E. James, Ph.D Thesis, University of Arizona, 1995 (unpublished).

[67] MU_SMEAR, DØLIBRARY program package.

[68] "A Measurement of Bottom Quark Production in $p\overline{p}$ Collisions at $\sqrt{s}$ = 1.8 TeV", T. Huehn, Ph.D Thesis, University of California, Riverside, 1995 (unpublished), and references therein.

[69] M. Mangano, Program HQOUNW.FOR, described in "Quarkonium Production Codes: Documentation", (unpublished).

[70] CDF Collaboration, F. Abe *et al.*, Phys. Rev. Lett. **75**, 4358 (1995).

[71] DELPHI Collaboration, Abreu *et al.*, Nucl. Phys. **B418**, 403 (1994).

[72] D. Hedin, "Preliminary DØ Punchthrough Rates", DØ Internal Note #1738 (1993).

[73] C. Gerber, P. Quintas, D. Wood, "Cross Section Measurements of $W$ and $Z$ to Muons at DØ ", DØ Internal Note #2099 (1994).

[74] D. Hedin, "Eye–scanning for unbiased events", FNALD0::USR$ROOT3:[HEDIN]SCANXXX.DOC.

[75] F. James, MINUIT, CERN Program Library Entry *D506*, (1992).

[76] D. Wood, private communication.

[77] E. James, private communication.

[78] C. Gerber and P. Quintas, "Muon Momentum Resolution from DØ Reco V10", DØ Internal Note #1985 (1993).

[79] G. D'Agostini, "A Multidimensional Unfolding Method Based on Bayes' Theorem", DESY 94-099.

[80] T. Huffman, Ph.D Thesis, Purdue University, 1992 (unpublished).

[81] Kamel Bazizi, "Muon and $b$-Quark Production Cross Sections from the 1992-1993 Run", DØ Internal Note #2593 (1995).

[82] DØ Collaboration, S. Abachi, *et al.*, Report No. FERMILAB-PUB-96/03-E (1996).

[83] J. Geiser, Ph.D Thesis, University of Aachen, Germany, 1992.

[84] M. Mangano, "Heavy Quark Production in Hadronic Collisions", Report No. CERN-TH/95-191 (1995).

[85] A.D. Martin, R.G. Roberts, and W.J. Stirling, Phys. Rev. D **50**, 6734 (1994).

[86] M. Diemoz, F. Ferroni, E. Longo, and G. Martinelli, Zeit. Phys. C **39**, 21 (1988).

[87] CDF Collaboration, F. Abe *et al.*, Report No. FERMILAB-PUB-95/289-E (1995).

[88] CDF Collaboration, F. Abe *et al.*, Report No. FERMILAB-CONF-95/223-E (1995).